USING LONG-TERM MILLISECOND PULSAR TIMING TO MODEL PULSAR COMPANIONS AND THEIR HOST STAR CLUSTERS.

Brian James Prager
Silver Spring, Maryland

B.S. Astronomy & Physics, University of Maryland, 2011

M.S. Astronomy, University of Virginia, 2013

A Dissertation Presented to the Graduate
Faculty of the University of Virginia
in Candidacy for the Degree of
Doctor of Philosophy

Department of Astronomy

University of Virginia
August 2017

Committee Members:

Scott M. Ransom
Phil Arras
Remy Indebetouw
Brad Cox

Dedicated to Molly and Kyle, because every journey worth taking needs a few close friends to walk alongside...

Abstract

Since their discovery in 1967, neutron stars have been of great interest to the scientific community for their extreme physical characteristics. With supra-nuclear core densities and magnetic field strengths anywhere from 10^9 to 10^{15} Gauss, these objects exist on the boundaries of science as we know it. Of particular interest are those neutron stars with extraordinarily stable rotational periods of a few milliseconds. These millisecond pulsars are thought to be the end result of a neutron star that has accreted mass from a companion star, giving it the angular momentum needed to spin rapidly.

While we are beginning to find more pulsars in the process of turning into millisecond pulsars in the spiral disk of the Milky Way, we have traditionally found more systems close to this evolutionary stage in massive star clusters known as globular clusters. The large stellar interaction rate within globular clusters effectively increases the chances that a pulsar will have a nearby companion to interact with. More than 15 years of observations have been accumulated of millisecond pulsars in globular clusters, with some systems containing as many as 37 known pulsars within their core (with evidence of many more yet to be discovered).

My thesis is broken into three broad areas of study. The first is designed to take the more than fifteen years of pulsar data available for the globular cluster Terzan 5 and use it to model the physical characteristics of the system. Terzan 5 is a unique globular cluster in that it is thought to be the remnant of a smaller galaxy that was

absorbed by the Milky Way, yet studies of the system have been made difficult due to strong foreground contamination. Using pulsars as accelerometers to map out the density of the cluster I have derived the mass and physical extent of the cluster, which can better inform our understanding of the origin of Terzan 5. We have also used pulsar data to find an upper limit on the mass of any potential intermediate mass black holes in the core of the system, something which has not been possible in previous studies of the system.

The second goal of my thesis is to model the interior of stars orbiting a type of pulsar called a redback. Redbacks are those pulsars that have millisecond rotational periods yet are still interacting strongly with a low-mass ($M_c \geq 0.08\ M_\odot$, where $M_\odot$ is a solar mass) non-degenerate companion star. Contained within the globular cluster data I am analyzing are six known redback systems that have not received much attention from the scientific community to date. My work on these six systems will approximately double the number of redback sources studied in available literature. By looking at the long-term orbital period evolution I have measured changes in the orbital period of the pulsars and their companions and related it to changes in the gravitational field between the two stars. As pulsars are highly degenerate forms of matter, this change must arise due to changes in the companion stars interior density. These density perturbations allow me to provide better constraints on models of similar stars; these results also help to rule out the existence of large deformations in the companion star due to magnetic field realignments.

My final goal for my thesis is to determine the exact mechanism by which a pulsar's radio emission interacts with unbound gas given off by the binary companion star. In redback systems, outer layers of gas may be stripped from the companion star due to a stellar wind or interactions with the pulsar. This unbound gas can cause eclipses

that obscure radio emission from the pulsar at both regular and irregular intervals of its orbit. Using four of the six redbacks previously mentioned, I have analyzed hundreds of eclipses to produce average eclipse properties for my sample of pulsars. My goal is to use these average eclipse properties to produce better estimates on the typical amount of unbound gas in these systems, as well as predict the distribution of the gas in each system. If possible, we will also determine the most likely physical mechanism that is actually obscuring the emission from the pulsar.

Acknowledgements

While the path that has brought me to writing this document has been circuitous, there are a few exceptional friends, family, and colleagues that must receive their due due credit for helping me along the way.

To my bulwark against the hardships and insecurities that life can bring, Molly Cincotta, I thank you for all that you have done. You have been there to listen to me talk about everything from work, life, and general silliness. Without your cheers when things went well and support when things got tough, I am sure I would have burned out long ago and this thesis would have never seen the light of day.

To my best friend and co-conspirator Kyle Roe, I've been incredibly lucky to know that no matter what happens in life I would always have at least one person at my back. Despite the teasing that "Oh no, he is talking science again", you were always keen to know what was going on in my life, which means more than I can say. Thank you.

To my family, you have provided me with support even though I am sure you didn't understand half of what I am working on. Without your long-standing support, I would have never made it this far in life.

So much gratitude goes out to my fellow graduate students. Together we have worked through some of the toughest years of our life and have grown closer throughout. You all have not only been co-workers, but friends that I will remember forever.

I wish you all the best luck on your own journeys and research.

Special thanks to the other members of the pulsar research group (Dr. Siraprapa Sanpa-arsa, Dr. Anya Bilous, Dr. Tim Pennucci, Dr. Dustin Madison, Dr. Jintao Luo, Dr. Paul Demorest, Thankful Cromartie, and Allison Matthews) thank you for sharing your own work with me and listening to my own research. Especially to my fellow students of this group, we were always attempting to find our own path through the world of research and sharing this experience with you has been irreplaceable.

I would also like to express gratitude to my advisor Dr. Scott Ransom for sharing some of his time and immense knowledge about pulsars and Astronomy in an attempt to help me reach this point.

Thank you to the rest of my committee Dr. Phil Arras, Dr. Remy Indebetouw, and Dr. Bradley Cox. The breadth of knowledge in this group has been amazing to witness and has helped me produce a much stronger body of research than I would have been possible of producing on my own.

Thank you to the Department of Astronomy of the University of Virginia, the National Radio Astronomy Observatory, and their researches and staff. You all have provided an environment where I was well supported as I completed my research and provided a wealth of knowledge I could plumb the depths of.

Table of contents

List of Figures

List of Tables

List of Variables

Greek Variables

$\boldsymbol{\alpha}$	Spectral index of the pulsar density distribution in a globular cluster.
$\boldsymbol{\alpha_{J2000}}$	J2000 Epoch Right Ascension
$\boldsymbol{\Delta\phi_{eclipse}}$	Eclipse duration
$\boldsymbol{\delta_{J2000}}$	J2000 Epoch Declination
$\boldsymbol{\phi_{orb}}$	Orbital phase
$\boldsymbol{\phi_{I}}$	Orbital phase for eclipse ingress
$\boldsymbol{\phi_{E}}$	Orbital phase for eclipse ingress
$\boldsymbol{\rho_c}$	Core density of a globular cluster
$\boldsymbol{\nu_{obs}}$	Observing Frequency
$\boldsymbol{\nu_p}$	Plasma Frequency

Roman variables

$\boldsymbol{a_c}$	Acceleration due to the globular cluster potential
$\boldsymbol{a_g}$	Acceleration due to galactic rotation
$\boldsymbol{a_p}$	De-projected pulsar semi-major axis
$\boldsymbol{a_s}$	Acceleration due to the pulsar's proper motion
$\boldsymbol{B}$	Pulsar magnetic field strength
$\boldsymbol{f}$	Pulsar spin frequency
$\boldsymbol{M_c}$	Pulsar companion mass
$\boldsymbol{M_{c,min}}$	Minimum pulsar companion mass assuming an edge-on orbit
$\boldsymbol{P}$	Pulsar spin-period
$\boldsymbol{\dot{P}}$	Pulsar spin-period derivative
$\boldsymbol{P_b}$	Pulsar orbital-period
$\boldsymbol{P_{cyc}}$	Magnetic cycle period
$\boldsymbol{\dot{P}_b}$	Pulsar orbital-period derivative
$\boldsymbol{R}$	Pulsar-companion separation
$\boldsymbol{r_c}$	Core radius of a globular cluster
$\boldsymbol{R_c}$	Pulsar companion radius
$\boldsymbol{R_l}$	Roche lobe radius
$\boldsymbol{w_I}$	Width of eclipse ingress
$\boldsymbol{w_E}$	Width of eclipse egress
$\boldsymbol{x_p}$	Projected pulsar semi-major axis

Chapter 1

Introduction

For nearly fifty years, pulsars have been cosmic lighthouses, guiding us towards a better understanding of the most extreme types of physics as we know it. These extraordinary stars have given us insights into matter at supra-nuclear densities, general relativity, magnetic fields, the interstellar medium, binary evolution, and much more. Despite these numerous advances however, we are still only beginning to scratch the surface of the potential uses of pulsars in understanding our universe.

Much of this work has been accomplished by predicting the arrival time of pulsed radio emission — and more recently gammma ray emission — from pulsars using a process called "pulsar timing". Timing is the process by which a model must account for various aspects of the pulsar's motion and environment in order to accurately predict the arrival time of each pulse. A more detailed description of pulsar timing is given in Section 1.7

This thesis is focused on studying what the timing of a pulsar can tell us about its local environment (ie. properties of the most nearby stars) as well the properties of its host environment. We have focused on pulsars in globular clusters (GCs) — which are small regions of space containing millions of old stars that formed alongside the Milky Way — as a single observation of a GC can contain dozens of a unique type of pulsar called a millisecond pulsar (MSP).

1.1 Millisecond pulsars

Pulsars are a type of rapidly rotating neutron star (NS) — which in itself is the degenerate core of a massive star that has undergone a supernova explosion – which displays coherent radio emission along its magnetic axes. At the time of its formation, the conservation of angular momentum between the progenitor star and the NS is believed to result in a rapidly rotating object. In the case that the rotational and

the magnetic axes are misaligned, we see pulsed emission corresponding to the spin period of the pulsar. An example of what a pulsar might look like if we could see its magnetic field lines is shown in Figure 1.1.

To date, there are approximately 2500 known pulsars in the radio sky [1] (Manchester et al. 2005). The majority of these pulsars have rotational periods ranging between $P{\sim}0.1{-}10$ seconds and have magnetic field strengths of $B{\sim}10^{12}$ G. For a typical spin period derivative of $\dot{P}{\sim}10^{-15}$ s s^{-1}, these so-called "slow pulsars" are typically only visible for a few hundred million years before the emission — which is powered by the rotation of the pulsar (i.e. "rotationally powered") — is too weak to detect.

In 1982, the discovery of B1937+21 revealed that an additional subclass of pulsars exist (Backer et al. 1982). These pulsars rotate much more rapidly than their slower counterparts, with typical periods of a few milliseconds, earning them the aforementioned title of "millisecond pulsars". The current theory for MSP formation was first suggested by Alpar et al. (1982). In their theory MSPs are formed when a pulsar with a much slower rotation rate experiences mass transfer from a companion star. As the companion star fills its Roche lobe — which is defined as the volume where the equipotential is less than one — the outer most gas is stripped away and accreted onto the pulsar, depositing angular momentum. This results in the pulsar reaching rotational periods of a few milliseconds, as well as serving to dampen the magnetic field to values of approximately $B{\sim}10^{8}$ G.

The smaller magnetic field significantly reduces the amount of rotational energy lost from the system due to magnetic braking, giving most MSPs a spin period derivative of $\dot{P}{\sim}10^{-20}$ s s^{-1}. This much smaller spin period derivative implies a spin-down timescale for these systems that is longer than the current age of the Universe. MSPs

[1] http://www.atnf.csiro.au/people/pulsar/psrcat/

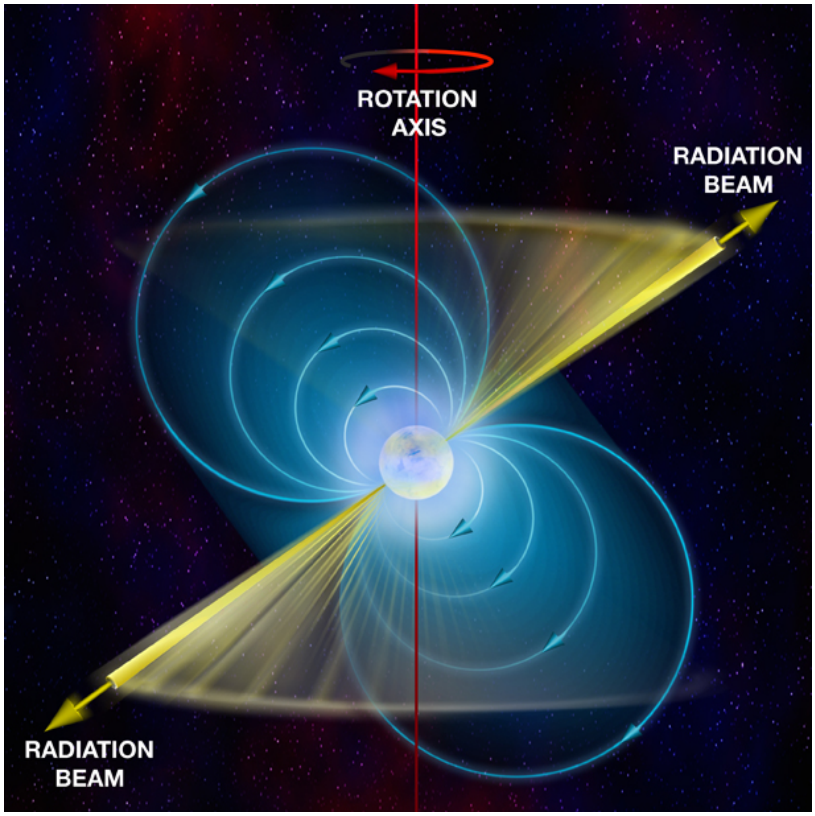

Fig. 1.1.— An example pulsar. The magnetic and rotational axis of the system are misaligned, causing the coherent radio emission from the magnetic poles to sweep across the Earth like a lighthouse. Credit: Bill Saxton; NRAO/AUI/NSF

are therefore incredibly stable rotators and may even rival the long-term accuracy of atomic clocks. In support of this theory, subsequent discoveries of MSPs have shown that MSPs are very often in systems with a white dwarf (WD) binary companion — thought to be the remnant of the original mass donor — and currently the estimated binary fraction for MSPs is ∼80% (Manchester et al. 2005).

During the process of forming a MSP, unbound gas from the companion star will surround the binary with diffuse but optically thick material. Some of the gas may settle into an accretion disk before ultimately reaching the pulsar surface. The disk and the material being accreted onto the pulsar result in no observable pulsar flux reaching the Earth, though copious amounts of X-rays are visible. This type of binary system is often referred to as a low-mass X-ray binary (LMXB) (Tauris & van den Heuvel 2006).

The LMXB stage of a MSP's evolution takes place over timescales of a few tens of millions of years (Bhattacharya & van den Heuvel 1991). Because this is a very short time scale compared to the spin-down lifetime of a MSP, being able to observe rotationally powered emission from the MSP (rather than X-ray emission) such that we may use pulsar timing techniques to study the system at its nascent stage, is highly unlikely. Comparing the time spent in transition from an LMXB to MSP to that of the spin-down timescale for a typical MSP predicts that much less than a percent of its lifetime is spent in this stage.

Without observations of this stage, however, we cannot improve upon our current understanding of how MSPs form. One means for improving our chances of observing nascent MSPs is to blindly survey the whole sky. Large pulsar surveys such as the Green Bank North Celestial Cap survey (GBNCC) (Stovall et al. 2014), the Arecibo pulsar survey (Swiggum et al. 2014), and the Parkes Multibeam Pulsar

survey (Lorimer et al. 2006) have led to the discovery of large numbers of slow pulsars and MSPs as well as a handful of pulsars near this transitional stage.

Perhaps the most useful tool for finding pulsars near this transition between being an LMXB and a MSP has been the Fermi Large Area Telescope (Fermi-LAT) (Atwood et al. 2009; Abdo et al. 2013). Following observations of pulsars such as the Crab and Vela, it was quickly discovered that pulsars can also emit in the gamma-rays (Cheng et al. 1986). While the developement of a theory for how this emission arises is still an area of active research, the spectral energy distribution (SED) of these gamma ray pulsars have been well studied. By looking for gamma-ray sources with a SED characteristic of known pulsars, an all sky gamma ray survey telescope like Fermi is capable of finding incredible numbers of MSPs.

While not well understood, it also has become apparent that searching for pulsars that are gamma-ray emitters is an excellent way of finding pulsars near this nascent/transitional stage between LMXB and MSP. To date, Fermi has found just over a dozen MSPs with non-degenerate companion stars (Roberts 2013). These companions could be stars which have already donated some mass to the pulsar yet have not entirely evolved into a WD or they could be a new companion star brought to the pulsar through pair exhchange and may soon begin to donate mass to the MSP. In either case, these systems may be our best chance for understanding some of the phenomenology that occurs when an MSP is formed, some of which we discuss in the next section.

1.2 Eclipsing & Transitioning Pulsars

MSPs with a non-degenerate companion star possess a number of distinct observational differences from the more common MSP-WD systems. Perhaps the most

striking difference is the presence of long-duration eclipses at low radio frequencies of ∼100-2000 MHz, earning these pulsars the title of "Eclipsing pulsars". These eclipses are thought to be caused by ionized material which has become unbound from the companion star (Stappers et al. 2001) and can last up to half the orbit (which adds to the difficulty of finding these systems in blind surveys).

Eclipsing systems can be broadly divided into two different sub-populations, the "black widows" (BWs) and the "redbacks" (RBs), which are named as such because the pulsars "consume" mass from their companion star much like their arachnid namesakes. Further distinction between a black widow and redback is often based on the observed orbital period (P_b), the companion mass (M_c), and the typical duration of an eclipse ($\Delta\phi_{\rm eclipse}$). Systems with $\rm M_c \lesssim 0.08\ M_\odot$, P_b less than a few hours, and $\Delta\phi_{\rm eclipse} \lesssim$ 5-10% of P_b at an observing frequency of 1500 MHz (L-band) are typically considered to be black widows. Alternatively, systems with $\rm M_c \gtrsim 0.08\ M_\odot$, P_b greater than a few hours, and radio eclipses tending towards 40-50% of P_b at L-band are redbacks (Roberts 2013).

An example of this distinction between black widows and redbacks can be seen in Figure 1.2 using P_b and the mass function for the system assuming an edge on orbit (i=90°) — which defines a minimum companion mass $M_{\rm c,min}$ — and the median pulsar mass taken from recent simulations of M_p=1.55 $\rm M_\odot$ (Kiziltan et al. 2013; Ozel & Freire 2016; Antoniadis et al. 2016). The mass function relates properties of a binary orbit to the masses of the two bodies as follows:

$$f = \frac{(M_c \sin i)^3}{(M_p + M_c)^2} = \frac{4\pi^2}{G}\frac{(a_p \sin i)^3}{P_b^2} = \frac{4\pi^2}{G}\frac{x_p^3}{P_b^2}\,, \tag{1.1}$$

where a_p is the true semi-major axis of the pulsar and x_p is the projected semi-major axis as measured by long-term timing. Since we do not know the pulsar mass or

the inclination of the orbit exactly, we often must assume a pulsar mass and make assumptions about the inclination of the orbit based on properties of the pulsar binary population as a whole or secondary information about the specific source.

The first black widow, B1957+20, was discovered by Fruchter et al. (1988) with a measured P_b=9.1 hour orbital period and $M_{\rm c,min}$=0.023 $M_\odot$ ($\sim$ 20$M_{\rm J}$, where $M_{\rm J}$ is a Jupiter mass) companion. While the mass of the star is comparable to those of brown dwarfs (Burrows & Liebert 1993), the star does not in fact need to have been born at such a low mass. Due to the mass transfer taking place during the spin-up of a MSP, and the strong irradiation from the pulsar wind, much of the companion's original mass may have been lost (Ruderman et al. 1989).

The first redback, J1748-2446A, was discovered a few years later in the globular cluster (GC) Terzan 5 (Lyne et al. 1990). This system has a measured P_b of 1.8 hours and is orbited by a $M_{\rm c,min}$=0.08 $M_\odot$ companion, which puts it near the hydrogen burning limit for the main sequence. While the orbital period of this system is short enough to qualify it as a black widow, the slightly larger value of M_c as compared to other black widow systems and the measured value of $\Delta\phi_{\rm eclipse}\sim$ 40-50% of P_b at L-band make this system more likely a uniquely short period redback.

Currently, only three redbacks have been observed to actively transition between the LMXB and MSP state; J1023+0038 (Archibald et al. 2009) and J1227−4853 (Roy et al. 2015) were discovered in the field of the Milky Way whereas J1824−2452I (Papitto et al. 2013) is located in the globular cluster M28. These systems have been incredibly useful for understanding various physical properties such as the typical amount of mass transfer that can take place during the LMXB phase. With only three sources known however, we must use the more quiescent redbacks and black widows to study the phenomenology of this evolutionary stage.

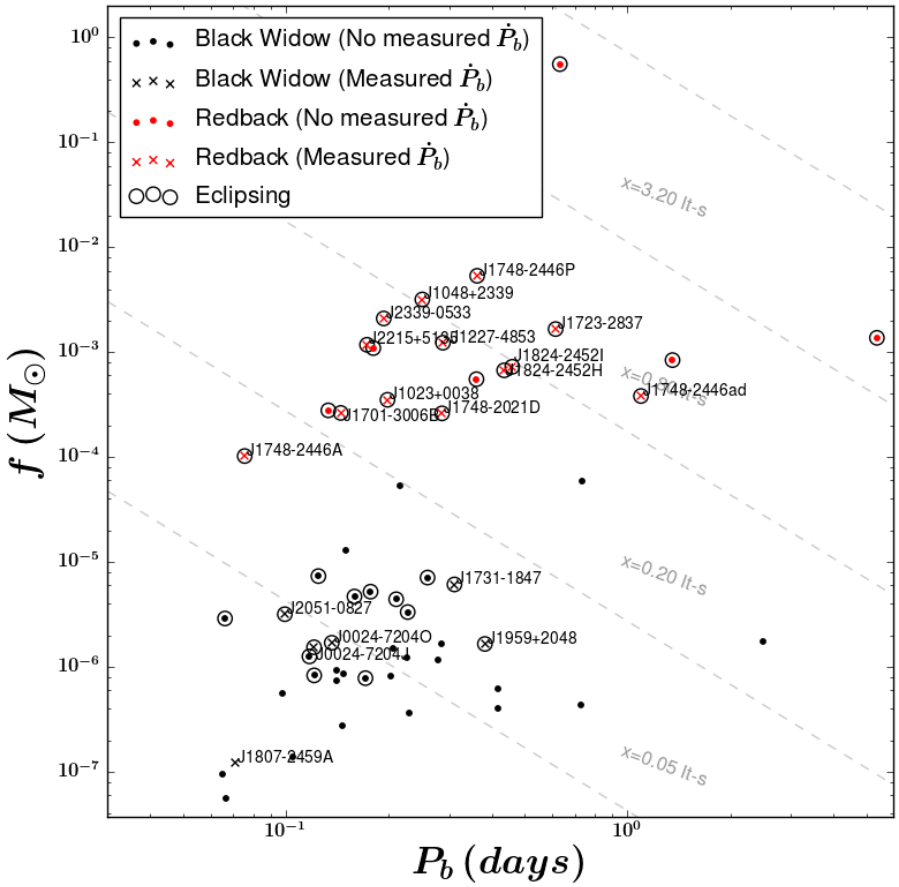

Fig. 1.2.— P_b versus the mass function for all of the currently published black widows and redbacks using each system's minimum companion mass $M_{\rm c,min}$. Lines of projected semi-major axis (x) are shown as dashed lines. Systems with a measured orbital period derivative are plotted with crosses and are labeled. Those systems with observable eclipses are plotted with a black circle around the main point.

One such piece of phenomenology is the presence of stochastic wander in the reference orbital phase of the binary. Over the course of a few years, changes in the orbital period can be seen on the order of $\Delta P_b/P_b \sim 10^{-6}$. As this effect is not seen in the timing of pulsars orbited by WD companions, it is thought to be related to the interior structure of the companion star. While it is not believed to be unique to pulsar binaries, pulsar timing is precise enough that we may be able to test various models against our data to determine the underlying physical effect that gives rise to orbital period wander.

As we would like to be able to measure this effect over a long period of time, we have decided to focus our efforts on those sources in GCs, and not in the field of the Milky Way. In many cases, data for these GC pulsars go back much further, and may allow us to draw more inferences about the underlying physics of these systems than is currently available for nearby pulsars not in GCs..

1.3 The globular cluster pulsar population

GCs are extraordinary factories of recycled pulsars; over the last 30 years, 146 pulsars have been discovered in Galactic GCs, with several thousands more still to be discovered (Bagchi et al. 2011; Hessels et al. 2015). This pulsar population is completely different from the Galactic population, with a very high fraction of MSPs. One reason this happens is because GCs are very old stellar systems, so most "normal" pulsars in them have long faded into inactive NSs.

Even accounting for the number of inactive NSs, GCs have a very large number of MSPs per unit mass compared to the Galaxy. The reason for this is the high stellar density in the cores of GCs, which permits exchange encounters, and the formation of new binaries consisting of old, inactive NSs with low-mass main sequence stars.

The evolution of the latter then causes the system to evolve into a LMXB, of which there are many in GCs, and which will likely evolve into an MSP with some sort of companion star, be it the typical WD or occasionally a low-mass non-degenerate star. In clusters with very dense cores however, this general evolution could be disturbed by further encounters, generating systems that one would not expect to result from the evolution of LMXBs, such as partially recycled pulsars and secondary exchange encounter products (Verbunt & Freire 2014).

Even with the large rate of stellar interactions in the core of GCs, BWs and RBs are relatively rare. Terzan 5, a GC located in the bulge of the galaxy containing 37 MSPs within the inner arcminute of the core, only has 3 redbacks and 2 black widows. The enchanced population of MSPs can be used to study more than just the eclipsing pulsars, however. As we will see in more detail in Chapter 2, the observed variation of the pulsars spin and orbital period derivatives ($\dot{P}$ and $\dot{P}_b$) can be used to constrain and measure (respectively) the acceleration produced by the gravitational potential of the spherically symmetric host cluster and the second order spin-period derivative ($\ddot{P}$) can be used to measure the combined "jerk" (the time derivative of acceleration) from both the nearby stars and from the overall cluster potential.

Relating changes in the arrival time of pulses from the pulsar to the cluster potential is possible because the pulsar acts much like an accelerometer in space. As the pulsar moves through the gravitational field of the cluster, the time between pulses will experience a doppler acceleration. We also know that the cluster itself is moving through the field of the galaxy. We can therefore decompose the observed timing model that defines the arrival time between pulses into measurements that tell us more about the pulsars intrinsic spin-down, the proper motion of the pulsar, Galactic rotation, and most importantly the gravitational field the pulsar is sitting in. More

details about this process are given in Chapter 2.

Once we have isolated the components of the pulsar timing model that arise due to the cluster itself, we can use Markov Chain Monte Carlo (MCMC) sampling to learn more about the pulsar's host environment. We therefore take a moment to discuss what a MCMC sampler does, and why it is useful for this research.

1.4 Markov Chain Monte Carlo Sampling

MCMC sampling is a statistical tool used to capitalize on increasingly powerful computers. At its very core, it allows us to fully sample the final probability of a given distribution using Bayesian inference without having to analytically derive the final probability density function (PDF).

In Bayesian statistics, the simplest description for the probability of calculating a series of parameters θ with a given set of data x is:

$$p(\theta|x) \propto p(x|\theta)p(\theta)\,, \tag{1.2}$$

where $p(x|\theta)$ is the likelihood of measuring x given θ, and $p(\theta)$ is the likelihood of having a set of parameters θ (otherwise known as the 'prior').

Another way of interpreting Equation 1.2 is that we wish to measure the joint probability of how well our data x follows a model with an arbitrary set of parameters θ and how likely it is to measure any given parameter in the set of θ. Producing an analytical solution for such a joint distribution can be incredibly difficult in most circumstances as an integral over multiple complex functions may be required.

If we instead allow a computer to randomly sample over a large number of trial values for θ, calculating the likelihood according to $p(x|\theta)$ and $p(\theta)$ at each step,

we can find the posterior likelihood — which is the probability distribution for the parameter set θ after the data has been considered — much more readily. This can be accomplished by creating a large number of initial guesses for the set θ. Each of these initial guesses is the beginning of a "chain", where the chain records θ for each step in the trial. At each step of the trial, the likelihood for $p(x|\theta)$ and $p(\theta)$ is calculated. If the combined probability is better than the last step of the trial, the chain records a new set of θ. In the case of the combined probability being less than the previous step, there is an acceptance ratio that allows the chain a slight chance to update to a less ideal solution. This prevents the code from becoming trapped at local maximum likelihoods, instead allowing the code to fully explore the global likelihood for the entire data set and give a full picture of the covariances in our model.

This method also lends itself well to characterizing a set of parameters θ where some of the variables are global and apply to each data point x and others parameters only describe an individual data point x_i. An example of this can be drawn from the work of Chapter 2, where we have a measured on-sky position and line of sight acceleration for each pulsar. In order to derive the global density profile of the system, θ must be able to both describe a series of variables that define the density profile for all of the pulsars, as well as assign a line of sight position with respect to the core for each pulsar individually. Finding an analytical solution for such a series of variables would be incredibly difficult whereas using an MCMC sampler is much simpler (though computationally intensive).

In Chapters 2 and 4 we will discuss two different uses of MCMC sampling that can be applied to pulsar timing data, and discuss how they allow us to probe different types of physics that are difficult to study using traditional astronomical observing techniques.

1.5 Pulsar Data

In this section, we introduce pulsar observing and the concept of how to remove the effects of the intervening interstellar medium (ISM) between us and the pulsar from our data through a process called "dedispersion".

1.5.1 Telescope Selection

The vast majority of MSPs are found using large single-dish radio telescopes and not interferometers. This is because the angular resolution of a single dish telescope is often much coarser and allows us to survey the sky much faster and with less computing power required. The angular resolution of a telescope (θ) scales approximately as:

$$\theta \sim \frac{\lambda}{D}\,, \tag{1.3}$$

where λ is the observing wavelength, and D is the effective diameter of the telescope.

For comparison, the Robert C. Byrd Green Bank Telescope (GBT) in West Virginia has a diameter of 100 meters, whereas the Karl G Jansky Very Large Array telescope (VLA) is comprised of 27 dishes, each with a diameter of 25 meters. Even if the VLA were at its most compact configuration, the dishes are spread out over an area of approximately 1 kilometer. This gives an angular resolution of $\sim$46 arcseconds at L-band (a very typical pulsar observing frequency), whereas the GBT has an effective beamwidth of $\sim$8.5 arcminutes. This allows us to survey the sky much faster when searching for new pulsars.

1.5.2 Data Collection & Dedispersion

Pulsar instruments are typically designed to measure and integrate raw voltages from the telescope before storing the data as a function of time. Due to the rapid rotation rates of pulsars, the telescope must be able to dump data at a rate faster than the rotational frequency of the pulsar. This typically results in data being recorded every few tens of microseconds in order to properly sample the entirety of the pulsar's rotational phase. Data is also recorded for a variety of different observing frequencies, typically centered on values ranging between a few hundred MHz to a few GHz with a large fractional bandwidth (when possible).

One difficulty with this method however, is the presence of the cold plasma that makes up the ISM between the telescope and the pulsar. Low frequency radiation is preferentially delayed more than higher frequencies, which spreads out the pulsar signal over some timescale that depends on the observing frequency and the bandwidth of the observation. Following the discussion of Lorimer & Kramer (2012), we know that the refractive index (μ) of such a medium is given by:

$$\mu = \left[1 - \left(\frac{\nu_p}{\nu}\right)^2\right]^{1/2}, \tag{1.4}$$

where ν is observing frequency and ν_p is the plasma frequency, which is given by:

$$\nu_p = \sqrt{\frac{n_e e^2}{\pi m_e}}. \tag{1.5}$$

For most radio observations we can ignore the thermal component of the plasma in the ISM, which allows us to define the group velocity of the radiation to be:

$$v_g \simeq c\left(1 - \frac{\nu_p^2}{2\nu^2}\right). \tag{1.6}$$

In Chapter 4 we will discuss this limit further when the pulsar signal is surrounded by a potentially hot plasma given off by a companion star.

As a result, the delay produced along a distance d for a certain group velocity is given by $t = \int_0^d v_g^{-1} dl$. Using Equations 1.5 and 1.6, we can redefine the integral to give the time delay at any given observing frequency:

$$\left(\frac{t}{\text{sec}}\right) \simeq 4.149 \times 10^3 \left(\frac{\text{DM}}{\text{pc cm}^{-3}}\right) \left(\frac{\nu}{\text{MHz}}\right)^{-2} , \tag{1.7}$$

where DM is the dispersion measure and is:

$$\text{DM} \equiv \int_0^d n_e dl \, . \tag{1.8}$$

Without accounting for the dispersion measure, it is nearly impossible to find periodicity in the pulsar data across all frequency channels. This is because when searching for new pulsars, the DM of the pulsar is not known, therefore there is an unknown amount time delay in each frequency channel. To get around this, we must first account for the time delay in each frequency channel by dedispersing the data at numerous trial DM values. Only once we have removed dispersion can we take the Fourier transform of our data to look for periodicity.

This type of dedispersion is called "incoherent dedispersion", and is useful when searching for new pulsars with unknown DM values. While it corrects for the time delay between individual frequency channels, it does not account for the dispersion *within* each channel. Another method of dedispersion is available that does account for this issue when observing pulsars with a known value of DM, though. This other dispersion method improves our timing of the pulsar and allows us to better sample pulsar emission as a function of rotational phase.

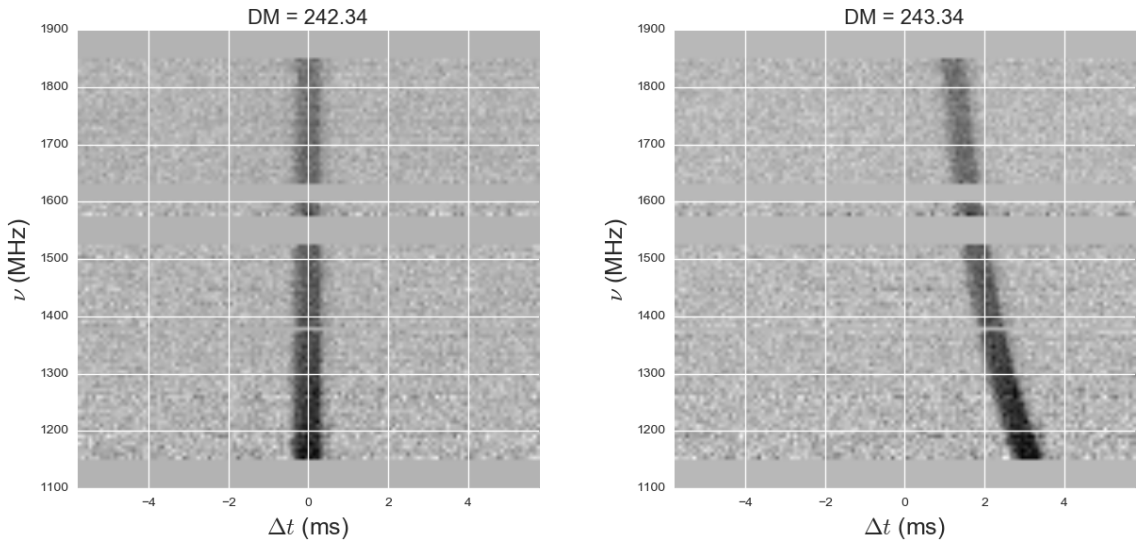

Fig. 1.3.— Example of dispersive delays for the pulsar J1748-2446A, a MSP in the GC Terzan 5. Both plots show the intensity of the pulsar in grayscale as a function of the offset from the expected pulse arrival time on the x-axis and the observing frequency on the y-axis. The left-hand plot shows the data dispersed at the true DM value. The right-hand plot shows the delays introduced by using a slightly incorrect DM value.

1.5.3 Coherent Dedispersion

Instead of sampling the data across discreet frequency channels and applying dedispersion afterwards, it is also possible to account for the dispersive delay before data is recorded. This process is called "coherent dedispersion".

Coherent dedispersion is accomplished by convolving the input signal from the pulsar with the transfer function of the ISM. From Stairs (2002), the transfer function for a given value of DM is approximately:

$$H(\nu_0 + \nu_1) = \exp\left[2\pi i \frac{\mathrm{DM}}{2.41 \times 10^{-10}} \frac{\nu_1^2}{\nu_0^2(\nu_0 + \nu_1)}\right], \tag{1.9}$$

where ν_0 is the center frequency of the observation and ν_1 is the offset from the center of the band ($|\nu_1| < B/2$), where B is the bandwidth of the observation).

Convolving the inverse of Equation 1.9 with the measured voltages as they come in to the telescope produces dedispersed data before recording. This allows us to save data with greater time resolution than incoherently dedispersed data.

1.6 Radio Frequency Interference

In addition to needing to dedisperse our data in order to find or produce a timing model for a pulsar, we must also account for the possibility that our data may be contaminated by terrestrial —or satellite— radiation. This contamination to pulsar timing data is called Radio Frequency Interference (RFI) and can often overshadow signal from a pulsar. RFI can manifest itself as significant signal within discreet frequency channels or sub-integrations of time or as a periodic signal that shows passing similarity to a pulsar signal.

RFI can be produced through a variety of means. Common sources include wire-

less devices, nearby aircraft, and even activity in the atmosphere or electrical storms. While attempts to mitigate this effect by building telescopes away from populous regions or by shielding electronics helps remove some of the interference in our data, it is effectively impossible to remove all RFI before observations are made. This means that data must undergo processing to remove these sources before we can perform any analysis meant to find or time a pulsar.

This process of RFI removal can be broken down into two broad categories, though in practice the identification of RFI can be achieved through a number of different data processing means. The first category is sigma-clipping of the raw data. By identifying strong sources in the raw data that are transitory or are not broadband in frequency, we can effectively mask the corresponding frequency channels and sub-integrations before dedispersion.

The second method is to identify RFI that appears as a periodic signal using a power spectrum analysis. This periodic RFI can be caused by various sources, such as radar technology. As this RFI is terrestrial in origin, we expect that the dispersion measure of any periodic signal associated with this RFI to be zero. Removing strong periodic sources in the raw data can therefore effectively remove significant amounts of RFI before any further analysis is performed.

Even removing RFI using both of these methods, when searching for a new pulsar, a majority of the periodic signals found at a candidate DM will correspond to RFI. Pattern recognition of likely pulsar pulse profile shapes and pulsar properties are needed to identify likely candidates from the overwhelming number of RFI sources, and it is only through follow-up observations, that we can truly confirm the identification of a new pulsar.

1.7 Pulsar Timing

As previously stated, pulsar timing is designed to create models that can account for the arrival time of each pulse down to microsecond — and possible even nanosecond — precision. Following the discussion provided by Lorimer & Kramer (2012), we introduce the basic concepts of pulsar timing below and discuss how the physical models for this thesis make use of these techniques.

In order to predict the arrival time of a pulse coming from the poles of a pulsar, we must be able to accurately predict its rotational phase. This can be accomplished by taking a Taylor expansion of the rotational frequency of the pulsar f:

$$f(t) = f_0 + \dot{f}(t - t_0) + \frac{1}{2}\ddot{f}(t - t_0)^2 + \dots , \tag{1.10}$$

where t is the time at which a pulse is emitted and t_0 is a reference epoch.

Equation 1.10 is the simplest approach to pulsar timing, however it does not take into account other extrinsic effects that may change the time a pulse is seen by an observer. Therefore it is often easier to describe the arrival time of a pulsar in the reference frame of the the Solar System barycenter, including effects such as the motion of the pulsar, the effects of the ISM, and warps in space-time around the Earth and the pulsar. A better way to characterize the arrival time of the pulse can therefore be described as follows:

$$\begin{aligned} t_{\rm SSB} = & t_{\rm topo} + t_{\rm corr} - \Delta D/f^2 + (\Delta_{\rm R\odot} + \Delta_{\rm RB}) + (\Delta_{\rm S\odot} + \Delta_{\rm SB}) \\ & + (\Delta_{\rm E\odot} + \Delta_{\rm EB}) + \Delta_{\rm AB} \, . \end{aligned} \tag{1.11}$$

The terms in Equation 1.11 can be broken down into the following physical effects:

- $t_{\rm topo}$: This term is the topocentric arrival time of a pulse.

- $t_{\rm corr}$: A correction to the pulsar arrival time that accounts for telescope dependent effects oftentimes by matching the local observatory time to an international atomic time standard.

- $\Delta D/f^2$: The dispersion measure correction, which takes into account the effect of the cold ionized medium between us and the pulsar that preferentially delays longer wavelength emission.

- $(\Delta_{\rm R\odot} + \Delta_{\rm RB})$: This term is the Römer delay and is due to the light travel time in an orbit. The first term takes into account the telescopes position relative to the the solar system barycenter and the second term is the light travel time from the pulsars position to the center of gravity if the pulsar is in a binary system.

- $(\Delta_{\rm S\odot} + \Delta_{\rm SB})$: This term is the Shapiro delay, and accounts for the curvature of space-time due to the planets and the Sun in our solar system in the first term and the curvature due to a binary companion (if present) in the second term.

- $\Delta_{\rm E\odot} + \Delta_{\rm EB}$: This term is the Einstein delay, which is the time dilation caused by the Earth and the other bodies in the solar system in the first term and the time dilation and gravitational redshift due to a binary companion (if present) in the second term.

- $\Delta_{\rm AB}$: This term is the aberration due to the orbital motion if the pulsar is in a binary system.

Timing campaigns are used to measure these various effects using a boot-strapping technique. Pulsars are often discovered by searching for a strong periodic signal in the power spectrum of radio data at a trial dispersion measure. Typically, timing models begin with only the

If the pulsar has a large first order spin period derivative it might be measurable in the course of a single observation. More typically, however, we only start with the position of the radio beam on sky, the dispersion measure, and the spin period of a pulsar. Subsequent observations over the course of weeks, months, and years are used to add in additional physics that improve our models for the pulsar over the entire baseline and obtain progressively more precise measurements of pulse arrival times and physical parameters of the pulsar system. An example timing model is shown in Figure 1.5.

For most pulsars, this bootstrapping technique is capable of detecting both f and $\dot{f}$ for a pulsar from Equation 1.10. Measurements of higher order spin-frequency derivatives are often associated with timing noise (i.e. the inherent variability of pulsar emission) (Verbiest et al. 2009) or the perturbations due to nearby stars (Blandford et al. 1987). Timing noise is not thought to be a large effect in most MSPs (Verbiest et al. 2009), which means that spin-period derivatives can often be related to the local environment around the pulsar. Similarly, this combination of a lack of timing noise and slight variations in the expected spin-period of the pulsar can be used in other ways and has given rise to an entire field of gravitational wave detection using large collections of pulsars (Arzoumanian et al. 2016; Babak et al. 2016; Hobbs 2013).

1.8 Thesis layout

This thesis focuses on using timing models made from over a decade's worth of data to (1) explore more physically robust models of GCs containing pulsars, and (2) explore the properties of eclipsing pulsar companions.

In Chapter 2 we study the physical characteristics of the globular cluster Terzan 5 using the long-term timing of 36 of the pulsars in the core. We produced a de-

projected mass density profile for the system using a parallel tempered MCMC sampler which allowed us to produce a distribution of likely positions for each pulsar along our line of sight. Using the density profile and the position of each pulsar, we can calculate the total mass of the system and place an upper-limit on the mass of any possible intermediate mass black hole (IMBH) in the core. We also use these measurements to argue that Terzan 5 is likely a remnant of the formation of the Milky Way bulge and not a stripped dwarf galaxy, which is important for understanding why Terzan 5 has such a large number of pulsars as compared to other GCs.

In Chapter 3 we shift our focus to a series of six redbacks spread out over three GCs in an attempt to understand the mechanism driving orbital period wander. Using published density profiles for each cluster, we show that these redbacks should be similar to those in the field of the galaxy in that the globular cluster is not producing the observed variations in the orbital period. We then calculate the orbital period that gives the most accurate timing model possible for each pulsar on any individual date. This allows us to show that the mechanism often invoked to explain this effect is not capable of reproducing our data. Following is a discussion of some of the important pieces of missing physics needed to improve upon the model. We also include a discussion on the possible uses of orbital period wander in pulsar timing as a means for studying magnetic activity in low-mass, rapidly rotating, stars.

In Chapter 4 we use the timing models produced in Chapter 3 to identify those observations where the pulsar is seen to switch between being visible and being eclipsed. We then fit for the light curve that defines the phase at which ingress or egress occurs, and use a MCMC sampler to define global eclipse properties for each pulsar. This is accomplished over a large range of frequencies, allowing us to rule out different models that define how the gas may be interacting with the pulsar emission. We also

describe the potential geometry of the gas in the system and place constraints on the mass loss from the companion star.

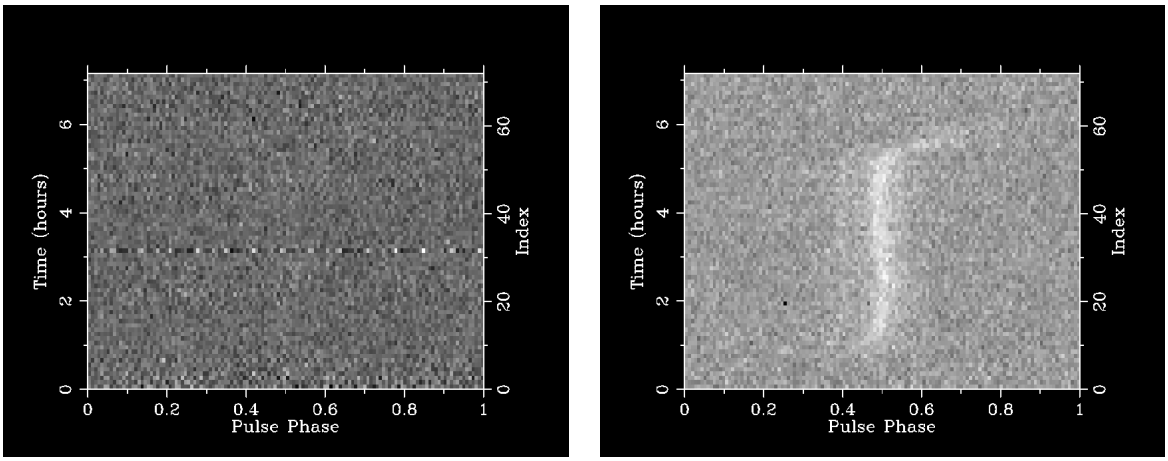

Fig. 1.4.— Example of RFI in an observation of the pulsar J1748-2446P. The left-hand plot shows data folded using the best timing model for the pulsar without RFI removal. We can see strong interference is visible half-way through the observation in a single sub-integration. The right-hand plot shows the same data folded using the best timing model with RFI removed. We find a strong signal from the pulsar was entirely masked by the single sub-integration with RFI.

Ecliptic Longitude, λ (deg)	245.78827556(5)
Ecliptic Latitude, β (deg)	-1.256744(2)
Proper Motion in λ (mas yr^{-1})	9.79(7)
Proper Motion in β (mas yr^{-1})	-30(3)
Parallax (mas)	0.5(6)
Pulsar Spin Period (ms)	3.1508076534271(6)
Period Derivative (s/s)	$9.6216(9)\times10^{-21}$
Reference Epoch (MJD)	53600
Dispersion Measure (pc cm^{-3})	34.4865[†]
Orbital Period (days)	8.6866194196(2)
Projected Semi-Major Axis (lt-s)	11.2911975(2)
1st Laplace Parameter, $e\sin\omega$	$1.1(3)\times10^{-7}$
2nd Laplace Parameter, $e\cos\omega$	$-1.29(3)\times10^{-6}$
Companion Mass ($M_\odot$)	0.500(6)
Sine of Inclination Angle	0.999894(5)
Epoch of Ascending Node (MJD)	52331.1701098(3)
Span of Timing Data (MJD)	52469−55330
Number of TOAs	2,206 (454 / 1,752)[‡]
RMS TOA Residual (μs)	1.1
Right Ascension (J2000)	$16^h\,14^m\,36\overset{s}{.}5051(5)$
Declination (J2000)	$-22^\circ\,30'\,31\overset{''}{.}081(7)$
Orbital Eccentricity, e	$1.30(4)\times10^{-6}$
Inclination Angle (deg)	89.17(2)
Pulsar Mass ($M_\odot$)	1.97(4)
DM-derived Distance (kpc)	1.2[§]
Parallax Distance (kpc)	>0.9
Surface Magnetic Field (10^8 G)	1.8
Characteristic Age (Gyr)	5.2
Spin-down Luminosity (10^{34} erg s^{-1})	1.2
Average Flux Density at 1.4 GHz (mJy)	1.2[†]
Spectral Index, 1.1–1.9 GHz	-1.9(1)
Rotation Measure (rad m^{-2})	-28.0(3)

Fig. 1.5.— Properties of PSR J1614-2230 as obtained through pulsar timing (Demorest et al. 2010). This timing model accounts for the properties of the pulsar's position on sky, intrinsic spin-down, the binary properties, and more.

Chapter 2

Using long-term millisecond pulsar timing to obtain physical characteristics of the bulge globular cluster Terzan 5.

2.1 Abstract

Over the past decade the discovery of three unique stellar populations and a large number of confirmed pulsars within the globular cluster Terzan 5 has raised questions over its classification. Using the long-term radio pulsar timing of 36 millisecond pulsars in the cluster core, we provide new measurements of key physical properties of the system. As Terzan 5 is located within the galactic bulge, stellar crowding and reddening make optical and near infrared observations difficult. Pulsar accelerations, however, allow us to study the intrinsic characteristics of the cluster independent of reddening and stellar crowding and probe the mass density profile without needing to quantify the mass to light ratio. Relating the spin and orbital periods of each pulsar to the King acceleration, we find a core density of $\rho_c = 1.58^{+0.13}_{-0.13}\times10^6$ $M_\odot$ pc^{-3}, a core radius of $r_c = 0.16^{+0.01}_{-0.01}$ pc, a pulsar density profile $n \propto r^{-3.14^{+0.52}_{-0.53}}$, and a total mass of $M_T(R_\perp$ <1.0 pc)$\simeq 3.0\times10^5$ $M_\odot$ assuming a cluster distance of d=5.9 kpc. Using this information we argue against Terzan 5 being a disrupted dwarf galaxy and discuss the possibility of Terzan 5 being a fragment of the Milky Way's proto-bulge. We also discuss whether the pulsars were formed via electron capture supernovae or exist in a core full of heavy white dwarfs and hard binaries. Finally we provide an upper limit for the mass of a possible black hole at the core of the cluster of $M_{BH} \simeq 3 \times 10^4\, M_\odot$.

2.2 Introduction

2.2.1 Pulsars in Globular Clusters

The study of the abundant GC pulsar population has already resulted in a large number of scientific results, such as NS mass measurements (Ferraro et al. 2003; Bassa et al. 2006; Cocozza et al. 2006; Jacoby et al. 2006; Lynch et al. 2012), tests of

general relativity (Jacoby et al. 2006), the detection of intracluster gas (Freire et al. 2001b), and also constraints on the properties of the parent clusters (Phinney 1993; Anderson 1993; Freire et al. 2003). This last application is especially relevant for this thesis.

Among all Galactic GCs, Terzan 5 has the largest number of known pulsars, 37, which represent almost a quarter of the total population of pulsars in GCs[1]. The first discovery, J1748−2446A, is a very bright pulsar in an eclipsing system (Lyne et al. 1990), hich we would now label as a "redback". Ten years later, a second pulsar was announced, J1748−2446C (Lyne et al. 2000). In 2004, with the commissioning of the S-band receiver at the GBT and the 800-MHz-wide pulsar SPIGOT back-end (Kaplan et al. 2005) provided a large increase in sensitivity, which together with better search procedures (Ransom 2011) resulted in the discovery 21 new pulsars (Ransom et al. 2005). Since then another 13 pulsars have been discovered, two of which will soon be reported upon by Cadelano et al. (2017) (J1748−2446aj & J1748−2446ak). This population is quite extraordinary, it includes seven highly eccentric MSP systems, and 5 BWs and RBs, one of which, J1748−2446ad, is the fastest-spinning pulsar known (Hessels et al. 2006). More details about the BWs and RBs in Terzan 5 are discussed in Section 2.6.2.

This uniquely large pulsar population of pulsars orbiting in the shared gravitational potential of Terzan 5 can provide a wealth of information about that cluster that is difficult to obtain with optical and infrared observations. Coincidentally, Terzan 5 is one of the most intriguing and least understood GCs in the Galaxy.

[1] http://www.naic.edu/∼pfreire/GCpsr.html

2.2.2 The unusual GC Terzan 5 in the near infrared and X-rays.

Historically, Terzan 5 has been a very difficult globular cluster to study using optical and infrared telescopes. Located within the bulge of the Milky Way, it suffers from an average color excess of E(B-V) of 2.38 (Barbuy et al. 1998; Valenti et al. 2007) and strong differential reddening (Massari et al. 2012). As a result, it has only been through the use of space-based telescopes and adaptive optics in the near infrared that this cluster has become better understood in the past few years. Currently, the most accurate measurement of the cluster distance places Terzan 5 at d=5.9±0.5 kpc (Valenti et al. 2007), the exact value of which can influence the inferred physical characteristics of the system.

Ferraro et al. (2009) uncovered two distinct stellar populations in Terzan 5, one metal rich with [Fe/H]≃0.3 and a fainter, metal poor population with [Fe/H]≃-0.2. Additional observations (Origlia et al. 2013) of this cluster have revealed a third, even more metal poor component with [Fe/H]≃-0.79. All of these findings point to the fact that this system has had a unique history and may not be a true globular cluster; instead it may have originally been a dwarf galaxy and undergone tidal stripping due to repeated interactions with the Milky Way's potential (Massari et al. 2014).

Ferraro et al. (2009) and Lanzoni et al. (2010) give improved measurements of the physical characteristics of the cluster. Ferraro et al. (2009) found the center of gravity (CoG) for Terzan 5 using the absolute positions of stars taken with the European Southern Observatory's Multi-Conjugate Adaptive Optics Demonstrator (ESO-MAD) to be at $\alpha_{J2000} = 17^h48^m4.85^s \pm 0.5^s$ and $\delta_{J2000} = -24°46^m44.6^s \pm 0.5^s$. Lanzoni et al. (2010) used the observed number density of luminous red giants about the CoG to find a central mass density of ρ_c =(1-4)×10^6 $M_\odot$ pc^{-3}, a core radius for

the red giants of $r_c = 0.26\,\mathrm{pc}$, and a total mass of $M_T = 2{\times}10^6\ \mathrm{M}_\odot$, though exact errors are not provided by their work. Using high resolution Hubble Space Telescope data, further studies by Miocchi et al. (2013) found a core radius of the luminous red giants of $r_c = 0.22 \pm 0.01\,\mathrm{pc}$.

In terms of MSP formation, Terzan 5 is interesting for a number of reasons. Studies of the radio luminosity function place the number of potentially observable pulsars in the cluster at ∼150, which is the largest predicted pulsar population for all known globular clusters (Chennamangalam et al. 2013; Turk & Lorimer 2013). With 50 X-ray sources identified in the cluster (Heinke et al. 2006) and one of the largest stellar collision rates for globular clusters (Pooley et al. 2003; Lanzoni et al. 2010), Terzan 5 has a set of physical characteristics that are particularly favorable for the formation of LMXBs and MSPs.

A common concern in previous optical and infrared studies of the structural parameters of Terzan 5 has been finding a way to circumvent the difficulties introduced by the severe reddening and stellar crowding. Pulsar timing allows us to study the mass density of the cluster directly and is, with the exception of needing to determine the distance to the cluster using additional optical data, independent of the reddening. This work accomplishes this by synthesizing and improving upon previously used methods for converting pulsar positions and accelerations into information about the global properties of the system.

2.2.3 Constraints on the potential of the cluster from pulsar observations

The measured accelerations and jerks felt by the pulsars due to the cluster potential can be related to a cluster model through the use of a MCMC sampler. This produces

a global measurement of the cluster core density, core radius, spectral index of the pulsar density profile (defined in more detail in Section 2.7), and de-projected position for each pulsar within the inner few core radii of Terzan 5. Using this method, additional tests can be performed to determine whether an offset is needed in the optical CoG of the cluster as well as provide upper limits on the mass of any central black hole in Terzan 5.

As these measurements of the cluster parameters are both reddening independent and calculated using only the gravitating mass of the cluster, we can directly measure the total mass of the cluster at a given radius. This allows us to provide independent measurements of the mass to light ratio that can be used to discuss the most likely formation scenario for the cluster. These measurements also allow us to comment on the dominant mass class within Terzan 5, which can play an important role in understanding the formation mechanism for the large population of MSPs in Terzan 5.

2.2.4 Structure of the Chapter

In the remainder of this chapter, we begin by discussing the observations and timing campaign of Terzan 5 (Section 2.3). We then introduce the models that describe the predicted accelerations and jerks of each pulsar (Section 2.4) and compare these models to globular cluster data produced by the star cluster initializer McLuster (Küpper et al. 2011) (Section 2.5). Finally, we convert our pulsar timing data into accelerations (Section 2.6) and proceed to derive key cluster parameters for Terzan 5 using more traditional timing methods (Section 2.7) as well as with our MCMC models (Sections 2.8, 2.9, and 2.10), including a comparison of each method against previously quoted values in the literature for 47 Tucanae. We finish the chapter by

discussing our results in the context of what this means for the physical state and origin of Terzan 5 and propose future improvements to our models (Section 3.8).

2.3 Data

To date there are 37 known pulsars in Terzan 5, all of which lie within the inner arcminute of the cluster, and the majority within the inner 20 arcseconds. Table 2.1 gives some of the basic parameters from the timing of these pulsars, including the range of dates used to produce the timing models. Data were taken with the 100-m Robert C. Byrd Green Bank Telescope (GBT) in West Virginia. Observations taken prior to June of 2008 were carried out on the SPIGOT backend (Kaplan et al. 2005) and are summarized in the papers by Ransom et al. (2005) and Hessels et al. (2006) along with a discussion of twenty four of the pulsars in our sample. Observations taken after this date used the GUPPI (Green Bank Ultimate Pulsar Processing Instrument) (DuPlain et al. 2008) in the coherent search mode. Both observations with SPIGOT and GUPPI were taken with approximately 600 MHz of bandwidth after RFI and band-pass removal and were centered at either 1500 MHz or 2000 MHz.

Search mode observations using coherent dedispersion accumulate full Stokes parameter data in real time before saving the data in a filterbank format. Further details of this process for all 37 pulsars in Terzan 5 will be presented in an upcoming paper by Ransom et al. (in prep 2017). For this work we will only discuss 36 of the known pulsars as J1748−2446al does not yet have a timing solution.

Of the 36 available pulsars for study in the cluster, all have measured first-order spin period derivatives (due, as already mentioned, to the intrinsic spin-down of the pulsars and the acceleration of the cluster potential), 34 have measured second-order spin period derivatives (due in equal parts to nearby stars and the cluster potential),

and an additional 13 have a measured third-order spin period derivative or higher.

These higher order spin period derivatives are likely not caused by timing noise, as MSPs are generally very stable rotators. If we instead compare our population of MSPs to those in the field of the galaxy, only ∼4% have measured second order spin period derivatives and none have a measured third order spin period derivative. Comparing this to the 33 out of 36 timed pulsars in Terzan 5 with a second order spin period derivative (13 of which also have a measured third order spin period derivative) we note that the magnitude of these derivatives can be a few orders of magnitude larger than those seen in the field of the galaxy. We therefore argue that second order and higher spin period derivatives are caused almost exclusively by the presence and movement of nearby stars. Additional arguments for this scenario are given by Blandford et al. (1987).

Furthermore, 18 of the 36 pulsars are in binaries, 13 of which have measured orbital period derivatives, which in most cases provide direct measurements of the line of sight acceleration of the system, which is dominated by the cluster potential. Combined, we have an unprecedented amount of information from which we can produce a global model for the physical characteristics of the cluster using pulsar timing

2.4 Theory

In this section we derive the accelerations and jerks for a King potential (King 1962). For the accelerations we show that the nearest stellar neighbor contribution is negligible, leaving us with a single equation based on the mean-field of the cluster. We discuss the distribution of likelihoods around this mean-field equation in Section 2.8.2.

Blandford et al. (1987) showed that the nearest stellar neighbors produce a non-negligible jerk on pulsars in globular clusters. We calculate an analytic solution for the characteristic jerk on a pulsar from all the stars at once to account for this effect. We also calculate the expected distribution of jerks around this characteristic value assuming the inter-stellar distance is much smaller than the size of the cluster.

Finally, we discuss the inclusion of a central black hole in the system and show how this may perturb solutions for the innermost stars. In Section 2.5 we compare our models for the accelerations and jerks to simulated data before applying these methods to Terzan 5.

2.4.1 Cluster Geometry

We begin by defining a coordinate system for the globular cluster which will be referenced for the rest of this work (Figure 2.1).

The plane running through the CoG and perpendicular to our line of sight (i.e. the plane of the sky) is defined to be O. The impact parameter for each pulsar from the CoG is defined to be $R_\perp$. The core radius is defined to be r_c, which corresponds to where the mass density drops to a third of its central value. The variables r_h and r_t are the half-mass and the tidal radii of the cluster, respectively.

The line of sight position going perpendicularly through O is defined to be l. Positions l_1 and l_2 represent the two line of sight positions in the cluster where a measured line of sight acceleration a_l may occur. The maximum possible line of sight acceleration at a given value of $R_\perp$ is given by $a_{\mathrm{l,max}}(R_\perp)$. The line of sight acceleration rises sharply out to approximately a core radius before declining proportionally to l/r^3 out of the plane of the sky.

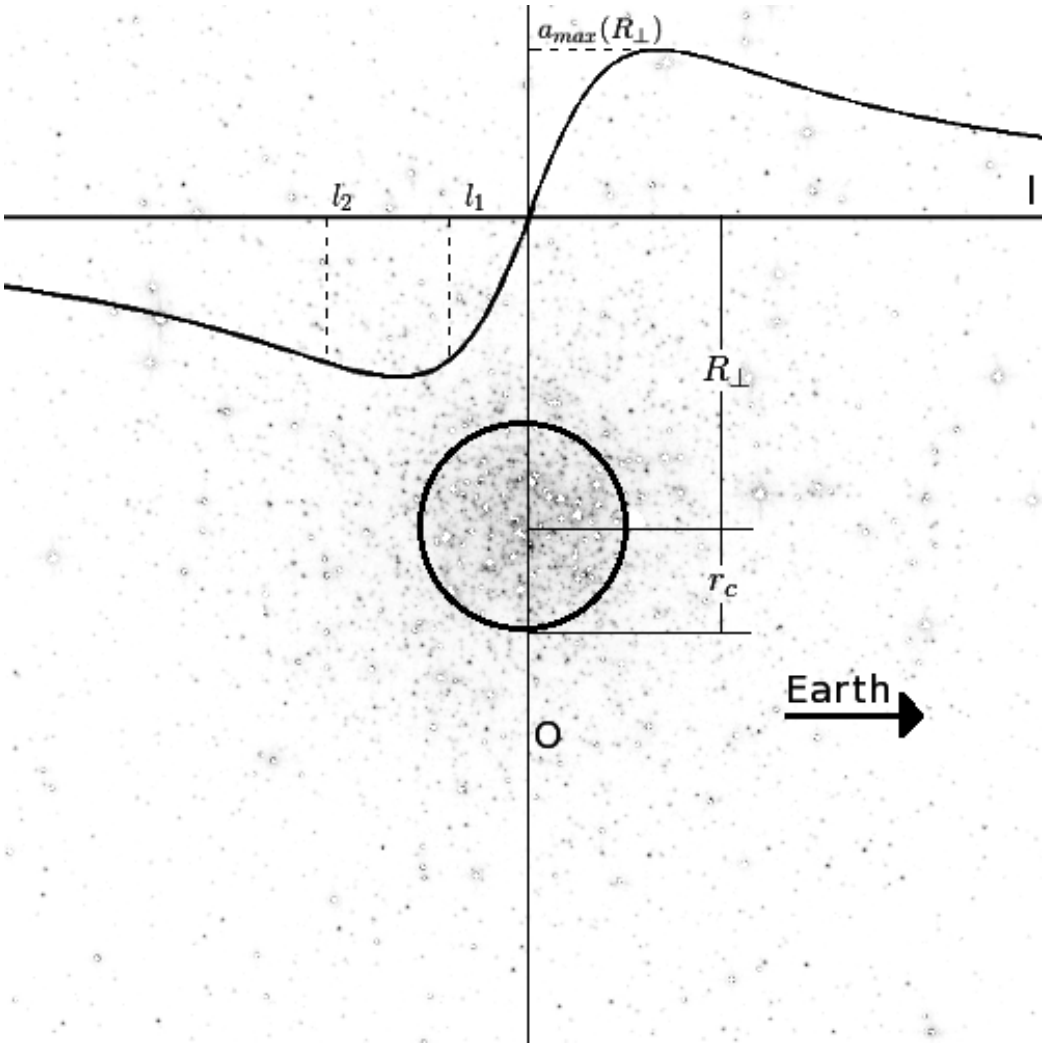

Fig. 2.1.— Geometry of a pulsar's location with respect to the core of the cluster with an example core radius encircled and the line of sight acceleration over-plotted on top of the optical image of Terzan 5 taken with the Hubble Space Telescope[2]. O is the plane of the sky that runs through the center of gravity for the cluster. l is the line of sight distance out from O. $R_\perp$ is the projected separation on the plane of the sky from the center of gravity and r_c is the core radius. For a measured line of sight acceleration below the maximum possible line of sight acceleration $a_{\mathrm{l,max}}(R_\perp)$ there are two possible line of sight positions that give the same acceleration, marked by l_1 and l_2.

2.4.2 Acceleration Profile

In this section we derive the contribution of a pulsar's acceleration that arises due to the GCs mean-field and the nearest neighbors.

Mean-field Acceleration

In order to turn measured accelerations into a probe of the cluster potential we need acceleration as a function of r_c, the core density (ρ_c), and the pulsar's spherical radius (r). We begin with a King density profile (King 1962) for the dominant mass class of the cluster, which most strongly sets the inferred potential:

$$\rho(r) \simeq \rho_c \left[1 + \left(\frac{r}{r_c}\right)^2\right]^{-\frac{3}{2}}. \tag{2.1}$$

Integrating this equation radially yields the interior mass at any given radius r. We multiplied this by $-G/r^2$ to obtain a general form of the cluster acceleration felt at any given radius out from the core:

$$a_{\rm r}(r) = -4\pi G \rho_c r_c^3 r^{-2} \left[\sin^{-1}\left(\frac{r}{r_c}\right) - \frac{r}{r_c\sqrt{1+(r/r_c)^2}}\right] \tag{2.2}$$

where $a_{\rm r}(r)$ is the predicted radial mean-field acceleration and was derived for the first time explicitely by Freire et al. (2005).

Projecting the acceleration along our line of sight by a factor of l/r and substituting in typical values for globular clusters like Terzan 5, Equation 2.2 reduces

to:

$$a_{\rm l}(l,r) = -3.5{\times}10^{-7}\left(\frac{\rho_c}{10^6\,M_\odot\,pc^{-3}}\right)\left(\frac{l}{0.2\,pc}\right)\left(\frac{r}{r_c}\right)^{-3}\left[\sin^{-1}\left(\frac{r}{r_c}\right) - \frac{r}{r_c\sqrt{1+(r/r_c)^2}}\right]\,{\rm m\,s^{-2}}\,, \tag{2.3}$$

where we define $a_l = a_{\rm l}(l,r)$ to be the predicted mean-field line of sight acceleration for the rest of this chapter. The shape of this distribution is shown in Figure 2.1.

Nearest Neighbor Accelerations

Chandrasekhar (1943) derives the *Holtzmark* probability distribution for acceleration due to an infinite distribution of stars with a given mean density. In Appendix A, we use this method to determine the probability that a nearest-neigbor can produce an acceleration equivalent to, or greather than, the mean field.

The cumulative probability ($P_{\rm c}$) that the nearest neighbor acceleration $a_{\rm NN}$ is larger than a value a_l is given by Equation .6:

$$P_{\rm c}(a_l) = \int_{a_l}^{\infty} da_l' P(a_l') = \frac{1}{\sqrt{2\pi}}\left(\frac{a_{\rm NN}}{|a_l|}\right)^{3/2}\,. \tag{2.4}$$

In Section 2.5.1 we will compare our predicted probability to the mean-field acceleration using simulated cluster data in order to show that the acceleration due to the nearest stellar neighbor a is a negligibly small effect in our models.

2.4.3 Jerk Profile

In order to use the higher order spin period derivative information, we also calculate the distribution of jerks felt by a pulsar at any given location in the cluster assuming an infinitely smooth potential in the cluster core. The full derivation for the

distribution of jerks produced by the nearest neighbors can be found in Appendix B.

Mean-field Jerks

From Phinney (1993) we use Equation 4.3 for defining the mean-field jerk felt by a pulsar within the inner few core radii of the cluster:

$$\left(\frac{\ddot{P}}{P}\right)_{\rm mf} = \dot{\boldsymbol{a}}_{\rm mf} \cdot \frac{\boldsymbol{n}}{c} = \frac{4}{3}\pi G\rho(r)\frac{v_l(r)}{c}\,, \tag{2.5}$$

where $v_l(r)$ is the line-of-sight velocity of the pulsar.

In Section 2.5.2 we will compare the distribution of measured mean-field jerks from simulations to Equation 2.5.

2.4.4 Nearest Neighbor Jerks

The characteristic jerk experienced at the location of the pulsar due to the surrounding stars is given by the following:

$$\dot{a}_0 = \frac{2\pi\xi}{3} G\langle m\rangle \sigma n\,, \tag{2.6}$$

where $\dot{a}_0$ is the characteristic jerk and ξ is a numerical factor that arises from integrating over the Maxwell-Boltzmann distribution in the vicinity of the pulsars and can be approximated by $\xi \simeq 3.04$. The variables m, σ, and n are the mass of the nearby stars, the velocity dispersion of the nearby stars, and the number density of stars nearby to the pulsar, respectively.

2.4.5 Central Black Hole

We tested for the presence of an intermediate mass black hole (IMBH) in Terzan 5 by perturbing the standard King density profile with a central point source. For a given mass, the black hole will have a radius of influence (r_i) given by Equation 3 from Baumgardt et al. (2004a)

$$r_i = \frac{3M_{\rm BH}}{8\pi\rho_c r_c^2}\,, \tag{2.7}$$

where $M_{\rm BH}$ is the mass of the central black hole.

At r_i and beyond, the density profile follows the standard King model for globular clusters (Baumgardt et al. 2004b). Within this radius the density profile obeys the following formula:

$$\rho_{\rm BH} \propto r^{-1.55}\,, \tag{2.8}$$

where our selection of a density profile following a -1.55 power law is taken from Baumgardt et al. (2004b), where they found through N-body simulations that a system with multiple component masses in the core follows this density profile. This is close to the results of Bahcall & Wolf (1976), which find that for a more top-heavy initial mass function (IMF) around a black hole, the density profile must scale as $r^{-1.5}$.

Using this modified density profile within the radius of influence, we derive a perturbed model equation:

$$a_l(l,r) = \frac{4\pi G}{r^2}\frac{l}{r}\left[\int_0^{r_i} r^2\rho_{\rm BH}dr + \int_{r_i}^{r} r^2\rho_{\rm King}\right]\,, \tag{2.9}$$

where $\rho_{\rm King}$ is the King model for density in Equation 2.1.

Allowing the black hole mass to vary in our simulation allows the pulsars to potentially enter its the radius of influence, drastically altering their modeled acceleration.

The expected posterior distribution should therefore show that for small black hole masses the black hole is not massive enough to produce a measurable acceleration at the position of a pulsar. As the black hole mass grows, so does the chances of strongly perturbing a pulsar, thereby giving better sensitivity to the likelihood of having a black hole in the system.

For the purposes of this work, we do not consider the jerk produced by the black hole, though we do consider the jerk felt by each pulsar due to the modified density profile in the core.

2.5 Cluster Simulations

Using simulations, we verified the results of Section 2.4 as well as those originally presented by Phinney (1993) and Anderson (1993). We accomplished this using the C-based artificial star cluster initializer, McLuster (Küpper et al. 2011), which allows us to create star clusters with a variety of different cluster potentials, masses, ages, and various other structural parameters. In order to simulate Terzan 5, we used the results of Miocchi et al. (2013) to set the cluster potential to a King model with $r_{\rm h}$=0.98 pc and a concentration parameter of W_0=7.2.

We used the Kroupa IMF (Kroupa 2001) for our simulations, which has a slope of $\alpha = -1.3$ over the mass ranges $0.08\,{\rm M}_\odot \leq m \leq 0.5\,{\rm M}_\odot$ and a slope of $\alpha = -2.3$ for masses $0.5\,{\rm M}_\odot \leq m \leq 100\,{\rm M}_\odot$. We then evolved all the stars in the cluster in place for 12 Gyr to create data consistent with the oldest population in Terzan 5 (Origlia et al. 2013).

For our models we varied the total mass of the cluster M_t, r_t, and r_c while holding all other cluster parameters constant. To ensure that models of the same mass but different limiting radii were consistent, we used a single seed to hold constant

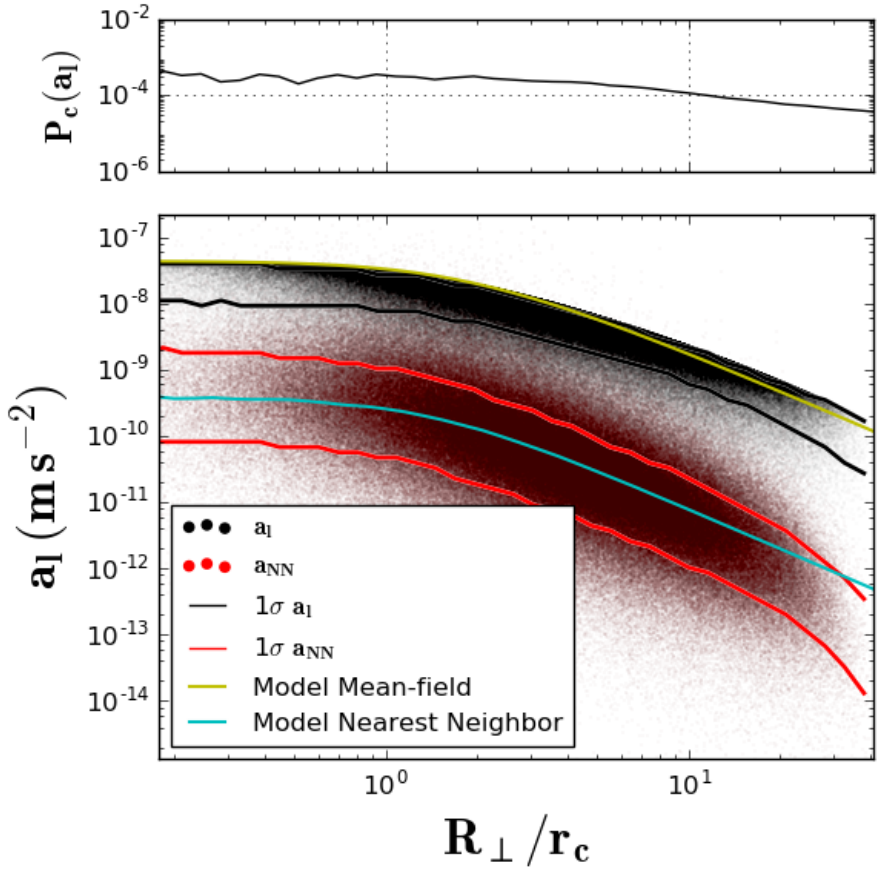

Fig. 2.2.— Measured line of sight accelerations within cylindrical shells for a simulated Terzan 5 cluster with M_t=2×10^5 M$_\odot$ and a r_c=0.2 pc showing that nearest neighbor accelerations matching or exceeding the mean-field value are rare. The black points show the measured mean-field acceleration and the red points show the measured nearest neighbor values. The black and red lines show the 1-σ confidence intervals for the mean-field and the nearest neighbors respectively. Overplotted are the model accelerations given by Equations 2.3 and .2. The upper plot shows the probability of the measured nearest neighbor acceleration exceeding the mean-field according to Equation 2.4.

the stellar masses of individuals stars drawn from the IMF as we varied the cluster parameters.

We then output a list of positions and velocities for each star from the simulation and calculated the acceleration and jerk due to the collection of all the particles in the simulation in order to test our model equations. The details of these calculations are discussed in Sections 2.5.1 and 2.5.2.

2.5.1 Pulsar Accelerations

Using McLuster, we measured the mean-field acceleration on each particle in the simulation, as well as contributions from the nearest neighbors. For the mean-field we calculated the mass interior to the radial position of each particle to compare to our model acceleration given by Equation 2.3. The nearest neighbor accelerations were calculated for each particle by finding its nearest companion and calculating its acceleration directly.

We find that for all values of M_t, r_c, and r_t that would be applicable to a Terzan 5 like system, the accelerations are dominated by the mean-field. We present our results for one such cluster simulation with M_t=2×10^5 M$_\odot$ and r_c=0.2 pc as these simulation parameters are close to those derived in Section 2.10 while still having few enough particles to model efficiently.

Figure 2.2 shows the measured values of a_l and a_{NN} for one of the Terzan 5 simulations in equally log-spaced cylindrical shells centered around the CoG. From this figure we estimate the probability of a nearest neighbor being the dominant source of acceleration for a pulsar according to Equation 2.4.

For an acceleration $a_{\rm l}$=10^{-7} m s^{-2} and a nearest neighbor acceleration of $a_{\rm NN} \sim$ 10^{-9} m s^{-2}, we find $P_c(a_{\rm l}) \sim 10^{-4}$. This agrees with the simulated data as shown

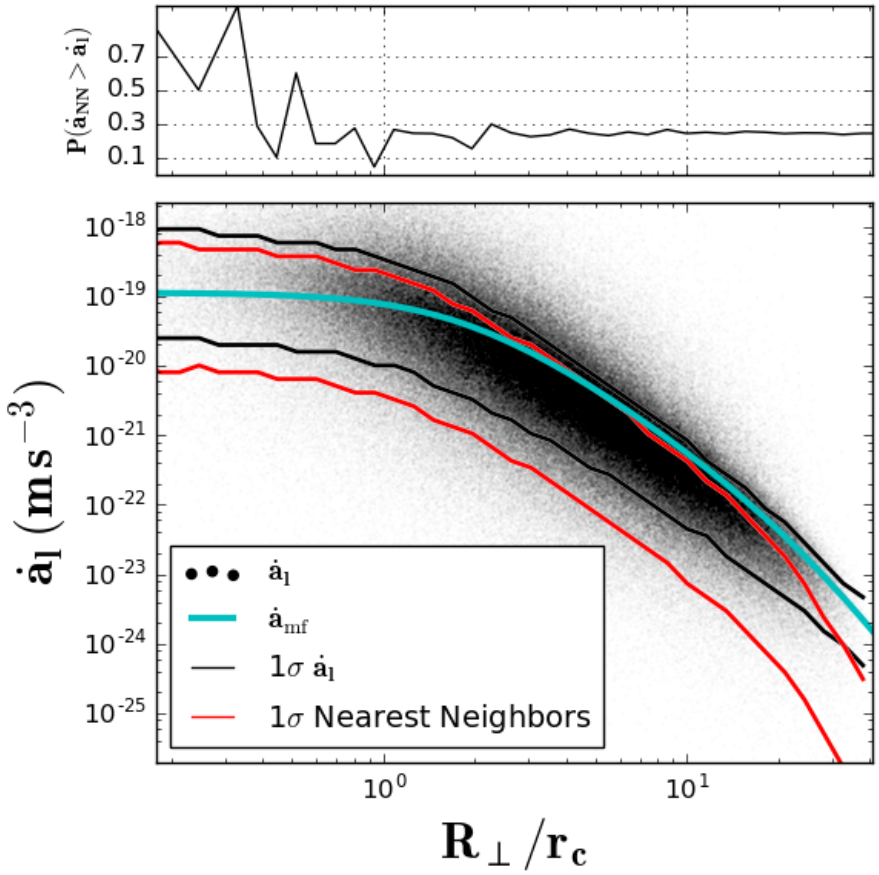

Fig. 2.3.— Measured line of sight jerks within cylindrical shells for a simulated Terzan 5 with M_t=2×10^5 M$_\odot$ and r_c=0.2 pc. The black points show the combined pair-wise jerk from all the stars in the simulation for any given particle. The black and red lines show the 1-σ confidence intervals for the combined and nearest neighbor values respectively. Overplotted is the mean-field jerk given by Equation 2.5. The upper plot shows the probability of the measured nearest neighbor jerk exceeding the the combined jerk within each cylindrical bin.

in the top panel of Figure 2.2, which shows that the nearest neighbors represent a negligible contribution to the acceleration felt by any single star. We therefore consider it unlikely that nearest neighbors can account for the accelerations felt by each pulsar and do not consider their effect in our calculations.

2.5.2 Pulsar Jerks

Figure 2.3 shows the measured jerk due to the pair-wise interaction of all particles in the simulation ($\dot{a}_l$) as well as the 1-σ region containing the measured nearest neighbor induced jerks within log-spaced cylindrical shells for a simulated Terzan 5 cluster. The top panel shows the ratio of measured nearest neighbor jerks greater than, or equal to, the total jerk.

We find that the nearest neighbor jerks are always of a similar magnitude as the mean-field measurement, regardless of the cluster's M_t, r_c, and r_t. We have plotted the mean-field jerk defined by Equation 2.5 in cyan and find good agreement with the data. We present our results for one such cluster simulation with M_t=2×10^5 M$_\odot$ and r_c=0.2 pc as these simulation parameters are close to those derived in Section 2.10 while still having few enough particles to model efficiently.

From Appendix B the distribution of possible line of sight jerks ($\dot{a}_l$) for the pulsar due to its nearest neighbor is given by the following Lorentzian formula:

$$P(\dot{a}_l) = \frac{\dot{a}_0/\pi}{\dot{a}_l^2 + \dot{a}_0^2}\,. \tag{2.10}$$

Figure 2.4 shows the measured PDF for the distribution of nearest neighbors in a single spherical shell for a simulated Terzan 5 cluster. Over-plotted is the predicted PDF for pulsar jerks given by Equation 2.10. This derived PDF has good agreement across all cluster masses and radii for spherical shells out to intermediate radii ($r \lesssim$

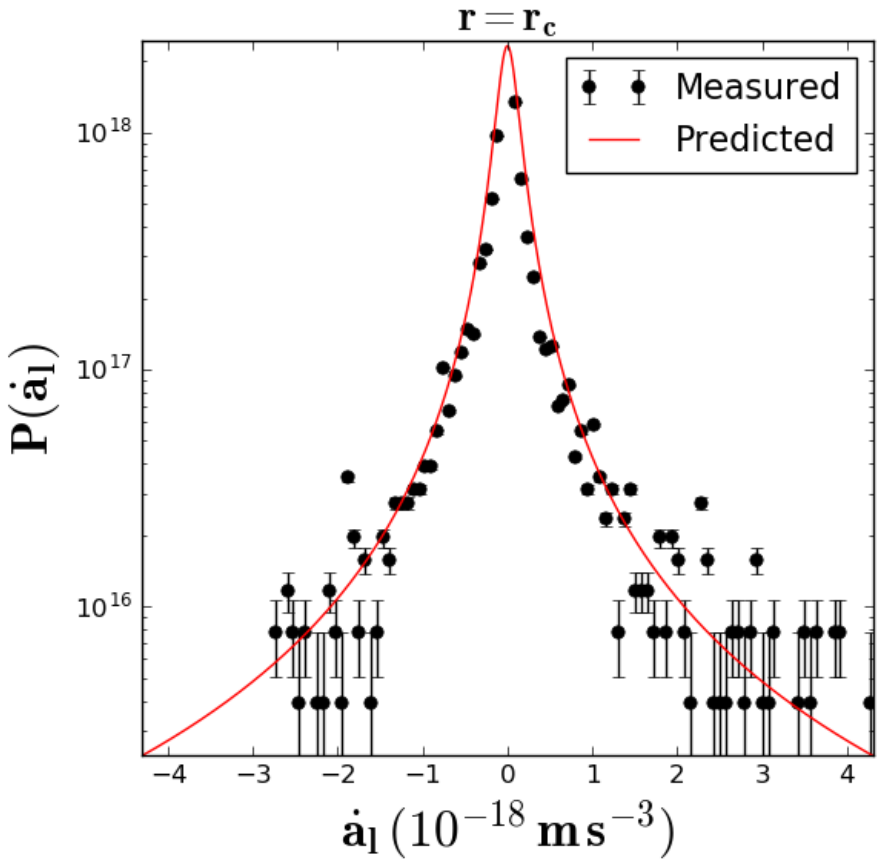

Fig. 2.4.— Measured jerks within three spherical shells centered about the core of a simulated Terzan 5 cluster with M_t=2×10^5 M$_\odot$ and r_c=0.2 pc. The data points show the measured probability of finding a given value of jerk along with its error for bins with greater than 10 counts. The red line shows the calculated nearest neighbor PDF from Equation 2.10.

$3.0r_c$). Beyond these radii we begin to see deviations in the tail of the distribution, which is likely due to the stars no longer following a lowered Maxwellian distribution.

When performing our final analysis we do not consider the jerks of those pulsars with $r > 3.0r_c$, though we still use the acceleration information for these pulsars to inform us about the outer parts of the cluster.

2.6 Converting Pulsar Timing to Accelerations

2.6.1 Isolating Cluster Acceleration

Before studying the cluster potential further, we define our method for converting pulsar timing data into an acceleration. To do so, we follow the prescription of Phinney (1993) and Anderson (1993), which relate changes in the pulsar's spin and orbital periods to an acceleration.

For a pulsar sitting in a smooth, spherically symmetric potential the observed change in a pulsar's spin period is the result of the intrinsic spin down of the pulsar and any additional acceleration along our line of sight. The measured spin period changes can therefore be decomposed into the following form:

$$\frac{a_{\rm meas}}{c} \equiv \left(\frac{\dot{P}}{P}\right)_{\rm meas} = \left(\frac{\dot{P}}{P}\right)_{\rm int} + \frac{a_c}{c} + \frac{a_g}{c} + \frac{a_s}{c} + \frac{a_{\rm DM}}{c}\,, \tag{2.11}$$

where $\left(\dot{P}/P\right)_{\rm int}$ is the spin period change associated with the intrinsic pulsar spin-down, a_c is the line of sight acceleration due to the globular cluster potential on a pulsar, a_g is the acceleration due to the Galactic potential, a_s is the apparent acceleration from the Shklovskii effect (i.e. the proper motion of the pulsar) (Shklovskii 1970), and $a_{\rm DM}$ is the apparent acceleration due to errors in the changing dispersion measure (DM)

towards the pulsar.

Figure 5 shows the measured acceleration for each pulsar in Terzan 5 along with the predicted accelerations one would measure for different intrinsic spin-down rates of a pulsar; additionally, the expected acceleration due to the Galactic potential at the core of the cluster is plotted as a dashed black line.

Accelerations from intrinsic spin-down

We calculated the intrinsic spin-down by relating the magnetic field strength of the pulsars to their spin period derivative for isolated pulsars and those binary systems without a measured orbital period derivative. In Section 2.6.2 we discuss how we can circumvent the need to measure the intrinsic spin-down of some of our pulsar binaries.

For a simple model of a pulsar with magnetic dipole emission and a braking index of n=3, the $\dot{P}$ for a typical MSP is given by:

$$c\left(\frac{\dot{P}}{P}\right)_{\rm int} = 7.96\times10^{-10}\left(\frac{B}{2\times10^{8}\,{\rm G}}\right)^{2}\left(\frac{2\,{\rm ms}}{P}\right)^{2}\,{\rm m\,s^{-2}}\,, \tag{2.12}$$

where B is the surface magnetic field strength of the pulsar and the numerical factor has been scaled to appropriate values for an MSP.

Magnetic field strengths for pulsars are typically measured using the pulsar's P and $\dot{P}$ values. Since pulsars in GCs have measured values of $\dot{P}$ that are dominated by the cluster potential however, measurements of magnetic field strengths for these systems have not been extensively studied to date.

To get around this problem we used the known magnetic field strengths for similar Galactic MSPs taken from the ATNF catalog[3] (Manchester et al. 2005). These values of magnetic field strength were then fit to a log-normal PDF. We have plotted the

[3]http://www.atnf.csiro.au/people/pulsar/psrcat/

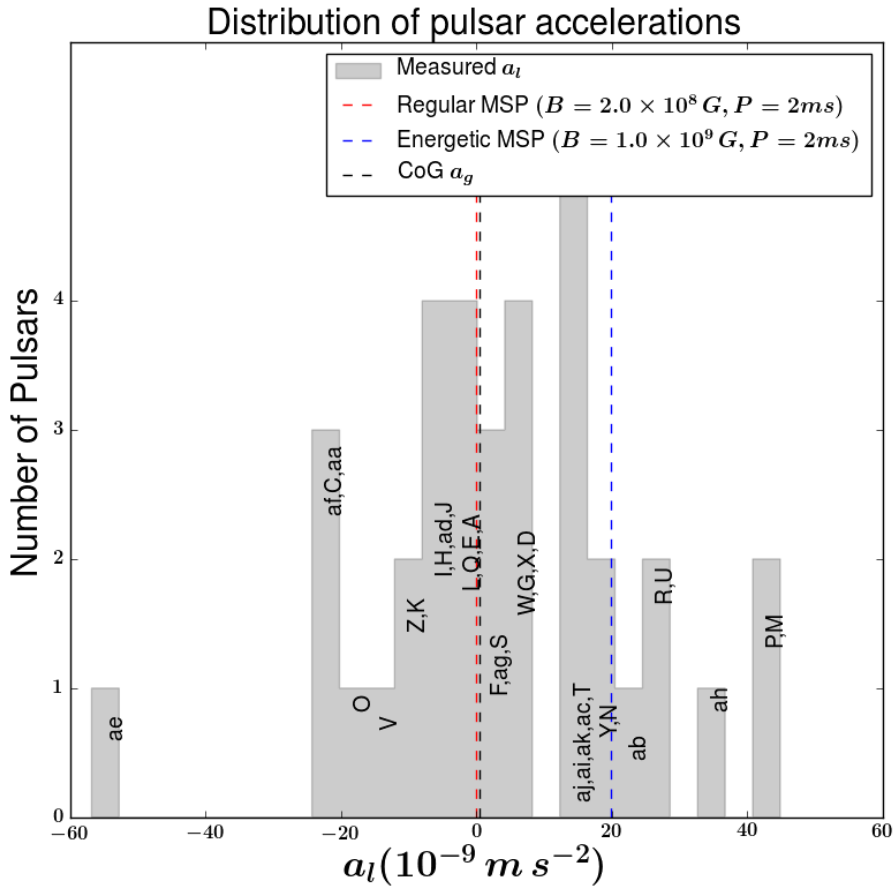

Fig. 2.5.— Histogram of the measured accelerations a_l for Terzan 5 pulsars. Overplotted in red is a typical MSP spin-down shown as an apparent acceleration and in blue is an example of an energetic MSP's spin-down shown as an apparent acceleration. Lying nearly coincident with the acceleration for the spin-down of a typical MSP is the acceleration due to the Galactic potential on the CoG of the cluster, which is shown in black and is largely overlapped by the red line. For all but the most energetic pulsars the cluster potential is the dominant source of acceleration.

results of these fits for pulsars with a spin frequency greater than 33 Hz and magnetic field strengths less than 1.5×10^9 G as a function of $\ln(B)$ in Figure 2.6. We find that the median and standard deviation of the resulting normal distribution in $\ln(B)$ are given by $\mu_{\ln(B)} = 19.51$ and $\sigma_{\ln(B)} = 0.76$. This corresponds to a location parameter of $\mu = 1.25\times10^8$ G and a scale parameter of $\sigma = 0.53\times10^8$ G, which we use later in this paper to define the log-normal likelihood function.

In Section 2.8 we will discuss how Equation 2.12 and the log-normal fit shown in Figure 2.6 are used to fit for cluster parameters in our MCMC sampler.

Accelerations from the Galactic potential

Next we calculate the acceleration due to the Galactic potential for each pulsar. To do this, we used a distance for the Sun from the Galactic center of $R_0 = 8.34 \pm 0.16$ kpc and a rotational speed of the Galaxy at the Sun of $\Theta_0 = 240 \pm 8$ km/s, as measured by modeling of the Radial Velocity Experiment and the Geneva-Copenhagen Survey (Sharma et al. 2014). For a flat rotation curve and a distance to Terzan 5 of $d = 5.9 \pm 0.5$ kpc, Equation 5 from Nice & Taylor (1995) gives the acceleration due to the differential Galactic rotation at the location of each pulsar as observed from the Earth:

$$a_g \cdot \boldsymbol{n} = -\cos(b)\left(\frac{\Theta_0^2}{R_0}\right)\left(\cos(l) + \frac{\beta}{\sin^2(l)+\beta^2}\right)\,\mathrm{m\,s^{-2}}\,, \tag{2.13}$$

where $\beta = (d/R_0)\cos(b) - \cos(l)$.

At the CoG for Terzan 5 ($l = 3.8°$, $b = 1.7°$) we find an acceleration of $a_g = 5.1 \times 10^{-10} \pm 1.4 \times 10^{-10}\,\mathrm{m\,s^{-2}}$. This is shown in Figure 2.5 as the dashed black line, which is much smaller than the observed apparent accelerations and is nearly coincident with the plotted apparent acceleration of a typical MSP spin-down rate.

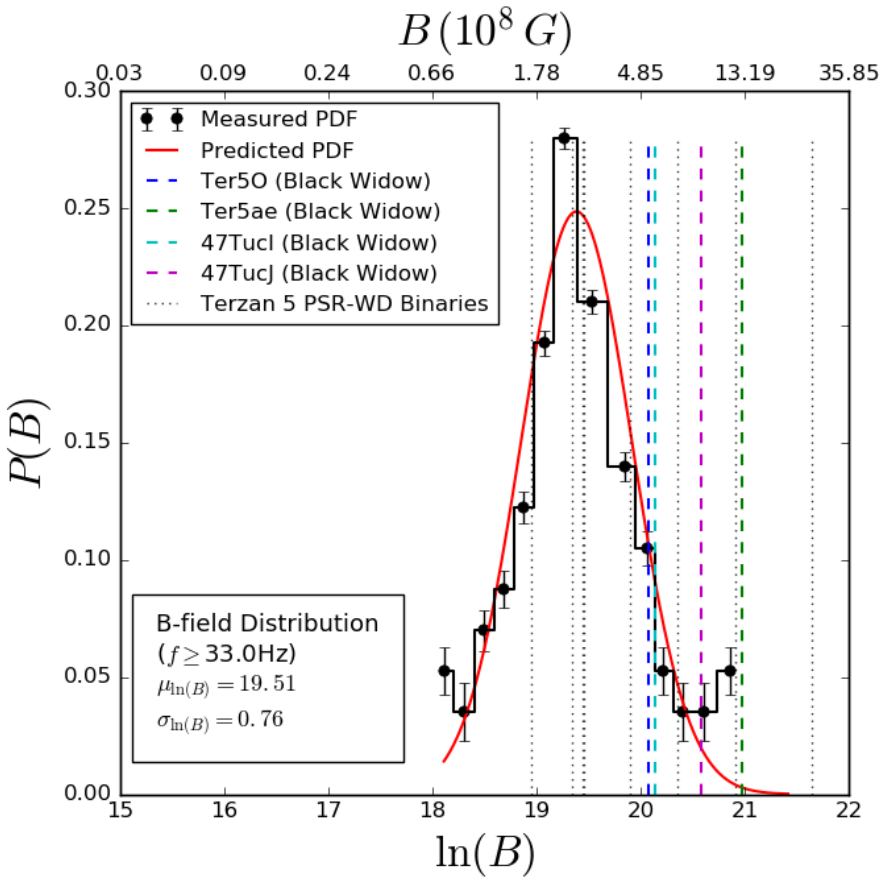

Fig. 2.6.— Measured distribution of magnetic field strengths for millisecond pulsars with a spin frequency greater than 33 Hz and magnetic field strengths less than 1.5×10^9 G in the field of the Galaxy. Over-plotted is a log-normal fit to the data used to draw a log-likelihood of finding a pulsar with a given magnetic field strength. Vertical lines show the measured magnetic field strength of globular cluster black widows (dashed lines) and pulsar-white dwarf binaries in Terzan 5 (dotted lines) after using the measured $\dot{P}_b$ to remove the cluster induced spin-down as shown in Equation 2.20.

Accelerations from Shklovskii effect

Next we estimated the Shklovskii effect at the distance of Terzan 5, which is an apparent acceleration due to the proper motion of the pulsar. From Shklovskii (1970) we have:

$$a_s = 4.29 \times 10^{-12} \left(\frac{d}{5.9\,\mathrm{kpc}}\right) \left(\frac{\mu_T}{\mathrm{mas\,yr^{-1}}}\right)^2 \mathrm{m\,s^{-2}}, \tag{2.14}$$

where d is the cluster distance and μ_T is the proper motion.

As Terzan 5 is near the center of the Galaxy, we used the tangential velocity of the Sun with respect to the center of the Galaxy, Θ_0. The proper motion is therefore given by:

$$\mu_T = 8.5 \left(\frac{\Theta_0}{240\mathrm{kms}}\right) \left(\frac{5.9\,\mathrm{kpc}}{d}\right) \mathrm{mas\,yr^{-1}} \tag{2.15}$$

which gives μ_T=8.5 mas yr^{-1}.

Using Equation 2.14 we find $a_s \sim 4.2 \times 10^{-12}$ m s^{-2}, which is much smaller than the other sources of acceleration. Given the relative scale of this term, the Shklovskii effect is a very tiny contribution to the measured acceleration for any reasonable value of transverse velocity.

Accelerations from DM errors

Propagating radio waves in the ionized interstellar medium undergo delays in their arrival time at Earth due to dispersion. For a pulsar this means that the arrival time of the pulse is delayed as a function of the observing frequency:

$$\Delta t_{\mathrm{DM}} = 1.85 \left(\frac{DM}{\mathrm{pc\,cm^{-3}}}\right) \left(\frac{\nu}{1500\,\mathrm{MHz}}\right)^{-2} \mathrm{ms} \tag{2.16}$$

where Δt_{DM} is the dispersive delay time, the DM is the dispersion measure of the pulsar and is related to the number of free electrons between us and the pulsar, and

ν is the observing frequency.

If there are unaccounted for errors in the DM as a function of time ($\Delta\mathrm{DM}(t)$), it is possible to produce apparent accelerations in the pulsar's timing. In the upcoming Ransom et al. (in prep 2017) paper, the observed DM errors were measured to be $\Delta\mathrm{DM} \lesssim 10^{-2}$ pc cm^{-3} for all pulsars as observed over a 10 year time period. Using this as an upper limit on the possible values of $\Delta\mathrm{DM}(t)$ at an observing frequency of 1500 MHz, Equation 2.16 gives an excess delay of $\Delta t_{\mathrm{DM}} \lesssim 18$ μs for our uncertainty in DM over the past ten years of timing.

We convert the observed change in arrival time of a given pulse into a frequency derivative by looking at the change in the phase of the pulse over a given timescale:

$$\dot{f} = 2\left(\frac{\Delta t_{\mathrm{DM}}}{PT^2}\right), \tag{2.17}$$

where T is the timescale over which we measure the error in DM.

Converting this into a period derivative, the acceleration from the stochastic DM error is given by:

$$a_{\mathrm{DM}} = -2c\left(\frac{\Delta t_{\mathrm{DM}}}{T^2}\right), \tag{2.18}$$

which can be expressed in more convenient units of:

$$a_{\mathrm{DM}} = -6.1 \times 10^{-14}\left(\frac{\Delta t_{\mathrm{DM}}}{1\,\mu\mathrm{s}}\right)\left(\frac{10\,\mathrm{yrs}}{T}\right)^2. \tag{2.19}$$

For a delay of Δt_{DM}=18 μs due to unexplained DM variations over a baseline of T=10 years, the apparent acceleration is $a_{\mathrm{DM}} \sim 10^{-13}$ m s^{-2}. This is a very minor contribution to our measured acceleration and as such is not corrected for in our data. Also, as it is very unlikely for the DM variations to be monotonic over this span of time, the actual contribution to the measured acceleration of each pulsar from the

DM is likely much smaller than this value (Keith et al. 2013).

These measurements of acceleration from intrinsic spin-down, the Galactic potential, the Shklovskii effect, and the error in DM place strong constraints on the allowed range of accelerations any cluster model may produce. In the next few sections we will discuss how we used the timing of pulsar binaries to provide even better constraints on our models by avoiding any assumptions of intrinsic pulsar spin-down rates.

2.6.2 Measuring a_c using pulsar binaries

In addition to the spin periods of each pulsar, we also used the orbital period (P_b) and orbital period derivatives ($\dot{P}_b$) of pulsar binaries to probe the cluster potential. Each of the thirteen systems with a measured value of $\dot{P}_b$ appear to be cluster dominated, and do not experience any measurable orbital decay due to general relativistic effects (Damour & Deruelle 1985). Without an intrinsic effect within the binary system causing the orbital period derivative, this means changes in the orbital period are almost entirely due to the cluster potential.

We have already shown that the Galactic rotation and observed Shklovskii effect are small and can be well accounted for in our timing. We therefore may express the orbital period derivative in a similar form as Equation 2.11

$$\left(\frac{\dot{P}_b}{P_b}\right)_{meas} = \frac{a_c}{c} + \frac{a_g}{c} + \frac{a_s}{c}\,. \tag{2.20}$$

In the next section, we discuss briefly a subclass of MSPs with measurable orbital period derivatives that must be carefully examined before applying Equation 2.20 to their timing results.

Black Widow & Redback Pulsars

Of the thirteen pulsar binaries with a measured $\dot{P}_b$, eight are in binaries with a white dwarf companion and are well characterized by Equation 2.20. The remaining five pulsars are either BWs or RBs. An important characteristic of these systems is that some experience stochastic changes in their orbital parameters which could manifest as an apparent acceleration in the timing data.

While some black widow systems do not show orbital phase variations, all redbacks systems discovered to date show changes in their orbital properties that are on average an order of magnitude larger than any seen in black widows. Even over a few year time scale the timing of a redback becomes nearly intractable as the stochastic wander of orbital properties evolve.

Within Terzan 5 there are three redbacks (J1748−2446A, J1748−2446P, and J1748−2446ad) and two black widows (J1748−2446O and J1748−2446ae). Due to the severity of the orbital phase changes seen in redbacks, we do not use the measured orbital period derivatives for these three systems. As for the two black widows (J1748−2446ae and J1748−2446O), which have measured orbital period derivatives, we motivate our inclusion of these two pulsars with two different arguments.

The first argument is that observed variations in the orbital parameters of black widows and redbacks are believed to be stochastic or quasi-periodic in nature (Applegate & Shaham 1994). It is therefore unlikely that the changes in the orbital period would be sufficiently monotonic to produce a large apparent acceleration for these systems. The second argument is that if either of these two systems possess some sort of intrinsic pulsar property that sets them apart from more typical pulsar-white dwarf binaries, then that may be indicative of a timing model influenced by changing orbital properties.

Table 2.2 shows the apparent line of sight accelerations for eight black widows using the measured values of $\dot{P}_b$ and Equation 2.20. Of these eight systems, four have been confirmed to have orbital phase wander. These systems show line of sight accelerations in excess of 10^{-7} m s^{-2}, whereas the remaining black widows all have accelerations ranging between $5{\times}10^{-9}$ and $5{\times}10^{-8}$ m s^{-2}. This may imply that only a handful of black widows are in a state where the mechanism that drives orbital wander is enhanced.

We also confirmed that the measured values of $\dot{P}_b$ are cluster-induced by looking at the energetics of the system. Taking the difference between the measured acceleration given by Equation 2.11 and the binary acceleration given by Equation 2.20 we are left with the intrinsic spin-down component of the pulsar in the binary system:

$$\left(\frac{\dot{P}}{P}\right)_{\rm int} = \left(\frac{\dot{P}}{P}\right)_{\rm meas} - \left(\frac{\dot{P}_b}{P_b}\right). \tag{2.21}$$

Table 2.2 shows the magnetic field strength for the inferred intrinsic spin down rate of each black widow for which a $\dot{P}_b$ value has been measured in 47 Tucanae and Terzan 5. Figure 2.6 shows the inferred magnetic field strength of each of these black widows as compared to the observed magnetic field distribution in the field of the Galaxy as recorded by the ATNF catalog (Manchester et al. 2005). Also plotted are the inferred magnetic field strengths of regular pulsar-white dwarf binaries. The only exception is 47TucO, which has been confirmed to have orbital phase wander and as such produces an unphysical magnetic field strength, implying the measured value of $\dot{P}_b$ for this system is dominated by the physics of its orbital phase wander. These results show that the energetics of the two black widows J1748−2446O and J1748−2446ae appear to be cluster dominated and do not have an excess in their measured values of $\dot{P}_b$ from phase wander.

For the rest of this chapter, we will assume that the orbital period derivatives of both J1748−2446O and J1748−2446ae are dominated by the cluster potential, and will use the measured values of $\dot{P}_b$ for each to help constrain the cluster parameters.

2.6.3 Converting $\ddot{P}$ to Jerks

Due to the motion of a pulsar through its potential relative to the observer, a pulsar with a rest frame period of P_0 is observed to have a period P of

$$P = [1 + (\boldsymbol{V}_p - \boldsymbol{V}_{\rm bary}) \cdot \boldsymbol{n}/c]\, P_0 \; . \tag{2.22}$$

where $\boldsymbol{V}_p$ is the pulsar velocity, $\boldsymbol{V}_{\rm bary}$ is the velocity of the solar system barycenter, and $\boldsymbol{n}$ is the unit vector along our line of sight.

Following the prescription of Phinney (1993) the derivative of Equation 2.22 yields expansions of the spin-period derivatives that can be expressed as an acceleration or its time derivatives. Limiting ourselves to a pulsars jerk, this becomes

$$\frac{\ddot{P}}{P} = \frac{1}{c}\dot{a} \cdot \boldsymbol{n} \, , \tag{2.23}$$

which allows us to derive the pulsar's jerk using the second order derivative of the pulsar acceleration, $\ddot{P}$.

2.7 Traditional Parameter Fits Using Pulsar Timing

In this section we used the methods of Phinney (1993), Anderson (1993), Freire et al. (2001b), and Freire et al. (2003) to relate the on-sky position of a pulsar and the

predicted cluster parameters of the host system. We will use this method to find an initial estimate of the Terzan 5 cluster characteristics as well as to compare our methodology to the results of Freire et al. (2001a) for the globular cluster 47 Tucanae. We then compare these results to those found using our MCMC fits in Section 2.10.

2.7.1 Column Density of Pulsars

We begin by calculating the column density using the locations of our MSPs as well as the positions of bright X-ray sources as these have been shown to arise mostly from neutron stars in LMXBs (Lewin et al. 1993). Thirty six X-ray sources were selected from Heinke et al. (2006), using sources with ten or more counts between $0.5-6$ keV, as well as removing two X-ray sources coincident with known pulsars J1748−2446P and J1748−2446ad in order to avoid double counting (Heinke et al. 2006). We then measure $R_\perp$ for the X-ray sources and pulsars separately and calculate the cumulative distribution function (CDF) for the column density as a function of $R_\perp$.

We verify that the X-ray sources and pulsars are drawn from the same parent density distribution by applying a two sample KS-test to the data. The embedded plot of Figure 2.7 shows the two distributions. We find a p-value of $\sim$0.99, meaning the pulsars and X-ray sources are likely drawn from the same parent distribution.

The spectral index for the neutron star population (α) defines how centrally concentrated the pulsars are in the cluster. The observed column density profile for the neutron stars is given by Equation 1 from Lugger et al. (1995):

$$n(R_\perp) = n_0 \left[1 + \left(\frac{R_\perp}{r_0}\right)^2\right]^{\frac{\alpha}{2}}, \tag{2.24}$$

where r_0 is a radial scale and is related to r_c.

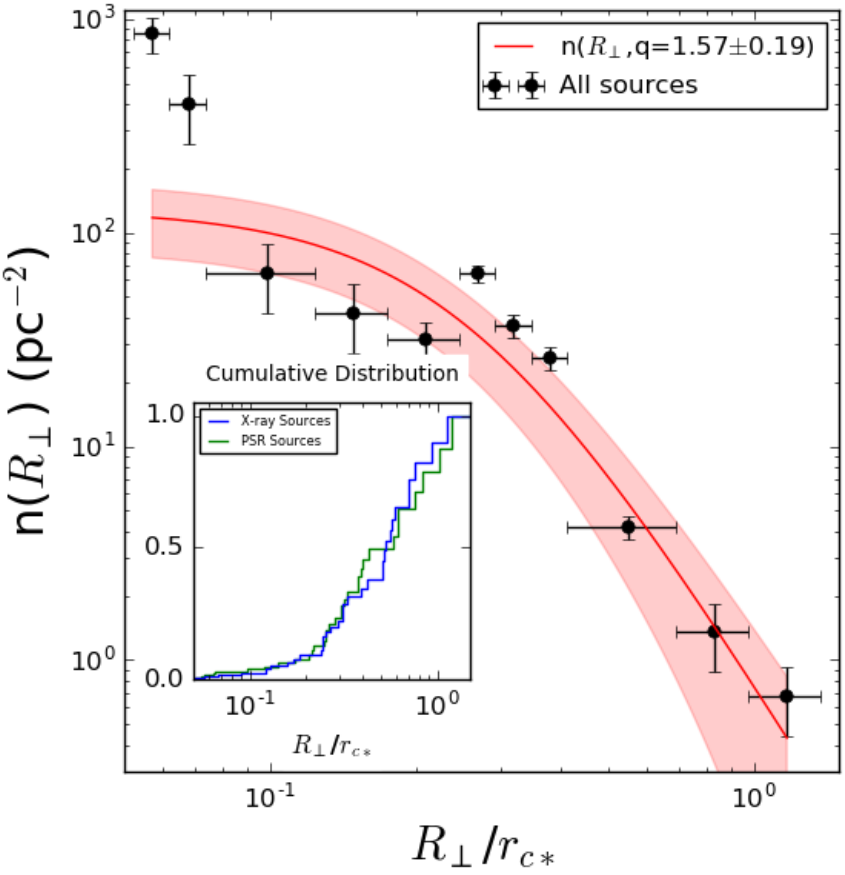

Fig. 2.7.— Column density of the combined MSP and LMXB populations as a function of $R_\perp/r_{c*}$ for Terzan 5. Over-plotted in red is Equation 2.26 for a mass ratio of $q = 1.57 \pm 0.19$ and a dominant mass class core radius of r_{c*}=0.26 pc. (Lanzoni et al. 2010). The embedded plot shows the cumulative distributions of the pulsars and X-ray sources (Heinke et al. 2006) separately, along with the p-value obtained from the two sample KS-test used to confirm that they are drawn from the same distribution.

We relate r_0 and r_c by $r_c \equiv \left(2^{-2/\alpha} - 1\right)^{1/2} r_0$. For $\alpha = -2$ this equation reduces to the single mass analytical King model (King 1962).

For the multi-mass King model, the dominant mass class (M_*) in the cluster has a spectral index of α=-2 and sets the potential for the GC most strongly. Different mass classes can be related to the dominant mass class according to the following relationships:

$$\begin{aligned} r_{cX} &= \left(2^{-2/(1-3q)} - 1\right)^{1/2} r_{c*} \\ \alpha_X &= 1 - 3q\,, \end{aligned} \tag{2.25}$$

where we define q to be the mass ratio between a mass class M_X and the dominant mass class M_* ($q = M_X/M_*$). r_{c*} is the core radius associated with M_*. (Heinke et al. 2003). For the purposes of this work, we include both the isolated pulsars and the pulsar binaries in this calculation of q, as the neutron star mass is expected to have a wide distribution (Ozel & Freire 2016) and the removal of the isolated pulsars from our sample does not significantly change our results.

We use the generalized form of Equation 2.24 from Heinke et al. (2003) to relate the pulsars to the dominant mass class:

$$n(r) = n_0 \left[1 + \left(\frac{R_\perp}{r_{c*}}\right)^2\right]^{\frac{1-3q}{2}}. \tag{2.26}$$

Grindlay et al. (2002) found that the most visible stellar population in a cluster should have a spectral index of $\alpha = -2$. We therefore use the core radius (0.26 pc) of bright main sequence turn off (MSTO) stars found by Lanzoni et al. (2010) to approximate r_{c*} and solve for the mass ratio of neutron stars and MSTO stars.

For the given value of r_{c*}=0.26 pc at a cluster distance of d=5.9 kpc, we perform

a non-linear least squares fit for the expected number density of stars as a function of n_0 and q. We find $q = 1.57 \pm 0.19$, which gives a spectral index of $\alpha = -3.71 \pm 0.57$. Figure 2.7 shows the best fit to Equation 2.26 for both the pulsars and the X-ray sources combined.

This mass ratio agrees within the 1-σ confidence intervals reported by Heinke et al. (2006) ($q = 1.43 \pm 0.11$), which used only the LMXB population of Terzan 5 to calculate q. The turnoff mass of Terzan 5 is not well constrained, but using the results of (Bergbusch & VandenBerg 2001) of M_X=0.9 $M_\odot$, our mass ratio predicts an approximate pulsar or LMXB system mass of $M_X = 1.33 \pm 0.07\,M_\odot$. We will discuss the implications of our derived system mass in Section 3.8.

2.7.2 Core Density & Core Radius

Procedure

In order to derive the core density and core radius of Terzan 5 using $R_\perp$ for each pulsar, we begin with Equation 3.5 from Phinney (1993):

$$a_{\rm l,max} = \frac{2\pi G \rho_c r_c^2}{\sqrt{r_c^2 + R_\perp^2}}\,, \tag{2.27}$$

where the velocity dispersion (σ) from Equation 3.5 (Phinney 1993) was replaced by $\sigma^2 = (4\pi/9)G\rho_c r_c^2$ from Heggie & Hut (2003). This form of the acceleration equation is accurate to within 10% for $r < 2r_c$ and to within 50% for intermediate radii and is useful when line of sight positions for each source are unknown.

From Equation 3.12 from Phinney (1993) we find the probability of having a

measured $a_{\rm l}$ less than $a_{\rm l,max}(R_\perp)$ for our measured value of α:

$$p(a_l|a_{\rm l,max}(R_\perp))d\,|a_l| = P(\alpha)\left(\frac{a^{\alpha-2}}{\sqrt{1-a^2}}\right)\left[\left(1-\sqrt{1-a^2}\right)^{1-\alpha/2}+\left(1+\sqrt{1-a^2}\right)^{1-\alpha/2}\right]da\,, \tag{2.28}$$

where $a = a_{\rm l}/a_{\rm l,max}(R_\perp)$ and $P(\alpha)$ is a normalization constant given by:

$$P(\alpha) = \frac{\Gamma(\alpha/2)2^{(2-\alpha)/2}}{\sqrt{\pi}\Gamma([\alpha-1]/2)}\,, \tag{2.29}$$

where Γ is the gamma function.

Using the measured value of $\dot{P}_b$ when available and solving Equation 2.11 assuming the median expected magnetic field strength of our isolated pulsars (Section 2.6.1), we obtain a measurement of the cluster-only acceleration to use with Equation 2.28 for all of our pulsars.

We find the probability of a given set of cluster parameters producing each pulsar's measured acceleration by multiplying the result of Equation 2.28 with the measurement error associated with $a_{\rm l}$ from the timing noise and the removal of a_g, a_s, and $\left(\dot{P}/P\right)_{\rm int}$. We then convert this probability into a log likelihood and sum up the total log likelihood for all of the pulsars for a given set of model parameters.

Errors in our cluster parameters are calculated by finding the contour region about the maximum likelihood that contains 68% of the total probability in our simulation grid. We report the median of the marginalized distribution of each parameter as the best fit to the cluster potential, with the extent of the 1-σ confidence interval out from the median as the errors in each parameter.

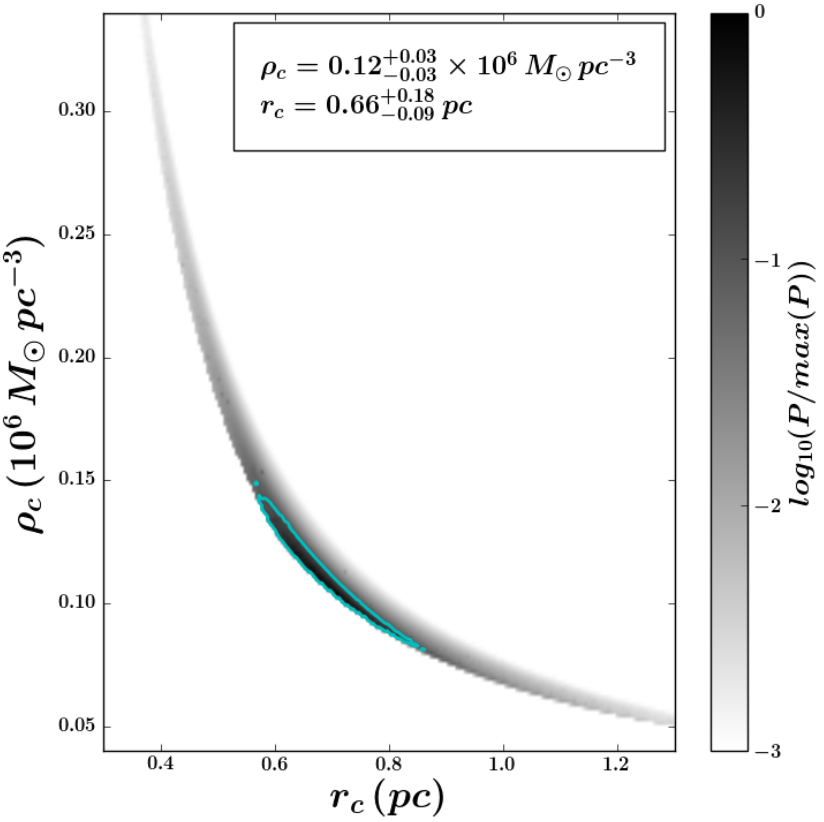

Fig. 2.8.— The log likelihood for all possible combinations of model parameters ρ_c and r_c for 47 Tucanae. The contour shows the 1-σ confidence region. We take the median of the marginalized parameters as our best fit and the extent out from the median to the 1-σ contour region as the errors. When using only projected positions of each pulsar, there is strong covariance between ρ_c and r_c.

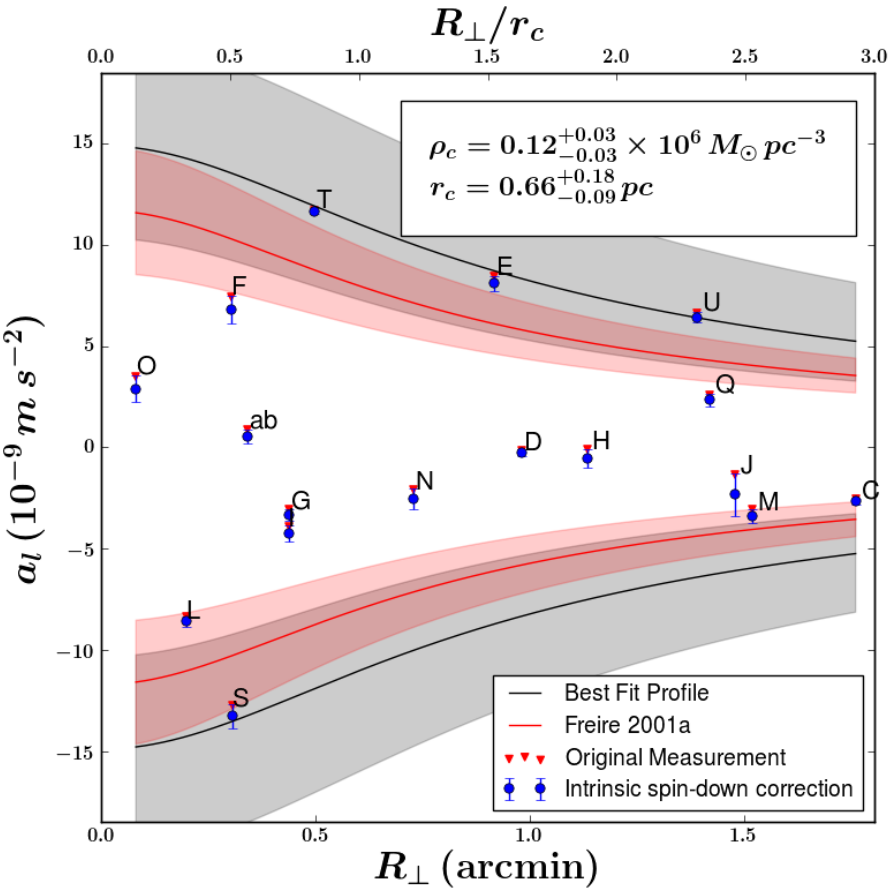

Fig. 2.9.— The best acceleration profile for 47 Tucanae using Equation 2.27. Plotted in red are the measured a_l values and in blue are the values of a_c for the pulsars where we modeled $P_{\rm int}$ using the ATNF catalog. Shaded regions show the 1-σ confidence interval for our fits. Over-plotted in red is the fit used previously by Freire et al. (2001a). When using only the projected positions for each pulsar and no additional information from optical measurements, there is strong covariance between the core density and core radius.

47 Tucanae

Before analyzing the timing data of Terzan 5, we compare how well our model reproduces results found previously using the 25 known pulsars in 47 Tucanae. We use the timing properties derived by Freire et al. (2003) for each pulsar referenced to a CoG located at $\alpha_{J2000} = 00^h24^m05.36^s$ and $\delta_{J2000} = -72°04^m53.2^s$ (Skrutskie et al. 2006).

Heinke et al. (2005) found that for 47 Tucanae $q = 1.63 \pm 0.11$, giving a spectral index of $\alpha = -3.9 \pm 0.33$. For the timing solutions provided by Freire et al. (2003), Equation 2.28 gives the log-likelihood plane defined by our trial values of ρ_c and r_c for this cluster. Figure 2.8 shows the results of our analysis.

Without knowing the true line of sight position for each pulsar, large covariances between ρ_c and r_c can arise. Also, if a system does not have any pulsars at small values of $R_\perp$ with large values of $a_\parallel$ near $a_{\parallel,\max}(R_\perp)$, we cannot limit the allowed parameter space in terms of the central density very strongly.

Our analysis finds a peak likelihood at $\rho_c = (1.2^{+0.3}_{-0.3}) \times 10^5\,\mathrm{M_\odot\,pc^{-3}}$ and $r_c = 0.66^{+0.18}_{-0.08}\,\mathrm{pc}$. Freire et al. (2001a) found in a similar analysis a core radius of $r_c = 0.6 \pm 0.04$ pc. Previous studies by Pryor & Meylan (1993), which was taken to be a fixed value by Freire et al. (2001a), also found $\rho_c = 10^5\ \mathrm{M_\odot\ pc^{-3}}$. Comparing our results to the literature, we find good agreement for both cluster core parameters.

Figure 2.9 shows the best fit acceleration profile along with the measured pulsar accelerations. We have also plotted the best fit acceleration profile used by Freire et al. (2001a) in red. We find good agreement with their results to within the 1-σ confidence interval, which are plotted as the shaded regions.

Terzan 5 Results

We show the results of our search over the likelihood space for the core density and core radius for Terzan 5 in Figure 2.10 with the spectral index found in Section 2.7.1.

The maximum likelihood was found at ρ_c=$1.67^{+0.37}_{-0.29}\times10^6$ $M_\odot$ pc^{-3} and r_c = $0.17^{+0.02}_{-0.02}$ pc, which corresponds to an angular size of 5.94 arcseconds at the cluster distance of 5.9 kpc. Table 2.3 compares our results against previously quoted values from the literature, finding good agreement for each parameter.

The acceleration profile associated with the maximum likelihood is shown in Figure 2.11. We can see that there are only a few pulsars near the maximum acceleration that provide the strongest constraints for this method of analyzing the data. Using a properly de-projected position for each pulsar will allow us to gain more insight into the cluster dynamics.

2.7.3 Line of Sight Positions

We can estimate the line of sight positions of each pulsar relative of the plane O of the cluster by solving Equation 2.3 for the line of sight positions that give our measured accelerations at a given $R_\perp$.

Table 2.4 shows the initial best fits for the line of sight position of each pulsar using the core density, core radius, and spectral index derived in Sections 2.7.1 and 2.7.2. We also include the relative probability of finding a pulsar at one of the two line of sight positions according to the prescription of Appendix D from Anderson (1993):

$$p(l|R_\perp)dl = \frac{n_p dl}{\int_{-\infty}^{\infty} n_p dl}\,, \tag{2.30}$$

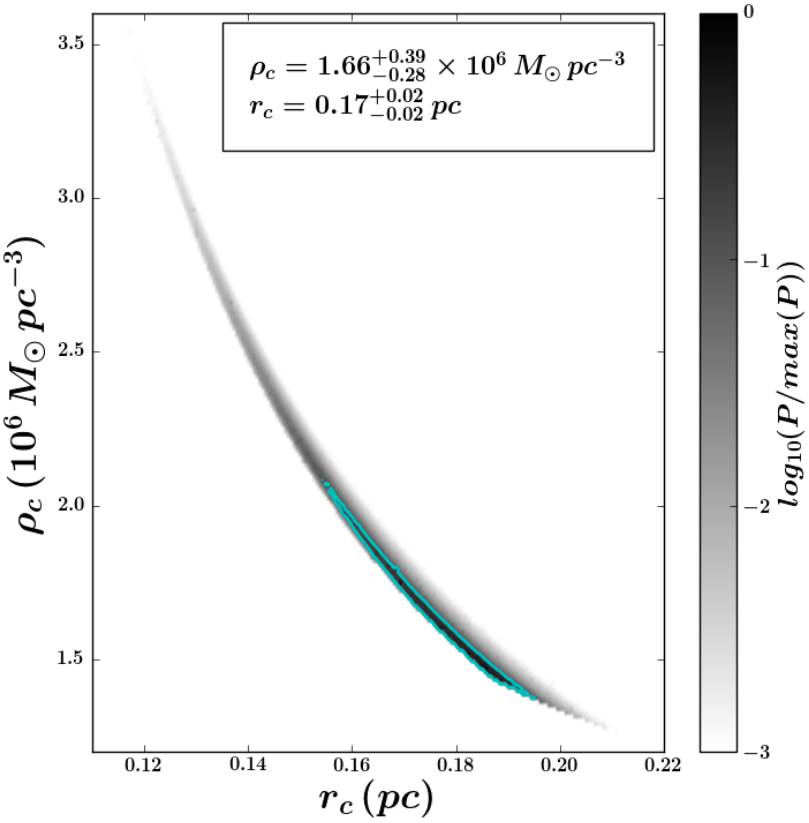

Fig. 2.10.— The log likelihood for all possible combinations of model parameters ρ_c and r_c for Terzan 5. The contour shows the 1-σ confidence region. We take the median of the marginalized parameters as our best fit and the extent out from the median to the 1-σ contour region as the errors. When using only the projected positions for each pulsar and no additional information from optical measurements, there is strong covariance between the core density and core radius.

where n_p is the pulsar number density given by:

$$n_p \propto \left(r_c^2 + R_\perp^2 + l^2\right)^{\alpha/2} . \tag{2.31}$$

This provides us with two solutions for the line of sight position, where each peak has roughly equal probabilities to within a factor of a few. Using our measurements of jerks, we can remove some of this degeneracy as the radial offset from the CoG factors heavily into the expected jerk felt by each pulsar. We discuss the resulting likelihood for the position of each pulsar in Sections 2.8.2 and 2.8.2 and introduce how we overcome the difficulty of modeling bimodal solutions in Section 2.8.5.

2.8 MCMC Analysis

In order to better derive the cluster parameters for Terzan 5 we used the sampling package `emcee` (Foreman-Mackey et al. 2013) to de-project our pulsar positions and obtain a fully 3-dimensional model for the cluster's density profile. We then directly solve for the acceleration produced by the mass interior to each pulsar. De-projecting each pulsar individually and comparing its measured acceleration to the model acceleration allows us to reduce the amount of covariance in our cluster parameters. To begin, we discuss the individual likelihood functions used and their priors before introducing the actual simulations and their results.

2.8.1 Likelihoods

From our pulsar timing data, we consider only the spin period, the spin period derivative, the second-order spin period derivative, the orbital period, and the orbital period derivative when defining the likelihood. The total probability of measuring a given

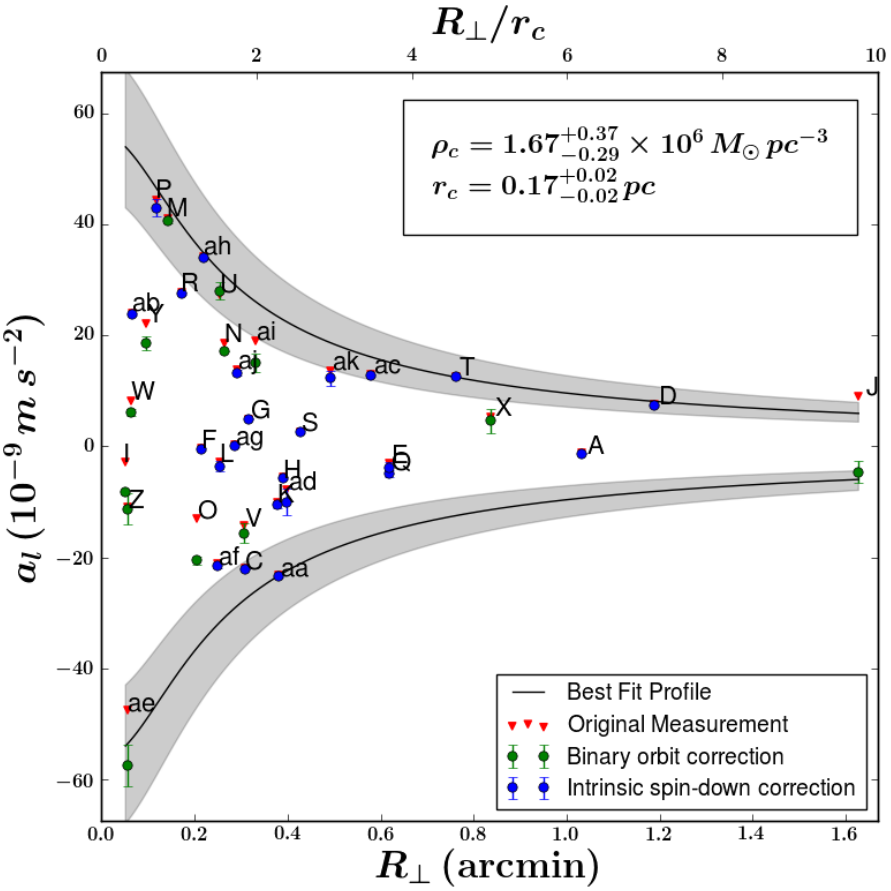

Fig. 2.11.— The best acceleration profile for Terzan 5 using Equation 2.27. Plotted in red are the measured a_l values, in green are the values of a_c for pulsars with a measured $\dot{P}_b$, and in blue are the values of a_c for the remaining pulsars where we modeled $P_{\rm int}$ using the ATNF catalog.

on-sky position, acceleration, and a jerk of a pulsar (if measured) is given by

$$p(R_\perp, a|\rho_c, r_c, \alpha) = p(l|R_\perp, r_c, \alpha) \times p(R_\perp|r_c, \alpha) p(a_r|\rho_c, r_c, \alpha]) \times p(\dot{a}_r|\rho_c, r_c, \alpha])\,, \quad (2.32)$$

where the first two terms are the probability associated with the position of the pulsar in the potential, and the final two terms give the probability of measuring a given acceleration or jerk respectively.

We defined the log-likelihood ($\mathcal{L}$) as follows:

$$\mathcal{L} = \mathcal{L}_{\rm pos} + \mathcal{L}_{\rm accel} + \mathcal{L}_{\rm jerk}\,, \quad (2.33)$$

where $\mathcal{L}$ is the total log-likelihood, $\mathcal{L}_{\rm pos}$ is the likelihood associated with the first two terms of Equation 2.32, $\mathcal{L}_{\rm accel}$ is the log likelihood from our acceleration measurements, and $\mathcal{L}_{\rm jerk}$ is the log likelihood from our jerk measurements.

2.8.2 Positional Likelihood

In order to calculate the likelihood of finding a pulsar at its observed on-sky location $R_\perp$ and at a given line of sight position l, we decomposed the likelihood for position into two components:

$$\mathcal{L}_{\rm pos} = \mathcal{L}_l + \mathcal{L}_{\rm R_\perp}\,, \quad (2.34)$$

where $\mathcal{L}_l$ is the likelihood for the line of sight position given by Equation 2.30.

$\mathcal{L}_{\rm R_\perp}$ is the likelihood for the on-sky position of each pulsar and is given by:

$$p(R_\perp|r_c, \alpha) dR_\perp = \frac{n_p dR_\perp}{\int_{-\infty}^{\infty} n_p dR_\perp}\,, \quad (2.35)$$

where n_p is the number density of pulsars and is readily defined by the on-sky form

of the King model (King 1962) proportional to

$$n_p \propto \left(1 + \left(\frac{R_\perp}{r_c}\right)^2\right)^{\alpha/2} . \tag{2.36}$$

If fitting for the offset in the CoG of the cluster, we measure a new spherical angular difference for each pulsar from the CoG to obtain a new value of $R_\perp$ before applying this likelihood function. In Section 2.8.3 we discuss the priors used on the allowed parameter space for the offset in the CoG position.

Converting Equation 2.30 into a likelihood, we find

$$\mathcal{L}_l \propto \sum_i \ln\left[(r_c^2 + R_{\perp,i}^2 + l_i^2)^{\alpha/2}\right] , \tag{2.37}$$

for the line of sight probability, where i is the summation over each pulsar in the system.

For the on-sky positional probability, the likelihood is given by taking the log of Equation 2.35:

$$\mathcal{L}_{R_\perp} \propto \sum_i \ln\left[\left(1 + \left(\frac{R_{\perp,i}}{r_c}\right)^2\right)^{\alpha/2}\right] . \tag{2.38}$$

Acceleration Likelihood

Using the results of Section 2.5.1 we identified that only the mean-field component of the acceleration is important for our analysis. As such, we further decomposed the acceleration likelihood into two components:

$$\mathcal{L}_{\text{accel}} = \mathcal{L}_{\text{binary}} + \mathcal{L}_{\text{spindown}} , \tag{2.39}$$

where $\mathcal{L}_{\text{binary}}$ is the log likelihood from the binary pulsars with measured values of $\dot{P}_b$ and $\mathcal{L}_{\text{spindown}}$ is the log likelihood from the remaining pulsars.

For the pulsars with a measured $\dot{P}_b$, we use Equations 2.3 and 2.20 to find the model and measured accelerations, respectively. The position r in Equation 2.3 is found by applying the Pythagorean theorem to $R_\perp$ and the line of sight estimate l from MCMC sampling.

Using a normal distribution about the predicted acceleration ($\hat{a}(r|\theta)$) for a given set of cluster parameters θ we derive the likelihood for the binary pulsars:

$$\mathcal{L}_{\text{binary}} \propto \sum_i \frac{1}{2e_{\text{i}}^2} \left(a_{\text{l,i}} - \hat{a}(r|\theta)\right)^2 , \tag{2.40}$$

where i is the summation over each binary pulsar with a measured $\dot{P}_b$ in the cluster, e is the error in each measured acceleration, and θ are the current cluster parameters to be tested.

For the remaining pulsars, Equations 2.3 and 2.11 are used to find the model and measured accelerations, again measuring the radial offset r from the CoG using the measured $R_\perp$ and sampling over l for each pulsar.

While the terms due to the Galactic acceleration and Shklovskii effect can be removed from the measured acceleration, the intrinsic spin-down due to magnetic braking is not necessarily known. Subtracting the model acceleration from the measured accelerations must then leave a residual component due to this effect, which is the dominant source of error in our measurements of the cluster acceleration.

This intrinsic spin-down component can be modeled using the magnetic field strength given by Equation 2.12, which follows a log-normal distribution that we can use to calculate a likelihood estimate according to the ATNF parameters shown in Figure 2.6.

For a location parameter of the distribution centered at $\mu = 1.25{\times}10^8$ G and a scale parameter of $\sigma = 0.53{\times}10^8$ G, this yields a log likelihood of the form:

$$\mathcal{L}_{\text{isolated}} \propto \sum_i \left[\frac{1}{2(0.53)^2} \left(\log B_8 - 1.25 \right)^2 + \log B_8 \right] , \tag{2.41}$$

where B_8 is defined to be $B/(10^8\,\text{Gauss})$.

Jerk Likelihood

In Section 2.5.2 we showed that by removing the mean-field component of the jerk from the total jerk felt by a pulsar, the residuals follow a Lorentzian given by Equation 2.10. The log likelihood for the jerk is then defined to be:

$$\mathcal{L}_{\text{jerk}} = \sum_i \log \left(\frac{\dot{a}_0}{\pi} \frac{1}{\left[\left(\dot{a}_{l,i} - \dot{a}_{\text{mf},i} \right)^2 + \dot{a}_0^2 \right]} \right) . \tag{2.42}$$

Using this likelihood we may have additional fitting power for each pulsar's line of sight position and therefore the cluster parameters. Using only accelerations, two different positions along our line of sight can produce the same value, whereas using a measured jerk allows for additional information about the pulsar's position, potentially breaking this degeneracy.

Central Black Hole Models

Following the prescription of Section 2.4.5, we introduced an additional fitting parameter for a point-like central mass in the system, allowing the density profile to vary accordingly. The likelihood for this was calculated using Equation 2.39. The model acceleration for both $\mathcal{L}_{\text{binary}}$ and $\mathcal{L}_{\text{spindown}}$ were calculated using Equation 2.9.

2.8.3 Priors

Flat priors were used for the range of cluster parameters, magnetic field strengths, pulsar positions, pulsar velocities, and black hole mass estimates. For all but the black hole mass estimates these priors were flat in linear spacing, whereas fits for the central black hole mass were performed with log-uniform flat spacing. The log-uniform prior was used to properly sample over the many orders of magnitude possible for a central black hole mass.

For the three main cluster parameters, the flat priors ranged from $10^4 \leq \rho_c \leq 10^7$ $M_\odot$ pc^{-3}, $0 \leq r_c \leq 2$ pc, and $2 \leq \alpha \leq 8$. The range in our spectral index was chosen to slightly expand upon the results of Phinney (1993), which found pulsars should have values of $2 < \alpha < 6$.

In the case that the cluster's CoG was fit for, a normal prior centered on a zero offset was used for the allowed variations in right ascension and declination.

2.8.4 MCMC Parameters

Our simulations were initialized using 256 walkers. When fitting for the cluster parameters of Terzan 5 using only the acceleration measurements, we fit for 37 parameters, which include the core density, core radius, spectral index, and pulsar line of sight positions.

For acceleration plus jerk fittings, we used the same parameters as the acceleration-only fits, while including a line of sight velocity estimate for each pulsar with a measured $\dot{a}_l$. This gives a total number of 69 parameters to fit for Terzan 5.

If performing a fit for the CoG, we used the same parameters as the acceleration-only fit, with two additional parameters that identify the offset in right ascension and declination. This gives a fit with 39 parameters for Terzan 5.

We also performed a simulation which looked for the presence of a central black hole in the system using the measured accelerations and jerks. This fit used all the previously described parameters, while including one additional parameter for the black hole mass, giving a total of 70 parameters for Terzan 5.

The initial parameter estimates were found using the results of Section 2.7 in order to reduce the required time for burn in. For the line of sight position of each pulsar, we assigned a line of sight position normally distributed around one of the two possible line of sight positions for each pulsar shown in Table 2.4. The number of walkers centered about a given line of sight position was selected according to the relative probability between l_1 and l_2.

2.8.5 Parallel Tempering

We addressed the issue of multi-modality in the line of sight position by adding parallel tempering to our simulations. When modeling parameters with strong multi-modality, the popular method of a single MCMC chain stochastically exploring the parameter space is an ill-suited approach as a single chain is unable to explore separate peaks in the log-likelihood parameter space.

If two solutions are separated by many standard deviations, a chain may end up stuck in a local over-density of probability. Using a parallel tempered sampler however, we can allow chains to more fully explore the parameter space (Marinari & Parisi 1992). Using the package `PTSampler` provided by Foreman-Mackey et al. (2013), we include an additional dimension to our simulation, which varies according to a temperature T. By applying an exponential factor to the likelihood function $\mathcal{L}^{1/T}$, the likelihood function becomes shallower and broader for higher temperatures.

The higher-temperature chains are then allowed to fully explore the parameter

space, and by exchanging positions with colder chains, the chain with the true likelihood function (T=1) is eventually able to fully explore the parameter space.

For our models, we have elected to use 16 different temperatures in order to fully explore the parameter space.

2.9 MCMC Results for 47 Tucanae

In order to verify that our MCMC method can produce valid results for the Terzan 5 system, we first performed the analysis on the measured accelerations within 47 Tucanae. The results of our simulation are shown in a corner plot (Foreman-Mackey et al. 2014) in Figure 2.12. We find ρ_c=$(1.19^{+0.61}_{-0.36})\times10^5$ $M_\odot$, r_c=$0.50^{+0.14}_{-0.10}$ pc, and α=$-5.73^{+1.57}_{-1.91}$. These results agree to within the 1-σ confidence intervals of those found by Freire et al. (2001a) (Shown in blue in Figure 2.12), as well as with our initial estimates using the projected positions of each pulsar in Section 2.7.2, for ρ_c and r_c.

In the case of α, we find our results to be largely unconstrained. Our flat prior from $2 < \alpha < 8$ is only constrained at the lowest values of α. We argue that the reason for this is likely due to the lack of pulsars with large values of a_l at small radii. Without more pulsars, we are unable to constrain the fits for the spectral index strongly, which requires a large number of pulsars at different locations in the cluster to determine with much accuracy. With the recent discovery of two new pulsars in this cluster however, it is promising that future studies will help to constrain these parameters further (Pan et al. 2016). In Terzan 5 however, the large number of pulsars should provide a stronger contraint on α due to the combined positional probabilities.

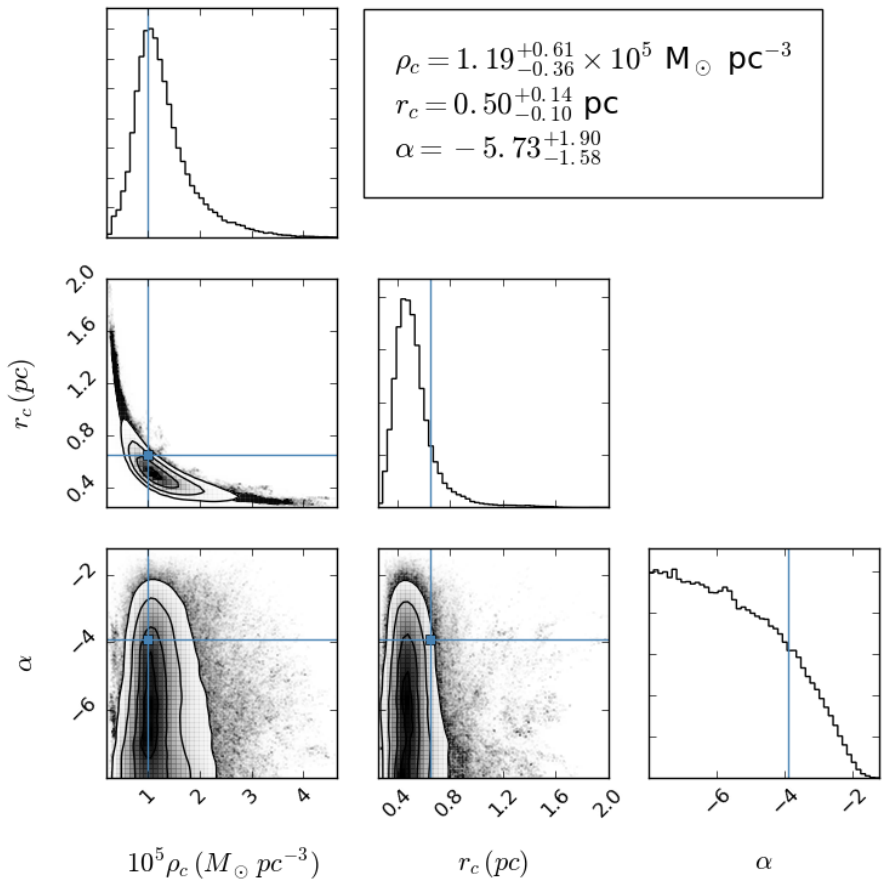

Fig. 2.12.— Corner plot showing the marginalized probabilities of finding a given cluster parameter for the cluster 47 Tucanae, along with the covariances between different parameters. These results use only the pulsar accelerations. Blue lines show previously derived estimates of each parameter from Freire et al. (2001a).

2.10 MCMC Results for Terzan 5

In this section we present the results of our MCMC analysis using only the measured accelerations to begin with, followed by the simultaneous analysis of the pulsar accelerations and jerks (if measured). We then compare these results to one another, as well as with the results from traditional pulsar timing techniques. Lastly, we discuss the results from our fits to a central black hole in Terzan 5 and discuss the implications of having such a black hole in the system.

All of our results are summarized in Table 2.3.

2.10.1 Acceleration Only

The cluster parameters found using the measured accelerations and the likelihood functions of Section 2.8.2 are shown in Table 2.3. We also compared our results to previously cited values in the literature as well as the values found using only the projected position of each pulsar and its acceleration. We also include a corner plot (Foreman-Mackey et al. 2014) in Figure 2.13 to show the marginalized PDFs of the three main cluster parameters as well as their covariances. The 1-σ confidence intervals were integrated out from the median of the marginalized distribution for each position.

Table 2.5 shows the line of sight position of each pulsar, sorted by the pulsar's measured value of $R_\perp$, after each walker completed its analysis of the parameter space. We also include the relative number of walkers in the l_1 and l_2 peaks as the ratio of probabilities in these two solutions (P_{ratio}).

Our MCMC analysis finds ρ_c=$(1.44^{+0.22}_{-0.21})\times10^6$ $M_\odot$ pc^{-3}, which is slightly lower, but in agreement with, our initial estimates of ρ_c=$(1.67^{+0.37}_{-0.29})\times10^6$ M$\odot$ pc^{-3}. These results are also consistent within the 1-σ confidence interval given by Lanzoni et al.

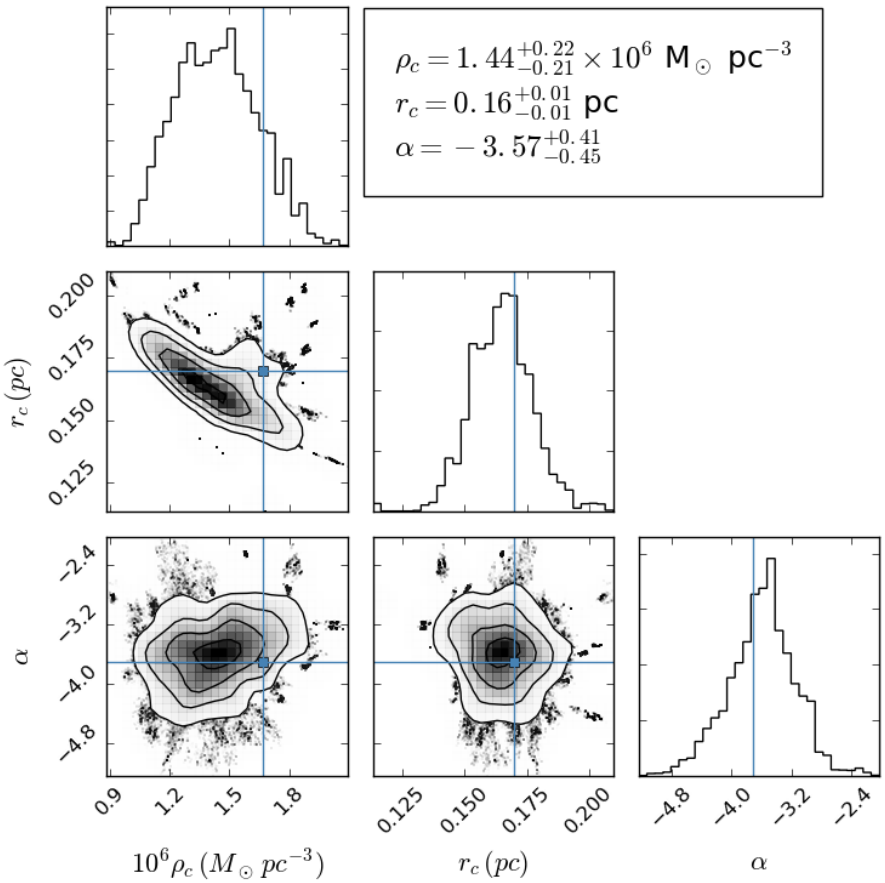

Fig. 2.13.— Corner plot showing the marginalized probabilities of finding a given cluster parameter for the cluster Terzan 5, along with the covariances between different parameters. These results use only the pulsar accelerations. Blue lines show previously derived estimates of each parameter from Section 2.7.2 using the projected position of each pulsar.

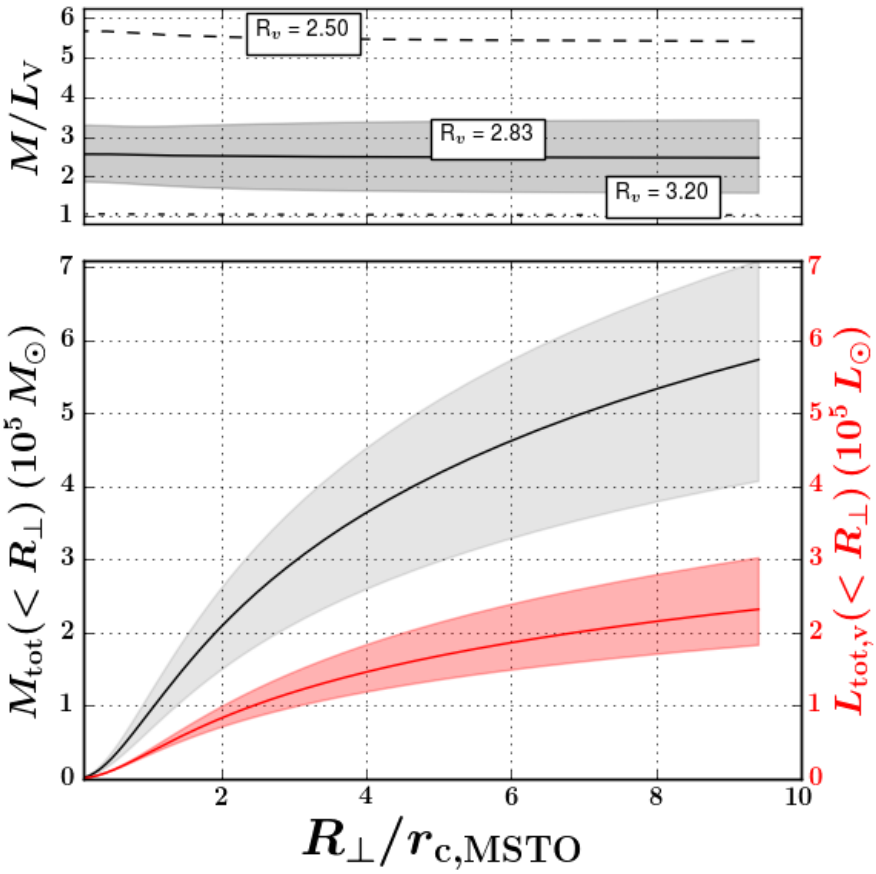

Fig. 2.14.— Mass and V-band luminosity profile as a function of $R_\perp$ using only the acceleration measurements shown in black on the left hand axis and in red on the right hand axis, respectively. Each profile has been expressed in terms of the dominant mass class within the cluster. We find a mass to light ratio of M/L$\simeq$2.8 in the core of the cluster. The top panel shows the systematic offsets in our median mass to light ratio using R$_v$ and not the extinction A$_v$ due to the strong dependence on the color excess E(B-V) depending on the line of sight through the cluster.

(2010). We find that our errors using the MCMC sampler are signficantly improved over these previous methods of study.

Our measurement of α=$-3.57^{+0.45}_{-0.41}$ is consistent with the one found using traditional projected techniques of α=-3.71 ± 0.57 though with an improved error estimate. Our spectral index from MCMC fitting gives a mass ratio of q=$1.52^{+0.15}_{-0.14}$ which agrees with Heinke et al. (2006). For a MSTO mass of 0.9 $M_\odot$, this gives a median pulsar system mass of 1.3 $M_\odot$.

Our core radius of r_c=$0.16^{+0.01}_{-0.01}$ pc using the MCMC analysis and acceleration only measurements is also consistent with the initial estimate r_c=$0.17^{+0.02}_{-0.02}$ pc. We compare our results to those of Lanzoni et al. (2010) and Miocchi et al. (2013) where the core radius of MSTO stars were measured using Equation 2.25 and the measured mass ratio. For a mass ratio of $1.52^{+0.15}_{-0.14}$, we find a MSTO star core radius of $r_{c,*}$=0.23 ± 0.02 pc. This agrees to within the error-bars of Miocchi et al. (2013), who found a core radius of 0.22 ± 0.01 pc.

In order to calculate the total mass of the cluster as a function of $R_\perp$, we expressed our results in terms of the classical single-mass King model. As we have solved for a mass class other than the dominant one, we scale our core radius to the expected dominant core radius according to Equation 2.25. We also use the expected spectral index of the dominant mass class of $\alpha = -2$. We then integrate up all the mass along within a given on-sky position $R_\perp$.

Figure 2.14 shows the mass within the cluster as a function of $R_\perp$. We find that the integrated mass along our line of sight within a cylindrical radius of 1 parsec to be M($R_\perp$ <1pc)$\sim3.5\times10^5$ $M_\odot$.

We have also calculated the observed V-band luminosity of Terzan 5 at matching radii using the measured surface brightness in the V-band from Lanzoni et al. (2010).

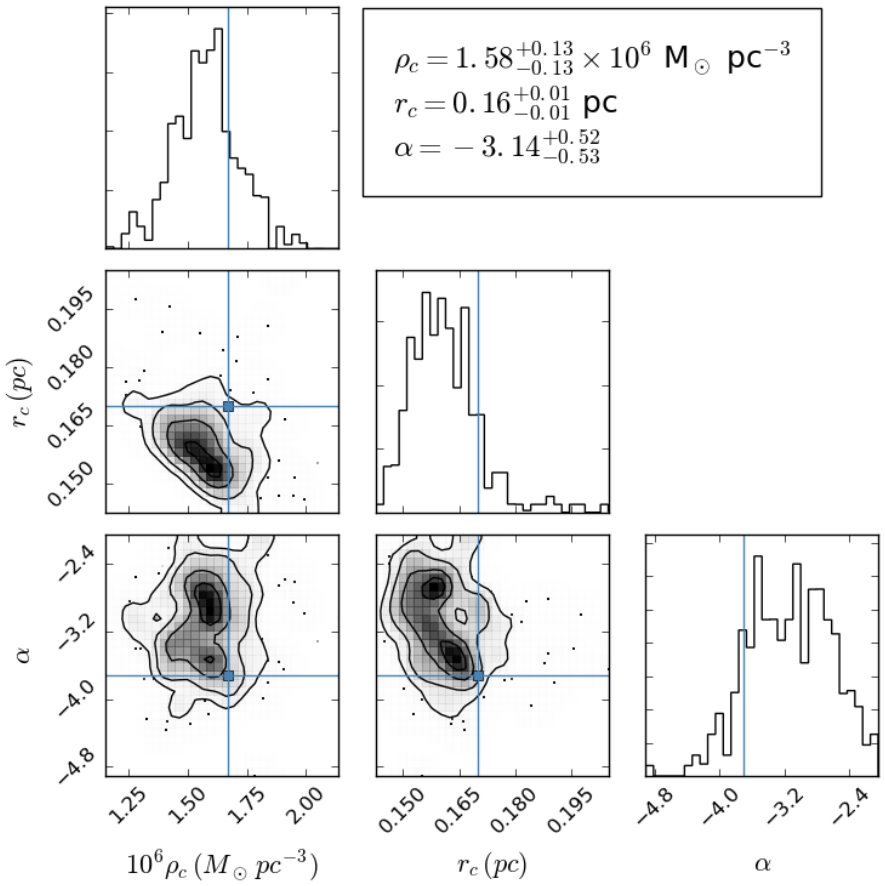

Fig. 2.15.— Corner plot showing the marginalized probabilities of finding a given cluster parameter for Terzan 5, along with the covariances between different parameters. These results use the pulsar accelerations as well as their jerks (when available). Blue lines show previously derived estimates of each parameter from Section 2.7.2 using the projected position of each pulsar.

We use the results of Massari et al. (2012) to find the color excess E(B-V) as a function of the radial distance from the CoG for an assumed extinction coefficient R_v=2.83 to convert the measured surface brightness into a luminosity measurement. Errors were found by taking the minimum and maximum value of E(B-V) in a radial bin out from the CoG.

We find a central mass to light ratio of $M/L_v \simeq 2.6^{+0.7}_{-0.7}$. It should be noted however that the exact value of R_v can drastically change our results for the mass to light ratio as shown in the top plot of Figure 2.14. Without a more constraining measurement for the extinction towards this region of the galaxy, our results are dominated by the errors in the photometry. We compare our results to those of Strader et al. (2009), who find a $M/L_v \simeq 1.75 \pm 0.1$ for metal-rich clusters. Given the additional errors in R_v, we consider this to be an acceptable agreement for the metal rich Terzan 5.

The line of sight positions for each pulsar are also shown in Table 2.5. We find that most of the pulsars lie close to the plane of the sky O as defined by the relative probability between the l_1 and l_2 positions. By including the jerks, we will investigate whether we can even better constrain the position of each pulsar along our line of sight.

2.10.2 Accelerations and Jerks

Starting with the same initial conditions as the acceleration only measurements (Table 2.4), a second simulation was run including jerk measurements according to the prescription of Section 2.8.2. Of the 36 pulsars, 32 have measured jerks. Pulsars without measured jerks were analyzed using only their accelerations and provided no weight to the likelihood for jerk measurements. Our results for this simulation are shown in Figure 2.15 and Tables 2.3 and 2.5.

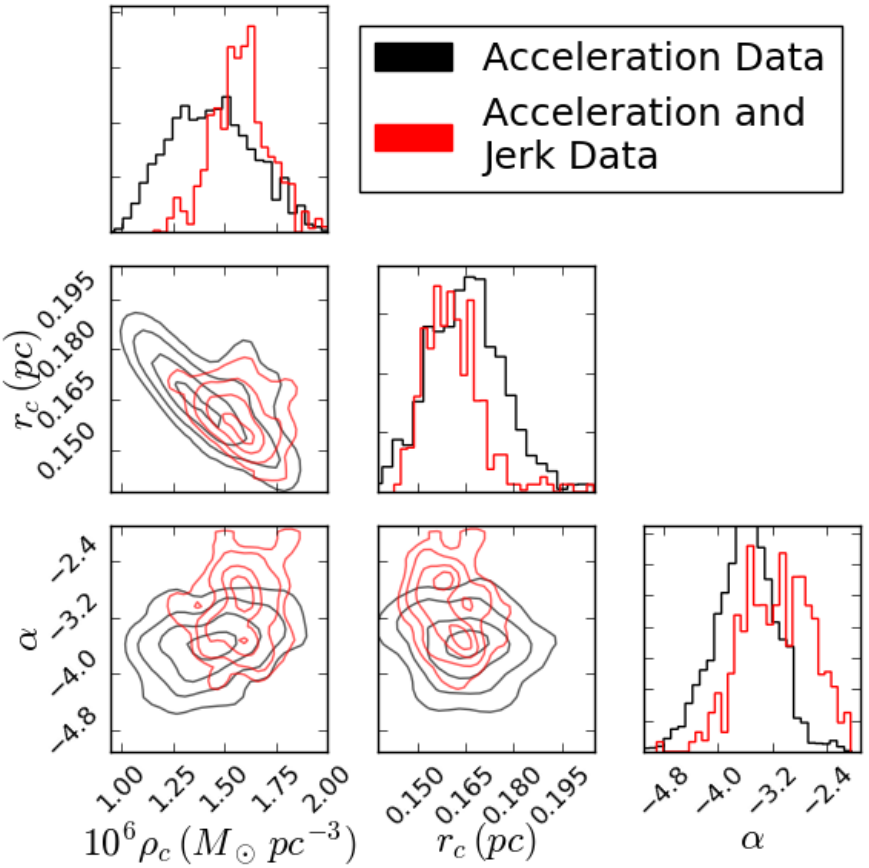

Fig. 2.16.— Posterior distributions of the core density, core radius, and the spectral index for simulations using only accelerations in black and accelerations plus jerks in red. We do not show individual data points for the acceleration plus jerk fits for clarity.

Using the jerks in addition to the accelerations, we found ρ_c=$(1.58^{+0.13}_{-0.13})\times10^6$ M$\odot$ pc^{-3}, r_c=$0.16^{+0.01}_{-0.01}$ pc, and α=$-3.14^{+0.52}_{-0.53}$. All of these values are in good agreement with those found using only the measured pulsar accelerations and are compared to the literature in Table 2.3 . Figure 2.16 shows an overlay of the two simulations, where we see slightly more constraining fits when analyzed using pulsar jerks.

We also find a bimodality arising in our fits of the specral index α when jerk fitting is turned on. This is likely due to the fact that the pulsar jerks provide additional line of sight information and may imply that some of our pulsars must lie at greater distances from the core in order to have a given value of jerk that goes beyond the line of sight probability given by Equation 2.30.

This implies that future studies of the GC potential will benefit from long-term timing of pulsars, as the jerks provide additional information about the overall dynamics of the system. Given the relationship between the dominant mass class and the neutron star massed objects, additional timing of pulsars and the MSTO stars in GCs may provide additional constraints on the neutron star mass distribution.

Figure 2.17 shows the measured cluster mass and V-band luminosity using the cluster parameters obtained from the measurements of acceleration and jerk. We find that the integrated mass along our line of sight within a cylindrical radius of 1 parsec to be M($R_\perp$ <1pc)$\sim$3.0$\times10^5$ M$_\odot$. We also find a similar central mass to light ratio in the core of M/L$_v$ $\simeq2.0^{+0.8}_{-0.7}$ when compared to the acceleration only measurements. Again, we note that the errors in the exact reddening towards Terzan 5 produce significant systematic offsets in these results and appears to be roughly consistent with previous literature.

The predicted root mean square velocity of a star in the core of a King model

cluster is given by:

$$v_c = \left(\frac{4\pi}{3} G\rho_c\right)^{1/2} r_c \,. \tag{2.43}$$

Figure 2.18 shows the distribution of all pulsar velocities over all chains for a model with flat priors in our velocity fitting. We find our models predict a roughly Gaussian distribution of line of sight velocities about the predicted value, confirming our jerk measurements are drawn from a cluster potential that obeys the King model.

We find a distribution of velocities for our pulsars centered about v_c=$\pm 26.3^{+3.6}_{-2.7}$ km/s, as shown in Figure 2.18. The measured one-dimensional velocity dispersion was measured to be σ=$\pm 15.2^{+2.1}_{-1.5}$ km/s.

Origlia et al. (2013) gives an estimate of the velocity dispersion for the most metal poor population in Terzan 5 of $\sigma \sim 15$ km/s. We verify our results by finding the velocity predicted by the Origlia et al. (2013) results if their population of stars are in equipartition with the pulsars and have q=$1.52^{+0.15}_{-0.14}$. We find that the results of Origlia et al. (2013) predict a pulsar line of sight velocity of ∼12 km/s, which is similar to our results. A more detailed study of the velocity dispersion of both the pulsars and the main sequence turn-off stars is required to further confirm this result.

From Gnedin et al. (2002) we find that the predicted escape velocity for Terzan 5 from the core of the cluster is 50.5 km/s. Figure 2.18 shows the escape velocity in red, a few standard deviations from the median of the observed distribution.

2.10.3 Center of gravity fits

The results of our fits for the cluster parameters ρ_c, r_c, and α including an offset in the CoG of the cluster using both pulsar accelerations and jerks are shown in Figure 2.19. Our analysis finds results consistent with the optical CoG published by Massari et al. (2012), with a posterior distribution centered on ΔRA=$0.05^{+0.17}_{-0.12}$ arcseconds

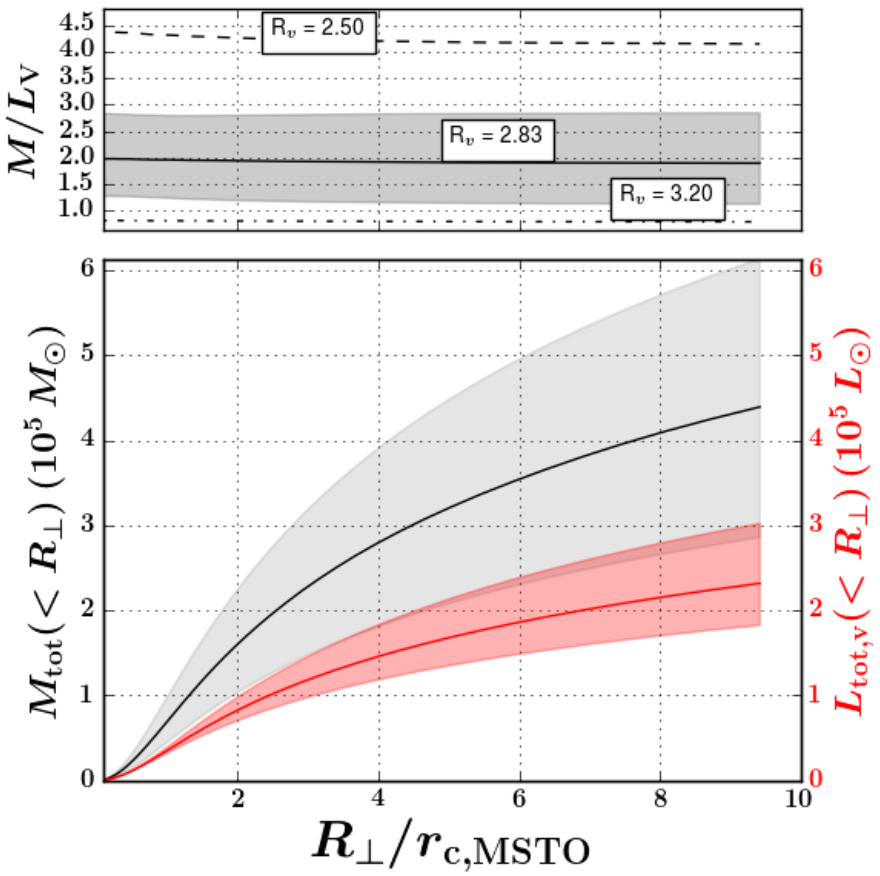

Fig. 2.17.— Mass and V-band luminosity profile as a function of $R_\perp$ using the acceleration and jerk measurements shown in black on the left hand axis and in red on the right hand axis, respectively. Each profile has been expressed in terms of the dominant mass class within the cluster. We find a mass to light ratio of M/L$\simeq$2.6 in the core of the cluster. The top panel shows the systematic offsets in our median mass to light ratio using R_v and not the extinction A_v due to the strong dependence on the color excess E(B-V) depending on the line of sight through the cluster.

and ΔDec=-0.03$^{+0.14}_{-0.14}$ arcseconds.

2.10.4 Central black hole results

The results of our black hole fits are shown in Figure 2.20. We find that 99% of all the chains in our simulation favor a black hole mass below $M_{\rm BH} \simeq 3 \times 10^4\,{\rm M}_\odot$. At the intermediate values of a few hundred solar masses however, we find a marginal detection for a black hole of mass $M_{\rm BH} \simeq 500\,{\rm M}_\odot$. We stress that additional analysis is required to confirm the existence of a black hole of this mass, however. More constraining fits could be accomplished by either finding new pulsars near to the core of the cluster or by implementing a more robust black hole model that allows the black hole to be offset from the CoG and accounting for the jerks produced by the black hole.

An upper limit on black hole mass of $M_{\rm BH} \simeq 3 \times 10^4\,{\rm M}_\odot$ is still within the bounds of current theory for hierarchical black hole formation in a natal globular cluster. Simulations by Baumgardt et al. (2004b) have found that at the end of growth of the black hole for these systems, the expected black hole masses according to their simulations should be between a few hundred and a thousand M$_\odot$. We also compare our results with those of van der Marel & Anderson (2010), which find an upper limit on a central black hole mass of 10^4 M$_\odot$ for ω Centauri.

2.11 Discussion

2.11.1 Terzan 5 Taxonomy

The primary goal of this work has been to derive a more accurate set of cluster parameters for Terzan 5 using an MCMC sampler to assign a proper location and

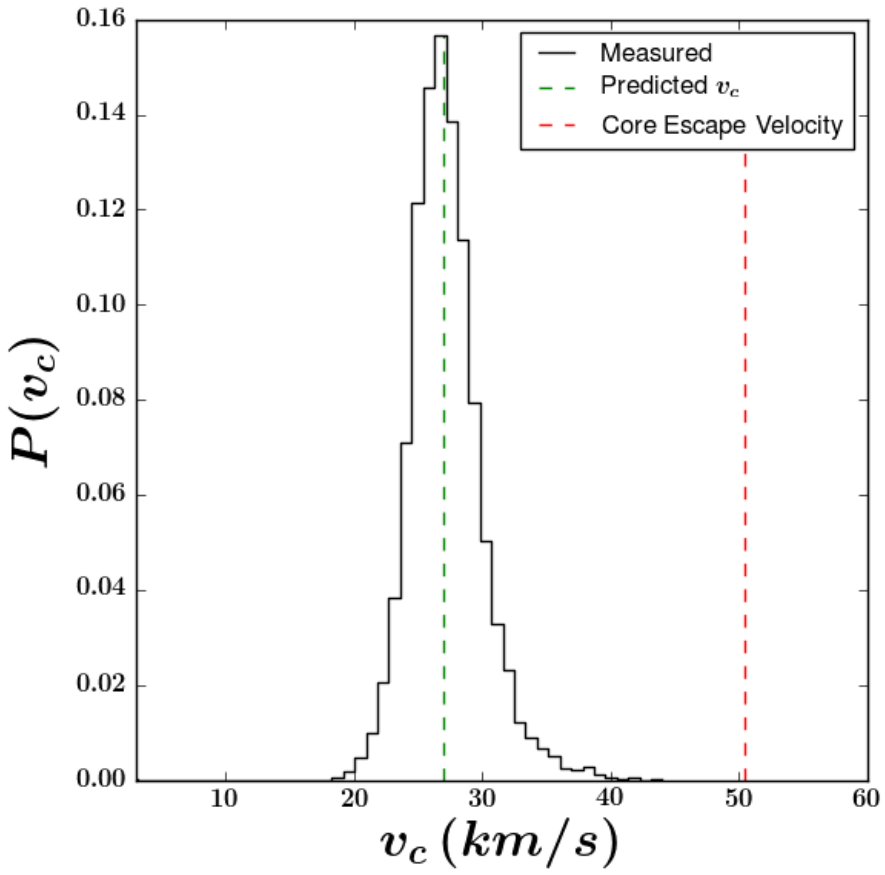

Fig. 2.18.— Distribution of measured velocities for all pulsars and across all chains. We plot the expected root mean square core velocity for the pulsars given by Equation 2.43 in green. We find that the pulsars follow an approximately Gaussian distribution about these predicted values. The escape velocity needed to escape from the core of the cluster is plotted in red (Gnedin et al. 2002).

spin-down rate to each pulsar in the system. This was accomplished by assuming the cluster obeys the King model (King 1962) and by varying the exact spectral index of the pulsar density distribution to be relative to the dominant mass class in the core of the cluster. Studying Terzan 5 in this manner is both reddening independent as well as a direct probe of the gravitating mass of the cluster, and does not make any assumptions about the mass to light ratio of the system.

As our models are only valid within the core, we cannot derive a total mass out to the tidal radius of Terzan 5. As the system is highly concentrated however, we expect that our integrated mass out to a few core radii is indicative of a lower total system mass than found by Lanzoni et al. (2010). For our measured core density and inferred core radius of the dominant mass class, we find a lower collision rate for Terzan 5 as compared to Lanzoni et al. (2010). Our results still a factor of a few larger than those measured for other massive globular clusters however, which maintains Terzan 5 as having the largest measured collision rate of any globular cluster studied to date.

We find that the total mass and the mass to light ratios place strong constraints on the possible taxonomy of Terzan 5. Ferraro et al. (2009) suggested that Terzan 5 might be the nuclear remnant of a dwarf galaxy. Without detailed knowledge of the original galactocentric distance, we use the results of Johnston et al. (1999) to estimate that the current mass of a dwarf galaxy over the past 10 Gyrs to be <1% of its original value. If Terzan 5 was a dwarf galaxy at its inception, then its current mass is on the lower end of the commonly accepted mass range for dwarf galaxies of 10^7-10^9 $M_\odot$ (Stierwalt et al. 2015). In addition to this, the mass to light ratio of Milky Way ultra-faint satellites are believed to be a factor of a few hundred (Simon & Geha 2007). Even accounting for tidal stripping as the progenitor galaxy enters the Milky-Way potential, the required change in the mass to light ratio is likely far

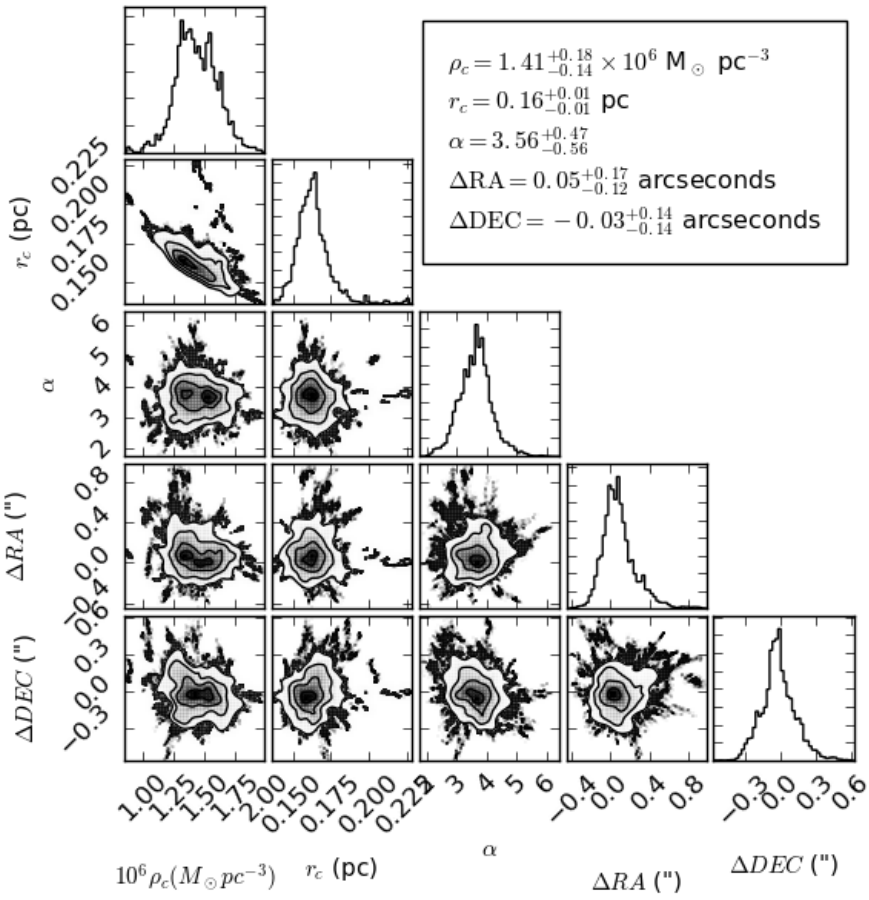

Fig. 2.19.— Corner plot showing the marginalized probabilities of finding a given cluster parameter for the cluster Terzan 5 with an allowed offset from the optical CoG as found by Massari et al. (2012) including the covariances between different parameters. These results use only the pulsar accelerations.

too large for Terzan 5 to have been a dwarf galaxy at its formation.

Ferraro et al. (2009) also predicted that Terzan 5 may be a possible fragment of the Milky Way's bulge. For Milky Way like spiral galaxies Yoshino & Ichikawa (2008) measured average mass to light ratios much smaller than those of dwarf galaxies. While we have a large systematic uncertainty in our measured mass to light ratio for Terzan 5, our results agree much better with this formation mechanism as the maximum mass to light ratio will always be much less than that of a disrupted dwarf galaxy.

2.11.2 Further improvements

We argue that further improvement to our method can be made by moving away from a simple King model (King 1962) to a model that accounts for the underlying IMF of the system and better accounts for the entire range of masses in the cluster. At this time our work only approximates a multi-mass system by referencing the pulsars to the dominant mass class in the core. Using a distribution function which accounts for the mass of each star in the globular cluster as well as its position and velocity, each step of our model would be able to more accurately determine the effect neighboring stars have on the pulsars.

It should also be noted that with first light from the next generation of radio telescopes such as MeerKAT (Booth et al. 2009), the number of timed pulsars in GCs, particular those in the southern hemisphere, will increase and allow us to probe the potential of more globular clusters using pulsar timing.

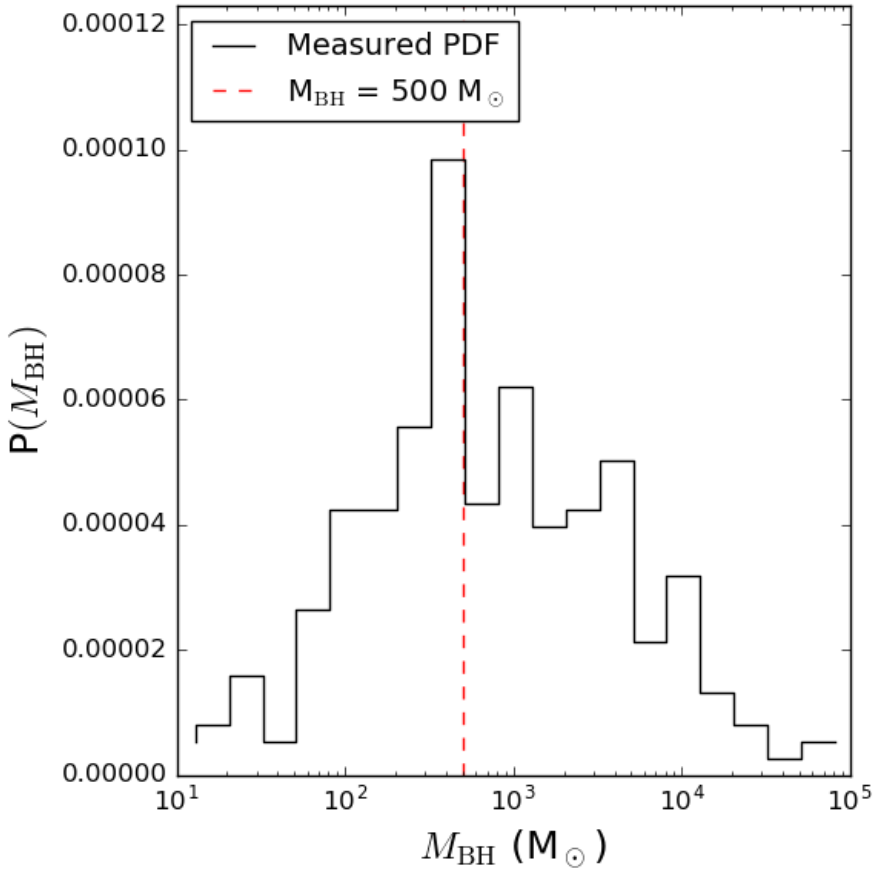

Fig. 2.20.— Observed posterior distribution for the central black hole mass in Terzan 5. We find a marginal detection of a black hole mass of $M_{\rm BH} \simeq 500\,{\rm M}_\odot$ using the measured accelerations and jerks. We also find that black hole masses greater than $M_{\rm BH} \simeq 3 \times 10^4\,{\rm M}_\odot$ are ruled out by our simulations.

2.11.3 Method Comparison

By assigning line of sight positions and spin-down rates for each pulsar at each possible set of cluster parameters, our work gains an important distinction from previous GC studies using pulsars. Models produced using only the on-sky positions and Equation 2.27 suffer from a strong covariance in the core density and core radius. Using the joint probability of the line of sight position for each pulsar and its expected acceleration, we can produce models that are far less covariant than previous works, as evidenced by comparing Figures 2.10 and 2.13.

2.11.4 Mass Ratios

As a result of determining the density profile for Terzan 5, we also infer the underlying system mass for the 36 pulsars in our study. We have found a mass ratio of pulsars to the dominant mass class of q=$1.52^{+0.15}_{-0.14}$. As we expect pulsars to follow the same mass distribution as LMXBs (inset plot of Figure 2.7), we compare this to the results of Heinke et al. (2006) ($q = 1.43 \pm 0.11$), finding good agreement between the two results. For a turn-off mass of 0.9 $M_\odot$ (Bergbusch & VandenBerg 2001) this predicts a system mass for the neutron star population in this study of only 1.3 $M_\odot$.

Comparing this to the work done by Kiziltan et al. (2013), Ozel & Freire (2016), and Antoniadis et al. (2016), we should expect the neutron star mass distribution to be broadly centered on $1.55^{+0.26}_{-0.20}$ $M_\odot$ for MSP-WD binaries. This is larger than our modeled system masses in our MSP population, which must also include the unknown mass of the WD companion present in most of our pulsar systems.

Two possible explanations for this discrepancy can be related back to our assumptions of the dominant mass class in the core of the cluster. The first is that should the core of Terzan 5 have a large population of heavy stellar systems, the resulting

system mass of the pulsars could be much closer to the expected neutron star mass range. These heavy stellar systems could be comprised of such systems as heavy WDs or hard binaries. The presence of hard binaries, which is a binary system with a binding energy greater than the average for other binaries in the cluster, can halt gravothermal collapse of the system (Heggie 1975) and is an ideal means of explaining why Terzan 5 has avoided gravothermal collapse. As for the presence of WDs, these massive stellar remnants and their progenitors would have reached the core quickly due to mass segregation. If these stars are the dominant mass class of the cluster, they too would provide a much more reasonable system mass for the pulsars according to our measured mass ratio.

The second explanation is that the pulsars in Terzan 5 were formed via an electron capture supernova. This argument also agrees with the hypothesis that the core may have an abundance of heavy white dwarfs, as these are believed to have been the possible progenitors for the Terzan 5 pulsars (Ivanova et al. 2008). Should this be the case, evidence exists that the median mass distribution of neutron stars formed via electron capture is ~ 1.25 $M_{\odot}$. If the pulsar binaries in our sample are orbitted by a white-dwarf of a few tenths of a solar mass, this agrees well with our measurements.

2.11.5 Black Hole Fits

To date, Terzan 5 is one of the best candidates for testing the existence of a central massive black hole given its large number of confirmed pulsars deep within its core. In order to expand this work to other globular clusters, and to improve our limits on the black hole mass for Terzan 5, we would either need to increase the number of available pulsars in each GC or create a more robust model for the physics governing the black hole.

We argue that increasing the number of known pulsars within a globular cluster can improve our constraints on the presence of a black hole for two separate reasons. The first is that the more pulsars we are able to sample the potential with, the more constraints we can put on the accelerations of each pulsar. We are therefore better able to discern if a pulsar is truly better fit by being within, or nearly within, the radius of influence of the black hole. We also argue that the likelihood of finding a pulsar that is very centrally concentrated is increased, which gives us the best constraints on the possible upper mass limit of a black hole. Finding these new pulsars is highly likely as the next generation of radio telescopes turn on and the sensitivity limit on finding weak pulsars is improved (Hessels et al. 2015). It is also expected that search methods for finding weak pulsars will improve over time, as evidenced by the discovery of two new (but as of yet not well timed enough to include in this work) pulsars in 47 Tucanae (Pan et al. 2016).

The latter method of improving our model for the black hole physics may be achieved by allowing the black hole to be offset from the center of the cluster and incorporating its contribution to the jerk of each pulsar. As the black holes mass is much less than the total mass of the cluster, we do not expect it to reside at the exact CoG of the system. Incorporating a positional offset in the black hole's position from the CoG may allow for individual pulsars to be closer or further from the black hole, thereby experiencing accelerations and jerks that cannot be explained by the King model.

Without these changes, we can only take our results as being suggestive in the singular case of Terzan 5 that there is an upper limit to the mass of an intermediate mass black hole in the system.

2.12 Summary

Using the MCMC sampler `emcee` (Foreman-Mackey et al. 2013), we have used 36 MSPs within the globular cluster Terzan 5 to better constrain the cluster parameters, including the core density ρ_c=$1.58^{+0.13}_{-0.13}\times10^6$ $M_\odot$ pc^{-3}, the core radius r_c=$0.16^{+0.01}_{-0.01}$ pc, and the spectral index of the neutron star density α=$-3.14^{+0.52}_{-0.53}$ by using a reddening independent method that probes the true mass density profile and does not rely on an assumed mass to light ratio. These values agree well with previously obtained quantities using HST and ESO-MAD, while using a method that allows us to avoid the issue of reddening or stellar counting towards the cluster center. This is a direct improvement on the previous methods of studying cluster dynamics via pulsar timing as we can better determine the line of sight position of each source.

As our density profile for the system is completely derived from the gravitating mass of the system, we are able to provide a more sensitive probe of the true mass of the system. Our methods find an integrated mass of M_T $\simeq$$3.5\times10^5$ $M_\odot$ along our line of sight and within an impact parameter of 1 parsec of the core. Without a better luminosity profile however, we cannot provide better estimates for the true mass to light ratio of the system. The best estimate for the mass to light ratio for the system is M/L_v $\simeq$$2.0^{+0.8}_{-0.7}$ when using all of the pulsar timing data available.

We find that this provides better evidence that Terzan 5 is likely a pristine fragment of the Galactic bulge (Ferraro et al. 2009) and not the disrupted nucleus of a dwarf galaxy that entered the tidal field of the Milky Way. We also find evidence that the core of the system may be comprised primarily of heavy white dwarfs, which could have provided the needed evolutionary channel to produce the large population of MSPs observed via accretion induced collapse. Finally we find that Terzan 5 has an upper limit on IMBH masses of $M_{\rm BH} \simeq 3\times10^4\,M_\odot$. Future work will be done to

better constrain the black hole mass of this system using more sophisticated acceleration models for the pulsar timing in order to help better constrain the formation history of the Terzan 5 core.

2.13 Acknowledgements

Observations were taken with the Green Bank Telescope, which are operated by the National Radio Astronomy Observatory, a facility of the National Science Foundation operated under cooperative agreement by Associated Universities, Inc.

B.P. acknowledges funding from the Grote Reber fellowship through the National Radio Astronomy Observatory and the Graduate Research STEM Fellowship Program through the Virginia Space Grant Consortium under the National Aeronautics and Space Administration (NASA).

J.W.T.H. acknowledges funding from an NWO Vidi fellowship and from the European Research Council under the European Union's Seventh Framework Programme (FP/2007-2013) / ERC Starting Grant agreement nr. 337062 ("DRAGNET").

I.S. acknowledges pulsar research at UBC is funded by an NSERC Discovery Grant and by the Canadian Institute for Advanced Research.

P.A. is supported by NASA Origins Grant NNX14AE16G and NASA ATP grant NNH12ZDA.

Table 2.1. Timing Parameters for Terzan 5 Pulsars

PSR	RA (17:48:)	DEC (−24:46:)	P (ms)	$\dot{P}$ (10^{-19} s s^{-1})	$\ddot{P}$ (10^{-30} s^{-1})	P_b (days)	$\dot{P}_b$ (10^{-12} s s^{-1})	Duration (yrs)
A[1]	02.251	37.37	12.00	-0.29	–	0.08	–	1.65
C	04.534	34.72	8.40	-6.00	0.52	–	–	17.67
D	05.922	05.67	4.70	1.30	-0.16	–	–	17.67
E	03.409	35.48	2.20	-0.18	2.00	60.00	–	14.84
F	05.118	38.05	5.50	0.04	-5.10	–	–	14.84
G	05.650	46.59	22.00	3.90	-7.70	–	–	14.84
H	05.634	53.06	4.90	-0.83	-0.74	–	–	14.84
I	04.874	46.37	9.60	-0.71	-26.00	1.30	-3.00	17.67
J	04.010	1:40.33	80.00	25.00	-8.20	1.10	-1.30	17.67
K	03.909	47.73	3.00	-0.94	-0.26	–	–	14.84
L	04.738	35.81	2.20	-0.17	1.10	–	–	14.84
M	04.618	40.75	3.60	4.90	3.30	0.44	5.20	14.84
N	04.919	53.78	8.70	5.50	2.00	0.39	2.00	17.67
O	04.682	51.40	1.70	-0.69	2.10	0.26	-1.50	11.26
P[1]	05.038	41.36	1.70	2.60	–	0.36	–	3.73
Q	04.336	1:05.03	2.80	-0.36	0.19	30.00	–	11.26
R	04.688	50.25	5.00	4.70	-18.00	–	–	14.84
S	04.293	31.71	6.10	0.64	0.69	–	–	14.84
T	02.991	52.81	7.10	3.10	0.71	–	–	14.84
U	04.244	47.86	3.30	3.00	0.01	3.60	29.00	11.26
V	05.106	34.46	2.10	-0.95	0.17	0.50	-2.20	11.26
W	04.840	42.38	4.20	1.20	-18.00	4.90	9.30	14.84
X	05.594	1:12.06	3.00	0.59	0.04	5.00	7.40	14.84
Y	05.097	44.57	2.00	1.50	-120.00	1.20	6.40	11.26
Z	04.946	46.11	2.50	-0.86	17.00	3.50	-11.00	14.84
aa	05.812	42.24	5.80	-4.40	0.91	–	–	14.84
ab	04.759	42.65	5.10	4.20	-3.10	–	–	14.84
ac	06.044	32.53	5.10	2.30	1.20	–	–	11.26
ad[1]	03.847	41.86	1.40	-0.34	–	1.10	–	4.16
ae	04.964	45.72	3.70	-5.70	-2.80	0.17	-2.80	11.26
af	04.212	44.87	3.30	-2.30	-0.21	–	–	11.26
ag	04.811	34.59	4.40	0.12	-1.20	–	–	11.26

Table 2.1—Continued

PSR	RA (17:48:)	DEC (−24:46:)	P (ms)	$\dot{P}$ (10^{-19} s s^{-1})	$\ddot{P}$ (10^{-30} s^{-1})	P_b (days)	$\dot{P}_b$ (10^{-12} s s^{-1})	Duration (yrs)
ah	04.321	42.03	5.00	5.70	0.60	–	–	11.26
ai	04.115	50.34	21.00	14.00	6.90	0.85	3.80	11.26
aj	05.012	34.69	3.00	1.40	1.70	–	–	11.96
ak	03.686	37.93	1.90	0.88	0.49	–	–	11.45

Note. — Timing parameters for the 36 pulsars in Terzan 5 used for this study. No pulsar with the name "B" exists within Terzan 5, as the pulsar originally given this designation was shown to be unassociated with Terzan 5 (Lyne et al. 2000). Right ascension and declination for each pulsar is recorded in seconds. The duration for these timing models span between 1.5 to 15 years, with most models being accurate for approximately eleven years of data.
[1] - Redback pulsars. These systems experience various forms of timing noise which limit the quality of higher order spin period derivatives and greatly complicates the creation of a long-term phase connected timing solution. We therefore do not show the orbital period derivatives for these systems as they track different physics that is unrelated to the cluster dynamics.

Table 2.2. Black Widow & Pulsar-White Dwarf Binary Orbital Properties

PSR	$c\left\lvert\dot{P}_b/P_b\right\rvert$ (m s^{-2})	B (10^8 G)	Association
	Black Widows		
J2051−0827*	5.4×10^{-7}	-	Field[1]
J1959+2048*	1.3×10^{-7}	-	Field[2]
J1731−1847*	1.2×10^{-7}	-	Field[3]
J0021−7204I	6.1×10^{-9}	5.7	47 Tuc[4]
J0021−7204J	1.5×10^{-8}	8.7	47 Tuc[4]
J0021−7204O*	2.3×10^{-7}	**	47 Tuc[4]
J1748−2446ae	5.7×10^{-8}	12.0	Terzan 5[5]
J1748−2446O	2.0×10^{-8}	5.2	Terzan 5
	Pulsar-White Dwarfs		
J1748−2446M	4.0×10^{-10}	2.5	Terzan 5
J1748−2446N	1.5×10^{-9}	12.1	Terzan 5
J1748−2446V	1.5×10^{-9}	2.8	Terzan 5
J1748−2446W	2.1×10^{-9}	6.9	Terzan 5
J1748−2446X	7.0×10^{-10}	2.8	Terzan 5
J1748−2446Y	3.6×10^{-9}	4.4	Terzan 5
J1748−2446Z	3.8×10^{-10}	1.7	Terzan 5[5]

Note. — Black widows and pulsar-white dwarfs with measured values of $\dot{P}_b$ in the field of the galaxy, 47 Tucanae, and Terzan 5. The three field black widows have been observed to have orbital phase wander. Of the five globular cluster black widows, one pulsar (J0021−7204O) has confirmed orbital phase wander. For the pulsars in globular clusters we have also shown the derived magnetic field strength according to the derived value of $\dot{P}$ given by Equation 2.21, of which only J0021−7204O shows an irregular inferred magnetic field strength due to its confirmed orbital phase wander[4]. We find similar magnetic field strengths between the black widows and pulsar-white dwarf systems.

* - Has been confirmed to have orbital phase wander.

** - Due to phase wander, attempts to measure a magnetic field strength yield an non-physical negative value.

[1] - Lazaridis et al. (2011)

[2] - Fruchter et al. (1990)

[3] - Bates et al. (2011)

[4] - Freire et al. (2003)

[5] - Ransom et al. (in prep 2017)

Table 2.3. Cluster Parameters for Terzan 5

Fitting Method	ρ_c (10^6 $M_\odot pc^{-3}$)	r_c (pc)	α
Previously Cited	(1-4)[1]	0.16±0.02[2]	3.29±0.33[3]
Projected	$1.67^{+0.37}_{-0.29}$	$0.17^{+0.02}_{-0.02}$	-3.71 ± 0.57
Accelerations Only	$1.44^{+0.22}_{-0.21}$	$0.16^{+0.01}_{-0.01}$	$-3.57^{+0.45}_{-0.41}$
Accelerations & Jerks	$1.58^{+0.13}_{-0.13}$	$0.16^{+0.01}_{-0.01}$	$-3.14^{+0.52}_{-0.53}$
Accelerations & Jerks & Black Hole Fitting	$1.62^{+0.18}_{-0.16}$	$0.15^{+0.02}_{-0.01}$	$-3.59^{+0.33}_{-0.31}$
Accelerations & Jerks & Center of Gravity Offset	$1.41^{+0.18}_{-0.14}$	$0.16^{+0.01}_{-0.01}$	$-3.56^{+0.47}_{-0.56}$

Note. — Cluster parameters for Terzan 5 using different fitting methods.
[1] - Lanzoni et al. (2010)
[2] - Miocchi et al. (2013): Main sequence turn off star core radius scaled down to the neutron star core radius according to Equation 2.25 using the measured spectral index of Heinke et al. (2006)
[3] - Heinke et al. (2006)

Table 2.4. Line of sight positions using projected cluster parameters.
$\rho_c = 1.67^{+0.37}_{-0.29} \times 10^6$ M$_\odot$ pc^{-3}
$r_c = 0.17^{+0.02}_{-0.02}$ pc
$\alpha = -3.71 \pm 0.57$
d=5.9 kpc

PSR	$R_\perp$ (pc)	$a_{z,meas}$ (10^{-9} m s^{-2})	l_1 (pc)	l_2 (pc)	r_1 (pc)	r_2 (pc)	$P(l_1)$	$P(l_2)$	$\frac{P(l_1)}{P(l_2)}$
I	0.052	−7.779	0.009	1.390	0.052	1.391	3.82e−18	4.61e−18	0.83
ae	0.055	−56.908	0.079	0.311	0.096	0.315	2.86e−17	2.90e−17	0.99
Z	0.057	−10.795	0.013	1.138	0.059	1.140	5.41e−18	6.14e−18	0.88
W	0.063	6.632	−0.008	−1.527	0.064	1.528	3.39e−18	4.02e−18	0.84
ab	0.066	24.510	−0.030	−0.660	0.073	0.663	1.27e−17	1.30e−17	0.98
Y	0.096	19.053	−0.027	−0.782	0.100	0.788	1.15e−17	1.04e−17	1.11
P	0.118	44.924	−0.083	−0.374	0.145	0.392	2.96e−17	2.47e−17	1.19
M	0.142	41.097	−0.088	−0.396	0.168	0.421	3.07e−17	2.34e−17	1.31
R	0.173	28.264	−0.069	−0.553	0.187	0.579	2.60e−17	1.62e−17	1.60
O	0.205	−20.030	0.058	0.717	0.213	0.745	2.28e−17	1.16e−17	1.96
F	0.214	0.194	−0.001	−10.484	0.214	10.486	2.38e−19	2.28e−19	1.04
ah	0.218	34.654	−0.131	−0.407	0.255	0.462	3.63e−17	2.28e−17	1.59
af	0.248	−20.670	0.081	0.673	0.261	0.717	2.91e−17	1.26e−17	2.31
U	0.254	28.542	−0.130	−0.479	0.285	0.542	3.63e−17	1.91e−17	1.90
L	0.255	−2.256	0.009	2.807	0.255	2.818	3.70e−18	1.64e−18	2.26
N	0.264	17.625	−0.075	−0.758	0.275	0.803	2.77e−17	1.08e−17	2.57
ag	0.287	0.839	−0.004	−4.826	0.287	4.834	1.67e−18	7.30e−19	2.29
aj	0.290	14.275	−0.071	−0.879	0.299	0.926	2.64e−17	8.83e−18	2.99
V	0.306	−15.157	0.084	0.828	0.318	0.883	2.97e−17	9.58e−18	3.10
C	0.308	−21.474	0.131	0.597	0.335	0.672	3.63e−17	1.47e−17	2.47
G	0.317	5.449	−0.030	−1.668	0.318	1.698	1.27e−17	3.53e−18	3.60
ai	0.330	15.550	−0.100	−0.794	0.345	0.860	3.29e−17	1.01e−17	3.24
K	0.377	−9.501	0.076	1.133	0.385	1.194	2.78e−17	6.18e−18	4.50
aa	0.381	−22.737	0.284	0.408	0.475	0.558	3.09e−17	2.27e−17	1.36
H	0.390	−5.084	0.042	1.716	0.392	1.760	1.73e−17	3.39e−18	5.11
ad	0.398	−7.273	0.064	1.356	0.403	1.413	2.46e−17	4.78e−18	5.14
S	0.428	3.150	−0.032	−2.282	0.429	2.322	1.33e−17	2.23e−18	5.95
ak	0.492	14.025	−0.241	−0.690	0.547	0.847	3.41e−17	1.22e−17	2.79
ac	0.579	13.428	−0.479	−0.479	0.752	0.752	1.91e−17	1.91e−17	1.00
Q	0.618	−3.879	0.091	1.931	0.625	2.028	3.11e−17	2.85e−18	10.90
E	0.619	−2.450	0.056	2.583	0.621	2.657	2.22e−17	1.85e−18	12.00
T	0.761	13.067	−0.608	−0.608	0.974	0.974	1.44e−17	1.44e−17	1.00
X	0.837	5.156	−0.282	−1.384	0.884	1.617	3.11e−17	4.64e−18	6.70
A	1.033	−0.745	0.061	4.995	1.035	5.101	2.37e−17	6.93e−19	34.20
D	1.189	8.074	−0.914	−0.914	1.500	1.500	8.37e−18	8.37e−18	1.00
J	1.627	−4.087	1.228	1.228	2.039	2.039	5.51e−18	5.51e−18	1.00

Note. — Solutions for the line of sight positions of each pulsar using the cluster parameters derived using traditional parameter fitting methods. Pulsars are ordered by their projected distance from the centers of the cluster.

Table 2.5. Line of sight positions

PSR	Accelerations			Acceleration & Jerk		
	l_1 (pc)	l_2 (pc)	$P\left(\frac{l_1}{l_2}\right)$	l_1 (pc)	l_2 (pc)	$P\left(\frac{l_1}{l_2}\right)$
I	$1.1 \times 10^{-2} \pm 1.7 \times 10^{-3}$	$1.8 \times 10^{0} \pm 3.6 \times 10^{-2}$	230.0	$1.0 \times 10^{-2} \pm 1.2 \times 10^{-3}$	$1.6 \times 10^{0} \pm 1.5 \times 10^{-1}$	9.7
ae	$2.8 \times 10^{-1} \pm 5.3 \times 10^{-2}$	$1.0 \times 10^{-1} \pm 2.9 \times 10^{-2}$	1.3	$3.2 \times 10^{-1} \pm 2.7 \times 10^{-1}$	$8.6 \times 10^{-2} \pm 2.1 \times 10^{-2}$	1.3
Z	$1.5 \times 10^{-2} \pm 4.6 \times 10^{-3}$	$1.1 \times 10^{0} \pm 1.2 \times 10^{-1}$	230.0	$1.4 \times 10^{-2} \pm 3.7 \times 10^{-3}$	$7.4 \times 10^{-1} \pm 1.8 \times 10^{-1}$	14.0
W	$-8.6 \times 10^{-3} \pm 1.3 \times 10^{-3}$	$-5.4 \times 10^{-2} \pm 4.3 \times 10^{-4}$	230.0	$-7.8 \times 10^{-3} \pm 9.5 \times 10^{-4}$	$-1.7 \times 10^{0} \pm 2.3 \times 10^{-1}$	4.9
ab	$-3.2 \times 10^{-2} \pm 1.3 \times 10^{-1}$	$-3.2 \times 10^{-2} \pm 1.3 \times 10^{-1}$	1.0	$4.0 \times 10^{-2} \pm 1.9 \times 10^{-1}$	$4.0 \times 10^{-2} \pm 1.9 \times 10^{-1}$	1.0
Y[1]	$-3.0 \times 10^{-2} \pm 4.6 \times 10^{-3}$	$-8.7 \times 10^{-1} \pm 8.3 \times 10^{-2}$	2.1	$-2.7 \times 10^{-2} \pm 5.2 \times 10^{-3}$	$-8.0 \times 10^{-1} \pm 1.1 \times 10^{-1}$	1.0
P	$-6.5 \times 10^{-2} \pm 3.6 \times 10^{-2}$	$-4.9 \times 10^{-1} \pm 1.7 \times 10^{-1}$	10.0	$7.4 \times 10^{-2} \pm 1.4 \times 10^{-1}$	$7.4 \times 10^{-2} \pm 1.4 \times 10^{-1}$	1.0
M	$-1.0 \times 10^{-1} \pm 1.6 \times 10^{-2}$	$-4.1 \times 10^{-1} \pm 5.0 \times 10^{-2}$	3.0	$-8.8 \times 10^{-2} \pm 1.1 \times 10^{-2}$	$-4.3 \times 10^{-1} \pm 6.1 \times 10^{-2}$	3.6
R	$-7.0 \times 10^{-2} \pm 1.3 \times 10^{-1}$	$-7.0 \times 10^{-2} \pm 1.3 \times 10^{-1}$	1.0	$5.5 \times 10^{-2} \pm 1.2 \times 10^{-1}$	$5.5 \times 10^{-2} \pm 1.2 \times 10^{-1}$	1.0
O	$6.6 \times 10^{-2} \pm 8.7 \times 10^{-3}$	$8.2 \times 10^{-1} \pm 1.1 \times 10^{-1}$	23.0	$5.7 \times 10^{-2} \pm 8.3 \times 10^{-3}$	$7.4 \times 10^{-1} \pm 9.9 \times 10^{-2}$	8.0
F	$1.4 \times 10^{-3} \pm 2.4 \times 10^{-4}$	$1.4 \times 10^{-3} \pm 2.4 \times 10^{-4}$	1.0	$1.4 \times 10^{-3} \pm 2.0 \times 10^{-4}$	$1.4 \times 10^{-3} \pm 2.0 \times 10^{-4}$	1.0
ah	$-1.2 \times 10^{-1} \pm 3.6 \times 10^{-2}$	$-4.6 \times 10^{-1} \pm 1.6 \times 10^{-1}$	8.2	$-1.1 \times 10^{-1} \pm 1.9 \times 10^{-1}$	$-1.1 \times 10^{-1} \pm 1.9 \times 10^{-1}$	1.0
af	$1.1 \times 10^{-1} \pm 5.5 \times 10^{-2}$	$5.4 \times 10^{-1} \pm 1.4 \times 10^{-1}$	10.0	$9.5 \times 10^{-2} \pm 3.6 \times 10^{-2}$	$3.3 \times 10^{-1} \pm 1.4 \times 10^{-1}$	1.1
U	$-1.3 \times 10^{-1} \pm 3.0 \times 10^{-2}$	$-5.3 \times 10^{-1} \pm 8.6 \times 10^{-2}$	2.0	$-5.6 \times 10^{-1} \pm 1.5 \times 10^{-1}$	$-1.3 \times 10^{-1} \pm 4.1 \times 10^{-2}$	1.1
L	$2.0 \times 10^{-2} \pm 2.8 \times 10^{-2}$	$2.0 \times 10^{-2} \pm 2.8 \times 10^{-2}$	1.0	$1.5 \times 10^{-2} \pm 8.5 \times 10^{-2}$	$2.7 \times 10^{0} \pm 2.7 \times 10^{-1}$	26.0
N	$-7.8 \times 10^{-2} \pm 8.2 \times 10^{-3}$	$-9.1 \times 10^{-1} \pm 8.1 \times 10^{-2}$	8.8	$-7.2 \times 10^{-2} \pm 7.2 \times 10^{-3}$	$-9.6 \times 10^{-1} \pm 9.8 \times 10^{-2}$	12.0
ag	$-5.2 \times 10^{-4} \pm 7.1 \times 10^{-5}$	$-5.2 \times 10^{-4} \pm 7.1 \times 10^{-5}$	1.0	$-4.9 \times 10^{-4} \pm 8.2 \times 10^{-5}$	$-4.9 \times 10^{-4} \pm 8.2 \times 10^{-5}$	1.0
aj	$5.1 \times 10^{-2} \pm 2.2 \times 10^{-1}$	$5.1 \times 10^{-2} \pm 2.2 \times 10^{-1}$	1.0	$5.3 \times 10^{-2} \pm 1.0 \times 10^{-1}$	$5.3 \times 10^{-2} \pm 1.0 \times 10^{-1}$	1.0
V	$9.0 \times 10^{-2} \pm 1.7 \times 10^{-2}$	$8.9 \times 10^{-1} \pm 1.7 \times 10^{-1}$	11.0	$1.3 \times 10^{0} \pm 6.2 \times 10^{-1}$	$8.0 \times 10^{-2} \pm 3.2 \times 10^{-2}$	1.8
C	$1.5 \times 10^{-1} \pm 2.2 \times 10^{-2}$	$6.1 \times 10^{-1} \pm 1.5 \times 10^{-1}$	1.8	$2.7 \times 10^{-1} \pm 1.8 \times 10^{-1}$	$2.7 \times 10^{-1} \pm 1.8 \times 10^{-1}$	1.0
G	$2.8 \times 10^{-2} \pm 1.7 \times 10^{-1}$	$2.8 \times 10^{-2} \pm 1.7 \times 10^{-1}$	1.0	$2.2 \times 10^{-2} \pm 1.8 \times 10^{-2}$	$1.9 \times 10^{0} \pm 6.0 \times 10^{-1}$	1.1
ai	$-9.8 \times 10^{-2} \pm 1.7 \times 10^{-2}$	$-9.5 \times 10^{-1} \pm 2.4 \times 10^{-1}$	3.1	$-9.0 \times 10^{-2} \pm 2.4 \times 10^{-2}$	$-6.5 \times 10^{-1} \pm 3.0 \times 10^{-1}$	8.4
K	$1.3 \times 10^{-1} \pm 2.5 \times 10^{-1}$	$1.3 \times 10^{-1} \pm 2.5 \times 10^{-1}$	1.0	$1.2 \times 10^{-1} \pm 2.1 \times 10^{-1}$	$1.2 \times 10^{-1} \pm 2.1 \times 10^{-1}$	1.0
aa	$3.5 \times 10^{-1} \pm 1.1 \times 10^{-1}$	$3.5 \times 10^{-1} \pm 1.1 \times 10^{-1}$	1.0	$3.5 \times 10^{-1} \pm 1.2 \times 10^{-1}$	$3.5 \times 10^{-1} \pm 1.2 \times 10^{-1}$	1.0
H	$6.2 \times 10^{-2} \pm 2.4 \times 10^{-1}$	$6.2 \times 10^{-2} \pm 2.4 \times 10^{-1}$	1.0	$5.3 \times 10^{-2} \pm 1.7 \times 10^{-1}$	$5.3 \times 10^{-2} \pm 1.7 \times 10^{-1}$	1.0
ad	$1.8 \times 10^{-1} \pm 2.1 \times 10^{-1}$	$1.8 \times 10^{-1} \pm 2.1 \times 10^{-1}$	1.0	$1.2 \times 10^{-1} \pm 2.9 \times 10^{-1}$	$1.2 \times 10^{-1} \pm 2.9 \times 10^{-1}$	1.0
S	$1.7 \times 10^{-2} \pm 1.8 \times 10^{-2}$	$1.9 \times 10^{0} \pm 5.5 \times 10^{-1}$	120.0	$-2.0 \times 10^{-2} \pm 2.3 \times 10^{-1}$	$-2.0 \times 10^{-2} \pm 2.3 \times 10^{-1}$	1.0
ak	$-1.0 \times 10^{-1} \pm 1.3 \times 10^{-1}$	$-1.3 \times 10^{0} \pm 4.4 \times 10^{-1}$	7.7	$1.2 \times 10^{-1} \pm 8.2 \times 10^{-2}$	$9.4 \times 10^{-1} \pm 4.3 \times 10^{-1}$	3.7
ac	$-2.4 \times 10^{-1} \pm 6.9 \times 10^{-2}$	$-1.0 \times 10^{0} \pm 2.6 \times 10^{-1}$	4.3	$-2.0 \times 10^{-1} \pm 3.1 \times 10^{-1}$	$-2.0 \times 10^{-1} \pm 3.1 \times 10^{-1}$	1.0
Q	$2.0 \times 10^{-1} \pm 2.7 \times 10^{-1}$	$2.0 \times 10^{-1} \pm 2.7 \times 10^{-1}$	1.0	$1.1 \times 10^{-1} \pm 3.8 \times 10^{-2}$	$1.7 \times 10^{0} \pm 7.7 \times 10^{-1}$	2.6
E	$1.4 \times 10^{-1} \pm 1.4 \times 10^{-1}$	$1.4 \times 10^{-1} \pm 1.4 \times 10^{-1}$	1.0	$1.3 \times 10^{-1} \pm 3.4 \times 10^{-1}$	$1.3 \times 10^{-1} \pm 3.4 \times 10^{-1}$	1.0
T	$-6.2 \times 10^{-1} \pm 2.9 \times 10^{-1}$	$-6.2 \times 10^{-1} \pm 2.9 \times 10^{-1}$	1.0	$-5.0 \times 10^{-1} \pm 6.1 \times 10^{-1}$	$-5.0 \times 10^{-1} \pm 6.1 \times 10^{-1}$	1.0
X	$-2.7 \times 10^{-1} \pm 6.3 \times 10^{-1}$	$-2.7 \times 10^{-1} \pm 6.3 \times 10^{-1}$	1.0	$2.7 \times 10^{-1} \pm 6.2 \times 10^{-1}$	$2.7 \times 10^{-1} \pm 6.2 \times 10^{-1}$	1.0
A	$1.1 \times 10^{-1} \pm 2.3 \times 10^{-1}$	$1.1 \times 10^{-1} \pm 2.3 \times 10^{-1}$	1.0	$1.3 \times 10^{-1} \pm 5.1 \times 10^{-1}$	$1.3 \times 10^{-1} \pm 5.1 \times 10^{-1}$	1.0
D	$-9.2 \times 10^{-1} \pm 3.8 \times 10^{-1}$	$-9.2 \times 10^{-1} \pm 3.8 \times 10^{-1}$	1.0	$-1.1 \times 10^{0} \pm 4.3 \times 10^{-1}$	$-1.1 \times 10^{0} \pm 4.3 \times 10^{-1}$	1.0
J	$1.3 \times 10^{0} \pm 4.6 \times 10^{-1}$	$1.3 \times 10^{0} \pm 4.6 \times 10^{-1}$	1.0	$1.2 \times 10^{0} \pm 4.3 \times 10^{-1}$	$1.2 \times 10^{0} \pm 4.3 \times 10^{-1}$	1.0

Note. — Final fits to the line of sight position for each pulsar. Pulsars are ordered by their projected distance from the centers of the cluster. We include the line of sight position for both the l_1 and l_2 position, as well as the relative probability between the two. Results are given for the acceleration only fits as well as the acceleration plus jerk fitting. If the distributions for l_1 and l_2 are strongly mixed, or one solution is too small to detect, we only report statistics for the single observable peak in the posterior distribution for both the l_1 and l_2 solution.

Chapter 3

Phase Variations

3.1 Abstract

Over the past few years, the number of known millisecond pulsars being orbited by low mass non-degenerate companion stars has increased dramatically. We present the long-term timing of six of these pulsars in globular clusters, finding stochastic changes in the orbital period with a characteristic magnitude $\Delta P_b/P_b \sim 5 \times 10^{-6}$. Assuming an axisymmetric potential, these changes correspond with an average change in the quardrupolar moment of the companion's density profile of $\delta J_2 \sim 10^{-5}$. We find no evidence for a magnetic cycle less than ∼25 years using a least-squares spectral analysis of our measured orbital phase changes. We argue that these results rule out magnetic deformations as described by the Applegate mechanism, which has been suggested as the driving mechanism in other redback systems. Finally, we include a discussion on how pulsar timing might be used in the future to better study the magnetic properties of rapidly rotating low-mass stars, which may allow us to circumvent the need for high resolution spectra of these systems, which can only study slowly rotating stars.

3.2 Introduction

3.2.1 Black Widow & Redback Pulsars

After the discovery of the first MSP by Backer et al. (1982), the formation mechanism by which MSPs are created has been an active topic of research. The currently accepted theory proposed by Alpar et al. (1982) suggests that accretion of angular momentum in LMXBs is responsible for turning slow pulsars into MSPs. As a companion star fills its Roche lobe, mass transfer onto the slowly rotating neutron star provides enough angular momentum to recycle the neutron star to rotational periods

of only a few milliseconds over the course of a few tens of millions of years.

Of the approximately 2500 known pulsars, nearly 375 are considered MSPs. Roughly two thirds of these MSPs have retained their companion star, most of which have already evolved into a low mass WD [1] (Manchester et al. 2005). As mentioned in Chapter 1, on rare occasion a pulsar is found to be interacting with a not yet degenerate companion star. These systems are commonly referred to as "black widows" or "redbacks", due to the fact that the pulsars "consume" the companion during possible episodes of mass transfer.

While searches within the field of the Milky Way are able to uncover nearer and brighter redbacks, long duration eclipses (Δt_e ~50% of P_b at ν =1500 MHz) bias us against finding eclipsing pulsars in any single observation. Over the past few years we have begun to overcome this detection bias through the work of the Fermi large area telescope (Fermi-LAT). By searching for gamma ray sources with spectra characteristic of a pulsar, Fermi-LAT has helped to discover nearly two dozen additional redbacks over the course of its mission, though data for these systems only goes back a few years and does not provide a clear image of the long-term evolution for redbacks as of yet (Abdo et al. 2013).

Compared to observations within the field of the galaxy, however, targeted searches of eight GCs have discovered twelve redbacks over the past two decades[2]. Due to the low signal to noise associated with studying distant globular cluster pulsars, long intergration times on the largest radio telescopes are needed to give strong constraints on the pulsar's timing properties. For this reason, only a few studies have been performed on the globular cluster redbacks J1748−2446A (Lyne et al. 1990; Nice et al. 2000), J0024−7204W (Camilo et al. 2000), J1701−3006B (Lynch et al. 2012), J1740−5340

[1] http://www.atnf.csiro.au/people/pulsar/psrcat/

[2] A complete list of all confirmed globular cluster pulsars can be found at: http://www.naic.edu/ pfreire/GCpsr.html

(D'Amico et al. 2001; Ferraro et al. 2001), J1823−3021F (Lynch et al. 2012), and J2140−2310A (Ransom et al. 2004). In this work we will present both the long-term and short term orbital properties of six redbacks (J1748−2446A, J1748−2446P, J1748−2446ad, J1824−2452H, J1824−2452I, and J1748−2021D) using over a decade of data for each system.

3.2.2 Explanations for orbital phase wander

For this work, we investigated whether the Applegate mechanism is capable of producing the orbital phase wander seen in black widow and redback systems. The theory behind this mechanism was first proposed by Applegate (1992) and Applegate & Shaham (1994), and seeks to relate any magnetic activity in the companion star to the orbital properties of the system.

As the star undergoes its magnetic cycle, deformations in the star will produce changes in the quadrupolar gravity field at the position of the pulsar. The orbital period and semi-major axis will then change slightly, producing quasi-periodic changes in the orbit and luminosity of the companion star over the duration of the magnetic cycle ($P_{\rm cyc}$) as the star continuously redistributes its mass. This model has been applied to a number of black widows and redbacks in the field of the galaxy, the majority of which only used a few years of data to draw their conclusions from (Applegate & Shaham 1994; Nice & Thorsett 1996; Lazaridis et al. 2011; Archibald et al. 2013; Pletsch & Clark 2015).

In the Applegate model, the available energy budget of the companion star can be drawn from the total nuclear burning luminosity or through tidal-heating. This energy budget for deformations can vary by orders of magnitude depending on the evolutionary stage of the companion star. Depending on whether the system is evolu-

tionarily closer to a canonical MSP or a LMXB, the companion could be significantly filling its Roche lobe. Even with optical measurements of the companion star, we would not be able to constrain the radius using the observed spectral properties without first having a reliable model for how the lightcurve of these systems should behave in close proximity to the pulsar (Romani & Sanchez 2016).

Callanan et al. (1995) and Reynolds et al. (2007) have found that the optical lightcurve of B1957+20's companion implies the star is highly irradiated and has a strong temperature gradient across the star. Modeling the resulting lightcurve for this scenario is made difficult by our lack of understanding of how the pulsar flux reaches the surface of the companion star through the intra-binary shock (Romani & Sanchez 2016). This limits our understanding of how much extra energy is deposited into the companion star, which could further push the star off the main sequence.

For the purposes of this work, we will show results for the Applegate model in the limiting cases: 1) the companion's radius follows a main-sequence scaling relationship with stellar mass ($R/R_{\odot} \sim [M/M_{\odot}]^{0.8}$) and 2) the star is fully filling the Roche lobe of the system. We discuss how this additional heating of the companion may be important in Section 3.8.

3.2.3 Structure of the chapter

We begin this chapter with a brief introduction to the previous studies and relevant physical characteristics for each of our six redback sources in Section 3.3. We follow this with a discussion of the observing campaigns for each pulsar and how the timing models were produced in Section 3.4. Using these timing models, we discuss the role the GC potential plays in our analysis and motivate that these redbacks should behave no differently than those in the field of the Galaxy for the purposes of this

work in Section 3.5.

We then proceed to calculate the distribution of quadrupolar moments which arise due to the wander in the orbital phase for each redback in Section 3.6, assuming an axisymmetric potential. We then investigate whether the Applegate model is capable of producing the observed effects in our pulsar timing in Section 3.7.

As part of our analysis for the Applegate model, we will attempt to identify a periodicity to the magnetic cycle in the companion star. We then calculate the magnitude of luminosity changes needed produce torques that can drive angular momentum transfer between the differentially rotating layers of the companion star. We then compare these measurements to the total available energy in the companion star to drive these changes using the nuclear burning luminosity or tidal heating.

Finally, in Section 3.8 we discuss the most likely driving mechanism behind the orbital phase wander in these eclipsing pulsar binaries. We also include a discussion detailing what these measurements can tell us about the length of the magnetic cycle in low-mass stars and the strength of their subsurface magetic fields. We then revisit the previous studies of well-timed spider pulsars, arguing that their results only make use of quasi-periodic behavior to characterize the magnetic field behavior in the Applegate framework. Finally we discuss what these results mean in the context of pulsar timing and future studies of redbacks.

3.3 Sources

In this section we briefly summarize previous studies for each of our sources. Additional information on each pulsar can be found in Table 3.1. Calculations of the projected Roche lobe radius ($R_{l,i}$) were made using Equation 2 from Eggleton (1983) assuming a pulsar mass of M_p=1.55 $M_\odot$ (Kiziltan et al. 2013) and inclination angle

i=90° in order to convert the measured mass function into a minimum companion mass.

3.3.1 Individual Pulsars

J1748-2446A

J1748-2446A (hereafter Ter5A) was the second eclipsing millisecond pulsar to be discovered and the first redback (Lyne et al. 1990). Ter5A is in a P_b=1.8 hour orbit with a companion of mass $M_{\rm c,min}$=0.08 $M_\odot$. The projected semi-major axis of the pulsar ($x_{\rm p,}i$) has been measured to be $x_{p,i}$=0.1196 lt-s, which implies $R_{{\rm l},i}$=0.418 lt-s.

The eclipse properties for this system can be highly variable due to the unbound gas filling most of the orbit and the strong irradiation of the companion (Podsiadlowski 1991). Ter5A was studied extensively by both Lyne et al. (1990) and Nice & Thorsett (1996) which found the median eclipse length for this system to be Δt_e ∼40% of the orbit at 1500 MHz for most of its eclipses, though this eclipse duration can vary greatly depending on the observing frequency.

Ter5A is also one of the earliest examples where orbital phase wander was measured in a binary pulsar. Nice et al. (2000) observed variations of the orbital period at the level of $|\Delta P_b/P_b| \sim 10^{-7}$ within the first five years of timing. This is the only system in our sample with an already measured value of $|\Delta P_b/P_b|$ and provides a comparison to our own results in Section 3.5.1.

J1748-2446P

J1748-244P (hereafter Ter5P) was discovered by Ransom et al. (2005) and is one of the top 10% rapidly rotating millisecond pulsars known to date with a spin-period of 1.72 ms. It is in a 8.7 hour orbit with a $M_{\rm c,min}$=0.38 $M_\odot$ companion, and lies at

$x_{\mathrm{p},i}$=1.2718 lt-s from the center of gravity.

Given the large minimum companion mass, the Ter5P system has the second largest mass fraction of any redback. It is likely that this companion star is the result of a pair exchange, where the original star that spun up the pulsar has been ejected from the system and has left behind a more massive star (Ransom et al. 2005).

Ter5P also undergoes regular eclipses that last for approximately 45% of its orbit at L-Band; though, unlike Ter5A, Ter5P does not show any evidence of irregular eclipses (Prager et al. In Prep). The projected Roche lobe size for Ter5P is $R_{\mathrm{l},i}$=1.726 lt-s.

J1748-2446ad

J1748-2446ad (hereafter Ter5ad) is the fastest known MSP, with a spin period of 1.39 ms and has an incredibly low signal to noise, making it difficult to study (Hessels et al. 2006). Pulsar timing has constrained this system to have a $M_{\mathrm{c,min}}$=0.14 $\mathrm{M}_{\odot}$ companion, P_b=26.3 hour orbit, $x_{\mathrm{p},i}$=1.1028 lt-s pulsar projected semi-major axis, and $\mathrm{R}_{\mathrm{l},i}$=2.691 lt-s project Roche lobe.

In terms of its eclipses, Ter5ad is most similar to Ter5A. It experiences highly irregular eclipses that have a median duration of ∼40% of its orbit at L-Band, which is rare for a pulsar in such a long orbit (Hessels et al. 2006). Its companion is likely bloated and fully filling its Roche lobe, causing long periods of quenched pulsar emission.

J1824-2452H

J1824-2452H (hereafter M28H) is a redback in the globular cluster M28. It is in a P_b=10.4 hour orbit with a pulsar semi-major axis of $x_{\mathrm{p},i}$=0.7194 lt-s. The companion

star has a minimum companion mass $M_{\rm c,min}$=0.20 $M_\odot$ star which implies a projected Roche lobe of size $R_{{\rm l},i}$=1.409 lt-s.

The companion star for this system is likely tidally distorted and undergoing periodic mass loss, suggesting that this star was captured through pair exchange in the dense cluster core of M28 and is not the star that spun up the pulsar (Pallanca et al. 2010; Bogdanov et al. 2011). Alternatively, these unique system properties could also indicate that M28H may have recently transitioned from an LMXB state (Bogdanov et al. 2011) to rotation powered emission.

M28H shows both regular and irregular eclipses, with the regular eclipses having a median duration of 50% at L-Band .

J1824-2452I

J1824-2452I (hereafter M28I), also known as IGR J18245-2452, is a redback in M28 that has been seen to go between an LMXB state and a radio pulsar state over short timescales (Linares et al. 2014). This means this source belongs to the sub-population of pulsars known as transitional pulsars (systems observed to alternate between X-ray emission and radio pulsations), and may help provide a better understanding of how LMXBs evolve into MSPs.

The pulsar is in a P_b=11.0 hour orbit with a semi-major axis of $x_{{\rm p},i}$=0.7659 lt-s. The companion star has a mass $M_{\rm c,min}$=0.17 $M_\odot$ and has a Roche lobe of size $R_{{\rm l},i}$=1.656 lt-s, which should be almost fully filled with material as the source is actively accreting material on to the pulsar in order to power its transitions into an LMXB state.

J1748-2021D

J1748-2021D (hereafter NGC6440D) is located in the globular cluster NGC 6440. It is in a P_b=6.9 hour orbit with a $M_{\rm c,min}$=0.14 $M_\odot$ companion. The semi-major axis for the pulsar is $x_{{\rm p},i}$=0.3972 lt-s and the Roche lobe of the companion is $R_{{\rm l},i}$=0.969 lt-s. NGC6440D has a short eclipse duration for a redback pulsar, with eclipses of ∼10% at L-Band and occassional observations of the system possible at superior conjunction. This suggests a variable amount of gas in the system and an inclination angle for the orbit substantially less than edge on ($i < 90°$).

3.4 Timing Campaigns

In this section we discuss how the data were taken and analyzed for each of our six redbacks. We then discuss how a single timing model was produced for each observation of each pulsar by expanding upon phase connected timing solutions spanning only a few years.

3.4.1 Observations

Terzan 5

Terzan 5 has 37 known pulsars within the inner arcminute of the cluster. Data were taken using the GBT using the SPIGOT backend (Kaplan et al. 2005) prior to June of 2008 and by the GUPPI (Green Bank Ultimate Pulsar Processing Instrument) backend (DuPlain et al. 2008) after this date. Observations with both backends resulted in approximately 600 MHz of usable bandwidth after band-pass and RFI removal. Observations were centered on ∼1500 MHz or ∼2000 MHz for L-Band and S-Band respectively. Data were taken using the incoherent and coherent search mode

for SPIGOT and GUPPI respectively. Coherent search mode allows for real time de-dispersion on the raw voltages before saving the data in a filterbank format. More information summarizing these observations can be found in Ransom et al. (2005) and Hessels et al. (2006). Further details about the observing of the 37 pulsars in this system will be presented in an upcoming paper by Ransom et al. (in prep 2017).

M28

M28 plays host to 12 pulsars, which is the third largest GC pulsar population behind 47 Tucanae and Terzan 5. Observations of this cluster were performed similarly to Terzan 5, using the SPIGOT backend for dates prior to June 2008 and the GUPPI backend for subsequent observations. More details on the initial timing of these pulsars are summarized by Bogdanov et al. (2011).

NGC6440

NGC6440 has 6 pulsars and was observed in the same manner as Terzan 5 and M28. Discussion of the original observations are detailed by Freire et al. (2008).

3.4.2 Timing Solutions

In this section, we briefly introduce the timing models used to obtain the phase connected timing solution for each of our pulsars before discussing how single epehemrides were produced for each observation of each pulsar.

3.4.3 Phase Connected Timing Solutions

Table 3.1 shows the results of the pulsar timing campaigns carried out by Ransom et al. (in prep 2017) for the Terzan 5 pulsars, Stairs et al. (2006) and Begin (2006)

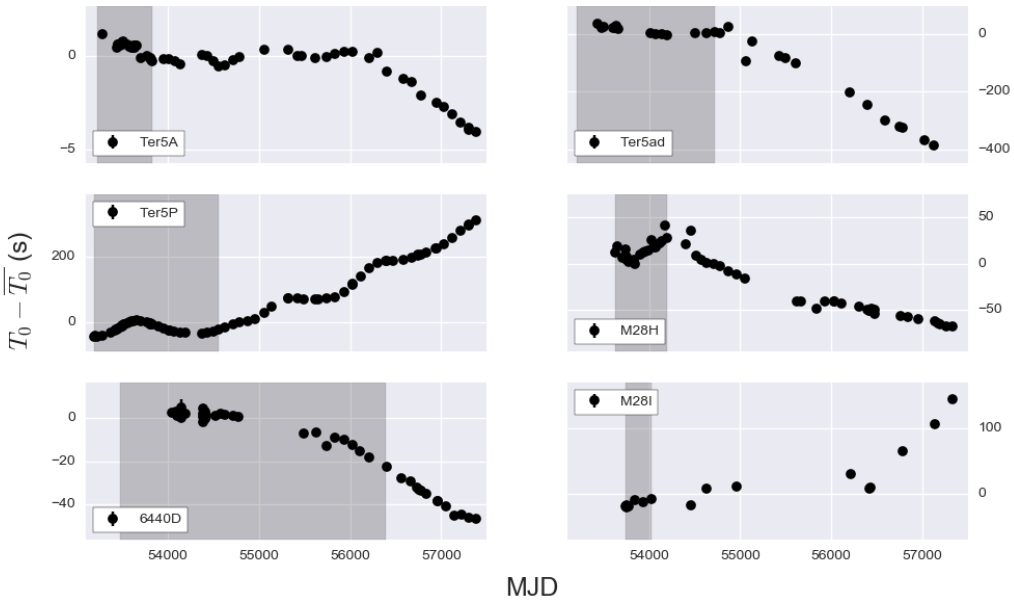

Fig. 3.1.— Measured orbital phase T_0 for all six redbacks plotted as a function of the observing MJD at the middle of the observation. Errorbars are included, but are much smaller than the total change in T_0 over the entire baseline. Shaded regions show the span of time for which a phase connected timing model is available for a given system.

for the M28 pulsars, and Freire et al. (2008) for the NGC6440 pulsars.

Pulsar properties from these studies were derived using the timing package TEMPO and a binary model of Newtonian orbits which includes secular changes in the orbital elements (the 'BTX' model). A single ephemeris for the system was produced using the ranges in MJD given by the entry 'Phase Connected MJDs' in Table 3.1 as shown in gray in Figure 3.1. Outside of these MJD ranges, phase connection becomes nearly intractable due to the increasing number of orbital period derivatives that must be included in the timing model. In addition to this, the switch from a monthly cadence to quarterly observing makes phase connection even more difficult.

3.4.4 Individual Ephemerides

In order to study the evolution of the orbital properties for each system, we used spin parameters fixed based on the phase-connected timing solution to obtain a single timing model for each observation.

In order to obtain these measurements, we took the total intensity from the Stokes parameters for each pulsar and excised any eclipses or RFI using the pulsar data analysis software PSRCHIVE (Hotan et al. 2004). In order to turn the multi-hour observations into a few high signal-to-noise pulse time of arrivals (TOAs), we averaged over the entire frequency bandwidth and down-sampled the time series by a factor of two to four. This method gives approximately 30 TOAs for each observation, with each TOA referenced to 1500 MHz for L-Band observations and 2000 MHz for S-Band observations.

Using the phase connected timing models, the average orbital period ($\overline{P}_b$) and semi-major axis are known to incredible precision (typically twelve and seven significant figures, respectively). Without phase connection, however, it is impossible to

measure small deviations in these values using any single observation.

If we instead assume long-term stability in these orbital properties, we *can* measure the phase shifts in the sinusoid that defines the pulsar's orbit about the center of gravity. We therefore express the slight pertubations on the orbit using only the periastron passage time (T_0) of the system. All other timing properties of the system are held constant for our analysis.

We further motivate this choice by noting that if the semi-major axis or orbital period were strongly varying over our MJD range, we would not be able to accurately predict the arrival time of each TOA during any given observation using the average values. A more detailed discussion about pulsar timing and the measurement of orbital properties and their errors is given by Damour & Taylor (1991).

The observed evolution of T_0 as a function of the observing MJD is shown in Figure 3.1. While the absolute magnitude of these changes are small compared to $\overline{P}_b$, these errors can lead to thousands of missed phase rotations of the pulsar. Trying to maintain phase connection across the entire observing baseline while accounting for the stochastic wander in T_0 for each system only becomes prohibitively more difficult.

3.5 Globular Cluster Redbacks

3.5.1 Converting T_0 into $\dot{P}_b$

In order to compare globular cluster redbacks to those in the field of the galaxy, we begin by showing that the cluster potential is a negligible contribution to any observed changes in T_0. We accomplish this by converting our measured value of ΔT_0 into a characteristic value of P_b and its derivative $\dot{P}_b$. We then convert the maximum possible cluster acceleration ($a_{\rm c,max}$) along our line of sight at the projected position

of each pulsar into an apparent $\dot{P}_b$ in order to compare it to the value found through pulsar timing.

The change in the orbital phase is related to the varying T_0 value as follows

$$\Delta\phi = n\Delta T_0 = \frac{2\pi}{P_b}\Delta T_0\,, \tag{3.1}$$

where n is the orbital frequency ($n = 2\pi/P_b$). The change in the orbital phase of the system can also be expressed in terms of:

$$\Delta\phi = \frac{1}{2}\dot{n}\Delta t^2 = \frac{-\pi\dot{P}_b}{P_b^2}\Delta t^2\,. \tag{3.2}$$

The characteristic change in P_b is therefore related to the observed wander in T_0 over the timescale Δt as follows

$$\frac{\Delta P_b}{P_b} \sim 2\frac{\Delta T_0}{\Delta t}\,. \tag{3.3}$$

We relate this to the characteristic orbital period derivative as follows:

$$\dot{P}_b \simeq \frac{\Delta P_b}{\Delta t} = 2P_b\frac{\Delta T_0}{\Delta t^2}. \tag{3.4}$$

Figures 3.3 and 3.2 show the observed distributions of $|\Delta P_b/P_b|$ and $\dot{P}_b$, respectively. The distribution of values were measured using a Monte Carlo analysis where the measurement error in T_0 was incorporated into our fits. In order to accomplish this, we assumed Gaussian errors in T_0 and randomly drew new values of T_0 from a distribution centered on the measured T_0 with a standard deviation given by δT_0. This was performed tens of thousands of time to obtain a better understanding of the parent distribution from which our data was sampled.

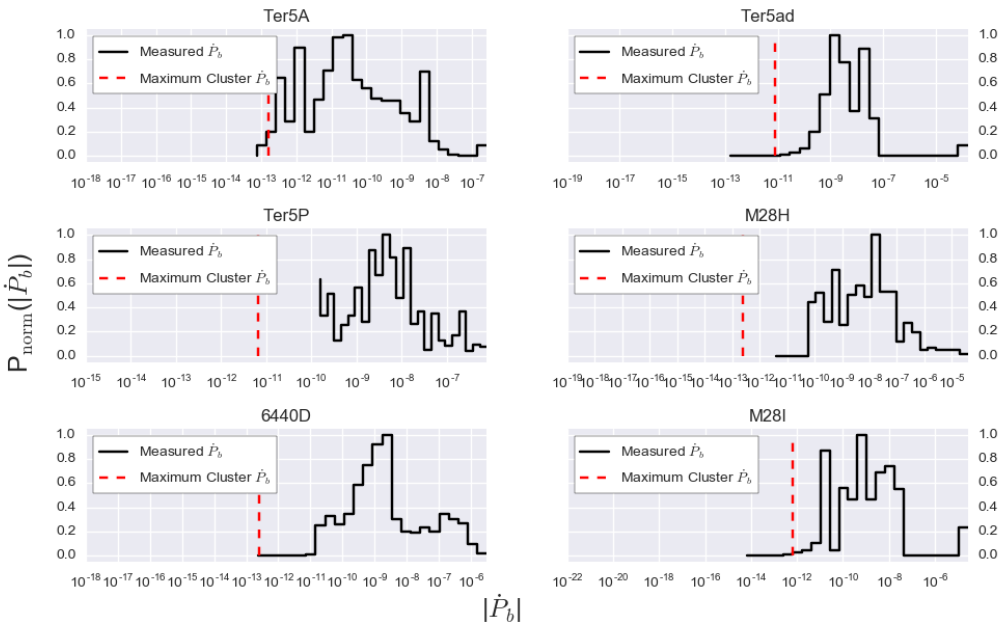

Fig. 3.2.— The probability distribution of $|\dot{P}_b|$ values for all six redback systems. A Monte Carlo analysis was used to derive the distribution using the measured value of T_0 and its associated error. The maximum possible cluster induced orbital period derivative at the position of each redback according to the cluster parameters given in Table 3.2 is shown in red.

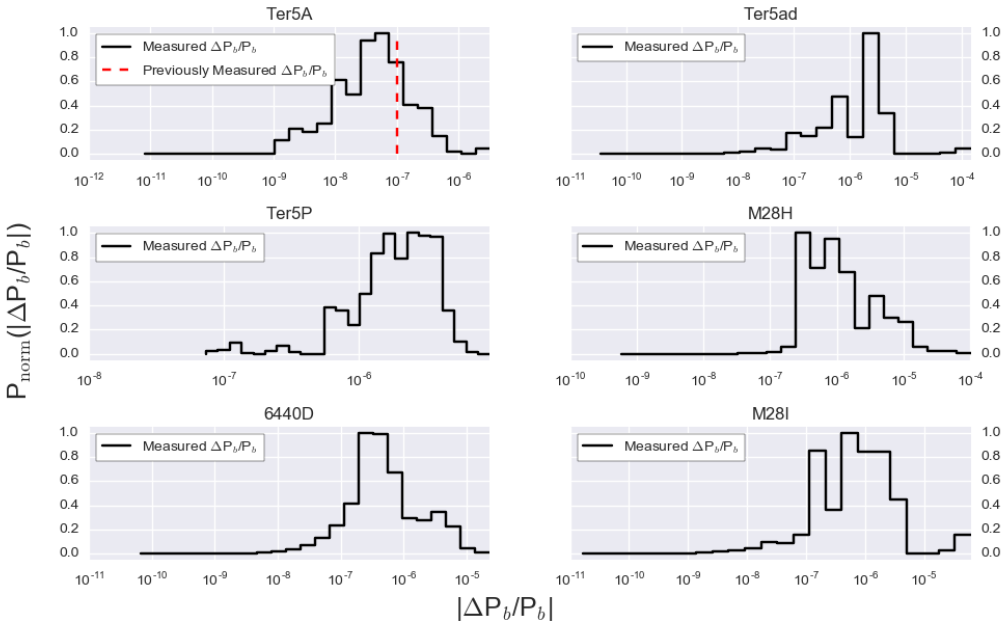

Fig. 3.3.— The probability distribution of $|\Delta P_b/P_b|$ values for all six redback systems. A Monte Carlo analysis was used to derive the distribution using the measured value of T_0 and its associated error. The measured value of $|\Delta P_b/P_b|$ for Ter5A as measured by Nice et al. (2000) is shown in red.

Medians for the distributions in $|\Delta P_b/P_b|$ and $\dot{P}_b$ are reported in Table 3.2 and range between $10^{-7} \lesssim |\Delta P_b/P_b| \lesssim 10^{-5}$ and $10^{-9} \lesssim \dot{P}_b \lesssim 10^{-6}$, respectively.

Globular Cluster Potentials

As previously discussed in Chapter 2, a pulsar sitting in the potential of a globular cluster should show both intrinsic and extrinsic changes to its timing properties. We can account for the additional acceleration the pulsar is feeling along our line of sight using Equation 2.11.

Using Equation 2.3 at the on sky position of each pulsar, we found the maximum possible line of sight acceleration for each source across all possible line of sight positions l. We then converted this acceleration into a orbital period derivative for each pulsar using Equation 2.20.

The effects of galactic rotation, the Shklovskii effect, and DM errors were ignored as they tend to be approximately 10^{-2}, 10^{-4}, and 10^{-5} times smaller than the cluster acceleration for typical clusters, respectively (Prager et al. 2016).

Figure 3.2 shows the maximum possible cluster induced orbital period derivative for each system in red and is plotted alongside the distributions of measured $\dot{P}_b$ values. In none of our systems is the cluster capable of producing an acceleration large enough to reasonably explain the observed values of $\dot{P}_b$. We also note that from the results of Figure 2.2 that the nearest neighbors to the pulsar are unlikely to produce a perturbing acceleration large enough to explain the measured changes in $\dot{P}_b$.

Figure 3.4 shows the median values of $\dot{P}_b$ for the six redbacks in our sample as well as the measured values for all other black widows and redbacks. We find that our six sources are roughly consistent with the wide range of measured $\dot{P}_b$ values

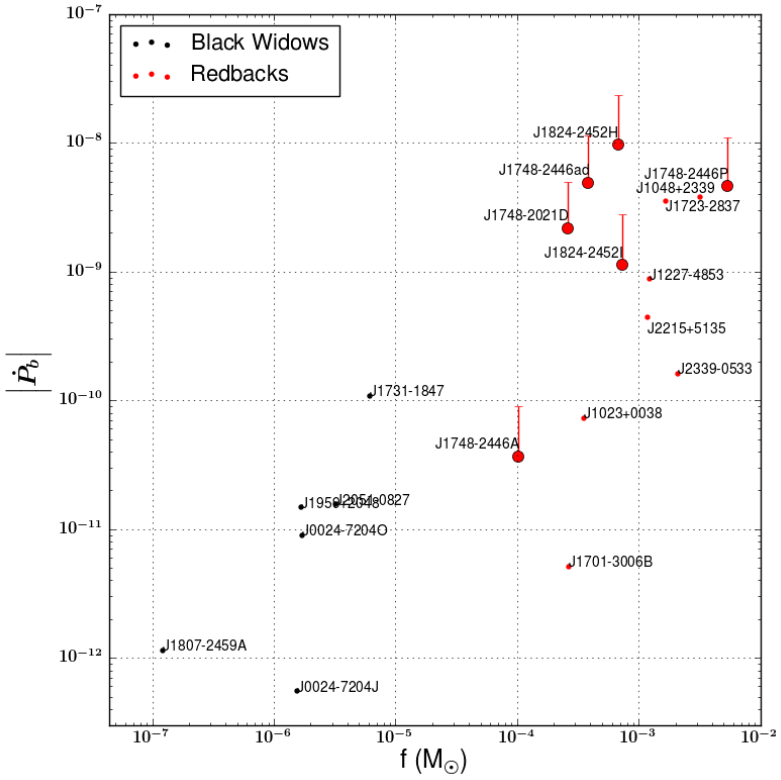

Fig. 3.4.— Observed distribution of orbital period derivatives for all known black widows and redbacks according to the mass function. The six sources in our study are plotted with their median measured values of $\dot{P}_b$ as well as the standard deviation as calculated by the median absolute deviation assuming a normally distributed dataset. We have not plotted the lower-bounds of the errorbars for the sake of clarity.

for redbacks within the field of the galaxy. The values of $\dot{P}_b$ seen in our sample of redbacks show negligible difference between galactic and GC RB populations, and we therefore assume that the physics driving orbital phase wander is well represented in the timing data of GC RBs.

3.6 Quadrupole Moments

Before testing our data against models for convective motions and magnetic activity, we include the required quadrupole moment of the gravity field needed to produce the

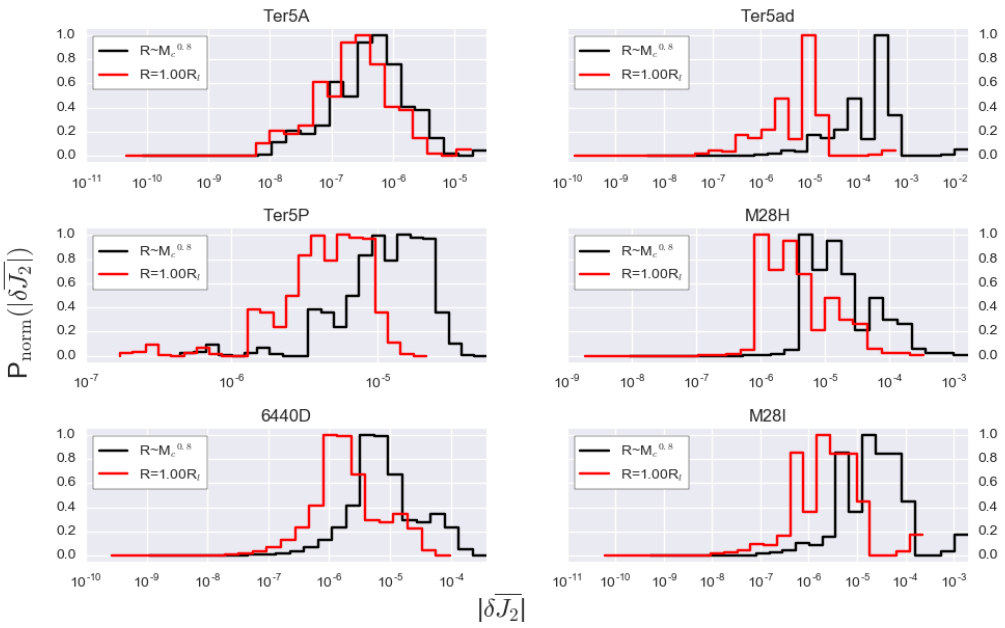

Fig. 3.5.— Plot of the probability distribution of $|\delta J_2|$ values for all six redback systems assuming an axisymmetric potential and a companion radius set by either the main-sequence mass-radius relationship or a filled Roche lobe radius. A Monte Carlo analysis was used to derive the distributions using the measured value of T_0 and its associated error.

measured changes in T_0. In doing so, we have a means of describing the magnitude of the changes in the orbital properties that can be used to compare results between different models and simulations

If we consider only the change in the second multipole moment J_2 for an axisymmetric potential, we can relate the change in the orbital phase to J_2 as follows::

$$\frac{\Delta T_0}{\Delta t} = 3\delta\overline{J}_2(t)\left(\frac{R_c}{\overline{R}}\right)^2 , \tag{3.5}$$

where $\delta\overline{J}_2(t)$ is the average change in the quadrupole moment, R_c is the companion radius, and R is the separation between the pulsar and the companion star. The separation R is calculated such that:

$$R = x_{\mathrm{p},i}\left(1 + \frac{M_p}{M_{\mathrm{c,min}}}\right) c\,. \tag{3.6}$$

Appendix C gives more detail on how we arrived at Equation 3.5.

Using the observed changes in T_0 as a function of time, we have measured $\delta\overline{J}_2$ at the epoch of each observation according to Equation 3.5. The companion radius R_c was tested for the two separate limiting cases. The first limit is that the star is the main sequence limit where the radius scales as $(R/R_\odot) \propto (M/M_\odot)^{0.8}$, whereas the second is that the companion is fully filling the projected Roche lobe ($R_c \sim R_{l,i}$).

The distribution of $|\delta J_2|$ for all six redbacks is shown in Figure 3.5 using the measured values of T_0 and its associated errors and the before mentioned Monte Carlo sampler. The median of each distribution is shown in Table 3.2 and ranges between $10^{-6} \lesssim |\delta\overline{J}_2| \lesssim 10^{-3}$.

These measurements are a mostly model independent means of quantifying the magnitude of the orbital phase wander in that we only assume the effect to be due

to the quadrupolar moment changing in the companion star and that the system has an axisymmetric potential. This provides a useful quantity that future models would need to be able to reproduce to explain this effect.

The most popular model currently for explaining this effect — which assumes changes in the quadrupole of the companion star — is the Applegate model.

3.7 Applegate Model

3.7.1 Theory

Applegate (1992) proposed that orbital period modulation in close binaries is linked to the subsurface magnetic field activity in one of the stars. For low-mass stars, the convective region can couple strongly with the magnetic field, providing efficient angular momentum transport throughout the differentially rotating layers. This energy transfer leads to hydrostatic configuration changes within the star, producing a time varying oblateness in the star. As the oblateness of the star evolves over a magnetic cycle ($P_{\rm cyc}$), the orbital period and semi-major axis of the system must change in order to conserve angular momentum.

Two key requirements of this theory are: 1) the presence of cyclic variations in T_0 which vary with the magnetic cycle $P_{\rm cyc}$ and 2) whether the companion star has a large enough energy resevoir to drive the required changes in the orbit.

3.7.2 Periodicity of orbital wander

Previous applications of the Applegate model to redbacks and black widows have all attempted to identify $P_{\rm cyc}$ with only a few years of data. In our work, we attempt to identify any periodicity using a least-squares spectral analysis to produce a Lomb-

Scargle periodogram, which allows us to account for the unevenly sampled data set. We chose this method because is an effective algorithim for sampling weaker periodic signals (Scargle 1982) and allows us introduce the observed errors in each value of T_0 to obtain a more accurate power spectrum.

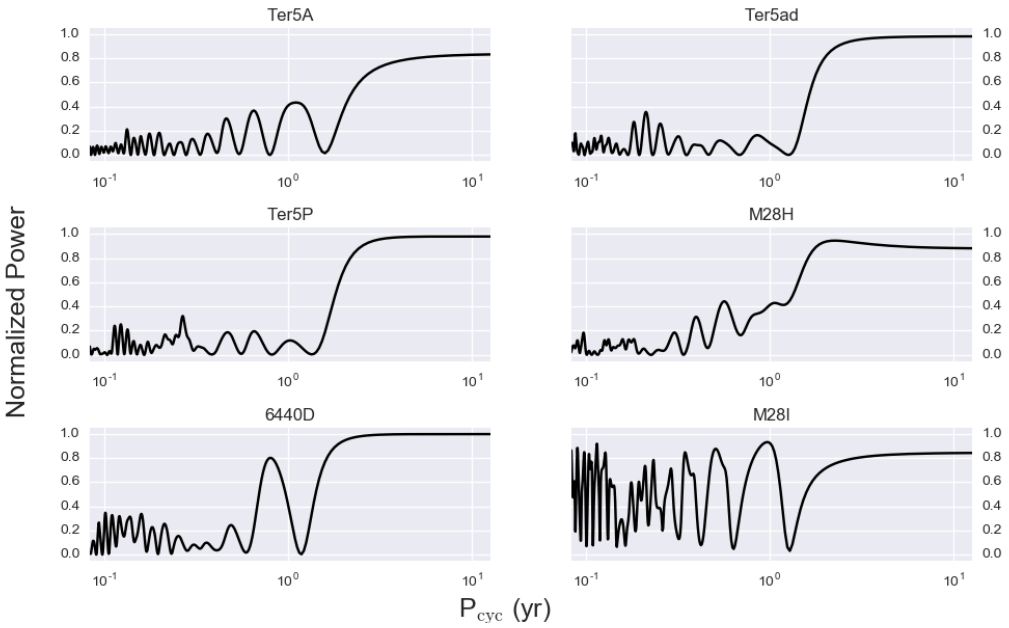

Fig. 3.6.— Lomb-scargle periodograms for all six pulsars calculated using the measured changes in T_0. We find no evidence of any strong periodic signal in any of the pulsars on timescales of less than ~ 25 years.

Figure 3.6 shows the normalized power spectrum for each source. We see either that most of the power lies within the lowest frequencies, implying a red noise process inconsistent with any strong signal, or that there is no one strong periodic signal. Looking at the raw data in Figure 3.1 as well, it is fairly apparent that there is no strong periodicity to the data that can be attributed to a magnetic cycle. We therefore rule out the existence of a measured $P_{\rm cyc}$ of only a few years duration.

Alternatively, if our data is still evolving according to a very low frequency periodic process, then this implies a lower limit to the periodicity of twice the entire timespan for which we have data ($P_{\rm cyc} \gtrsim 25$ years). These results are much longer than those

inferred for redbacks and black widows in the field of the galaxy. We discuss this discrepancy further and investigate its consequences for the Applegate model further in Section 3.8.

3.7.3 Energy Budget of the companion star

We also examined the energy budget of each pulsar companion in order to verify whether the Applegate model was energetically viable. We begin by expressing the change in energy (ΔE) associated with transporting angular momentum (ΔJ) between different rotating layers of the companion star as follows:

$$\Delta E = \Omega_{\rm dr} \Delta J \,, \tag{3.7}$$

where $\Omega_{\rm dr}$ is the difference in the angular velocities of the layers.

We calculate ΔJ according to Equation 27 from Applegate (1992):

$$\Delta J = \frac{1}{6\pi} \frac{G M_c^2 R^2}{R_c^3} \Delta P_b \,. \tag{3.8}$$

Unfortunately, the amount of differential rotation for our sources is not known. However, we can estimate this quantity to obtain an order of magnitude estimate on the amount of energy associated with orbital phase changes. If we assume that $\Omega_{\rm dr} \sim 0.1\Omega$, we can re-write Equation 3.7 as:

$$\Delta E = 6 \times 10^{43} \left(\frac{4\,\text{hours}}{P_b}\right) \left(\frac{M_c}{M_\odot}\right)^2 \left(\frac{10^{10}\,\text{cm}}{R_c}\right)^3 \left(\frac{R}{10^{10}\,\text{cm}}\right)^2 \left(\frac{\Omega_{\rm dr}}{0.1\Omega}\right) \left(\frac{\Delta P_b}{10\,\text{s}}\right) \text{ ergs} \,, \tag{3.9}$$

where we have expressed our variables in more natural units for the problem.

We can find an approximate power associated with this energy change by dividing

the results of Equation 3.9 over a given time interval Δt between measurements and noting that $\Delta P_b/\Delta t \sim \dot{P}_b$:

$$\Delta L = 6\times10^{33}\left(\frac{4\,\mathrm{hours}}{P_b}\right)\left(\frac{M_c}{M_\odot}\right)^2\left(\frac{10^{10}\,\mathrm{cm}}{R_c}\right)^3\left(\frac{R}{10^{10}\,\mathrm{cm}}\right)^2\left(\frac{\Omega_{\mathrm{dr}}}{0.1\Omega}\right)\left(\frac{\dot{P}_b}{10^{-9}}\right)\mathrm{ergs/s}\,. \tag{3.10}$$

Figure 3.7 shows the energy per unit time needed to drive the observed orbital phase changes assuming angular momentum is being transferred between layers of the companion star. The median values for this distribution range between 0.1−10 $L_\odot$. Also plotted are two potential energy resevoirs the star could draw from to drive these changes: (1) the bolometric luminosity of the companion star for a given value of $M_{\mathrm{c,min}}$ and (2) tidal luminosity produced by differential heating of the companion star.

The nuclear burning luminosities were calculated using the results of Baraffe et al. (1998), which assumes each star to be on the main sequence, with the exception of Ter5A. Given the small mass of the companion star in the Ter5A system, we instead use the predicted luminosity for a brown dwarf of mass $0.08M_\odot$ at 10 Gyrs in age as measured by Burrows et al. (2001).

Due to tidal locking with the pulsar, the companion star has a large temperature gradient between the day and night side. Energy flow associated with this temperature gradient drives magnetic activity that can in turn produce orbital phase wander. This influx of energy from the companion star intercepting the pulsar wind can be calculating using Equation 28 from Applegate & Shaham (1994):

$$L_{\mathrm{tidal}} = 4\times10^{32}\left(\frac{10^{11}\,\mathrm{cm}}{R}\right)^2 q\left(\frac{10^{8}\,\mathrm{yr}}{t_M}\right)\,\mathrm{ergs/s}\,, \tag{3.11}$$

where q is the mass ratio of the companion mass to the pulsar mass and t_M is the

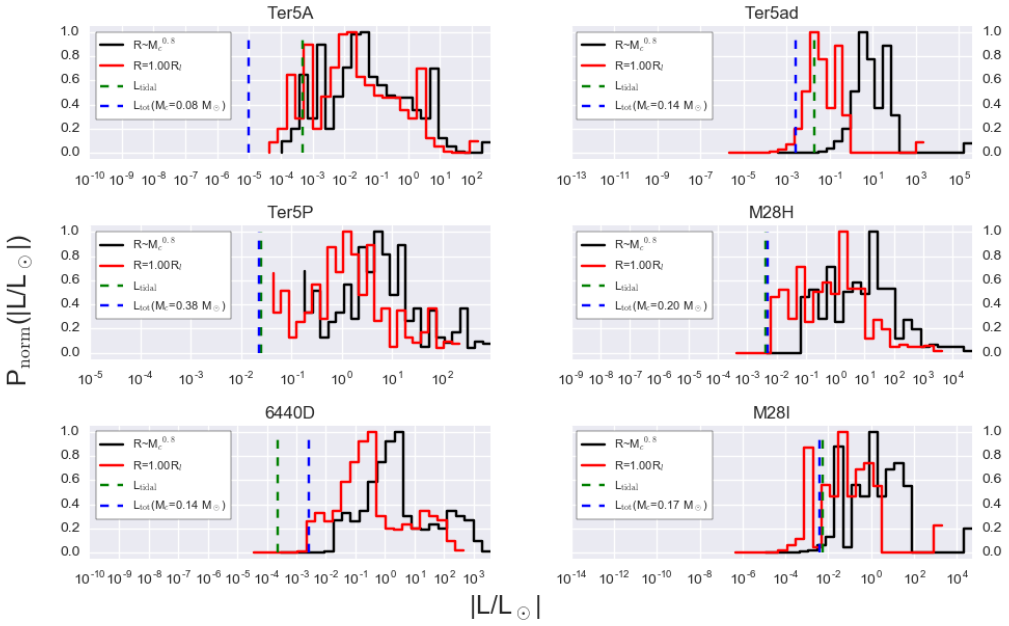

Fig. 3.7.— The measured energy per unit time (ΔL) required to produce the observed changes in T_0 for each of our six sources. These distributions were measured assuming a minimum companion mass, a differential rotation rate of $\Omega_{\rm dr} \sim 0.1\Omega$, and either a companion radius set by the main sequence mass to radius relationship or a filled Roche lobe radius. A Monte Carlo analysis was used to derive the distributions using the measured value of T_0 and its associated error. Also plotted are the predicted total nuclear burning luminosities for each system according to the results of Baraffe et al. (1998) for the given minimum companion mass and the predicted tidal luminosity given by Applegate & Shaham (1994).

timescale for evolution by mass loss ($t_M = M_c/\dot{M}$) as the pulsar wind strips mass from the companion star.

For RBs, there are two different ways of estimating the mass-loss rate from the companion star. The first is by measuring the excess dispersion measure going into and out of eclipse and calculating an approximate plasma density (ρ_E) at R_e assuming an isotropic distribution. For a wind velocity (v_w) of the order of the escape velocity of the companion star, we find a mass loss rate of $\dot{M} \sim 4\pi R_e^2 \rho_E v_w$ (Ransom et al. 2004). This produces a mass loss rate for all six of the redbacks of the order $\dot{M}$ $\sim 10^{-13}$–10^{-12} $M_\odot$ yr^{-1}.

The second method is to calculate the mass loss due to the pulsar spin-down power striking the surface of the companion star and is a common method for calculating mass loss rates in RBs (Archibald et al. 2013). If we assume that the pulsar emits its spin-down power isotropically, and we compare the fraction of the energy intercepted by the companion star to the binding energy of particles at its surfrace, we find mass loss rates of $\dot{M}$ $\sim 10^{-11}$–10^{-8} $M_\odot$ yr^{-1}.

We have elected to use this second method for calculating the mass loss rate from the companion star as it produces an upper-limit on $L_{\rm tidal}$ for the three Terzan 5 RBs. We do this by using the results of Chapter 2 to remove the cluster induced $\dot{P}$ on each pulsar at its de-projected location in the cluster to calculate the spin-down power. For the remaining three RBs, we cannot calculate an intrinsic value of $\dot{P}$ without knowing the pulsars position in the cluster.

From the results of the Fermi mission redbacks have been shown to be more energetic than typical MSPs (Abdo et al. 2013). From the ATNF catalogue [3] (Manchester et al. 2005) we can estimate the spin-down of our redbacks by looking at the distributon of $\dot{P}$ values for the most energetic MSPs. Figure 3.8 shows the distribution of

[3] http://www.atnf.csiro.au/people/pulsar/psrcat/

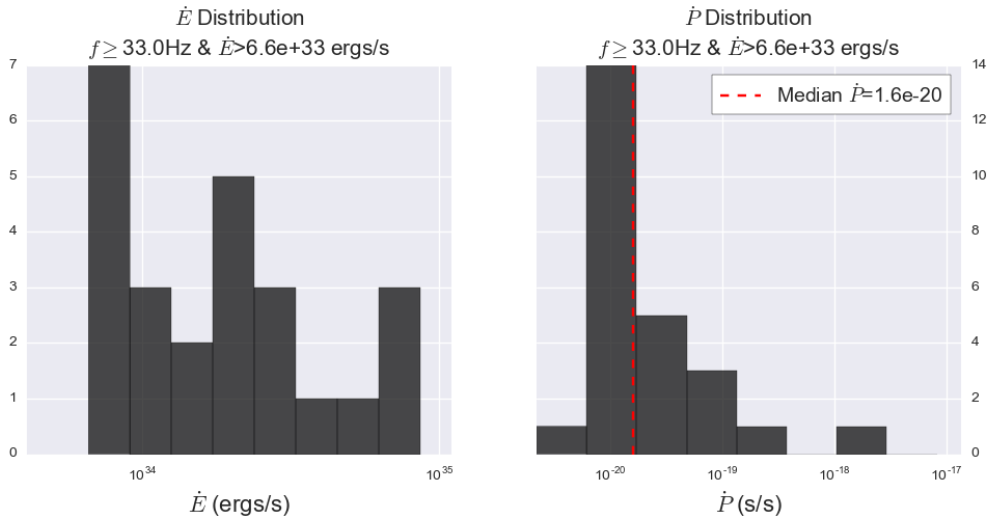

Fig. 3.8.— Left hand plot: The distribution of spin-down powers for the 25% most energetic ATNF MSPs with a spin frequency greater than 33 Hz. From the results of the Fermi mission, Redbacks appear to be more energetic than most MSPs and likely have spin-down powers somewhere in this distribution. Right hand plot: The spin period derivatives for those pulsars shwon in the left hand plot. The vertical red line shows the median of the distribution, which we can use to estimate the intrinsic spin-down of GC redbacks without know the pulsar's true position in the cluster.

the 25% most energetic MSPs in the field of the galaxy with a spin-frequency greater than 33 Hz. The median spin-down of these pulsars is $\dot{P} \simeq 1.6{\times}10^{-20}$ s s^{-1}. We use this value to obtain an estimate of the mass loss timescale for M28H, M28I, and NGC6440D.

We find that the required energy to drive the deformations predicted by the Applegate model is far too large to be supplied by the nuclear burning luminosity of the companion star or by tidal heating. Figure 3.7 shows that neither of these energey reservoirs is large enough to explain the full distribution of orbital phase changes. Even Ter5A, which has the smallest binary separation and therefore is the most efficient at creating tidal heating, regularly experiences orbital phase changes larger than the predicted tidal luminosity.

Recent studies have also found that the Applegate mechanism falls short of explaining the observed orbital period variations in other magnetically active binaries as well (Schwarz et al. 2009; Parsons et al. 2010). We discuss possible changes to the Applegate model to reconcile the theory with pulsar timing data in Section 3.8.

3.8 Discussion

3.8.1 The Applegate model for our sources

With the exception of B1957+20, previous studies of the Applegate model in spider pulsars only utilized data going back a few years. We argue that the short observing baseline used in these works led to discoveries of short-term quasi-periodic behavior in their timing due to some underlying red noise process.

Even the most recent studies of B1957+20 using twenty-one years of timing data only show marginal evidence for periodicity in its orbital properties (Shaifullah et al.

2016). If our sample of stars have solar cycles similar to those seen in RS CVns (Hall 1989) and our own Sun (Hathaway 2010), we would require decades worth of data to accurately identify any periodicity to the data.

It has been shown that the Applegate model may be energetically non-viable for explaining the evolution of the orbital properties of other stellar systems as well. Work done by Schwarz et al. (2009) using X-ray timing from XMM Newton found the Applegate model to be a poor explanation for thier observed changes in the orbital properties of the system. Observations tracking the midpoint of eclipse in post common envelope binaries by Parsons et al. (2010) have also found more than an order of magnitude deviation from the Applegate model. As MSP formation includes a common envelope binary phase, it is possible that our sources and those studied in Parsons et al. (2010) may show similarities in how they deviate from the Applegate model.

Two scenarios have been put forth to explain these deviations from prediction. The first explanation is the presence of a extremely low-mass third body in the system, whereas the second invokes magnetic braking (Parsons et al. 2010). Pulsar timing has already been shown to be an excellent tool for detecting planets around pulsars (Wolszczan & Frail 1992; Lorimer & Kramer 2012), and the presence of such a body has never been detected in any of the timing models produced for each system in over a decade of timing.

As for the case of magnetic braking, we calculate the approximate monotonic change in the orbital period due to a loss of angular momentum in the companion star. This effect has been studied extensively in cataclysmic variables (Patterson 1984), and for a two body system that is tidally locked with a mass ratio $q < 0.52$ (below which Patterson (1984) finds no departure in the assumed spherical geometry

of the Roche lobe), the change in the angular momentum of the orbit ($\dot{J}_{\rm orb}$) is given by:

$$\dot{J}_{\rm orb} = 2.7 \times 10^{43} \frac{M_p^{2/3}}{(1+q)^{1/3}} \frac{1}{\alpha} \left(\frac{P_b}{4\,{\rm hrs}} \right)^{1.55} \left(\frac{\dot{P}_b}{P_b} \right) {\rm ergs}\,, \tag{3.12}$$

where α is the companion stars deviation from the zero age main sequence radius and is given by $\alpha = 0.59\,(M_c/M_\odot)^{-0.55}\,(P_b/4{\rm hrs})^{2/3}$.

If the total mass of the system remains constant, the angular momentum lost from the orbit ($\dot{J}_{\rm orb}$) as the secondary star experiences rotational braking is given by:

$$\dot{J}_{\rm orb} = 1.14 \times 10^{52} \sqrt{\alpha} \frac{M_p^{0.27}}{(M_p + M_c)^{0.33}} \times (M_p - 0.79 M_c) \dot{M}_c\,{\rm ergs}\,, \tag{3.13}$$

where $\dot{M}_c$ is the mass loss rate from the companion star.

Using Equations 3.12 and 3.13, we can derive the magnitude of the required orbital period change produced by magnetic braking. For a conservative estimate of a quiescent mass loss rate of $\dot{M}_c \simeq 10^{-11}$ M$_\odot$ yr^{-1}, this produces a $\dot{P}_b$ of $\sim 10^{-6}$ for each of our redbacks. This is broadly consistent with the large spread of measured values of $\dot{P}_b$ seen in Figure 3.2, however it seems unlikely that magnetic braking is present in our timing. Unless the mass loss rate from the companion star is episodic and changing over the timescale of a few months, magnetic braking should produce a monotonic change in $\dot{P}_b$, which would be measured by our timing models.

We therefore argue that while the Applegate model is likely present in our data to some degree, it cannot be responsible for driving the majority of the observed changes in T_0. From previous studies of magnetically active close main sequence binaries, the expected range of $\Delta P_b/P_b$ can span between 10^{-7} and 10^{-5} (Lanza & Rodonò 1999). We argue therefore that the Applegate model only makes sense in the context of our data if it is a higher order effect on the order of 1-10% of our measured values of

$\Delta P_b/P_b$.

3.8.2 The Applegate model for BWs and RBs in the field of the galaxy

We also argue that it seems unlikely that the Applegate model is present in BWs and RBs studied in the field of the galaxy. Table 3.2 presents the results of previous studies of BWs and RBs in the field of the galaxy which investigated orbital phase variations (Applegate & Shaham 1994; Lazaridis et al. 2011; Freire et al. 2003; Archibald et al. 2013; Pletsch & Clark 2015).

Previous studies of these sources have attempted to characterize the magnetic cycle of the companion star using only a few years of data (with the exception of J2051-0827 which has twenty-one years of observations (Shaifullah et al. 2016)). If we consider a red noise process with power spectrum S^{-2}, the relative likelihood of measuring a periodic signal in only a few years of data can be quite large. We therefore argue that previous data does not serve as evidence for the Applegate mechanism. Longer observing baselines are required to confirm whether the variations in the timing are truly periodic in nature.

We have also calculated the change in luminosity for each of these BWs and RBs in the field of the galaxy using Equation 3.10 and a fully filled Roche lobe, which gives the minimum required energy change in the companion star. In none of these sources is it possible that the energy comes from the nuclear burning luminosity, and tidal heating is only marginally likely for the BWs. In reality, the companion stars are likely not fully Roche lobe filling, otherwise long-duration eclipses or quenched pulsar emission would be seen. This suggests that the true energy requirements for orbital phase variation are in fact much larger, as the energy scales as R_c^{-3}, making

tidal heating less likely in each scenario.

3.8.3 Additional Physics

We conclude from our work that additional physics is required to explain the observed changes in the orbital properties of redback systems. For this work, we considered only changes in the companion star that it would undergo if left in isolation. It is already well known that the pulsar can strongly irradiate its companion, producing strong differential heating across the star. Unfortunately, efforts to model the heating of the companion star are often unsuccessful in reproducing the observed lightcurve of the companion star, leaving much of the underlying physics of the pulsar's emission and the intershock region undiscovered (Romani & Sanchez 2016).

If energy from the heating of the companion's surface can be effectively carried deep into the star however, this can provide an energy source to drive changes in the mass distribution. An approximate luminosity associated with additional heating within the binary was provided by Applegate & Shaham (1994), however, as shown in Section 3.7.3 we find this insufficient to power these changes in the companion stars structure.

It is also possible that energy transport from the surface to the deepest layers of the companion star is more efficient than is predicted by the tidal heating discussed in the Applegate model. We therefore argue that future work may need to incorporate the pulsar irradiation into any explanation of the phase wander in redbacks and black widows.

3.8.4 Quadrupole Moments

From the results of Section 3.6, we provide the amplitude of δJ_2 needed to produce orbital phase wander in six redbacks. As this method only assumes that the orbital phase changes are primarily due the quadrupolar moment changing in the companion star and an axisymmetric potential, this is perhaps the most useful characterization of changes in the orbit to compare across different models.

We argue that these results can be used to inform future simulations of low-mass stars. Using the measured changes in J_2 for redbacks, we can provide constraints on models of the time evolution of rapidly rotating low-mass stars. While it is known that these stars should experience some degree of differential rotation and angular momentum transport due to activity within the star, there does not exist a full prescriptive MHD model to date. Our results, as well as future timing campaigns of redbacks, could therefore be used to better inform simulations about the required quadrupolar changes needed.

3.8.5 Pulsar timing & rapidly rotating low-mass stars

While the Applegate model is not applicable to our data, it is evident that the changes in the internal structure of the companion star can present themselves in pulsar timing. This implies that pulsar timing can be used as a means of studying the internal properties of a possible companion star. In most cases, this should provide us with insights into the interior physics that are not possible with more traditional observations of low-mass stars.

Examples of this can be drawn from the Applegate model, which related pulsar timing to the internal magnetic field structure of the companion. This is a very difficult property to measure in low-mass stars, and is heavily influenced by how

much rotation broadening or other effects in the spectra might be influencing the detectability of magnetic signatures such as Zeeman splitting.

Due to tidal locking, the companion stars to redback pulsars must be rapidly rotating. The rotation rates of these stars are likely sufficiently large enough to make the detection of magnetic field strengths using spectra alone impossible. A plausible relationship between the changes in P_b and the magnetic field of the companion star for redbacks and black widows systems would therefore allow us to test how the dynamo process in stars like those in a redback system act at rapid rotation rates. In particular, we may even be able to confirm whether magnetic saturation at rapid roation continues in the magnetic activity-stellar rotation relationship (Reiners et al. 2009).

3.9 Summary

Using the long-term timing of six globular cluster redbacks, we measured the changes in the orbital phase of each system as a function of time. We find that the median characteristic change in the orbital period for each of these systems range between $10^{-7} \lesssim |\Delta P_b/P_b| \lesssim 10^{-5}$. We argued that these changes are similar to those found in redbacks in the field of the galaxy, as the presence of the globular cluster potential cannot produce an apparent orbital period derivative large enough to match the data. This allowed us to study the underlying mechanism driving these changes in the orbital phase using a much longer timing baseline than is available for any other redback to date.

We were able to use our results to comment on the validity of the Applegate model in reproducing our data. We performed a search for any periodicity in the orbital phase changes that would correspond to a magnetic cycle in the companion

star and calculated the required energy per unit time needed to drive the changes in the orbit as predicted by the Applegate mechanism. We find no clear periodicity to the data, constraining the period to be greater than $P_{\rm cyc} \sim 25$ years using a least-squares spectral analysis if the system has not yet gone through a complete magnetic cycle. We also find that the required energy changes range between $0.1 \lesssim |\Delta L| \lesssim 10$ $L_\odot$ and are much larger than the allotted energy budget for this model (10^{-5}–10^{-2} $L_\odot$). We therefore argue that the Applegate mechanism is not responsible for orbital phase wander in our system and discuss this result in the context of previous studies of black widows and redbacks which used much shorter baselines for their work.

Without a viable model for explaining these changes, we also convert our measurements into a distribution of changes in the quadrupolar moment of the companion star for future comparison between different models. This assumes only that the potential is axisymmetric and that the changes in the orbit are somehow tied to the quadrupolar moment of the field. The medians for this distribution range between $10^{-6} \lesssim |\delta\overline{J}_2| \lesssim 10^{-3}$. We then discussed potential future applications of a model that explains these changes in the orbital phase to other areas of research such as magnetic activity in rapidly rotating low-mass stars.

3.10 Acknowledgements

Observations were taken with the Green Bank Telescope, which are operated by the National Radio Astronomy Observatory, a facility of the National Science Foundation operated under cooperative agreement by Associated Universities, Inc.

B.P. acknowledges funding from the University of Virginia Astronomy department, the Grote Reber fellowship through the National Radio Astronomy Observatory, and the Graduate Research STEM Fellowship Program through the Virginia Space Grant

Consortium under the National Aeronautics and Space Administration (NASA).

S.R. is also an staff Astronomer at the National Radio Astronomy Observatory.

J.W.T.H. acknowledges funding from an NWO Vidi fellowship and from the European Research Council under the European Union's Seventh Framework Programme (FP/2007-2013) / ERC Starting Grant agreement nr. 337062 ("DRAGNET").

I.S. acknowledges pulsar research at UBC is funded by an NSERC Discovery Grant and by the Canadian Institute for Advanced Research.

P.A. is supported by NASA Origins Grant NNX14AE16G and NASA ATP grant NNH12ZDA.

3.11 Tables

Table 3.1. Source properties for our sample of six redback pulsars

Property	J1748-2446A	J1748-2446P	J1748-2446ad	J1824-2452H	J1824-2452I	J1748-2021D
			Cluster Parameters			
Cluster	Terzan 5	Terzan 5	Terzan 5	M28	M28	NGC6440
RA_{CoG}	17:48:04.85	–	–	18:24:32.89	–	17:48:52.70
DEC_{CoG}	−24:46:44.6	–	–	−24:52:11.4	–	−20:21:36.9
d (kpc)	5.9±0.5	–	–	5.6±0.15	–	8.5±0.4
ρ_c (10^6 $M_\odot$ pc^{-3})	1.51[1]	–	–	0.08[2]	–	0.76[3]
r_c (pc)	0.17[1]	–	–	0.28[4]	–	0.18[4]
			Timing Measurements			
RA	17:48:02.25	17:48:05.03	17:48:03.84	18:24:31.61	18:24:32.50	17:48:51.65
DEC	−24:46:37.37	−24:46:41.36	−24:46:41.86	−24:52:17.22	−24:52:07.80	−20:21:07.43
P (ms)	11.5	1.73	1.39	4.63	3.93	13.5
$\dot{P}$ (10^{-20} s/s)	−2.87	25.88	−3.38	7.76	7.51	58.65
DM (pc cm^{-3})	24.27	238.72	235.45	121.45	118.87	225.01
Phase Connected MJDs	53228-53830	53193-54556	53204-54722	53629-54201	53738-54025	53478-56390
Complete MJD Range	TBD	TBD	TBD	TBD	TBD	TBD
			Binary Properties			
$\overline{P}_b$ (days)	0.0756	0.3626	1.0944	0.435	0.4594	0.286
$x_p \sin i$ (lt-s)	0.1196	1.2718	1.1028	0.7194	0.7659	0.3972
$a \sin i$ (lt-s)	2.437	6.459	13.312	6.295	7.749	4.795
f ($M_\odot$)	1.03×10^{-4}	5.35×10^{-3}	3.83×10^{-4}	6.73×10^{-4}	7.27×10^{-4}	2.62×10^{-4}
			Derived			
Maximum Cluster $\dot{P}_b$	1.78×10^{-13}	6.74×10^{-12}	8.72×10^{-12}	7.81×10^{-13}	1.14×10^{-12}	3.60×10^{-13}
Minimum M_c ($M_\odot$)	0.08	0.38	0.14	0.20	0.17	0.14
$R_l \sin i$ (lt-s)	0.418	1.726	2.691	1.409	1.656	0.969

Note. — Table of observed parameters for our six sources. Any value that were not measured are shown as N/M, and repetitions from the column before are shown as '-'. The companion mass was calculated assuming a i=90° and a neutron star mass of 1.55 $M_\odot$.

[1] – Prager et al. (2016)

[2] – Pryor & Meylan (1993)

[3] – Freire et al. (2008)

[4] – Miocchi et al. (2013)

Table 3.2. Phase wander properties for our sample of six redback pulsars

PSR	P_b (days)	$M_{\rm c,min}$ ($M_\odot$)	$\lvert\Delta P_b/P_b\rvert^\diamond$ (10^{-7})	$\log_{10}(\lvert\dot{P}_b\rvert)^\diamond$	$\log_{10}(\lvert J_2\rvert)$	$P_{\rm cyc}$ (years)	$\log_{10}(\Delta L)^\diamond$ ($L_\odot$)
Previously Studied Black Widows							
B1957+20[1]	0.38	0.023	1.5	−10.83	–	15	−1.27
J2051−0827[2]	0.099	0.029	1.0	−10.81	–	7.5	−2.89
J0024−7204O[3]	0.14	0.024	1.1	−11.04	–	>5.5	−2.25
Previously Studied Redbacks							
J1023+0038[4]	0.20	0.15	4.0	−10.1	–	0.55	−0.94
J2339−0533[5]	0.19	0.28	2.3	−9.8	–	5.15	−2.80
New Redbacks							
Ter5A	0.076	0.08	2.02	−8.7	−6.17	$\gtrsim 25$	−0.25
Ter5P	0.363	0.38	73.7	−6.4	−4.85	$\gtrsim\gtrsim 25$	1.74
Ter5ad	1.09	0.14	89.4	−6.3	−3.44	$\gtrsim\gtrsim 25$	2.09
M28H	0.435	0.20	52.9	−6.3	−4.57	$\gtrsim\gtrsim 25$	2.12
M28I	0.459	0.17	72.8	−7.0	−4.13	$\gtrsim\gtrsim 25$	1.33
NGC6440D	0.286	0.14	22.9	−7.2	−4.92	$\gtrsim 25$	1.43

Note. — Observed properties of the orbital phase wander in known spider pulsars. All properties were calculated for an exact pulsar mass of 1.55 $M_\odot$ and companion radius that scales according to $R \propto M^{0.8}$.
$^\diamond$: Calculated for the median observed change in T_0 including errorbars.
[1] - Original timing analysis carried out by Applegate & Shaham (1994)
[2] -Original timing analysis carried out by Lazaridis et al. (2011)
[3] -Original timing analysis carried out by Freire et al. (2003)
[4] -Original timing analysis carried out by Archibald et al. (2013)
[5] -Original timing analysis carried out by Pletsch & Clark (2015)

Chapter 4

Pulsar Eclipses

4.1 Abstract

Despite the increased number of pulsars with non-degenerate companion stars being discovered recently, the mechanism causing eclipses in these systems has gone largely unstudied. Using the long-term timing of four globular cluster redbacks, we have identified average eclipse properties for three systems and provide estimates regarding the fourth system (J1748-2446ad). We fit a light curve to each eclipse, finding a distribution of ingress and egress phases. We then calculate a power-law for ingress and egress as a function of the observing frequency across L-band and S-band combined. This allowed us to study the eclipse properties of systems with orbital periods much longer than a typical observing track. Using this method, we find evidence for slight asymmetries in the Ter5P and M28H systems, implying a potential tail of plasma coming off of the companion star. We also find electron column densities of $N_e \sim 10^{17}-10^{18}$ cm^{-2} for all four systems at the predicted ingress and egress phases. Using these column densities, we were able to rule out eclipsing by a few possible mechanisms, finding that stimulated Raman scattering explains our data best. We conclude with a discussion of how these measurements can help us understand the mass loss rate from the companion star, which could be used to determine the upper-limit on the mass-transfer rate in future pulsars shown to be transitioning from being a low-mass X-ray binary to a MSP.

4.2 Introduction

Despite black widows and redbacks both falling under the classification of "eclipsing pulsars", the observed fraction which show radio eclipsing is quite different between the two populations. To date, of the 62 known eclipsing pulsars, 41 are black widows

and 21 are redbacks. Of the black widows only 15 show eclipses (∼35%), whereas 20 out of the 21 redbacks (∼95%) experience significant eclipsing

Differences in the phenomenology of these two pulsar populations has led to a debate whether they are simply different evolutionary stages of a MSP or are formed from different intial populations of binaries (Chen et al. 2013; Benvenuto et al. 2014). Regardless of their exact evolutionary history, the current mass of the companion star appears to play a significant role in determining what sort of phenomenology is present when observing and timing eclipsing pulsars.

In the context of eclipses, the lower surface gravity of high-mass non-degenerate stars means more material will be allowed to flow off the star and fill the orbit. While this might explain the relative abundance of plasma in redback systems as compared to black widows, we still lack a description for how this gas leads to the loss of pulsar flux. Depending on the exact temperature and density of the plasma, there can exist multiple physical mechanisms responsible for eclipsing a pulsar.

4.2.1 Eclipse Physics

Despite the recent discovery of new BWs and RBs, the exact nature of the plasma processes that give rise to radio eclipsing are not well understood. Early work to study this effect for eclipsing pulsars such as B1957+20 (Fruchter et al. 1988; Phinney et al. 1988), Ter5A (Lyne et al. 1990; Thompson et al. 1994), and J2051-0827 (Stappers et al. 2001) could not provide a unified theory for the process.

An example showing the most likely geometry of a radio eclipse is shown in Figure 4.1. The more massive pulsar lies close to the center of mass, whereas the lighter companion star must complete a much larger orbit. In this example we consider a plasma flowing off of the companion star in the form of a wind, which gets increas-

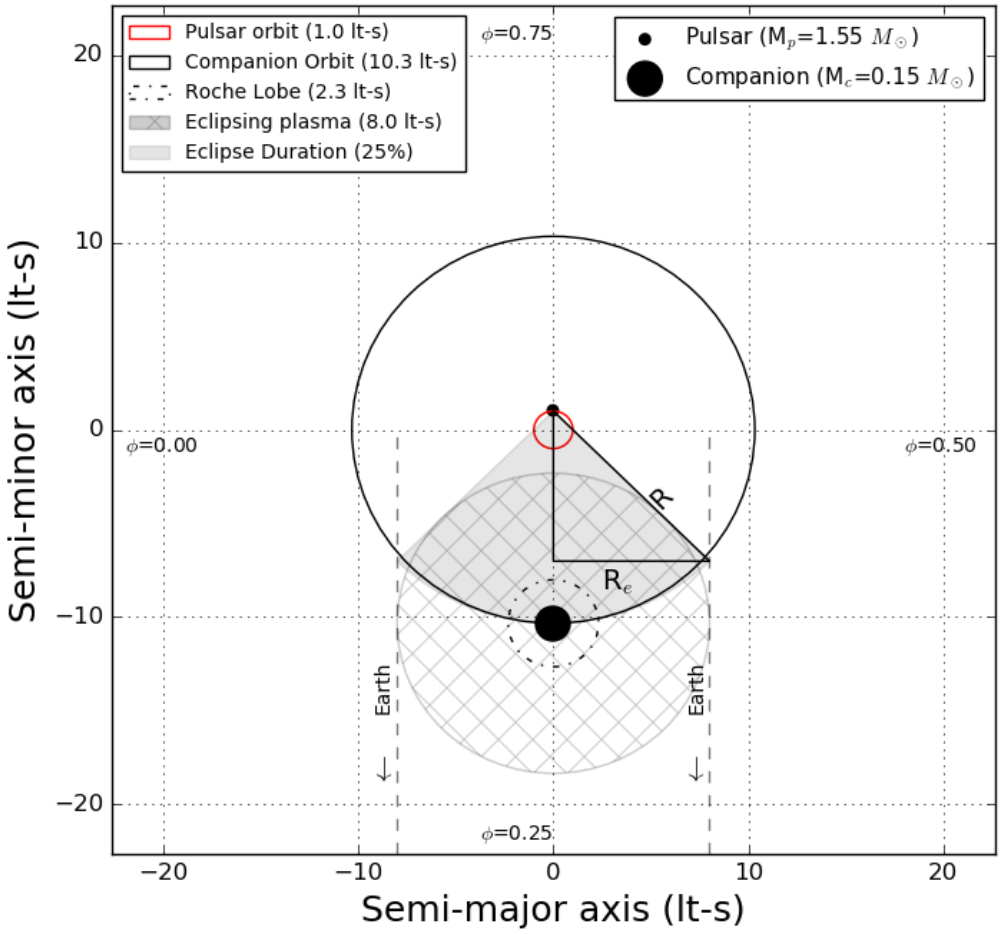

Fig. 4.1.— Example geometry of radio eclipses in redbacks and black widows. The pulsar and the companion star orbit a shared center of mass at the origin with a separation R. As the companion star orbits the pulsar it releases a plasma. When the companion star is in a phase of its orbit where the bulk of the plasma passes along our line of sight to the pulsar, there is a critical column density through which we can no longer see pulsed emission. The apparent size of this eclipse region is denoted with the variable R_e and may extend well past the Roche lobe of the companion star.

ingly rarefied the further it moves from the surface of the star. This gas likely fills much of the orbit for the whole system, however it is only as the companion star approaches superior conjunction (orbital phase ϕ=0.25) that the integrated column density becomes large enough that the signal from the pulsar is completely removed. Once the companion star begins to orbit closer to inferior conjunction (ϕ=0.75) radio pulsations become visible once more.

This example quickly becomes complicated when attempting to incorporate data from observed eclipses of some BWs and RBs. In Figure 4.1, we showed a spherically symmetric plasma surrounding the companion star. Some pulsars have shown evidence for asymmetries in the eclipse, with ingress and egress occurring closer or further away from superior conjunction than expected (Fruchter et al. 1990; Thompson et al. 1994). These asymmetries can change between consecutive orbits of the system and imply a non-uniform distribution of material in the system. Typically these asymmetries appear as a slight lengthening of the time it takes to go from superior conjunction to egress, implying that gas trails the companion through its orbit.

Another feature that has been noted are "micro-eclipses", which are defined to be loses of pulsar flux over short timescales of typically a few minutes. These micro-eclipses can occur at arbitrary orbital phases and can appear and disappear from one orbit to the next. This implies non-uniformity in the surrounding plasma — such as pockets of greater density or temperature than the surroundings — that can change on very short timescales.

These changes in the density and temperature of the plasma teach us a great deal about the properties of the companion star and the intra-binary medium. By studying this effect at different frequencies and different sight lines through the orbit,

we can begin to understand more about the conditions that lead to the formation of MSPs and the plasma physics that takes place in these systems.

4.2.2 Structure of this chapter

As this work requires high signal to noise observations of each pulsar at each observing epoch, we begin with the data and timing models produced in Chapter 3. We then proceed to discuss the additional data reduction required to obtain a measurement of the pulsar flux as a function of the orbital phase in Section 4.3.

In Section 4.4 we introduce the eclipse mechanisms that will be tested for each of our pulsars. We include a brief description of how each mechanism is believed to remove pulsar flux from our data, as well as introduce the criteria we will use to determine when a given model is capable of producing an eclipse. Much of this section will be taken from the results of Thompson et al. (1994), which goes into more detail about the plasma physics that might be present in a BW or RB system.

We then introduce the process of obtaining an average eclipse duration for each RB as a function of the observing frequency in Section 4.5. In order to do so, we discuss how a MCMC sampler was used to try and obtain an average power-law function for ingress and egress separately, producing a difference of power-laws for the full eclipse duration. We then move on to the special case of Ter5ad, which is too faint to measure ingress and egress properties using our MCMC analysis in Section 4.5.2. For this pulsar we obtain a rough estimate of the eclipse duration by applying a non-linear least squares fit to the few data points available in order to provide approximate eclipse properties.

In Section 4.6 we calculated an approximate measure of the free electron column density through the plasma using the dispersive delays in the pulsar signal during

ingress and egress. Also calculated is the electron number density in this region assuming a radial wind profile of $n_e \propto r^{-2}$. We then tested the likelihood of pulsar eclipses due to refraction, free-free absorption, induced compton scattering, stimulated raman scattering, or pulsar smearing using the measured column densities in Section 4.7.

Section 4.8 investigates how these models might change for different observing frequencies and how our measured column densities might vary from the true value when taking into account the unknown plasma temperature. Finally, we end by introducing possible applications of timing eclipses to understanding more about the mass loss from the companion star to establish an upper limit on the mass transfer rate in close pulsar binaries.

4.3 Data

In this section, we discuss how raw data is converted into measurements of the pulsar flux as a function of the orbital phase. We also fit a light curve to these data points in this section, as the reference phase associated with ingress and egress for these data will be used to calculate the average eclipse properties later in this chapter.

4.3.1 Sources

For this work, we analyzed eclipses for the GC RBs J1748−2446A (Ter5A), J1748−2446P (Ter5P), J1748−2446ad (Ter5ad), and J1824−2452H (M28H). More information about the specific properties of each of these systems can be found in Chapter 3, where we studied the orbital phase wander in each source. For each of these sources, we were able to observe the pulsar going into and out of eclipse at least a handful of times, allowing us to measure average eclipse properties for each system. An example of

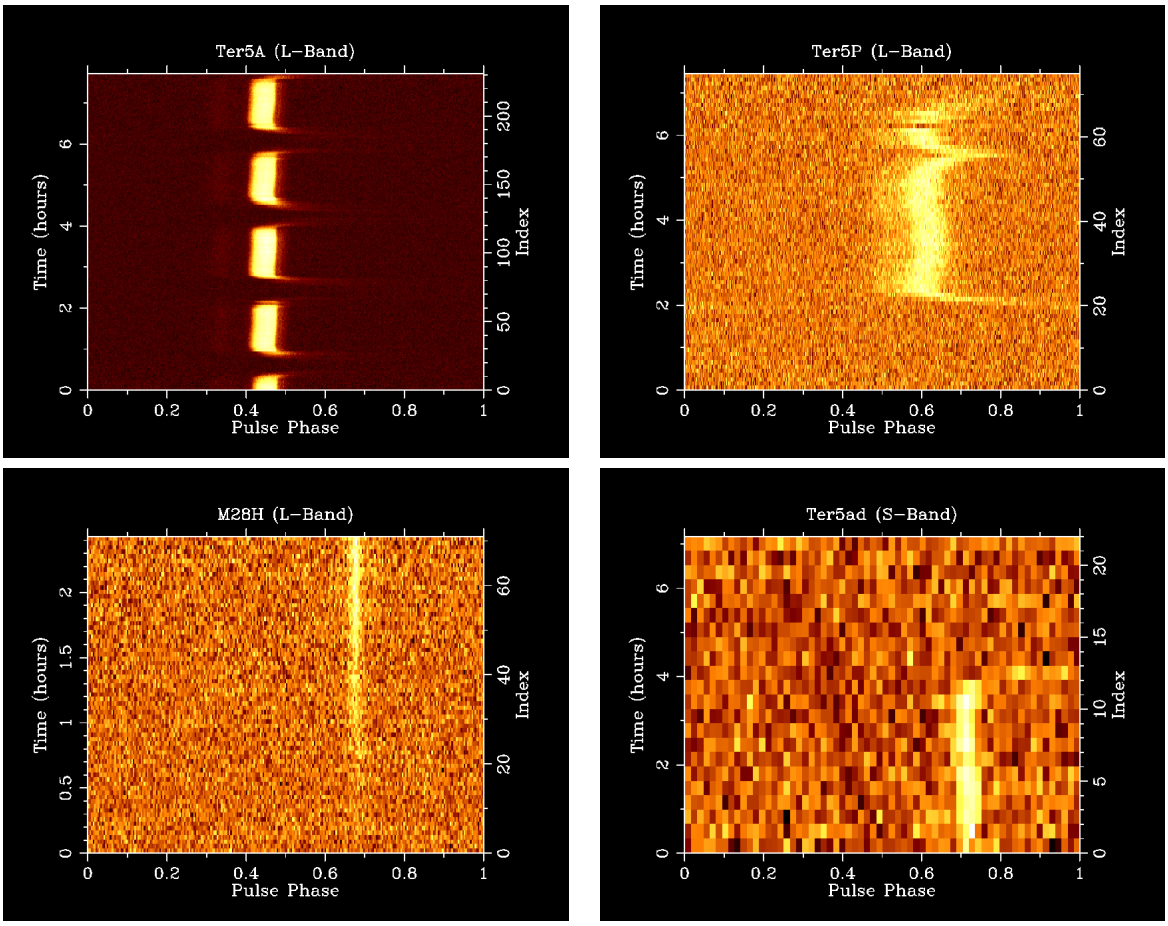

Fig. 4.2.— Example eclipses for the four RBs in our sample. Data for Ter5A, Ter5P, and M28H were taken at L-band and show either ingress, egress, or both. Given the small flux density of Ter5ad, we show the brightest day available for this pulsar with a visible eclipse transition, which happens to be at S-band. We see evidence for smearing in the pulsar signal due to extra plasma in the pulsars Ter5A, Ter5P and Ter5ad. In M28H we see a very long egress, implying that there is trailing plasma that extends out laterally and results in the pulsar signal passing through more plasma during egress than ingress. Ter5P also undergoes a micro-eclipse shortly before going into a full eclipse.

these eclipses is shown in Figure 4.2. We can see evidence for dispersive smearing in the signal due to extra plasma in the pulsars Ter5A, Ter5P and Ter5ad. In M28H we see a very long egress, implying that there is trailing plasma that extends out laterally and results in the pulsar signal passing through more plasma during egress than ingress.

We do not measure eclipse properties for the other two RBs discussed in Chapter 3, J1824−2452I (M28I) and J1748−2021D (NGC6440D). M28I poses a significant challenge when trying to study eclipses. This source is inherently quite weak, which makes measurements of the light-curve going into and out of eclipse quite difficult. Radio emission is also quenched for long periods of time during our timing baseline due to the system being in an active LMXB state. We therefore do not have enough data to provide any useful limits on the eclipse properties for this system.

As for NGC6440D, this system has a much larger flux density than M28I, however the system geometry is not ideal for observing eclipses. This system undergoes eclipsing irregularly and when present it only lasts for approximately 10% of its orbit when observed at L-band (Freire et al. 2008). This suggests that the orbit is not edge-on and as such we do not obtain many observations of this pulsar in eclipse. Additionally, in the case that we do observe an eclipse, the pulsar flux is often still observable during superior conjunction, albeit at a much diminished flux density. Our fitting routines do not fit eclipses such as these well and therefore we do not make attempts to study this system.

4.3.2 Data Reduction

In order to obtain average eclipse properties for the four RBs for which we have good eclipse data (Ter5A, Ter5P, Ter5ad, and M28H), we begin with raw data for each

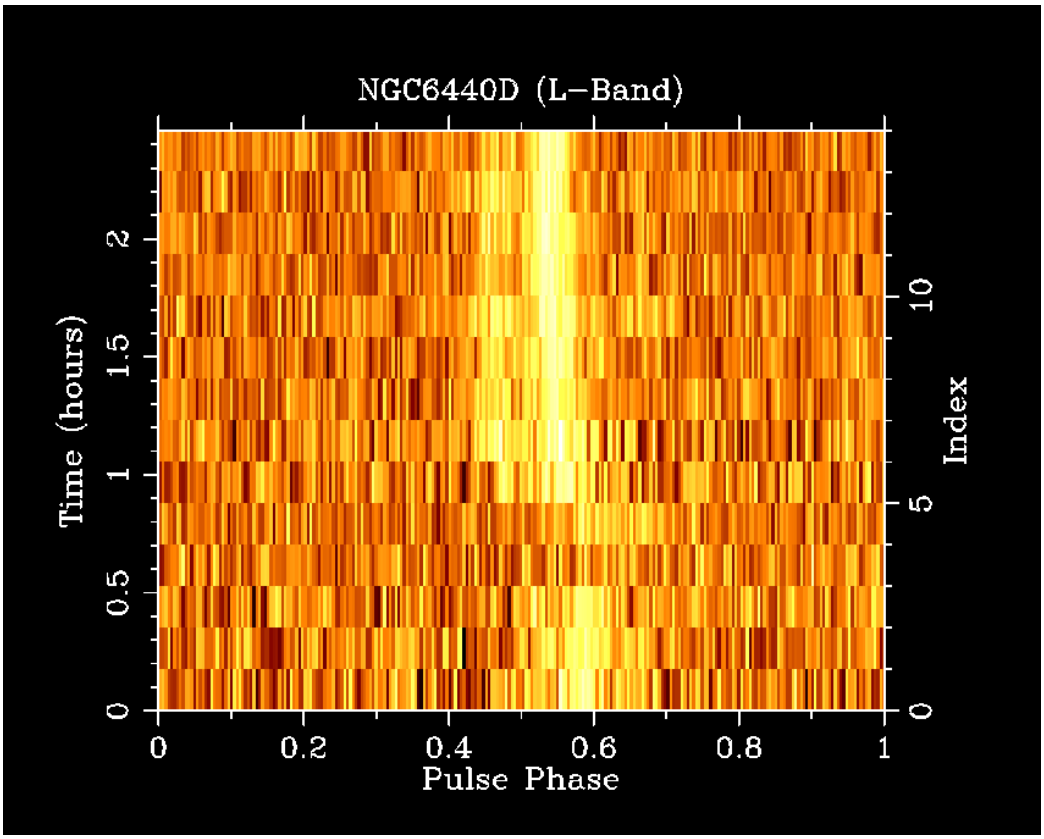

Fig. 4.3.— Example eclipse for NGC6440D at L-band. While this pulsar has a much larger flux density than redbacks like M28I, the system geometry is not ideal for observing eclipses. This system undergoes eclipsing irregularly and the eclipses are much shorter than most other redbacks when observed at L-band (∼10% of its orbit). This suggests that the orbit is not edge-on and as such we do not obtain many observations of this pulsar in eclipse. Of the approximately ten years of data, this figure shows one of the very few eclipses visible for this system, and significant flux is still visible in the few sub-integrations measured mid eclipse.

source from Chapter 3. We fold the raw data in each frequency channel and each sub-integration using the program PSRFITS (Hotan et al. 2004) according to the timing models for each observation of each pulsar as produced in Chapter 3 as well.

During this step, the signal of the pulsar is frequency averaged over 4 to 8 consecutive channels and time averaged such that we obtain measurements every 1-5 minutes depending on the intrinsic brightness of the pulsar. After this step we are left with a fits file that contains the total intensity of the pulsar in each frequency channel and sub-integration with the proper timing model encoded within. An example of the resulting data can be seen in Figure 4.2 where we have plotted the frequency summed data as a function of time and rotational phase of the pulsar.

For data taken with the GUPPI backend, we then flux calibrated the data using the "Pulsar Archive Calibration" (`pac`) program (Hotan et al. 2004) referenced to a quasar for each observation. We elected to use the interactive program `psrzap` to manually remove frequency channels or sub-integrations with obvious radio frequency interference (i.e. only those single channels and sub-integrations with a signal many standard deviations above the background). Data obtained using the SPIGOT backend were not flux calibrated for this study, though the relative flux densities between the eclipsed and not eclipsed regions were still utilized for fitting of the light curve.

4.3.3 Light curve fits

Due to the differences in the intrinsic brightness, the number of data points going through a single orbit for each of our pulsars can vary. We attempted to obtain as many frequency channels and sub-integrations as possible while still having a signal to noise of S/N$\gtrsim$7 for the pulsar signal. Table 4.1 shows the typical properties of our data used for producing light curves for each pulsar in our sample for the SPIGOT

Table 4.1. Average light curve properties

Pulsar	Backend	$\sim N_{orb}$	N_{obs}	N_{chan}	$\sim N_{subint}$
Ter5A	SPIGOT	4.00	22	8	60
	GUPPI	4.00	18	16	225
Ter5P	SPIGOT	0.80	34	4	15
	GUPPI	0.80	23	4	20
Ter5ad	SPIGOT	0.25	3	3	10
	GUPPI	0.25	1	4	10
M28H	SPIGOT	0.30	12	3	10
	GUPPI	0.30	10	4	20

Note. — Average light curve properties for the four redbacks in this study for the different pulsar back-ends on the GBT. N_{orb} is the approximate number of eclipses seen in a single observation of the cluster. N_{chan} is the average number of frequency channels used to fit the eclipse ingress or egress. N_{subint} is the average number of data points that sample the orbit in a single observation.

and GUPPI back-ends separately. N_{orb} is the approximate number of eclipses seen in a single observation of the cluster. N_{chan} is the average number of frequency channels used to fit the eclipse ingress or egress. N_{subint} is the average number of data points that sample the orbit in a single observation.

In the case of Ter5A, on average 3 to 4 eclipses were visible in each 7 hour observing track. Due to its large intrinsic brightness, we were able to obtain fits of the light curve using only minimal averaging over the observed frequency channels and sub-integrations for the approximately 150 available eclipses.

Comparatively, Ter5P and M28H are both much fainter pulsars and have much longer orbital periods. We therefore required greater frequency and time averaging to obtain sufficient signal to measure the eclipse properties, all of which resulted in approximately 60 and 20 eclipses to work with for each pulsar respectively.

Ter5ad however, has significantly less intrinsic brightness than the other three RBs studied in this work. Due to the brightness of this pulsar and the fact that the orbital period is 1.1 days long, we were only able to obtain a handful of measurements that were simultaneously detected in the data (as it experiences month long periods where it is not present in the data), bright enough, had a visible ingress or egress in the observation, and could be sampled with enough time resolution to see the pulsar flux transitioning between being eclipsed or being visible.

For each pulsar we converted the MJD of each sub-integration into an orbital phase measurement using the average orbital period of the system, and the best measurement of T_0 for the given observation. We aimed to obtain measurements of flux at approximately every 1-5% of the total orbital phase for each pulsar.

We apply a non-linear least squares fit to the observed ingress and egress portions of the light curve separately. We have chosen not to fit for the entire eclipse, as in

most cases, the orbital period of a RB is much longer than a single observing track. (As a note, we do not fit for any micro-eclipses using this method, as we are only interested in the average properties of regular eclipses for each system.)

We define the light curve function for ingress and egress as follows:

$$f(\phi) = \begin{cases} \dfrac{A}{\exp\left[1 + (\phi - \phi_{\rm I})/w_{\rm I}\right]} + B, & \text{Ingress} \\ \dfrac{A}{\exp\left[1 - (\phi - \phi_{\rm E})/w_{\rm E}\right]} + B, & \text{Egress} \end{cases} \tag{4.1}$$

where A is the flux density of the pulsar, B is the background flux level of the observation, and w is the half-width of the eclipse (i.e. the time it takes to reach the half flux density level of the pulsar going into or out of eclipse). $\phi_{\rm I}$ and $\phi_{\rm E}$ are the reference phases we will use to discuss ingress and egress in this work and correspond to the half flux level of ingress and egress.

Due to irregularities in the eclipsing material, the likelihood that a light curve can be fit to the data can change from one orbit to the next. Figures 4.4 and 4.5 show two different observations for the pulsar Ter5A. Figure 4.4 shows four consecutive eclipses where the pulsar does not show any significant micro-eclipsing and the flux is relatively constant through each of its orbits when near inferior conjunction. Figure 4.5, however, shows both micro-eclipsing (ϕ ~0.8) and the complete loss of signal from the pulsar near the third inferior conjunction measurement that continues for the rest of the observation.

This implies that, at least in the case of Ter5A, the gas properties of the system can change rapidly. In order to analyze the global properties of each system, we therefore do not assume that $\phi_{\rm I}$ and $\phi_{\rm E}$ remain constant from one eclipse to the next. In Section 4.5.1 we will examine the results of our MCMC models to see if there is an underlying distribution to the reference ingress and egress values.

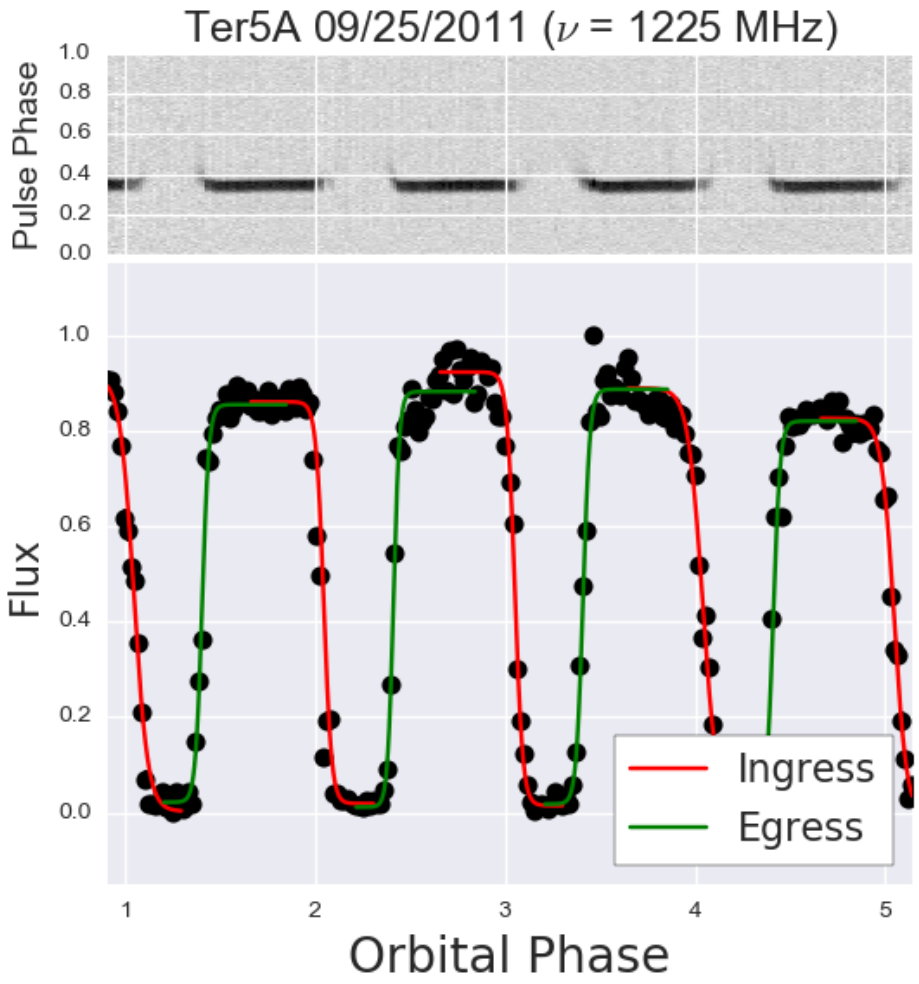

Fig. 4.4.— **Bottom Plot**: Relative light curve for Ter5A using the GUPPI back-end at L-band. We see well behaved eclipses centered on superior conjunction and strong pulsar flux throughout the orbit near inferior conjunction. **Top Plot**: The integrated flux of Ter5A as a function of the orbital phase and the pulsar's rotational phase. We can see the dispersive pulse smearing within a handful of sub-integrations before and after superior conjunction.

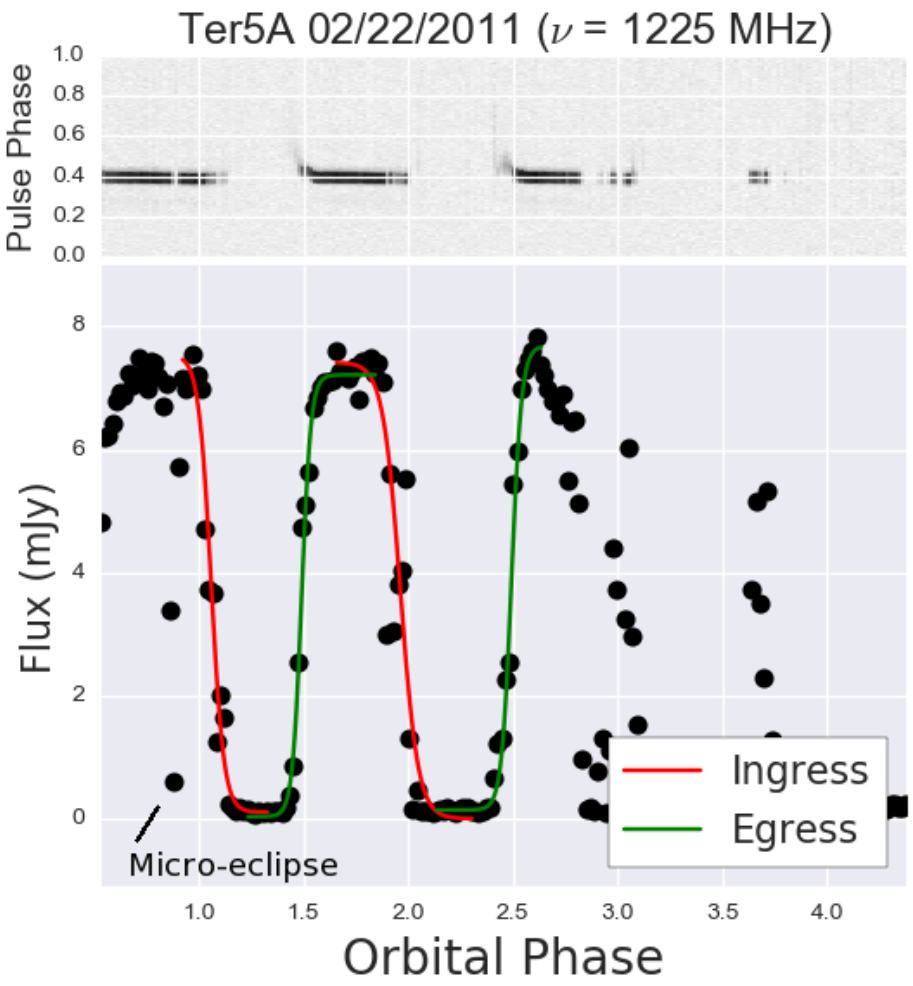

Fig. 4.5.— **Bottom Plot**: Relative light curve for Ter5A using the GUPPI back-end at L-band. We see well behaved eclipses centered on superior conjunction and strong pulsar flux throughout the beginning of the observation, whereas near the end the pulsar becomes eclipsed in a phase range where the pulsar is expected to be in front of the companion star. This implies a rapid restructuring of the gas in the orbit. We also see a micro-eclipse at an orbital phase of $\phi \sim 0.8$. **Top Plot**: The integrated flux of Ter5A as a function of the orbital phase and the pulsar's rotational phase. We can see the pulsar is eclipsed through most of its inferior conjunction in the second half of the observation, though occassionally the pulsar flux does appear for a few minutes at a time.

While the exact phase of ingress or egress may not remain constant at a given frequency across multiple orbits, we argue that it is likely safe to assume that the evolution of $\phi_{\rm I}$ and $\phi_{\rm E}$ as a function of frequency does remain constant from one orbit to the next. We argue that if there is a single dominant eclipse mechanism present in our data, the frequency dependence should not change between eclipses.

With the exception of occasional RFI in any given observation, we are typically able to fit ingress or egress across the entire bandwidth of the observation. This allows us to fully sample the frequency dependence of eclipse duration using all of the observed eclipses. It should be noted that at the highest frequency channels — where the optical depth is small enough and Δt_e become very short — we are unable to fit Equation 4.1 reliably. An example of such an observation is given in Figure 4.6. At superior conjunction, some pulsar flux is still visible.

Due to the variability of eclipses, we have elected to test our models using a MCMC sampler to fit for the eclipse properties in order to find a global power-law index while simultaneously fitting for different phases of ingress and egress. In Section 4.5 we discuss how the probability functions were defined and how the MCMC modeling was designed before applying the results to different eclipse mechanisms.

4.4 Eclipse Mechanisms

In this section we categorize and discuss different theories proposed by Thompson et al. (1994), all of which might explain how emission from the pulsar can be removed by interacting with the intra-binary plasma. We also introduce the criteria we will use to determine the likelihood of each eclipse mechanism in our sources.

We consider only the case that a single eclipse mechanism is responsible for removing most of the pulsar flux, though we discuss this assumption further in Section

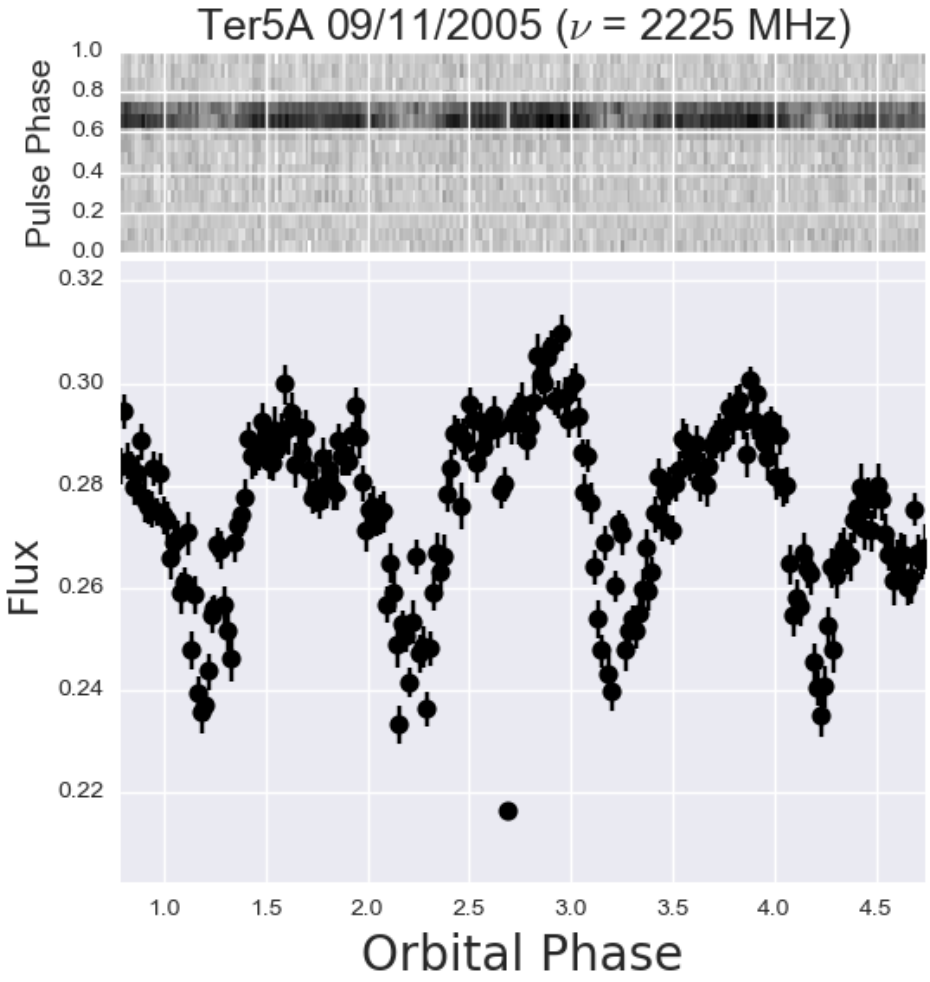

Fig. 4.6.— **Bottom Plot**: Relative light curve for Ter5A using the SPIGOT back-end at S-band. We see that at these higher frequencies the pulsar does not show well-behaved eclipsing. While some pulsar flux is lost near superior conjunction, the light-curve for data at this frequency is often unreliable. **Top Plot**: The integrated flux of Ter5A as a function of the orbital phase and the pulsar's rotational phase. We can see the pulsar flux is visible throughout the eclipse.

4.7 when we calculate the likelihood of a given eclipse mechanism using the average eclipse properties.

Refractive Eclipses

Following the discovery of B1957+20, one of the first proposed explanations for the loss of pulsar flux near superior conjunction was refraction (Fruchter et al. 1988; Phinney et al. 1988; Emmering & London 1990).

Assuming a sufficiently dense and charged plasma centered on the companion star, the refractive index in the region can grow large enough that at some critical eclipse radius the pulsar emission will form a caustic. As a result, the pulsar flux is deflected away from our line of sight, producing an eclipse until the viewing geometry no longer requires the pulsar flux to pass through this critically dense region. An example of this effect is shown in Figure 4.7 (which is borrowed from Thompson et al. (1994)).

In addition to the deflection of the pulsar ray bundle, having a caustic in the radio emissions predicts that there should be significant magnification shortly before and after eclipse. The exact magnitude of this effect and its duration depend on the density distribution about the companion star.

Assuming that refractive eclipses are possible when the plasma frequency approaches the observing frequency we define the criterion for deflection of the radio signal using Equation 4 from Thompson et al. (1994):

$$\left(\frac{\nu_{\rm p}}{\nu_{\rm obs}}\right)^2 = \frac{4\pi e^2}{m_e}\frac{n_e(b)}{\nu_{\rm obs}^2}\,, \tag{4.2}$$

where $\nu_{\rm p}$ is the plasma frequency, $\nu_{\rm obs}$ is the observing frequency, and $n_e(r)$ is the free electron number density at the impact parameter b of the caustic from the companion star.

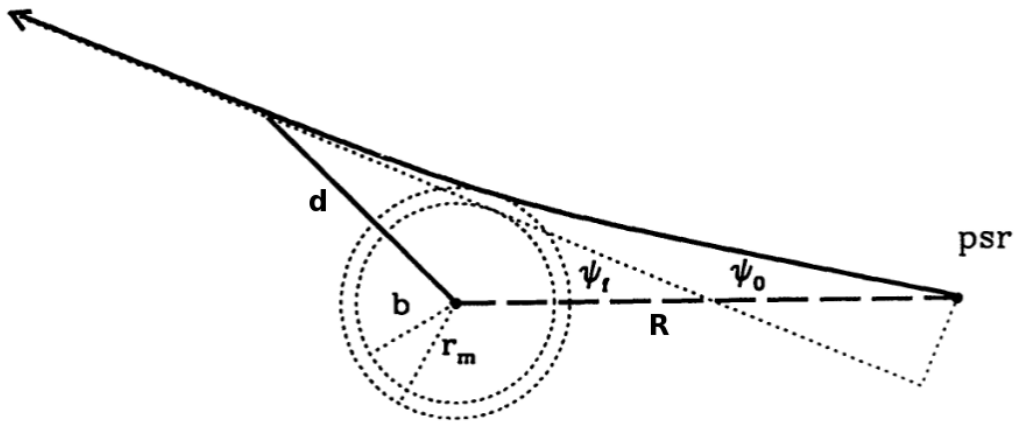

Fig. 4.7.— An example of refractive eclipsing as the pulsar flux passes nearby to its companion star taken from Thompson et al. (1994) with labels modified to reflect this work. Thompson et al. (1994) describes this diagram as follows "Refraction of the pulsar radio beam by a plasma cloud centered on the companion star. Here "psr" labels the position of the pulsar and R is the binary separation. When the plasma density decreases with distance d from the center of the companion, the beam is deflected outward. b is the impact parameter, r_m is the minimum separation between the beam trajectory and the companion, and Ψ_0 (Ψ_f) is the angle between the initial (final) beam direction and the line of centers."

Free-free Absorption

If the material surrounding the companion star is instead highly clumped and relatively cool ($\lesssim 10^3 - 10^4$ K), then free-free absorption might also play an important part in eclipsing the pulsar emission. In this scenario, the pulsar ray must again pass through a region of sufficient column density that the free electrons in the plasma nearby to the companion star can absorb the energy carried by the radio photons..

While the conditions for this model are strict — obtaining a cool and highly clumped plasma near a pulsar — it is not entirely impossible that for a given density distribution of gas the conditions for this mechanism can be met.

For an electron clumping ratio of $f_{cl} \equiv < n_e^2 > / < n_e >^2$, and adopting typical temperatures and observing frequencies relevant to pulsar binaries, Equation 11 from Thompson et al. (1994) defines the optical depth for free-free absorption to be:

$$\tau_{\rm ff} \simeq 3.1 \times 10^{-8} \frac{f_{cl}}{T_7^{3/2} \nu_9^2} N_{e,17}^2 L_{11}^{-1} \ln \left(1.6 \times 10^9 \frac{T_7^{3/2}}{\nu_9} \right) . \tag{4.3}$$

where T_7 is the plasma temperature in units of 10^7 K, ν_9 is the observing frequency in GHz, $N_{e,17}$ is the electron column density in units of 10^{17} cm^{-2}, and L_{11} is the length over which this absorption takes place in units of 10^{11} cm.

Induced Compton Scattering

We also consider the possibility that pulsar eclipses can be caused by induced Compton scattering. When incoming radiation interacts with the plasma, it is possible that the photon will be scattered into a different viewing angle with a new frequency. As the binary system goes through its orbit, the optical depth increases as the pulsar flux passes through an increasingly dense column of free electrons until the plasma

becomes sufficiently dense enough that Compton scattering will occur at some critical orbital phase. The presence of the pulsar flux helps to drive photons into a higher occupation number, which strengthens the process sufficiently to alter the radio flux sufficiently that it is not longer detectable.

The conditions for this model therefore depend heavily on the electron column density that the pulsar flux must pass through and the radio flux from the pulsar at the eclipsing radius. We define the optical depth for this model using Equation 26 from Thompson et al. (1994):

$$\tau_{\rm comp} \simeq 4 \times 10^{-5} \left(\frac{N_{e,17} S_\nu^0}{\nu_9^2} \right) |\alpha + 1| \left(\frac{d_{\rm kpc}}{a_{11}} \right)^2 M \,, \tag{4.4}$$

where S_ν^0 is the pulsar flux density at ν_9 at the Earth-pulsar distance $d_{\rm kpc}$, α is the spectral index of the pulsar, a_{11} is the binary separation in units of 10^{11} cm, and M is the demagnification factor.

The demagnification associated with this process is given approximately by $M \sim (R_{\rm curve}/2r_{\rm curve})^2$, where $R_{\rm curve}$ is the radius of curvature for the plasma cloud scattering the pulsar emission and $r_{\rm curve}$ is the distance from the center of curvature. This factor represents the incident angle at which radiation is striking the plasma and scattering the emission out of our line of sight depending on how close the pulsar lies to the center of the plasma cloud.

To first order, for the geometry shown in Figure 4.1, this factor is given by $M \sim R_e/2R$. While we cannot solve for the exact value of M, as we do not know the extent and distribution of the plasma in the system, we can test this model against different demagnification factors in order to see if their exists some set of parameters that make this model viable.

SRS Parametric Instability

Another possibility is stimulated Raman scattering (SRS) via parametric instability. In this model, the radio flux interacts with already existing density perturbations in the plasma. This incident flux will create a new mode within the plasma at the beat frequency between the incoming radiation wave and the plasma density waves. The original and new fluctuations in the plasma must then combine such that the density fluctuations in the plasma can grow. The associated plasmons in this density fluctuation will then be able to elastically scatter the incoming radio emission out of our line of sight.

In a similar manner to the induced Compton scattering case, this model can be investigated by looking for a set of ideal conditions such that the integrated column density and pulsar flux at the eclipse radius can produce large enough fluctuations in the plasma to scatter radio frequencies.

The condition for SRS is found by comparing the pulsar's flux at the eclipse radius to that of the critical flux density needed to stimulate the plasma. Assuming side-scattered radiation ($\Theta = \pi/2$) the critical flux needed to induce for Raman scattering is given by Equation 32 from Thompson et al. (1994):

$$S_\Gamma = 1.39 \times 10^{-5} n_e^{1/2} T_7^{-3/2} \nu_9 \,\mathrm{ergs\,cm^{-2}\,s^{-1}\,Hz^{-1}}\,, \tag{4.5}$$

where n_e is the number density of the free electrons at the eclipse radius.

Dispersive Pulse Smearing

As discussed in Sections 1.5.2 and 1.5.3, the presence of free electrons between the observer and the pulsar can produce an arrival time delay for a pulse as a function

of the observing frequency. If the dispersion of the pulsar changes significantly over the course of the orbit such that the time delay Δt (Equation 1.7) is greater than the rotational period of the pulsar, the signal can be lost. This increased dispersion can be a result of both a smoothly varying distribution of gas surrounding the star as well as a turbulent plasma.

As a result, this explanation implies that the pulsar signal is not lost through the eclipse. Proper dedispersion of the data should therefore once more show the pulsar's flux density, albeit at a larger DM, near superior conjunction. Assuming a cold plasma (i.e. non-relativistic), such that the dispersion relationship (Equation 1.7) is still valid, we can search for signal at a new DM near eclipse to test this theory. In Section 4.8 we discuss the validity of assuming a non-relativistic plasma further.

Physical Mechanisms Summary

For the purposes of this work, we do not derive the relevant equations for each eclipsing mechanism, nor do we try to cover all the various possibilities. These models represent the results of large bodies of work into radiative transfer and plasma physics. For a more detailed review of these models, we encourage the reader to consult Thompson et al. (1994), which derives the conditions needed for the above mentioned eclipse mechanisms and provides additional references to the pertinent physics.

4.5 Eclipse Durations

In order to probe the distribution of plasma surrounding each pulsar, we need to relate the individual measurements of ingress and egress to an average eclipse duration as a function of frequency. We adopt a slightly different model as compared to Nice & Thorsett (1992) and Thompson et al. (1994), which define the eclipse duration ($\Delta\phi$)

of B1957+20 and Ter5A as a single powerlaw in the observing frequency. We instead choose to model $\Delta\phi$ as a difference of power-laws of the form:

$$\Delta\phi = A_I \nu^{\beta_I} - A_E \nu^{\beta_E} \,, \tag{4.6}$$

where ν is the observing frequency and A and β are the scale parameter and spectral index of a power-law fit to the ingress and egress of the eclipse separately. As a note, we order this function as ingress minus egress to account for the fact that an additional phase wrap has been added into the ingress data to avoid discontinuities in the data.

Using Equation 4.6 provides a few advantages over trying to solve for the total eclipse duration directly. The most important reason for using a sum of two power-laws is that it allows us to find a functional form for the eclipse duration even if we cannot observe a full orbit or eclipse. We also argue that using a single power-law dependence on the eclipse duration does not properly account for possible asymmetries in the eclipse. Additionally, should the plasma surrounding the companion star not be spherically symmetric, there is no reason to expect that the a single power-law can define both ingress and egress.

Another important benefit to fitting for the eclipse duration using ingress and egress separately is that it helps mitigate the effects that irregular eclipsing can have on obtaining enough data for this work. Micro-eclipsing and unexpected drop outs of the pulsar flux at just ingress or egress can be ignored by just fitting for the other half of the eclipse that behaves normally. As shown in Figure 4.5, the plasma properties causing eclipse can change over the course of a single orbit, and fitting for ingress and egress separately allow us to recover some data from these observations.

For pulsars Ter5A, Ter5P, and M28H, we used the MCMC sampling package `emcee`

(Foreman-Mackey et al. 2013) to find a posterior distribution on A and β for both ingress and egress.

4.5.1 MCMC Sampling

For our modeling of the eclipse duration, we have elected to assign each individual measurement of ingress and egress its own value of $A_{\rm I}$ or $A_{\rm E}$. This is done in order to account for the possible irregularities in the column density along our line of sight that may be causing unique measurements of $\phi_{\rm I}$ or $\phi_{\rm E}$ between different eclipses. In Section 4.5.1 we discuss the combined posterior from all of our measurements.

The total probability of measuring a given phase ϕ_* is given by:

$$p(A_*, \beta|\phi_*) \propto p(\phi_*|A_*, \beta)p(A_*, \beta)\,, \tag{4.7}$$

where $p(\phi_*|A_*, \beta)$ is our likelihood function and $p(A_*, \beta)$ is our prior.

To begin, we discuss the likelihoods associated with this model and discuss the priors and initial conditions of our simulation before discussing our results in Section 4.5.1.

Likelihood Function

While the likelihood of measuring some eclipse phase with respect to a model is not already known, we can use the large number of observed eclipses for Ter5A to estimate the most likely form that the PDF of measured phases will take. From Figure 4.8 we found that the distributions appear to be approximately normally distributed at L and S-band.

This work therefore makes the assumption that the log likelihood ($\mathcal{L}$) of our mea-

surements is given by:

$$\mathcal{L} \propto \sum_i \frac{1}{2\epsilon_i^2} \left(\phi_i - \hat{\phi}(\nu|A_i, \beta)\right)^2 , \tag{4.8}$$

where i is the summation over each phase measurement, ϵ_i is the measurement error in ϕ_i, and $\hat{\phi}(\nu|A_i, \beta)$ is the predicted phase.

We define the predicted phase $\hat{\phi}(\nu|A_i, \beta)$ as follows:

$$\hat{\phi}(\nu|A_i, \beta) = A_i \left(\frac{\nu}{1600\,\mathrm{MHz}}\right)^{\beta} , \tag{4.9}$$

where A_i is a scaling parameter defined to be the position of ingress or egress at 1600 MHz. We have elected to scale our power-law to 1600 MHz in order to center our power-law near the middle of the combined L-band and S-band data.

Priors

Due to the broken power-law used in this work, we do not have access to previous results for Ter5A to produce a prior based on observed data. For Ter5P and M28H, neither of these pulsars have had their eclipses studied previously. We therefore have chosen to assume a flat prior for each pulsar.

Priors for the reference phase A ranged between $0 \leq A \leq \infty$. The spectral index β ranged between $-2 \leq \beta \leq 2$.

MCMC Posteriors

The eclipse properties for ingress and egress for each of our pulsars are shown in Figures 4.9 and 4.10 respectively. In each figure, we have stacked the posteriors for the powerlaw scale A in order to determine whether the parameter appears to be

drawn from some global distribution. For each of our pulsars, we find evidence that an underlying distribution of possible phase ranges for both ingress and egress exists and is approximately normally distributed. Properties of the normal distribution are given in Figures 4.9 and 4.10 and the implications of these results for our models are summarized in Section 4.8.

We find that the distribution of ingress and egress phases appear to be symmetric about superior conjunction for Ter5A as shown in Figure 4.11. In the case of Ter5P and M28H, there is slight evidence that egress occurs at a greater phase offset from superior conjunction, which could imply some trailing plasma behind the companion star as it goes through its orbit. It should be noted however that given the relatively small flux densities and small number of eclipses for these pulsars, fitting a light-curve to an extended distribution of plasma is difficult as the data points corresponding to the tail of the distribution have a small signal to noise. As such we likely need more data to entirely confirm that there is trailing plasma for both of these pulsars.

If there is trailing plasma behind the companion star in the M28H system however, this would agree with the results of Pallanca et al. (2010). By studying the optical light-curve of the companion star to M28H, Pallanca et al. (2010) found evidence that the star may be significantly tidally distorted and is actively losing large amounts of mass from irradiation from the pulsar. It is possible that the companion star to Ter5P, having been thought to be the result of pair exchange and containing a large plasma resevoir, is also releasing large volumes of plasma into the system.

4.5.2 Ter5ad

Due to the long orbital period and low signal to noise of this pulsar, we were not able to obtain many measurements of the eclipse properties of Ter5ad. In many cases, a

light curve fit to the eclipses was not even possible and the phase of eclipse could only be constrained to within one or two phase bins. We therefore do not attempt to model the eclipse properties using our MCMC sampler. From the results of Section 4.5.1, we make the assumption that in the limit of a large number of measured eclipses, the posterior solution for both A and β are normally distributed. Given this assumption, we derive a single value of A and β using a non-linear least squares fitting routine for the measured values of ingress and egress. The results for these fits are presented along with those of Ter5A, Ter5P, and M28H in Section 4.5.3.

4.5.3 Eclipse Durations

Once we have obtained a power-law fit to ingress and egress, we can define the broken power law that governs the observed eclipse duration for each system. Figure 4.13 shows the eclipse duration for all four redbacks. Ter5A, Ter5P, and M28H were all fit using the MCMC analysis described earlier and represent a more robust fit that allowed us to verify that average eclipse properties exist by examining the posteriors. Ter5ad was calculated under the assumption that there are simple average eclipse properties.

We also confirmed that our model can reproduce the true eclipse duration for our RBs by comparing the model to the available data for Ter5A, which is the only RB with a short enough P_b to measure large numbers of $\phi_{\rm eclipse}$ at different frequencies. Figure 4.12 shows the results to this fit for the L and S-band data. Eclipses where micro-eclipsing or flux drop out was observed near ingress or egress were not included. The black line and shaded region show the model eclipse duration as calculated by ten thousand random samples from the ingress and egress posterior at a thousand different frequencies between 1100 and 2500 MHz. The solid black line shows the

Table 4.2. Average eclipse duration properties

	Ter5A	Ter5P	M28H	Ter5ad[†]
$\nu_{\rm low}$	1100 MHz	1100 MHz	1100 MHz	1750 MHz
$\nu_{\rm high}$	2400 MHz	2400 MHz	2400 MHz	1950 MHz
A_I	1.06±0.07	1.03±0.03	0.99±0.02	0.997
β_I	0.096±0.001	0.013±0.008	0.04±0.06	0.078
A_E	0.42±0.06	0.49±0.03	0.52±0.03	0.526
β_E	−0.27±0.01	−0.09±0.01	−0.58±0.27	−1.153
$\Delta\phi^{\ddagger}_{\rm eclipse}$	0.36±0.10	0.47±0.04	0.54±0.04	–
R_e (10^{11} cm)[‡]	0.6±0.1	2.0±0.1	2.0±0.1	4.0

Note. — Average eclipse duration properties for all four redbacks in the frequency range $\nu_{\rm low} < \nu < \nu_{\rm high}$. The median and standard deviations from the combined posterior distribution are given for Ter5A, Ter5P, and M28H. The approximate eclipse duration properties from the non-linear least-squares fit to the Ter5ad data are also given.
[†]: Measurements of the eclipse properties for this system are only an approximate solution found using a non-linear least squares fit over the provided frequency range.
[‡]: Referenced to 1600 MHz.

median of the resulting distribution and the shaded region shows the 68% confidence interval. The red data points show the measured values of $\Delta\phi_{\rm eclipse}$ from our data. We find that our MCMC sampler is capable of producing models that accurately predict the true eclipse duration as a function of frequency. Table 4.2 provides the results of our power-law fit to the eclipse duration for each pulsar.

Table 4.2 shows the eclipse durations for Ter5A, Ter5P, and M28H at 1600 MHz. The durations for these systems are 0.36±0.10, 0.47±0.04, and 0.54±0.04, respectively. The large errors for Ter5A appear to be due to the strong variability in the eclipse properties for this system. We do not find an eclipse duration for Ter5ad at this observing frequency, though the approximate eclipse duration measured at the nearby frequency of 1800 is ∼0.45.

As shown in Figure 4.11, we find that ingress and egress are nearly symmetric for Ter5A, Ter5P, and M28H. As such, we also assumed this to be the case for Ter5ad for simplicity, though we do not have enough measurements to properly test the underlying distribution of this system. For a symmetric eclipse, the eclipse radius R_e is approximately given by $R_e \sim R\sin(0.5\Delta\phi)$. Table 4.2 gives the measured eclipse radius for each of our sources at 1600 MHz.

4.6 Dispersion

In order to determine the physical mechanism responsible for eclipsing the pulsar signal, we also need to determine how much plasma is filling the system. In this section we will discuss how we used changes in the dispersion measure through ingress and egress to estimate the column density (N_e) of eclipsing material along our line of sight assuming the cold plasma dispersion limit.

4.6.1 Measuring N_e

In order to fit for the column density going into and out of eclipse, we used the pulsar timing package TEMPO to find the new higher DM that produces the smallest difference between our timing model and the arrival time of the pulse. We then subtracted off the DM value associated with long term timing campaigns, as this difference in the DM (ΔDM) should remove the foreground effect of the ISM from our data and leave only the additional time delays due to the pulsar signal propagating through the unbound plasma. As DM measurements are simply column densities that have been scaled to a more appropriate unit for most science cases (pc/cm^3), we simply convert ΔDM into a measurement of N_e by returning the value to cgs units (cm^{-2}).

A further discussion of how our measured values of N_e might be altered due to the eclipse mechanism and the temperature of the gas is given in Section 4.8.

Figures 4.14, 4.15, and 4.16 show the measured values of N_e for each of our RBs. We observe a maximum column density for each pulsar of $N_e \sim 10^{17}-10^{18}$ cm^{-2} shortly before and after eclipse ($\phi \in [\phi_{\rm I} - w_{\rm I}, \phi_{\rm I} + w_{\rm I}]$ and $\phi \in [\phi_{\rm E} - w_{\rm E}, \phi_{\rm E} + w_{\rm E}]$, where w is the half-width of the eclipse as defined in Chapter 4.3.3). For symmetric eclipses, we have enough data to calculate the distribution of possible column densities in each system.

We used a Monte Carlo analysis to find the underlying distribution of N_e values by incorporating the measurement error in N_e into our fits. In order to accomplish this, we assumed Gaussian errors for N_e and randomly drew new values of N_e for each data point from a distribution centered on the measured N_e with a standard deviation given by δN_e. This resampling was performed tens of thousands of times to obtain the distributions shown in Figures 4.14, 4.15, 4.16, and 4.17.

As expected, the median value of N_e shows good agreement between L-band and S-band for Ter5A and Ter5P. These pulsars have enough measurements of the column density during the process of the pulsar going into and out of eclipse at both observing frequencies that we can get at the very least a rough estimate of the column density. M28H, however, shows significant differences between the L-band and S-band. We argue that this is due to the very few measurements of M28H at L-band, and as such we proceed using the S-band measurements only for this pulsar as we believe it to be more reliable.

In the case of Ter5ad, only a few observations with a measurable light curve have data points within the orbital phase window of $\phi \in [\phi_{\rm I} - w_{\rm I}, \phi_{\rm I} + w_{\rm I}]$ or $\phi \in [\phi_{\rm E} - w_{\rm E}, \phi_{\rm E} + w_{\rm E}]$, and those that were only existed for S-band data. We therefore present the results for the column density of this system only as a means of providing a order of magnitude estimate in Figure 4.17.

4.6.2 Measuring n_e

For each system, we can also approximate the number density of free electrons at the position of the pulsar using the measured values of N_e. As we do not know the orbital inclination of the system exactly, we assume the system to be edge on in order to calculate the absorption length scale L_{11}. As our systems undergo long duration eclipses, this is likely a valid assumption and should only introduces a minor error in the exact path length the pulsar signal must pass through the plasma to reach the observer.

If we consider only the case of a wind coming off of the companion star as the source of the eclipsing material, we can characterize $n_e(r)$ (where r is the distance

out from the companion star) as a simple power-law of the form:

$$n_e(r) = n_o r^{\gamma}\,, \tag{4.10}$$

where n_o sets the scale of the power-law distribution and γ is the wind density profile.

For a companion wind that scales as $\gamma = -2$, we integrated out from the companion star to the position of the pulsar to solve for n_o (Equation 4.10) such that we recover the measured values of N_e. In doing so, we can solve for the number density of electrons at different positions in the system. The electron number density at the pulsar distance is approximately $n_e(R)$ $\sim$$10^6$-$10^7$ cm^{-3}. The results for each pulsar at the binary separation R are shown in Table 4.3. (As a note, we may repeat this process for different values of γ to test our models against an unknown wind density profile.)

4.7 Eclipse Models

In this section we use our measured values of N_e just before and after eclipse to test the eclipse models discussed in Section 4.4. For each model, we discuss how the unknown quantities for each system (e.g. plasma temperature, demagnification factors, etc.) were handled and discuss the likelihood of each mechanism working for some combination of possible physical parameters.

4.7.1 Refractive Eclipses

Using the measured values of N_e at a number of trial values of γ to calculate $n_e(r)$, we used Equation 4.2 to find the ratio of the plasma frequency ν_p to the observing frequency $\nu_{\rm obs}$ (where $\nu_p \sim \nu_{\rm obs}$ is the criterion for refractive eclipsing to be present

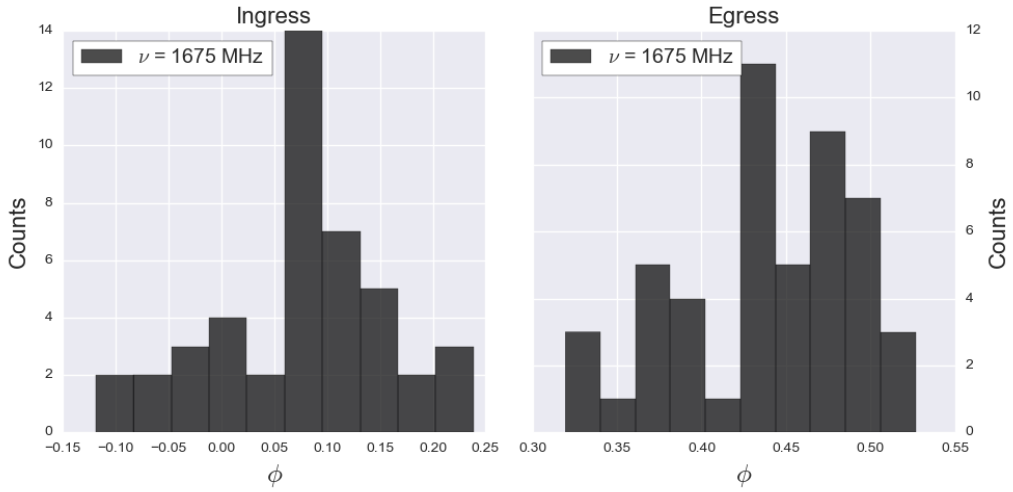

Fig. 4.8.— The observed distribution of ingress and egress values in the frequency channel centered on 1675 MHz. A roughly normal distribution is visible for L and S-band data, which is used to inform our selection of a likelihood function.

Table 4.3. Average dispersion properties

	Ter5A	Ter5P	M28H	Ter5ad
N_e (10^{17} cm^{-2})	3.0	2.0	30.0	10.0
n_e (10^6 cm^{-3})	2.0	0.8	6.1	1.2

Note. — Measured electron column and number densities for each pulsar. The median electron column density was calculated assuming a symmetric eclipse and the measured values of N_e and their associated errors within the orbital phase windows $\phi \in [\phi_{\rm I} - w_{\rm I}, \phi_{\rm I} + w_{\rm I}]$ and $\phi \in [\phi_{\rm E} - w_{\rm E}, \phi_{\rm E} + w_{\rm E}]$. The number density was found assuming a companion wind profile of $n_e \propto r^{-2}$ and is calculated at the distance of the pulsar from the companion star ($r = R$).

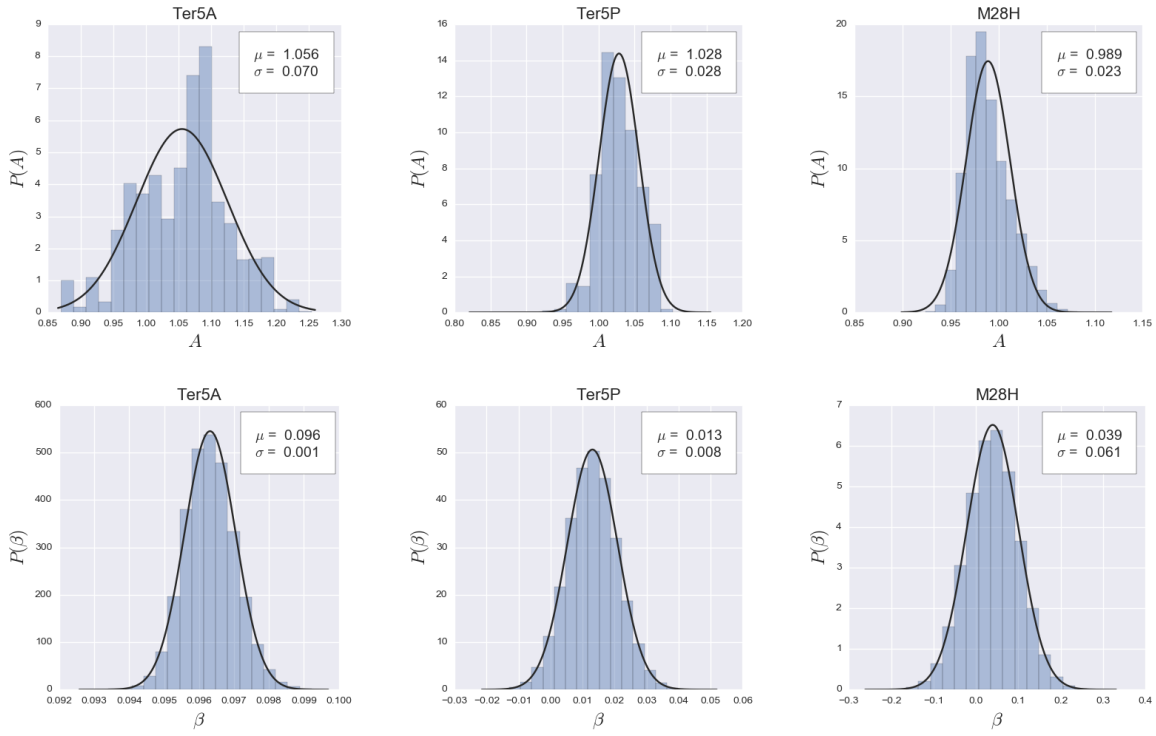

Fig. 4.9.— Posterior distributions in A and β for Ter5A, Ter5P, and M28H using the measured light curves of eclipse ingress. Over-plotted is the fit of the data to a normal distribution, the median and standard deviation of which are given in the legend of each plot.

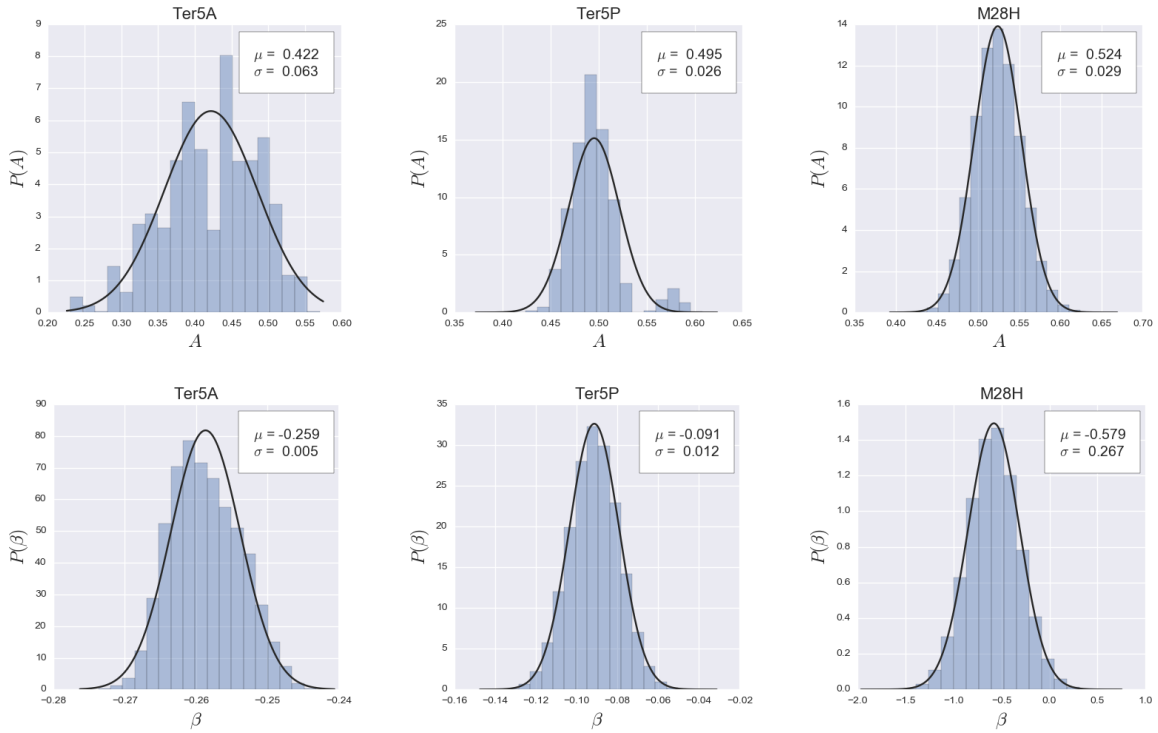

Fig. 4.10.— Posterior distributions in A and β for Ter5A, Ter5P, and M28H using the measured light curves of eclipse egress. Over-plotted is the fit of the data to a normal distribution, the median and standard deviation of which are given in the legend of each plot.

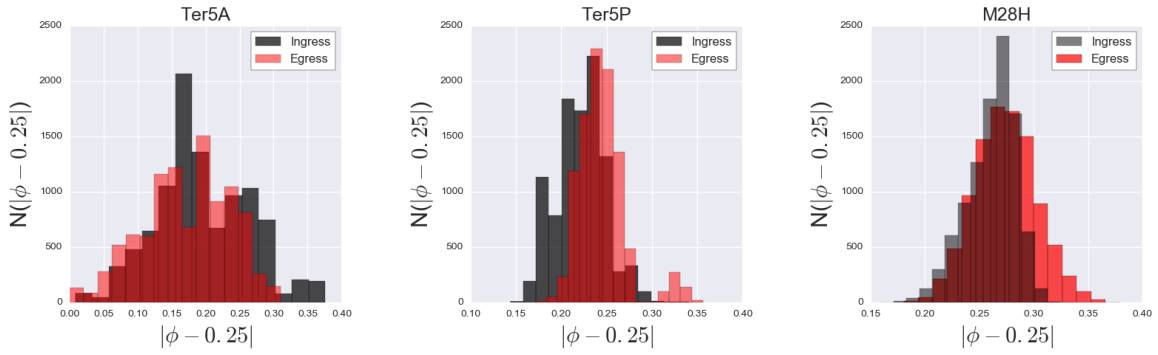

Fig. 4.11.— Observed distribution of the phase of ingress and egress at 1600 MHz, referenced to superior conjunction. We find that the eclipses are symmetric for Ter5A with slightly asymmetric distributions visible in the Ter5P and M28H data. This might imply that there is a tail of plasma that follows the companion star through its orbit.

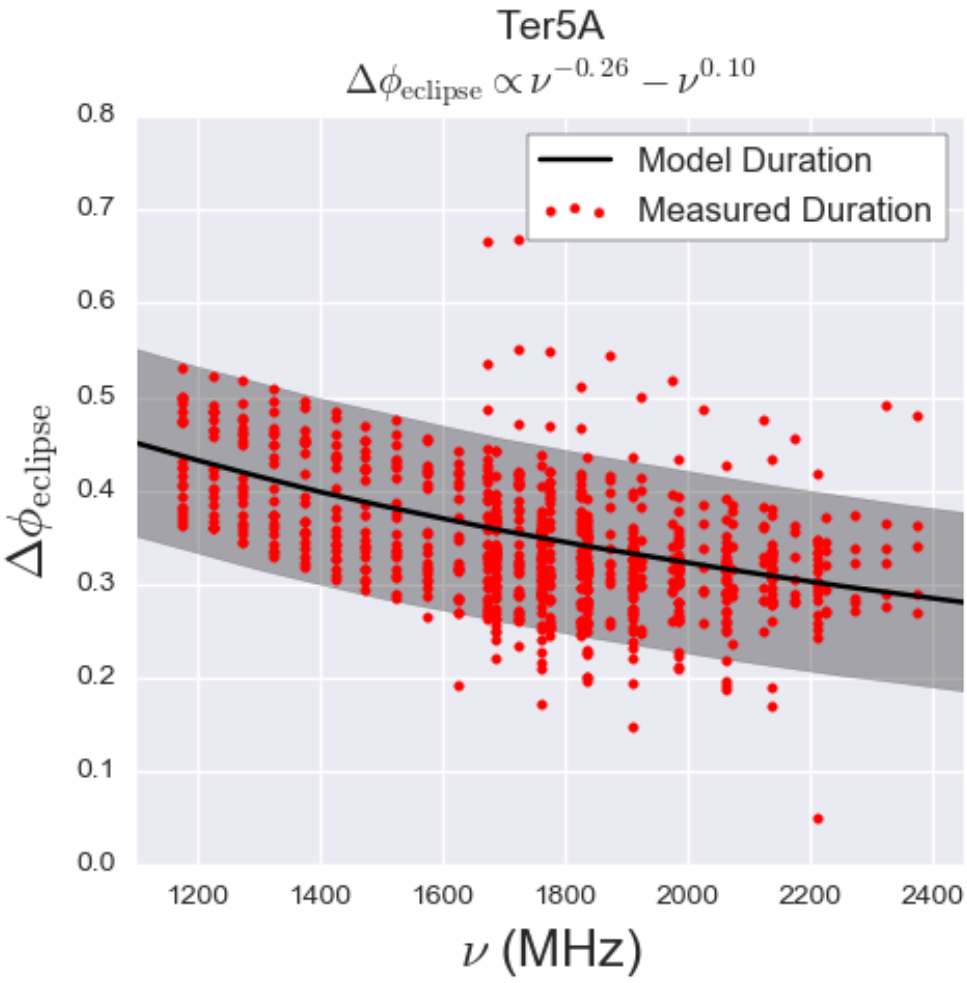

Fig. 4.12.— Eclipse duration for Ter5A as a function of observing frequency. The black line shows the difference between ten thousand random samples drawn from the ingress and egress posteriors at a thousand different frequencies between 1100 and 2500 MHz. The solid black line shows the median of the results distribution and the shaded region shows the 68% confidence interval. The red scatter points show the directly measured eclipse duration found in a single orbit. We find good agreement between the data and the model.

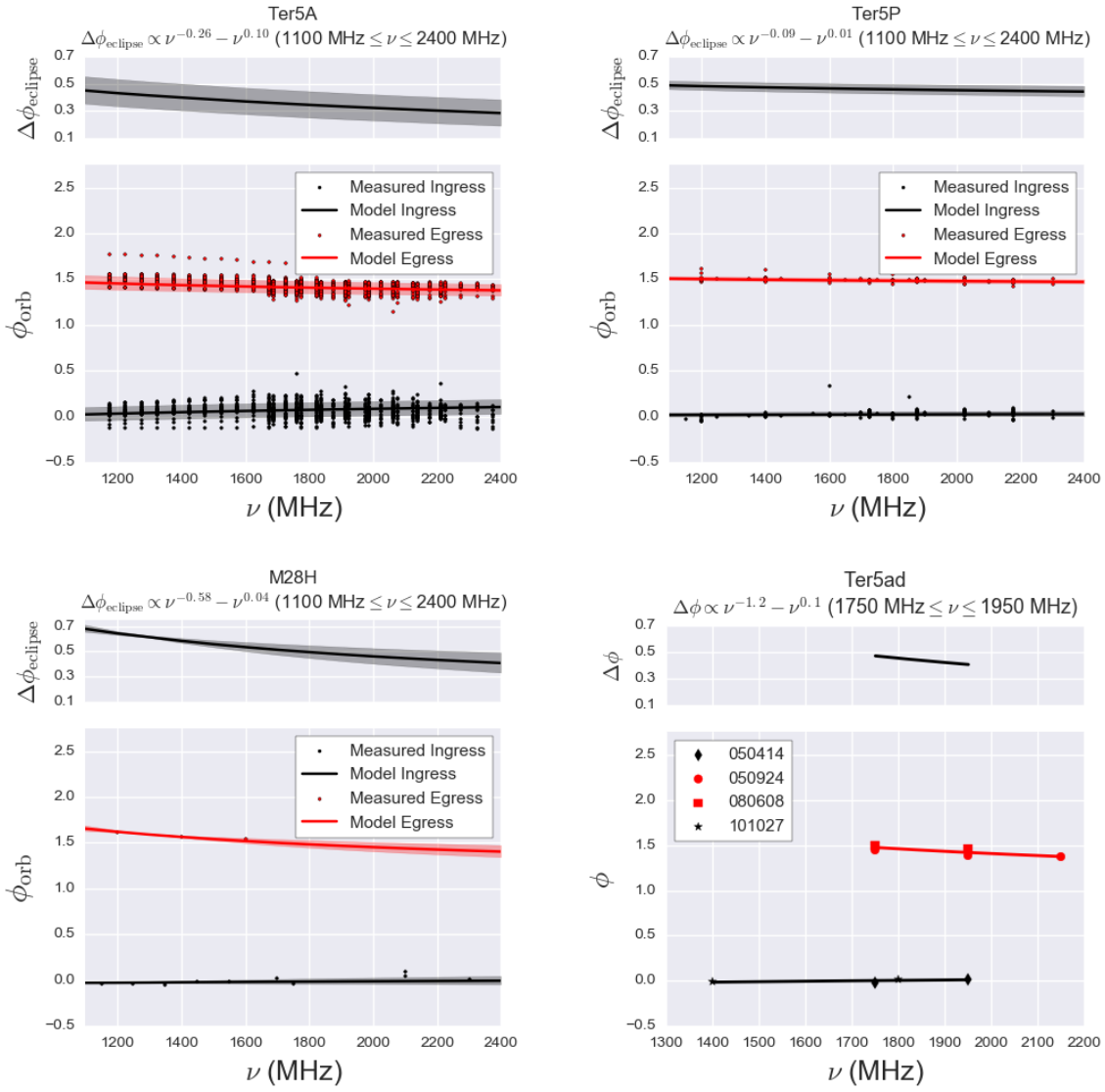

Fig. 4.13.— Eclipse durations for Ter5A, Ter5P, M28H, and Ter5ad as a function of observing frequency. The bottom panel shows the measured ingress and egress values (black and red scatter points respectively) as well as the power-law form that describes an average ingress or egress (black and red lines respectively). The top panel in each plot provides the difference of the ingress and egress power-laws, with the shaded region representing the 68% confidence interval (i.e. The eclipse duration and its error).

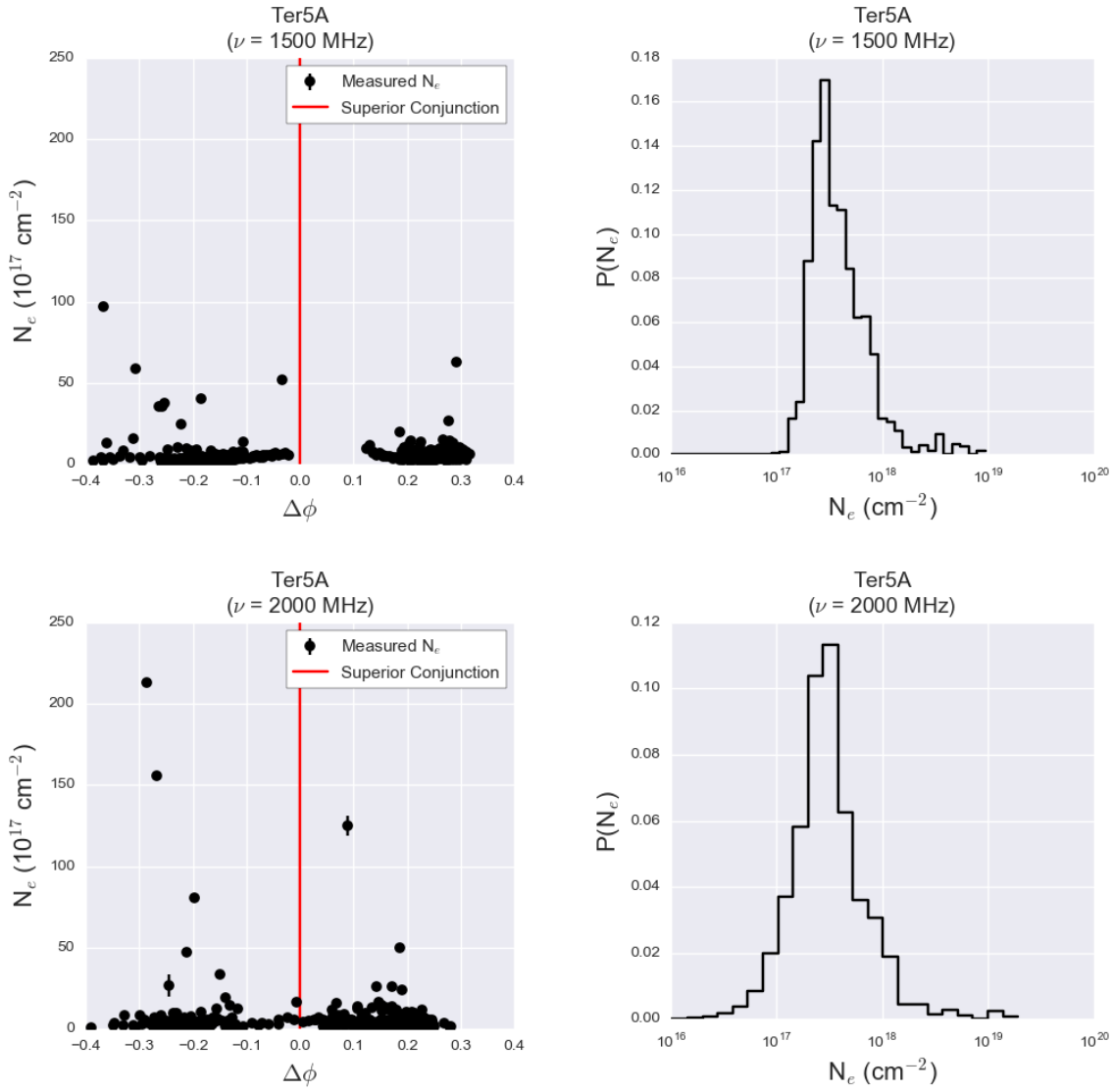

Fig. 4.14.— Measured N_e for Ter5A at L-band (Top plots) and S-band (Bottom plots). The left-hand plots show the data with respect to superior conjunction and show those data points with pulsar signal with a signal-to-noise ratio greater than 6 and within the orbital phase window where the pulsar is actively going into and out of eclipse ($\phi \in [\phi_{\rm I} - w_{\rm I}, \phi_{\rm I} + w_{\rm I}]$ and $\phi \in [\phi_{\rm E} - w_{\rm E}, \phi_{\rm E} + w_{\rm E}]$). The right-hand plots show the PDF of column densities where a Monte-Carlo sample was used to take into account the measurement errors. We find a median column density of $N_e \simeq 3{\times}10^{17}$ cm^{-2} right before eclipse as the pulsar signal passes through the absorption length L_{11}.

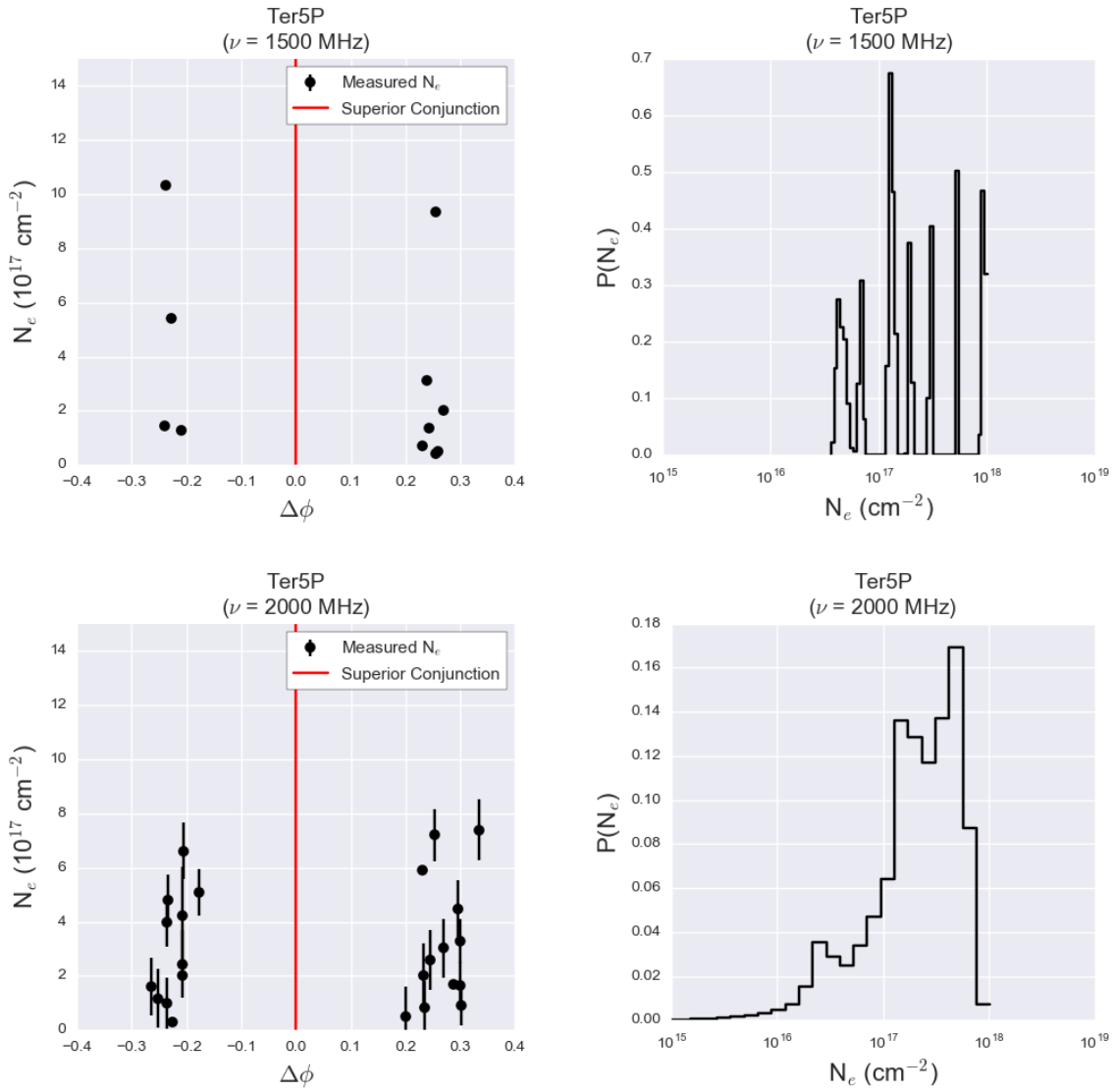

Fig. 4.15.— Measured N_e for Ter5P at L-band (Top plots) and S-band (Bottom plots). The left-hand plots show the data with respect to superior conjunction and show those data points with pulsar signal with a signal-to-noise ratio greater than 6 and within the orbital phase window where the pulsar is actively going into and out of eclipse ($\phi \in [\phi_{\rm I} - w_{\rm I}, \phi_{\rm I} + w_{\rm I}]$ and $\phi \in [\phi_{\rm E} - w_{\rm E}, \phi_{\rm E} + w_{\rm E}]$). The right-hand plots show the PDF of column densities where a Monte-Carlo sample was used to take into account the measurement errors. We do not have enough data for Ter5P at L-band to fully resolve the underlying distribution of possible N_e values, though the distribution is largely centered on the same values as those seen in the S-band data, as expected. We find a median column density of $N_e \simeq 2{\times}10^{17}$ cm^{-2} right before eclipse as the pulsar signal passes through the absorption length L_{11}.

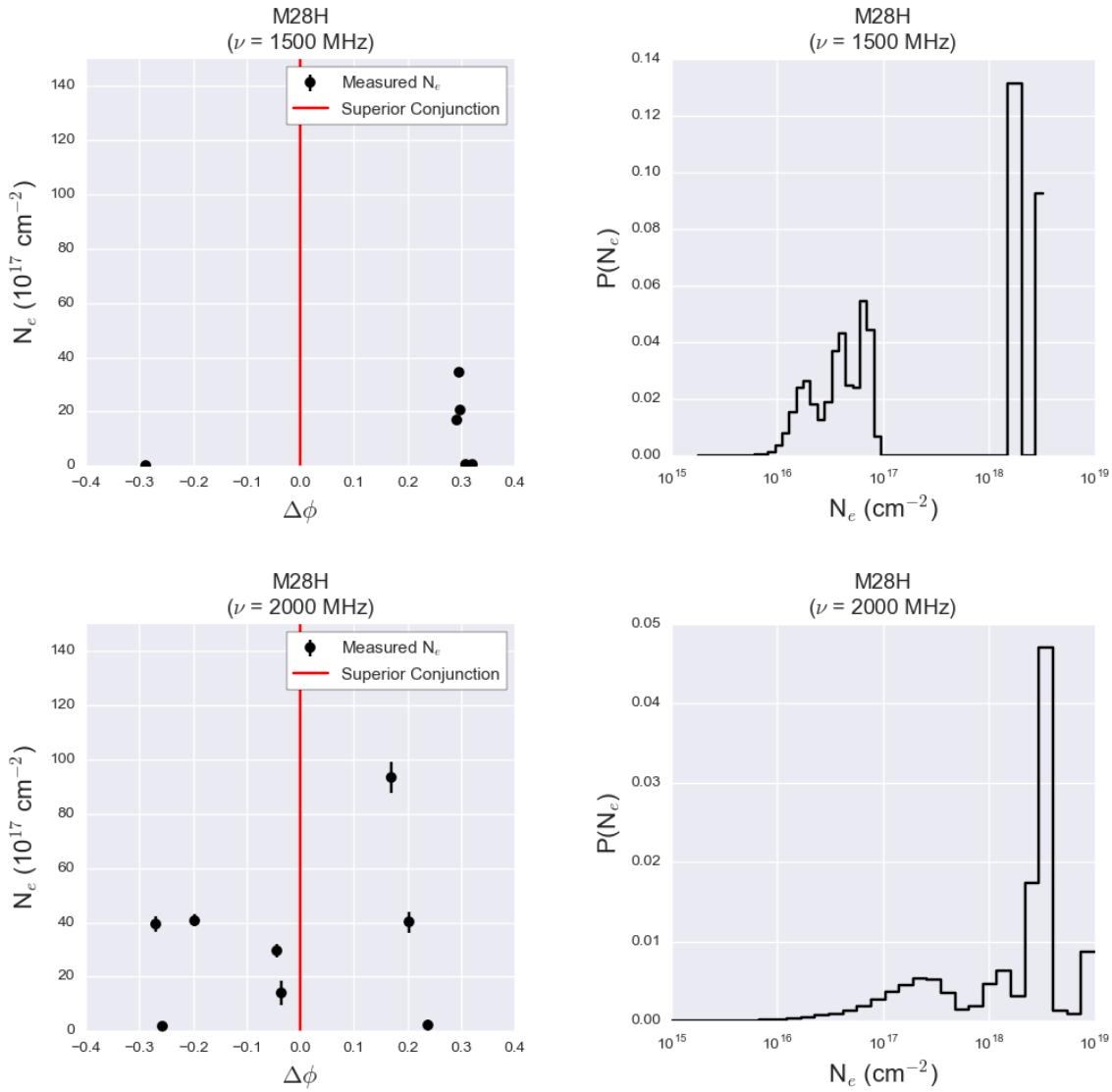

Fig. 4.16.— Measured N_e for M28H at L-band (Top plots) and S-band (Bottom plots). The left-hand plots show the data with respect to superior conjunction and show those data points with pulsar signal with a signal-to-noise ratio greater than 6 and within the orbital phase window where the pulsar is actively going into and out of eclipse ($\phi \in [\phi_{\rm I} - w_{\rm I}, \phi_{\rm I} + w_{\rm I}]$ and $\phi \in [\phi_{\rm E} - w_{\rm E}, \phi_{\rm E} + w_{\rm E}]$). The right-hand plots show the PDF of column densities where a Monte-Carlo sample was used to take into account the measurement errors. We find a median column density ranging between $N_e \simeq 10^{17}$ cm^{-2} and $N_e \simeq 3{\times}10^{18}$ cm^{-2} right before eclipse as the pulsar signal passes through the absorption length L_{11}.

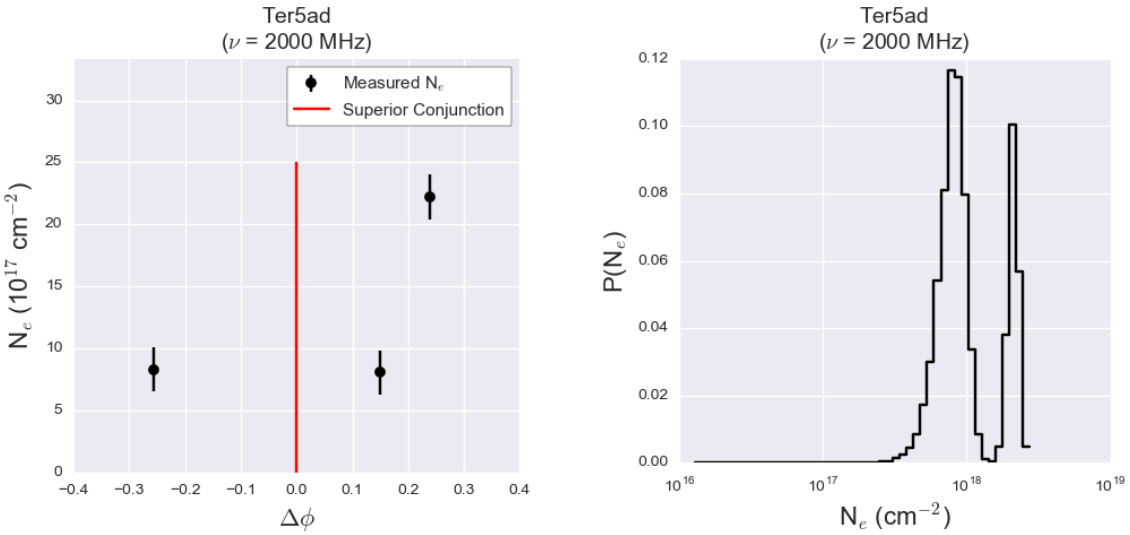

Fig. 4.17.— Approximate measurements of N_e for Ter5ad at S-band. The left-hand plot shows the data with respect to superior conjunction and show those data points with pulsar signal with a signal-to-noise ratio greater than 6 and within the orbital phase window where the pulsar is actively going into and out of eclipse ($\phi \in [\phi_{\rm I} - w_{\rm I}, \phi_{\rm I} + w_{\rm I}]$ and $\phi \in [\phi_{\rm E} - w_{\rm E}, \phi_{\rm E} + w_{\rm E}]$). The right-hand plots show the PDF of column densities where a Monte-Carlo sample was used to take into account the measurement errors. We find a median column density of $N_e \simeq 10^{18}$ cm^{-2} right before eclipse as the pulsar signal passes through the absorption length L_{11}.

in the system) near superior conjunction for an edge on (i=90°) binary. We tested this model at different values of the impact parameter b for the caustic, ranging from $b \in [R_c, R]$ for a companion radius R_c that scales as $(R_c/R_\odot) \propto (M_c/M_\odot)^{0.8}$. For each possible impact parameter, we also calculated the number density at that location $n_e(b)$.

Figure 4.18 shows the measured ratios of the plasma and observing frequency for Ter5A at 1600 MHz. The cyan line shows the measured eclipse radius, which is very nearly where we expect the caustic to reside.

We find that except for very steep density profiles and very small impact parameters, the probability for refractive eclipsing to take place is at most a few percent. In addition to this calculation, we do not see any evidence for increased pulsar flux near ingress or egress for any of our pulsars. We therefore conclude that refractive eclipses are not a feasible mechanism driving pulsar eclipses. This result agrees with those of Phinney et al. (1988) and Thompson et al. (1994), which found the physical conditions for refractive eclipsing in B1957+20 and Ter5A to be unfavorable.

4.7.2 Free-Free Absorption

As previously discussed in Section 4.4, the conditions for free-free absorption require that the plasma surrounding the companion star be cool and highly clumped. Using Equation 4.3 at the measured value of N_e for both ingress and egress, we have calculated the optical depth for free-free absorption. This model was tested for different trial plasma temperatures and clumping factors in an attempt to find some set of parameters that produce an optically thick plasma. We assume that the absoprtion length scale L_{11} is given by twice the eclipse radius R_e.

Figure 4.19 shows the results for Ter5A. Results for this system are typical of each

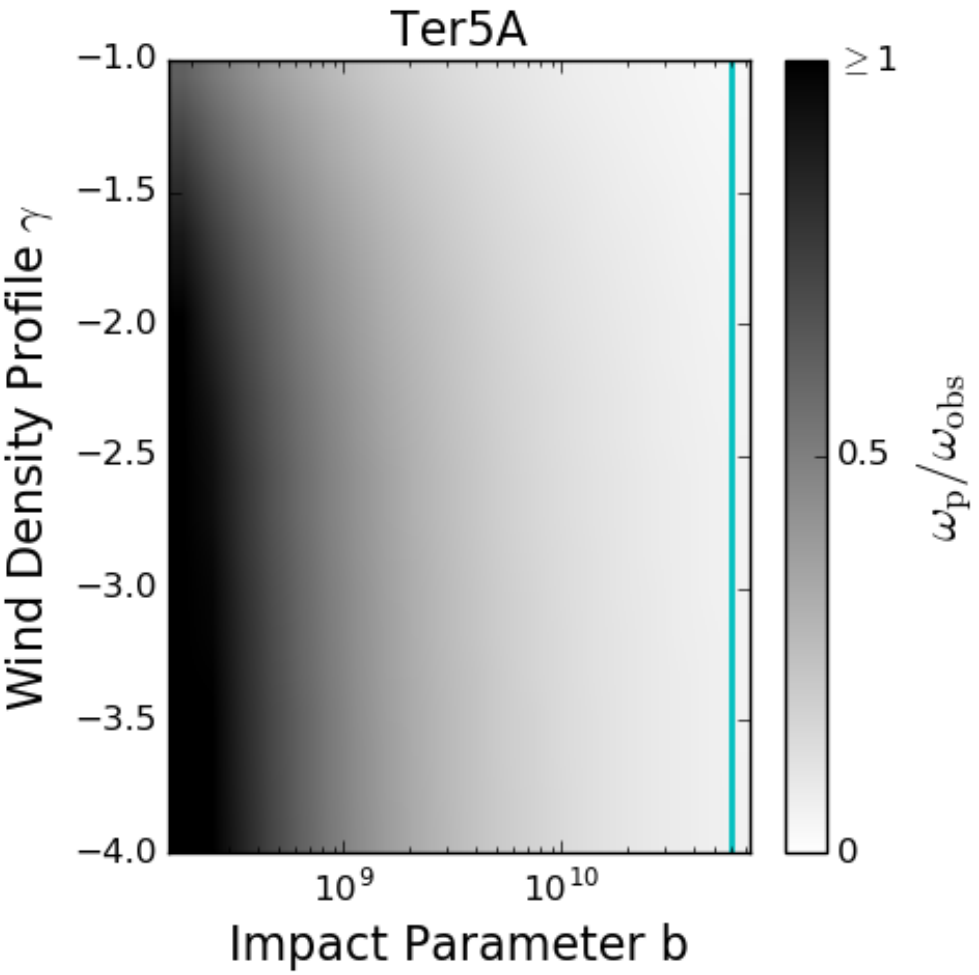

Fig. 4.18.— The probability for refractive eclipses in Ter5A using the measured values of N_e at a number of trial values of the impact parameter b for the caustic and for a number of trial wind density profiles γ used to calculate $n_e(r)$ at ν=1600 MHz. We find similar results for Ter5P, M28H, and Ter5ad. Only for very steep wind profiles does the number density near the surface of the companion star become large enough to allow for refractive eclipsing ($\nu_p \sim \nu_{\rm obs}$). The cyan line shows the measured eclipse radius, which is likely where the caustic should reside.

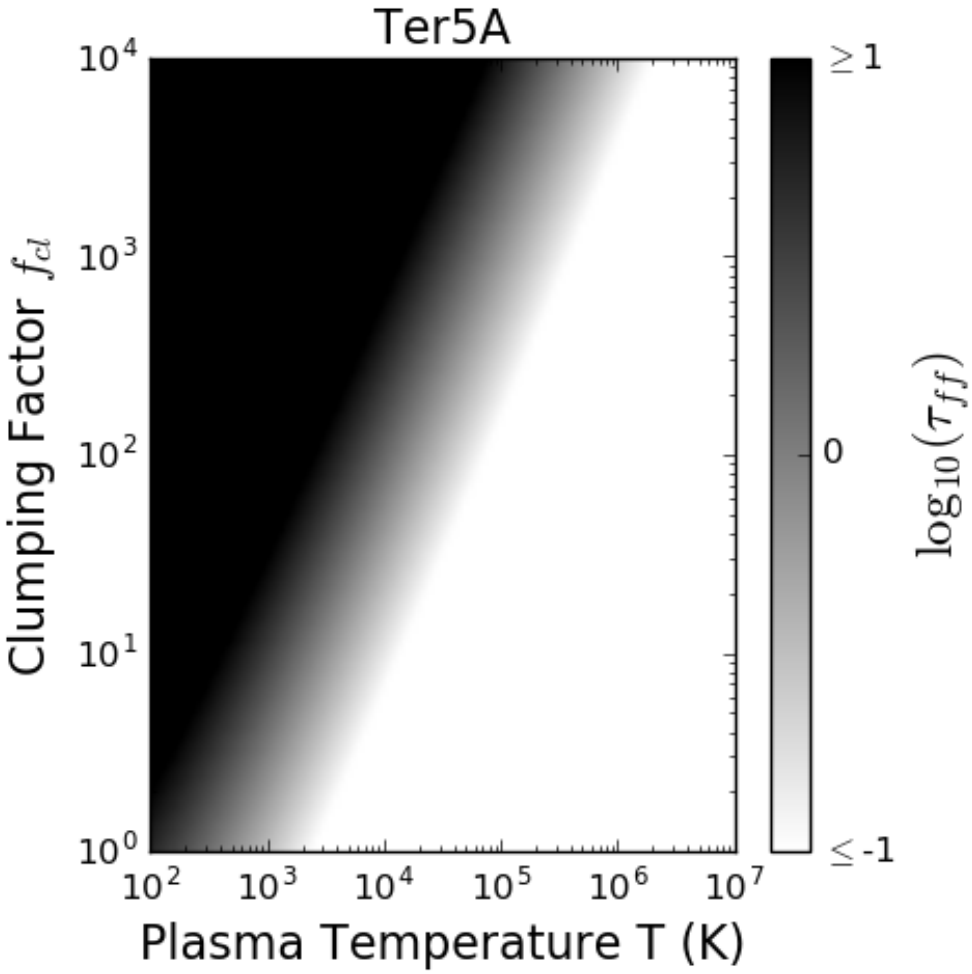

Fig. 4.19.— The optical depth for free-free absorption for Ter5A at the median value of N_e just before and after eclipse for a number of trial temperatures and clumping factors. We find similar results for Ter5P, M28H, and Ter5ad. In each case we find that the optical depth is much less than one except at the coolest temperatures and largest clumping factors.

of our pulsars, in which we find that the conditions for free-free absorption require clumping factors of greater than a hundred and temperatures no greater than a few thousand Kelvin.

While we cannot accurately determine the temperature of the plasma from timing data alone, we argue that near the pulsar the black body radiation from the surface of the neutron star alone likely heats the plasma to temperatures too large for free-free absorption. For a surface temperature of $\sim 10^6$ K, the plasma near the pulsar is too hot to allow for this eclipse mechanism to be efficient in any of our systems. A more detailed discussion about the expected plasma temperature surrounding the companion star, looking at different heating mechanisms, is given in Section 4.8.

4.7.3 Induced Compton Scattering

The predicted optical depth of induced Compton scattering for a number of trial demagnifications and spectral indices is given in Figure 4.20 for Ter5A, which has the largest possible optical depth for this mechanism out of all of our pulsars (typically 100-1000x larger than those seen in Ter5P, M28H, or Ter5ad) due to it being a much brighter source and having a much smaller binary separation.

In a study of a few hundred slow pulsars and MSPs, Bates et al. (2013) found a spectral index of α=-1.41$\pm$0.96 for the combined pulsar population. Though a study of the spectral index for MSPs alone has not been completed, Bates et al. (2013) argue that their data suggests that the distribution should not change drastically. We therefore focus our attention on spectral indices close to this value when testing induced Compton scattering. The black horizontal line in Figure 4.20 shows the best fit from their results.

The demagnification factor M, which is approximately $M \sim (R_{\rm curve}/2r_{\rm curve})^2$, is

a measure of how close the pulsar is sitting to the center of the cloud of plasma in the system. From the geometry of an eclipse given in Figure 4.1, this means that the demagnitication factor is most likely given by $M \sim (R_e/2R)^2$, and is less than one. We have tested this model for a number of trial demagnification factors, including the unlikely case that the pulsar is within the plasma cloud (and has not blown away the plasma via the pulsar wind), in Figure 4.20.

We find that for induced Compton scattering to be feasible, each redback must have a very steep spectral index and have a very large demagnification factor (i.e. a pulsar deep within the cloud of plasma surrounding the companion star). We therefore argue that this process is highly unlikely to be the driving process behind eclipses at L and S-band. If we instead consider the case of each pulsar observed at a lower observing frequency (e.g. 320 MHz), it is possible that Ter5A would experience induced Compton scattering. We do not believe that this mechanism is capable of producing eclipses in Ter5P, M28H, or Ter5ad even at these lower frequencies.

This increase in the optical depth is due to the sharp frequency dependence of this model, which scales as ν^{-2}. Combined with the intrinsic brightening of the pulsar at lower frequencies ($S \propto \nu^{\alpha}$), it is possible that the optical depth for this model could increase as much as 10^3-10^4 times in the observing range of a few hundred MHz. Further discussion of how the predicted eclipse mechanism might change with frequency is discussed in Section 4.8.

4.7.4 Stimulated Raman Scattering

The criteria for Raman scattering requires the pulsar flux to be approximately equal to a critical pumping flux needed to enhance the density perturbations in the plasma. We calculated the pulsar flux at the companion's orbit by taking the measured flux

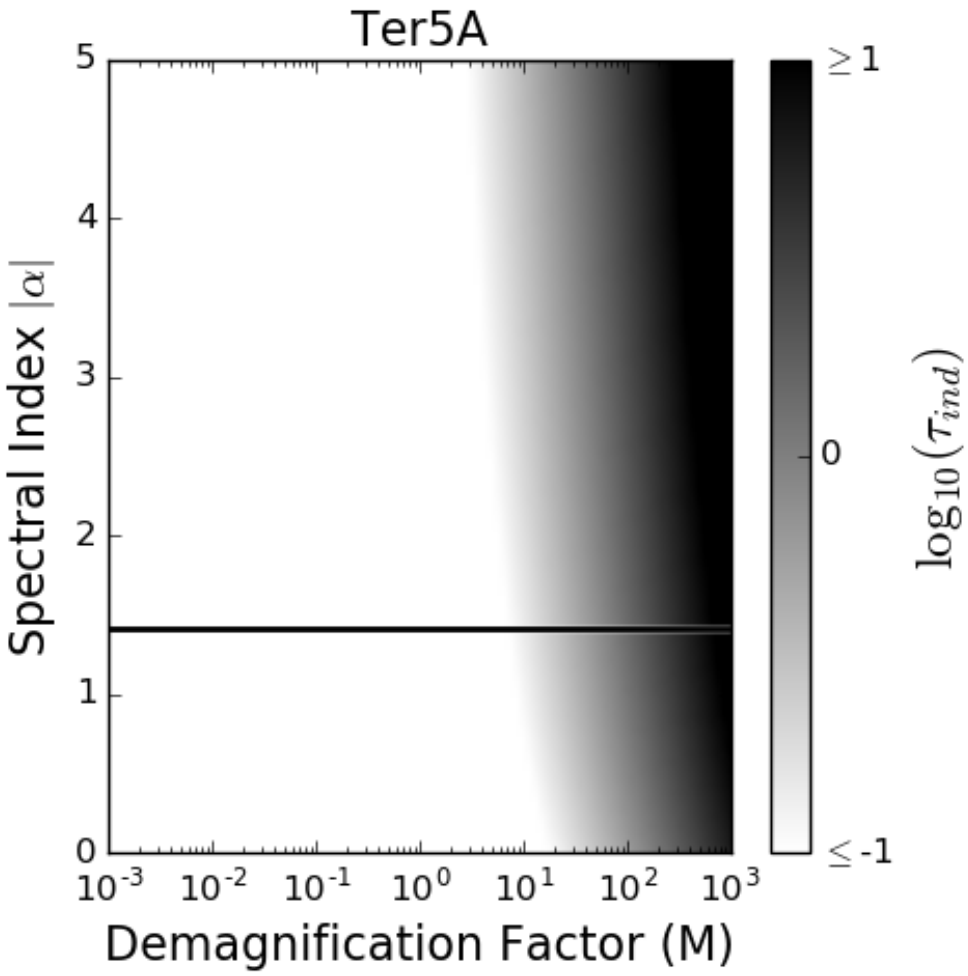

Fig. 4.20.— The optical depth for induced Compton scattering for Ter5A at the measured value of N_e near ingress and egress for a number of trial demagnification factors and spectral indices. We find that Ter5P, M28H, and Ter5ad all have even smaller optical depths than Ter5A by few orders of magnitude. The black horizontal line shows the results of Bates et al. (2013) which found a median spectral index for pulsars of α=-1.41. We conclude that induced Compton scattering is not possible for any of our pulsars at L-band and S-band.

and scaling it according to the cluster distance for each source and took this to be the pump flux required to drive Raman scattering.

Using Equations 4.4 and 4.10 we calculated the critical pumping flux needed for stimulated Raman scattering for a number of trial plasma temperatures and wind density profiles (which allows us to calculate $n_e(r)$ by solving for the power-law parameters that reproduce our measurements of N_e). We then took the ratio of the pulsar flux to the critical flux to see if we obtain values that are roughly consistent with Raman scattering.

Figure 4.21 shows our results for each pulsar. If we again assume blackbody radiation from a neutron star with a surface temperature of $T \lesssim 10^6$ K, we find that the plasma could potentially be hot enough for stimulated Raman scattering to be present in the Ter5A data, which is in agreement with the findings of Thompson et al. (1994). For the pulsars Ter5P and M28H, we find that the required plasma temperature to power this eclipse mechanism is slightly larger than that of Ter5A, which is likely due to the larger binary separation. For these two systems, a plasma temperature of closer to 10^7 K could produce eclipsing via this method, which is likely possible through the preesence of a hot coronal plasma. In Section 3.8 we discuss whether temperatures this large can be measured using the cold plasma dispersion relationship.

Of the four sources, the only redback that does not appear to be well described by stimulated raman scattering is Ter5ad. The required plasma temperature to bring the critical flux density down to the known flux density of the pulsar is approaching $\sim 10^8$ K. At these temperatures the cold plasma relationship is not a reliable means of measuring the column densities through pulsar timing and it is unknown whether the plasma coming off of the companion star can reach these temperatures.

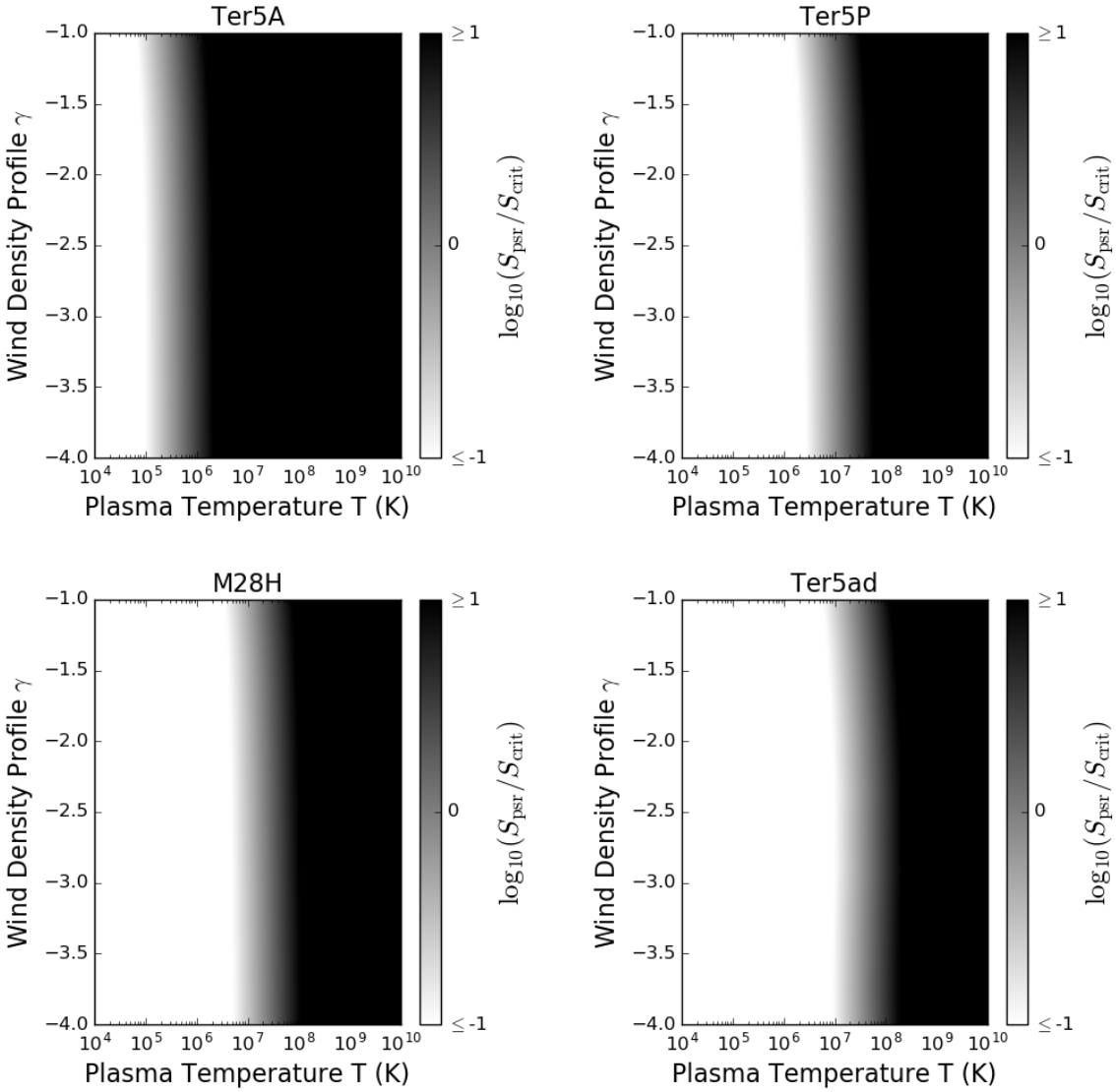

Fig. 4.21.— The likelihood for Raman scattering for the redbacks in our sample at different trial values of the companion wind profile and plasma temperature. We find that Raman scattering could be a potential explanation for Ter5A, Ter5P, and M28H depending on the plasma temperature and is slightly less likely for Ter5ad.

In Section 4.8 we discuss other sources of heating of the gas that might change these results.

4.7.5 Dispersive Pulse Smearing

In order to test dispersive pulse smearing, we used L-band GUPPI data for Ter5A, Ter5P, and M28H and calculated the flux of the pulsar as a function of orbital phase at a large number of trial DMs. We used L-band data because the time delays due to dispersion are larger at L-band and easier to fit for.

This was accomplished by taking the available PSRFITS files for each observation and shifting the pulsar pulse profile in each frequency channel and sub-integration according to the time delay given by Equation 1.7 for each trial DM. We then used the best value of P_b and T_0 for each observation to calculate the corresponding orbital phase of each sub-integration.

Figure 4.22 shows the summed flux in each orbital phase bin for different trial DM values for Ter5A. We find no evidence that an increased DM value recovers a significant amount of flux during eclipse for any of our pulsars. We do note however that some pulse smearing and dispersive pulse delay is expected near ingress and egress for Ter5A, as is shown in Figure 4.2.

We find similar results for Ter5P and M28H that dispersive pulse smearing does not appear to be the primary eclipsing mechansim. We do note that for both of these pulsars, however, that the intrinsic brightness is much fainter than that of Ter5A. In order to obtain high signal to noise measurements for these two systems, we could not produce as many sub-intervals across the orbit. This makes it much more difficult to obtain a measurement of these pulsars actively going into and out of eclipse.

We do not have enough data to test this model within the Ter5ad data, as the

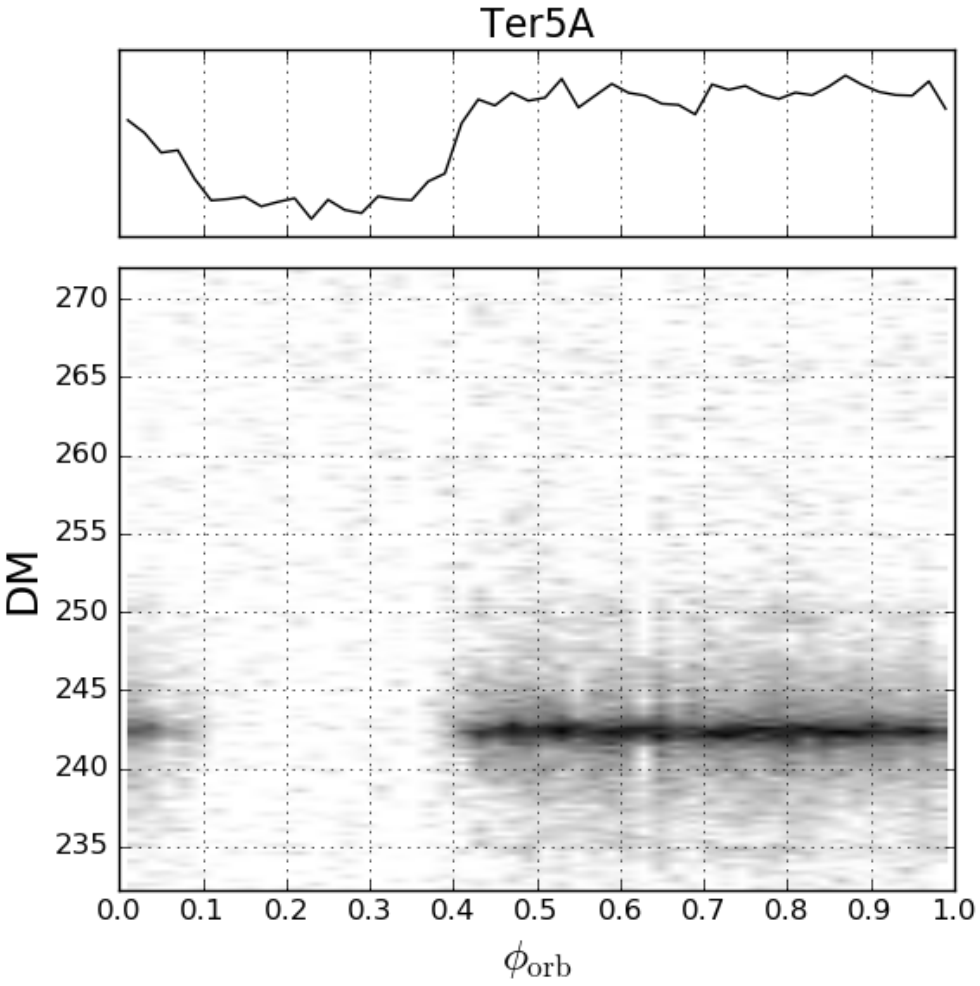

Fig. 4.22.— **Bottom plot**: Integrated L-band flux for Ter5A at L-band using the GUPPI backend for the brightest day 09/25/2011. We do not find evidence that the flux can be recovered in eclipse by a DM shift associated with dispersive pulse smearing. **Top plot**: The integrated flux profile as a function of the orbital phase at the DM value found from long-term timing of the pulsar, which is coincident with the bright stripe in the bottom plot.

pulsar is not bright enough in most observations to obtain a reliable flux measurement on short enough timescales to observe the pulsar at ingress and egress. In Section 3.8, we discuss how interferometric imaging could test this model more reliably than pulsar timing is capable of.

4.7.6 Results

Table 4.4 shows the physical conditions required to produce eclipses for a given mechansism, if at all possible. We find that stimulated Raman scattering appears to be the most likely scenario for explaining the eclipses of Ter5A. This is in good agreement with the results of Thompson et al. (1994) and their study of the L-band and S-band eclipses for this pulsar.

For the pulsars Ter5P and M28H, we also find that stimulated Raman scattering to be the best model available for explaining the data. Due to the large binary separation in these systems, the incident pulsar flux is much smaller, however. The plasma must be much hotter in this case for this model to be efficient. For each system, a temperature of T$\sim 10^7$ K is required, which is nearing the limit at which the cold plasma dispersion relationship starts to break down.

Finally, we do not find an ideal model for explaining the eclipses in Ter5ad. Like the other pulsars in this study, stimulated Raman scattering is the most likely, however the required plasma temperatures are still too large. Due to the large binary separation in this system, temperatures of T$\sim 10^8$ K are required for the pulsar flux to produce an instability in the plasma that can lead to scattering. The cold plasma dispersion relationship begins to break down strongly in this regime, however, and as such we do not believe pulsar timing can be used to calculate the plasma properties well enough to confirm this model for this system.

4.8 Discussion

The primary goal of this work has been to identify an average set of eclipse properties for four redbacks. This is in the hopes of understanding the distribution of plasma in the system and the density of this intra-binary medium. By identifying these properties, we aim to determine the most likely physical mechanism responsible for eclipsing the pulsar signal.

This does not give us information on the short-term variability of the system, but it does allow us to understand the average mass loss of plasma flowing off the companion star and its temperature. It also allows us to characterize the best orbital phase windows to observe a redback at different frequencies.

In this section, we discuss some of these results in the context of studying redbacks as an entire population and address in more depth some of the assumptions that went into this work.

4.8.1 Plasma Temperature

In this work, we have discussed the importance of the plasma temperature with respect to measuring accurate column densities and the likelihood of an eclipse mechanism being a viable explanation for our data. If the plasma is too hot, the limit that dispersive delays in the pulse arrival times can be converted into a measurement of N_e breaks down. Additionally, we cannot rule out the parameter space available to different models without knowing more about the plasma temperature.

In this section, we briefly discuss whether the cold plasma dispersion relationship is valid for our pulsars. We then attempt to place limits on the possible plasma temperatures through some basic approximations for each system.

Cold Plasma Limit

We argue that we are still in the limit of working with a cold plasma by examining the average kinetic energy of the plasma. The assumption behind the dispersion relationship derived for a cold ionized medium depends on whether the particles in the plasma are considered non-relativistic. To first order, the kinetic energy of a non-relativistic gas can be found by:

$$< KE >=< \frac{1}{2} m_i v^2 >= \frac{3}{2} kT \,, \tag{4.11}$$

where m_i is the mass of the particle in question and T is the temperature of the plasma.

For the protons in the plasma, temperatures of T$\sim 10^{10}$ K are required to reach relativistic speeds of $v \sim 0.1c$. Comparing this to the much less massive electrons, the temperature of the plasma needs to be slightly larger than T$\sim 10^{7}$ K in order to produce electron velocities a few percent of the speed of light.

If we consider the upper-limit of the plasma temperature across all the eclipse models discussed in this work (T$\lesssim 10^{7}$ K), we find that the cold plasma dispersion relationship is a reasonable assumption. The only subset of models that should be called into question are those for Raman scattering in the case of Ter5ad, which border on the relativistic limit.

We can attempt to estimate the plasma temperature in order to better constrain the eclipse models in three different ways. The first is by considering the blackbody radiation from the pulsar surface. The second is to try to estimate the effect of the intra-binary shock heating on the plasma. The final method is to consider the typical coronal temperatures of low-mass stars

Blackbody radiation

While we cannot know exactly the surface temperature of each pulsar, we can use the results of previous studies of young hot NSs to provide an upper limit on the temperature of the star. From the results of Lattimer & Prakash (2004), the average surface temperature of a young pulsar is believed to be $T \lesssim 10^6$ K. While we cannot be sure of the efficiency with which the X-rays couple with the plasma surrounding the companion star, in the limit that the plasma comes into thermal equilibrium with the NS, the temperature of this plasma is still cool enough that electrons will not be considered relativistic.

Even if the redbacks that are closer to the quiescent LMXB stage of their evolution were to have an accretion disk, the temperature that can be estimated for such an object would not be large enough to produce relativistic electrons. From the results of Heinke et al. (2003) light curve modeling of the observed X-ray flux from qLMXBs predicts a temperature of $T \sim 1$ keV. This is not hot enough to produce a relativistic plasma and as such we argue that the cold dispersive medium limit holds when considering only blackbody radiation from the NS and any potential surrounding material.

Pulsar Wind & Intra-binary shock heating

Examining the lightcurves of BW and RB companion stars, earlier works have discovered asymmetries and spectral variation inconsistent with direct heating of the companion star from the pulsar (Schroeder & Halpern 2014; Romani et al. 2015). A possible explanation for this is the presence of an intra-binary shock (IBS) region where the pulsar wind and companion wind meet (Romani & Sanchez 2016).

The physics governing the IBS region and how temperature is transfered through-

out the system is still not well understood. From the results of Romani & Sanchez (2016), we can estimate the effect pulsar spin-down would have on heating the plasma at the eclipse radius, however. Equation 2 from Romani & Sanchez (2016) defines the additional heating of the companion's day side to be:

$$\Delta T = \eta \dot{E}/4\pi R^2 \sigma \,, \tag{4.12}$$

where η is the heating efficiency and σ is the Stefan-Boltzmann constant. We redefine this for the heating of the plasma at R_e as follows:

$$\Delta T = \eta \dot{E}/4\pi (R - R_e)^2 \sigma \,. \tag{4.13}$$

Measurements of the light curve properties have shown that in some cases the inferred heating power implies a heating efficiency $\eta \geq 1$, which is likely due to the pulsar particles and high energy radiation being deflected before the reach the companion star (Romani & Sanchez 2016). If we assume however that η is of order unity, which implies isotropic emission of the pulsar radiation, then the heating due to the pulsar wind is of order $10^3 - 10^4$ K for all of our pulsars, using a spin-down power of $\dot{E} \sim 10^{34}$ ergs/s and the pulsar-companion separation and eclipse radii. This is well below the temperature needed to produce relativistic electrons and as such we argue that the pulsar wind and the IBS do not invalidate the cold plasma dispersion relationship for our systems.

Coronal Temperature

Studies of the X-ray properties of low-mass stars over the past few decades have begun to reveal important details about the properties of coronae. While the surface of a

M-dwarf star is too cool to produce X-ray emission, its corona can be much hotter. Fitting for the X-ray hardness of such a source can therefore give us a reasonable estimate of the plasma temperature for these systems.

X-ray observations of low-mass stars carried out by Giampapa et al. (1996) using the ROSAT (ROentgen SATellite) X-ray telescope found evidence of two thermal components. The average temperatures of these components was T$\sim 2\times10^6$ K for the soft component and T$\sim 10^7$ K for the hard component.

These temperatures produce electron velocities that are a few percent of the speed of light. While this is approaching the limit at which the cold plasma dispersion relationship is no longer valid, we argue that it likely only produces a slight change in our measured column densities and does not change our results regarding the driving mechanism behind pulsar eclipses.

4.8.2 Eclipses at different frequencies

Due to the strong frequency dependence on the incident radiation through the plasma, the eclipse mechanism might change as a function of observing frequency. Data for this study took advantage of the large bandwidth ($\sim$ 600 MHz after band-pass filtering and RFI removal) provided by the GUPPI back-end at L and S-band (DuPlain et al. 2008), yet many pulsar observations are made at much lower frequencies of only a few hundred MHz. In many cases, this can change the inferred optical depth through the plasma by nearly two orders of magnitude or more.

In the case of free-free absorption, the frequency dependence for the optical depth scales as $\tau \propto \nu^{-2}$. We find that for a likely plasma temperature of T$\sim 10^6$ K, the optical depth would need to increase by approximately a factor of 10^4 in order to obtain an optically thick plasma for free-free absorption. It is therefore unlikely that

this mechanism can be responsible for any observed pulsar eclipses, even at the lowest observing frequencies.

As for induced Compton scattering, the optical depth scales as $\tau \propto \nu^{-2-\alpha}$. Assuming that α=-1.41±0.96 from Bates et al. (2013), this means that at observing frequencies of a few hundred MHz, the optical depth should increase by a factor of $\sim 10^3$-10^4. For Ter5A, it is possible that eclipses at this lower frequency might experience signficant amounts of induced Compton scattering. Ter5P, M28H, and Ter5ad also become far more optically thick when considering this eclipse mechanism at this low of an observing frequency (though the wider binary separation in these systems makes this mechanism still an unlikely source of eclipses).

4.8.3 Mass Loss Rates

As mass transfer plays an important role in not only the eclipsing of a BW or a RB, but more generally the formation of an MSP, we would like to calculate the mass transfer rate in these systems using pulsar timing. From the general properties of the eclipses, it is possibly to estimate the mass *loss* rate from the companion star. This represents a very strict upper-limit to the mass transfer rate, which is known to be much lower due to blow back by the pulsar wind and the efficiency of Roche-lobe overflow.

In order to calculate the mass loss rate, we begin by assuming this value to be constant. If the mass loss is spherically symmetric in the form of a wind, then the flux of particles passing through the eclipse radius ($\dot{M} \simeq 4\pi R^2 \rho v_w$) can be posed as

the following:

$$\dot{M} \simeq 1.67 \times 10^{-13} \left(\frac{R_e}{10^6\,\mathrm{km}}\right)^2 \left(\frac{\langle m \rangle}{m_p}\right) \left(\frac{n_e(r=R_e)}{5\times10^5\,\mathrm{cm}^{-3}}\right) \left(\frac{v_w(r=R_e)}{10^3\,\mathrm{km/s}}\right) \mathrm{M}_\odot\,\mathrm{yr}^{-1}\,, \tag{4.14}$$

where $\langle m \rangle$ is the average particle mass in the plasma and $v_w(r=R)$ is the velocity of the wind at the eclipse radius.

In order to calculate an approximate mass loss rate, we assume that the eclipses are symmetric, which allows us to calculate the eclipse radius R_e using the results of Chapter 4.5.3. The two most difficult terms to estimate then are the number density of electrons at R_e and the wind velocity coming off of the companion star.

The wind velocity can be estimated in one of two ways. The first is by looking at the time variability ($t_{\rm var}$) in eclipses. This timescale allows us to determine how quickly an over-density in the plasma might be moving through the system. From an examination of our data, we see micro-eclipses and changes in the eclipse properties can occur over the course of a few minutes. If we assume that these changes must pass through a region of order the size of the eclipse radius, this implies a wind velocity of $v_w \sim R_e/t_{\rm var} \sim 10^3$ km/s. The second method is to calculate the escape velocity of the companion star, which produces similar wind velocities. The number density of electrons is calculated using the same methods discussed in Chapter 4.6.2 at the eclipse radius R_e.

Figure 4.23 shows mass loss rates for the companion stars to Ter5A, Ter5P, M28H, and Ter5ad for a wind velocity set by the escape velocity from the star and at a number of trial wind density profiles. We find that the mass loss rates for all four companion stars range between $\dot{M} \sim 10^{-12}$ M$_\odot$ yr^{-1} and $\dot{M} \sim 10^{-10}$ M$_\odot$ yr^{-1}. If in the future we are able to calculate a mass loss rate from eclipses of transitioning pulsars like M28I, these measurements might serve to place better constraints on how much material is

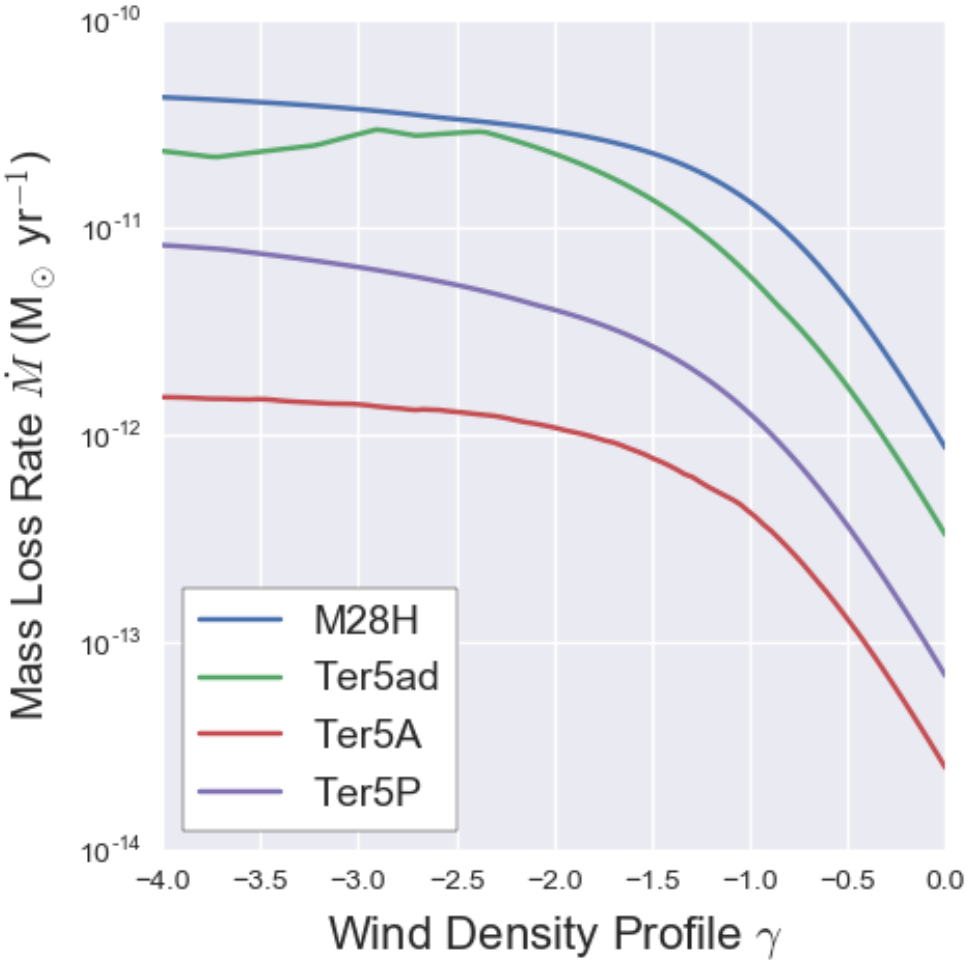

Fig. 4.23.— Mass loss rates for the companion stars to Ter5A, Ter5P, M28H, and Ter5ad for a wind velocity set by the escape velocity from the star and at a number of trial wind density profiles.

available for mass transfer onto the MSP.

4.9 Summary

Using the long-term timing of four globular cluster redbacks, we measured average eclipse properties for each system. Fitting a light curve to each eclipse, we found a power-law model for the ingress and egress of each system, the results of which are given in Table 4.2. The duration of eclipse at 1600 MHz is 0.36±0.10, 0.47±0.04, and 0.54±0.04 for Ter5A, Ter5P, and M28H respectively. The approximate eclipse duration for Ter5ad at 1800 MHz is 0.45, though more data is required to confirm this result. Examination of the distribution of ingress and egress phases distributed about superior conjunction shows evidence for a slight asymmetry in the plasma for the TerP and M28H systems. This may indicate that gas is coming off of these stars and is creating a tail behind the star as it orbits around the center of mass of the system. The eclipse radius associated with these eclipse durations range between $R_e \simeq 5\times\ 10^{10}$ cm and $R_e \simeq 5\times\ 10^{11}$ cm at 1600 MHz.

We find that the median free electron column density near the predicted ingress and egress range between $N_e \sim 10^{17}$–10^{18} cm^{-2} for the pulsars Ter5A, Ter5P, and Ter5ad. The column density for M28H is less well defined, with too few data points to reliably fit the column density at L-band and a range of possible densities between $N_e \sim 10^{17}$ cm^{-2} and $N_e \sim 10^{18}$ cm^{-2} at S-band. For a wind density profile coming off of the companion star of $n_e \propto r^{-2}$, this predicts a free electron number density at the position of the pulsar of $n_e \sim 10^6$ cm^{-3}.

From the measurements of R_e and N_e, we calculated the likelihood for eclipsing from refraction, free-free absorption, induced compton scattering, stimulated Raman scattering, and dispersive pulse delays. We find that eclipsing is unlikely for all of

these models with the exception of stimulated Raman scattering, which is possible at plasma temperatures of 10^6-10^8 K. We also use these measurements to find the approximate mass loss rate from the companion star.

4.10 Acknowledgements

Observations were taken with the Green Bank Telescope, which are operated by the National Radio Astronomy Observatory, a facility of the National Science Foundation operated under cooperative agreement by Associated Universities, Inc.

B.P. acknowledges funding from the Grote Reber fellowship through the National Radio Astronomy Observatory and the Graduate Research STEM Fellowship Program through the Virginia Space Grant Consortium under the National Aeronautics and Space Administration (NASA).

J.W.T.H. acknowledges funding from an NWO Vidi fellowship and from the European Research Council under the European Union's Seventh Framework Programme (FP/2007-2013) / ERC Starting Grant agreement nr. 337062 ("DRAGNET").

I.S. acknowledges pulsar research at UBC is funded by an NSERC Discovery Grant and by the Canadian Institute for Advanced Research.

P.A. is supported by NASA Origins Grant NNX14AE16G and NASA ATP grant NNH12ZDA.

Table 4.4. Eclipse Mechanism Results

Model	Results
Refractive Eclipse	N_e too small
Free-Free Absorption	Requires a very cold and very clumped plasma
Induced Compton Scattering	Insufficient flux density at L and S bands[1]
Dispersive Pulse Smearing	Insufficient dispersive smearing mid-eclipse
Raman Scattering	$\tau \sim 1$ at T$\gtrsim 10^6$ K[2]

Note. — Approximate physical conditions required for each eclipse model to effectively remove the pulsar signal for Ter5A and Ter5P.
[1] - $\tau_{ic} \lesssim 1$ at observing frequencies of $\nu \sim 320$ MHz are possible for Ter5A.
[2] - Ter5ad requires larger plasma temperatures for this model to work $\sim 10^8$ K, which is too hot to use the cold plasma dispersion relationship to measure column densities.

Chapter 5

Conclusions

5.1 Summary

This dissertation has focused on how long-term timing of millisecond pulsars can be used to study the host star clusters and binary companions with incredible timing precision. The first chapter discussed how pulsar timing arrays can be used to determine the physical characteristics of the globular cluster Terzan 5. We calculated the mass density profile for the system — which allows a rare look at the true mass to light ratio of the cluster that does not come from simulation — and found upper-limits on any potential black hole in the core of the cluster.

In the following chapter we used fifteen years of timing data to test the validity of the Applegate model (Applegate & Shaham 1994) in characterizing orbital phase wander in redback pulsars. We provide evidence that two key predictions of this model are not present in our data. We then proceed to argue that this model has likely been misattributed to other redback pulsars, which used much shorter observing baselines.

Finally we attempted to characterize the eclipses of four redback pulsars, including an analysis that determines the average eclipse duration as a function of observing frequency and the electron column density as a function of the orbital phase. We then attempt to identify the most likely eclipse mechanism by searching for some set of plasma properties that include our measurements that can produce sufficient optical depth and reproduce the observed plasma properties found through timing. We then discuss how these properties can help us understand the rate of mass loss taking place in these close binaries and how MSPs are formed.

Each of these areas of research — globular cluster morphology/dynamics, stellar magneto-hydrodynamics, and mass outflow from low-mass stars — are important topics in the current Astrophysical literature. While some of this work is only capable

of producing various limits or excluding certain models from future consideration, each topic presented here is likely to have a lasting impact on future research into various fields of Astronomy.

Chapter A

Nearest Neighbor Accelerations

Chandrasekhar (1943; hereafter C43) derives the *Holtzmark* probability distribution for acceleration due to an infinite distribution of point masses with mean number density n. This is accomplished by first computing the distribution for N stars uniformly distributed within a radius R, and then letting $N \to \infty$ and $R \to \infty$ keeping the ratio $n = 3N/4\pi R^3$ constant. A characteristic size of the acceleration, for a star of mass m, must be $a \sim Gmn^{2/3}$ by dimensional analysis. If the probability distribution for the mass of each star is $P(m)$, then the distribution for vector acceleration $\boldsymbol{a}$ due to N stars in radius R is (C43 Equation 524 and 525)

$$\begin{aligned} P(\boldsymbol{a}) &= \Pi_{i=1}^{N} \int_{r_i<R} \frac{d^3x_i}{4\pi R^3/3} \int dm_i P(m_i) \delta^3 \left(\boldsymbol{a} - \sum_{i=1}^{N} \frac{Gm_i \boldsymbol{x}_i}{r_i^3} \right) \\ &= \int \frac{d^3s}{(2\pi)^3} e^{-i\boldsymbol{s}\cdot\boldsymbol{a}} \left[\int_{r<R} \frac{d^3x}{4\pi R^3/3} P(m) dm \; e^{iGm\boldsymbol{x}\cdot\boldsymbol{s}/r^3} \right]^N \\ &\to \frac{1}{2\pi^2 a^3} \int_0^\infty dx x \sin(x) e^{(a_{\rm NN}x/a)^{3/2}}. \end{aligned} \tag{.1}$$

In the second step, the δ function was expressed as a Fourier integral, and the same probability distribution is used for each of the N stars. In the last step, the

integrals over d^3x as well as the "acceleration wavenumber" $\boldsymbol{s}$ have been computed analytically by C43, with the result given by his Equation 549. The characteristic nearest-neighbor acceleration is

$$a_{\rm NN} \;=\; 2\pi G\left(\frac{4}{15}\langle m^{3/2}\rangle n\right)^{2/3}, \tag{.2}$$

where $\langle m^{3/2}\rangle = \int dm P(m) m^{3/2}$. Equation .1 is the *Holtzmark* distribution for the acceleration due to an infinite sea of particles exerting a $1/r^2$ force. Note that $P(\boldsymbol{a})$ is independent of the direction of the acceleration, as expected for an infinite uniform medium, and only depends on $a \equiv |\boldsymbol{a}|$. The ratio of $a_{\rm NN}$ to the mean cluster acceleration, for a cluster of mass $M_{\rm cl} \sim Nm$ and radius $R_{\rm cl} \sim (N/n)^{1/3}$, and N stars of mass m, can be estimated as

$$\frac{a_{\rm NN}}{GM_{\rm cl}/R_{\rm cl}^2} \;\sim\; 10^{-2}\left(\frac{10^6}{N}\right)^{1/3}, \tag{.3}$$

where N is the number of stars in the cluster. Hence the mean cluster acceleration is expected to dominate over the nearest neighbor acceleration by a large margin.

Only accelerations $a \gg a_{\rm NN}$ may be comparable to that of the smooth cluster acceleration. C43 Equation 559 gives the expansion of our Equation .1 to be

$$P(\boldsymbol{a}) \;\simeq\; \frac{15}{32\pi a_{\rm NN}^3}\sqrt{\frac{2}{\pi}}\left(\frac{a_{\rm NN}}{a}\right)^{9/2}. \tag{.4}$$

This may be converted into a distribution for the line-of-sight acceleration a_l by integrating over the perpendicular directions as

$$P(a_l) \;=\; \int 2\pi a_\perp da_\perp P(\boldsymbol{a}) = 2\pi\int_0^\infty da_\perp a_\perp \frac{15}{32\pi a_{\rm NN}^3}\sqrt{\frac{2}{\pi}}\left(\frac{a_{\rm NN}^2}{a_\perp^2+a_l^2}\right)^{9/4} = \frac{3}{4}\sqrt{\frac{2}{\pi}}\frac{1}{a_{\rm NN}}\left(\frac{a_{\rm NN}}{|a_l|}\right)^{5/2} \tag{.5}$$

The integral of this distribution gives the cumulative probability, $P_{\rm c}(a_l)$, of finding a line-of-sight acceleration larger than a value a_l to be

$$P_{\rm c}(a_l) \;=\; \int_{a_l}^{\infty} da_l' P(a_l') = \frac{1}{\sqrt{2\pi}} \left(\frac{a_{\rm NN}}{|a_l|} \right)^{3/2} . \qquad (.6)$$

This result shows that the likelihood that a near neighbor imparts an acceleration $a_l \gg a_{\rm NN}$ goes down steeply with a_l.

Chapter B

Jerk Profile

Appendix A reviewed C43's derivation of the Holtzmark distribution for the acceleration due to an infinite medium of point masses. C43 goes on to derive a joint probability distribution for accelerations and jerks. However, in the discussion following our Equation .2, it was shown that the mean potential of the cluster is likely much larger than the acceleration due to nearest neighbors, hence this joint distribution derived for an infinite medium is not useful in the present context. Instead the distribution for the jerks, regardless of the value of acceleration, is derived here.

A star of mass m at position $\boldsymbol{x}$ and with velocity $\boldsymbol{v}$ produces a jerk

$$\dot{\boldsymbol{a}} = Gm\left(\frac{\boldsymbol{v}}{r^3} - 3\frac{\boldsymbol{v}\cdot\boldsymbol{x}\boldsymbol{x}}{r^5}\right) \tag{.1}$$

at the origin. The physical meaning of jerk is the rate of change gravitational acceleration due to the motion of the particle. The distribution of stars is taken to be uniform with mean number density n, and the velocities are given by a Maxwell

Boltzmann distribution

$$P(\boldsymbol{v})d^3v = \frac{d^3v}{(2\pi\sigma^2)^{3/2}}e^{-v^2/2\sigma^2}, \tag{.2}$$

where σ is the velocity dispersion. The jerk can then be estimated as

$$\dot{a} \sim \frac{Gmv}{r^3} \sim Gm\sigma n. \tag{.3}$$

As with the distribution for acceleration in Equation .1, the distribution for the three-dimensional jerk $\dot{\boldsymbol{a}}$ due to the N stars is

$$\begin{aligned} P(\dot{\boldsymbol{a}}) &= \Pi_{i=1}^{N}\int_{r_i<R}\frac{d^3x_i}{4\pi R^3/3}\int dm_i P(m_i)\int\frac{d^3v_i}{(2\pi\sigma^2)^{3/2}}e^{-v_i^2/2\sigma^2}\delta^3\left[\dot{\boldsymbol{a}}-\sum_{i=1}^{N}Gm_i\left(\frac{\boldsymbol{v}_i}{r_i^3}-3\frac{\boldsymbol{v}_i\cdot\boldsymbol{x}_i}{r_i^5}\right)\right] \\ &= \int\frac{d^3s}{(2\pi)^3}e^{-i\boldsymbol{s}\cdot\dot{\boldsymbol{a}}}\left[\int_{r<R}\frac{d^3x}{4\pi R^3/3}P(m)dm\ \frac{d^3v}{(2\pi\sigma^2)^{3/2}}e^{-v^2/2\sigma^2}\ e^{iGm(\boldsymbol{v}\cdot\boldsymbol{s}/r^3-3\boldsymbol{v}\cdot\boldsymbol{x}\boldsymbol{x}\cdot\boldsymbol{s}/r^5)}\right]^N. \end{aligned} \tag{.4}$$

As this integral is not done in C43, the steps are outlined here. The limit of $N = 4\pi nR^3/3 \to \infty$ while keeping n constant gives the simplified form

$$P(\dot{\boldsymbol{a}}) = \int\frac{d^3s}{(2\pi)^3}e^{-i\boldsymbol{s}\cdot\dot{\boldsymbol{a}}-nC(\boldsymbol{s})} \tag{.5}$$

where

$$C(\boldsymbol{s}) = \int_0^\infty drr^2\int d\Omega\int\frac{d^3v}{(2\pi\sigma^2)^{3/2}}e^{-v^2/2\sigma^2}\int dmP(m)\left(1-e^{iGm(\boldsymbol{v}\cdot\boldsymbol{s}/r^3-3\boldsymbol{v}\cdot\boldsymbol{x}\boldsymbol{x}\cdot\boldsymbol{s}/r^5)}\right) \tag{.6}$$

First the velocity integral can be done by completing the square. The integrand is independent of the azimuthal angle and $\int d\phi = 2\pi$. Defining a dimensionless radius $x = r^3/Gm\sigma s$ allows all dimensions in the problem to be collected out front leaving

the following integral

$$C(\boldsymbol{s}) \;=\; \frac{2\pi G s}{3}\int dm P(m) m\sigma \int_0^\infty dx \int_{-1}^{1} d\mu \left(1 - e^{-(1+3\mu^2)/2x^2}\right) \equiv \frac{2\pi\xi}{3} G\langle m\rangle\sigma s \quad (.7)$$

where $\langle m\rangle = \int dm m P(m)$ and $\xi \simeq 3.04$ is the numerical value of the integral. Plugging this result back into Equation .5, the remaining integrals can be carried out analytically with the result that the three-dimensional jerk distribution is

$$P(\dot{\boldsymbol{a}}) \;=\; \frac{1}{\pi^2}\frac{\dot{a}_0}{(\dot{a}^2 + \dot{a}_0^2)^2}, \quad (.8)$$

where the characteristics value of the jerk is

$$\dot{a}_0 \;=\; \frac{2\pi\xi}{3} G\langle m\rangle\sigma n. \quad (.9)$$

As with acceleration, the line-of-sight jerk distribution, $P(\dot{a}_l)$, can be computed by integrating over the perpendicular components

$$P(\dot{a}_l) \;=\; \int_0^\infty 2\pi\dot{a}_\perp d\dot{a}_\perp P(\dot{\boldsymbol{a}}) = 2\pi\frac{1}{\pi^2}\int_0^\infty \dot{a}_\perp d\dot{a}_\perp \frac{\dot{a}_0}{(\dot{a}_\perp^2 + \dot{a}_l^2 + \dot{a}_0^2)^2} = \frac{\dot{a}_0/\pi}{\dot{a}_l^2 + \dot{a}_0^2}, \quad (.10)$$

and is a Lorentzian distribution.

Chapter C

Quadrupolar Moments

Beginning with an axisymmetric potential, the field produced by the pulsar's companion star is given by the following equation:

$$\Phi = -\frac{GM_c}{r} - GM_c \sum_{l=2}^{\infty} J_l \left(\frac{R_c^l}{r^{l+1}}\right) P_l(\cos\theta)\,, \tag{.1}$$

where J is the multipole moment, R_c is the radius of the companion star, and P_l is the legendre polynomial.

In the case of $\cos\theta = 0$, the force due to the potential is given by:

$$\frac{d\Phi}{dr} = \frac{GM_c}{r^2} + \frac{GM_c}{r_c^2} \sum_{l=2}^{\infty} (l+1) J_l \left(\frac{R_c}{r}\right)^l P_l(0)\,. \tag{.2}$$

Defining the orbital frequency to be $n = 2\pi/P_b$ and using our assumption that the companion star is filling its roche lobe by some factor κ ($R_c = \kappa R_l$), we simplify Equation .2:

$$n^2 r = \frac{GM}{r^2}\left[1 + \sum_{l=2}^{\infty} (l+1) J_l \left(\frac{\kappa R_l}{r}\right)^l P_l(0)\right], \tag{.3}$$

where $n^2 r = \frac{d\Phi}{dr}$.

Limiting ourselves to the contributions of the quadrupolar moment (J_2), n becomes:

$$n = \sqrt{\frac{GM}{r^3}} \left[1 - \frac{3}{2} J_2 \left(\frac{\kappa R_l}{r} \right)^2 \right]^{1/2} . \tag{.4}$$

For an axisymmetric potential, the angular momentum l_z must be constant such that:

$$l_z = r^2 \frac{d\phi}{dt} = r^2 n \simeq \sqrt{GMr} \left[1 - \frac{3}{4} J_2 \left(\frac{\kappa R_l}{r} \right)^2 \right] ,, \tag{.5}$$

where ϕ is the orbital phase and we have Taylor expanded the orbital frequency out to first order.

If we perturb perturb r such that:

$$r = \overline{r} + \delta r \, , \tag{.6}$$

where $\overline{r}$ is the average orbital separation and δr is the perturbation, then Equation .5 becomes a function of the average separation and orbital frequency:

$$l_z = \overline{r}^2 \overline{n} \simeq \sqrt{GM\overline{r}} \left[1 - \frac{3}{4} J_2 \left(\frac{\kappa R_l}{\overline{r}} \right)^2 \right] . \tag{.7}$$

If we let the multipole moment J_2 vary, we are left with:

$$0 = \sqrt{GM\overline{r}} \left[\frac{1}{2} \frac{\delta r}{2\overline{r}} - \frac{3}{4} \delta J_2 \left(\frac{\kappa R_l}{\overline{r}} \right)^2 \right] . \tag{.8}$$

This lets us express the fractional change in the orbital separation and orbital

frequency as:

$$\begin{aligned} \frac{\delta r}{\overline{r}} &= \frac{3}{2}\delta J_2 \left(\frac{\kappa R_l}{\overline{r}}\right)^2 \\ \frac{\delta n}{\overline{n}} &= -2\frac{\delta r}{\overline{r}} = -3\delta J_2 \left(\frac{\kappa R_l}{\overline{r}}\right)^2 . \end{aligned} \tag{.9}$$

Using this expression for the perturbed value of n, we can now express the change in T_0 as a function of the multipole moment. We begin by finding the integrated change in phase over a period of time t due to the perturbed frequency:

$$\Delta\phi = \int_0^t dt' \delta n(t') = \overline{n} \int_0^t dt' \left[-3\delta J_2(t') \left(\frac{\kappa R_l}{\overline{r}}\right)^2 \right] . \tag{.10}$$

The time average of Equation .10 yields:

$$\frac{\Delta\phi}{n\Delta t} = -3\delta\overline{J_2}(t) \left(\frac{\kappa R_l}{\overline{r}}\right)^2 . \tag{.11}$$

The orbital phase ϕ is related to the periastron passage time by:

$$\Delta\phi = -n\Delta T_0 . \tag{.12}$$

Combining this with Equation .11, we obtain a formula that relates the observed changes in periastron passage time to the multipole moments:

$$\frac{\Delta T_0}{\Delta t} = 3\delta\overline{J_2}(t) \left(\frac{\kappa R_l}{\overline{r}}\right)^2 . \tag{.13}$$

References

Abdo, A. A., Ajello, M., Allafort, A., Baldini, L., Ballet, J., Barbiellini, G., Baring, M. G., Bastieri, D., Belfiore, A., Bellazzini, R., & et al. 2013, ApJS, 208, 17

Alpar, M. A., Cheng, A. F., Ruderman, M. A., & Shaham, J. 1982, Nature, 300, 728

Anderson, S. B. 1993, PhD thesis, California Institute of Technology, Pasadena.

Antoniadis, J., Tauris, T. M., Ozel, F., Barr, E., Champion, D. J., & Freire, P. C. C. 2016, ArXiv e-prints

Applegate, J. H. 1992, ApJ, 385, 621

Applegate, J. H. & Shaham, J. 1994, ApJ, 436, 312

Archibald, A. M., Kaspi, V. M., Hessels, J. W. T., Stappers, B., Janssen, G., & Lyne, A. 2013, ArXiv e-prints

Archibald, A. M., Stairs, I. H., Ransom, S. M., Kaspi, V. M., Kondratiev, V. I., Lorimer, D. R., McLaughlin, M. A., Boyles, J., Hessels, J. W. T., Lynch, R., van Leeuwen, J., Roberts, M. S. E., Jenet, F., Champion, D. J., Rosen, R., Barlow, B. N., Dunlap, B. H., & Remillard, R. A. 2009, Science, 324, 1411

Arzoumanian, Z., Brazier, A., Burke-Spolaor, S., Chamberlin, S. J., Chatterjee, S., Christy, B., Cordes, J. M., Cornish, N. J., Crowter, K., Demorest, P. B., Deng, X.,

Dolch, T., Ellis, J. A., Ferdman, R. D., Fonseca, E., Garver-Daniels, N., Gonzalez, M. E., Jenet, F., Jones, G., Jones, M. L., Kaspi, V. M., Koop, M., Lam, M. T., Lazio, T. J. W., Levin, L., Lommen, A. N., Lorimer, D. R., Luo, J., Lynch, R. S., Madison, D. R., McLaughlin, M. A., McWilliams, S. T., Mingarelli, C. M. F., Nice, D. J., Palliyaguru, N., Pennucci, T. T., Ransom, S. M., Sampson, L., Sanidas, S. A., Sesana, A., Siemens, X., Simon, J., Stairs, I. H., Stinebring, D. R., Stovall, K., Swiggum, J., Taylor, S. R., Vallisneri, M., van Haasteren, R., Wang, Y., Zhu, W. W., & NANOGrav Collaboration. 2016, ApJ, 821, 13

Atwood, W. B., Abdo, A. A., Ackermann, M., Althouse, W., Anderson, B., Axelsson, M., Baldini, L., Ballet, J., Band, D. L., Barbiellini, G., & et al. 2009, ApJ, 697, 1071

Babak, S., Petiteau, A., Sesana, A., Brem, P., Rosado, P. A., Taylor, S. R., Lassus, A., Hessels, J. W. T., Bassa, C. G., Burgay, M., Caballero, R. N., Champion, D. J., Cognard, I., Desvignes, G., Gair, J. R., Guillemot, L., Janssen, G. H., Karuppusamy, R., Kramer, M., Lazarus, P., Lee, K. J., Lentati, L., Liu, K., Mingarelli, C. M. F., Osłowski, S., Perrodin, D., Possenti, A., Purver, M. B., Sanidas, S., Smits, R., Stappers, B., Theureau, G., Tiburzi, C., van Haasteren, R., Vecchio, A., & Verbiest, J. P. W. 2016, MNRAS, 455, 1665

Backer, D. C., Kulkarni, S. R., Heiles, C., Davis, M. M., & Goss, W. M. 1982, Nature, 300, 615

Bagchi, M., Lorimer, D. R., & Chennamangalam, J. 2011, MNRAS, 418, 477

Bahcall, J. N. & Wolf, R. A. 1976, ApJ, 209, 214

Baraffe, I., Chabrier, G., Allard, F., & Hauschildt, P. H. 1998, A&A, 337, 403

Barbuy, B., Bica, E., & Ortolani, S. 1998, A&A, 333, 117

Bassa, C. G., van Kerkwijk, M. H., Koester, D., & Verbunt, F. 2006, A&A, 456, 295

Bates, S. D., Bailes, M., Bhat, N. D. R., Burgay, M., Burke-Spolaor, S., D'Amico, N., Jameson, A., Johnston, S., Keith, M. J., Kramer, M., Levin, L., Lyne, A., Milia, S., Possenti, A., Stappers, B., & van Straten, W. 2011, MNRAS, 416, 2455

Bates, S. D., Lorimer, D. R., & Verbiest, J. P. W. 2013, MNRAS, 431, 1352

Baumgardt, H., Makino, J., & Ebisuzaki, T. 2004a, ApJ, 613, 1133

—. 2004b, ApJ, 613, 1143

Begin, S. 2006, PhD thesis, University of British Columbia

Benvenuto, O. G., De Vito, M. A., & Horvath, J. E. 2014, ApJ, 786, L7

Bergbusch, P. A. & VandenBerg, D. A. 2001, ApJ, 556, 322

Bhattacharya, D. & van den Heuvel, E. P. J. 1991, Phys. Rep., 203, 1

Blandford, R. D., Romani, R. W., & Applegate, J. H. 1987, MNRAS, 225, 51P

Bogdanov, S., van den Berg, M., Servillat, M., Heinke, C. O., Grindlay, J. E., Stairs, I. H., Ransom, S. M., Freire, P. C. C., Bégin, S., & Becker, W. 2011, ApJ, 730, 81

Booth, R. S., de Blok, W. J. G., Jonas, J. L., & Fanaroff, B. 2009, ArXiv e-prints

Burrows, A., Hubbard, W. B., Lunine, J. I., & Liebert, J. 2001, Reviews of Modern Physics, 73, 719

Burrows, A. & Liebert, J. 1993, Reviews of Modern Physics, 65, 301

Callanan, P. J., van Paradijs, J., & Rengelink, R. 1995, ApJ, 439, 928

Camilo, F., Lorimer, D. R., Freire, P., Lyne, A. G., & Manchester, R. N. 2000, ApJ, 535, 975

Chandrasekhar, S. 1943, Reviews of Modern Physics, 15, 1

Chen, H.-L., Chen, X., Tauris, T. M., & Han, Z. 2013, ApJ, 775, 27

Cheng, K. S., Ho, C., & Ruderman, M. 1986, ApJ, 300, 500

Chennamangalam, J., Lorimer, D. R., Mandel, I., & Bagchi, M. 2013, MNRAS, 431, 874

Cocozza, G., Ferraro, F. R., Possenti, A., & D'Amico, N. 2006, ApJ, 641, L129

D'Amico, N., Possenti, A., Manchester, R. N., Sarkissian, J., Lyne, A. G., & Camilo, F. 2001, ApJ, 561, L89

Damour, T. & Deruelle, N. 1985, Ann. Inst. Henri Poincaré Phys. Théor., Vol. 43, No. 1, p. 107 - 132, 43, 107

Damour, T. & Taylor, J. H. 1991, NASA STI/Recon Technical Report N, 92

Demorest, P. B., Pennucci, T., Ransom, S. M., Roberts, M. S. E., & Hessels, J. W. T. 2010, Nature, 467, 1081

DuPlain, R., Ransom, S., Demorest, P., Brandt, P., Ford, J., & Shelton, A. L. 2008, in Proc. SPIE, Vol. 7019, Advanced Software and Control for Astronomy II, 70191D

Eggleton, P. P. 1983, ApJ, 268, 368

Emmering, R. T. & London, R. A. 1990, ApJ, 363, 589

Ferraro, F. R., Dalessandro, E., Mucciarelli, A., Beccari, G., Rich, R. M., Origlia, L., Lanzoni, B., Rood, R. T., Valenti, E., Bellazzini, M., Ransom, S. M., & Cocozza, G. 2009, Nature, 462, 483

Ferraro, F. R., Possenti, A., D'Amico, N., & Sabbi, E. 2001, ApJ, 561, L93

Ferraro, F. R., Sabbi, E., Gratton, R., Possenti, A., D'Amico, N., Bragaglia, A., & Camilo, F. 2003, ApJ, 584, L13

Foreman-Mackey, D., Hogg, D. W., Lang, D., & Goodman, J. 2013, PASP, 125, 306

Foreman-Mackey, D., Price-Whelan, A., Ryan, G., Emily, Smith, M., Barbary, K., Hogg, D. W., & Brewer, B. J. 2014, triangle.py v0.1.1

Freire, P. C., Camilo, F., Kramer, M., Lorimer, D. R., Lyne, A. G., Manchester, R. N., & D'Amico, N. 2003, MNRAS, 340, 1359

Freire, P. C., Camilo, F., Lorimer, D. R., Lyne, A. G., Manchester, R. N., & D'Amico, N. 2001a, MNRAS, 326, 901

Freire, P. C., Kramer, M., Lyne, A. G., Camilo, F., Manchester, R. N., & D'Amico, N. 2001b, ApJ, 557, L105

Freire, P. C. C., Hessels, J. W. T., Nice, D. J., Ransom, S. M., Lorimer, D. R., & Stairs, I. H. 2005, ApJ, 621, 959

Freire, P. C. C., Ransom, S. M., Bégin, S., Stairs, I. H., Hessels, J. W. T., Frey, L. H., & Camilo, F. 2008, ApJ, 675, 670

Fruchter, A. S., Berman, G., Bower, G., Convery, M., Goss, W. M., Hankins, T. H., Klein, J. R., Nice, D. J., Ryba, M. F., Stinebring, D. R., Taylor, J. H., Thorsett, S. E., & Weisberg, J. M. 1990, ApJ, 351, 642

Fruchter, A. S., Stinebring, D. R., & Taylor, J. H. 1988, Nature, 333, 237

Giampapa, M. S., Rosner, R., Kashyap, V., Fleming, T. A., Schmitt, J. H. M. M., & Bookbinder, J. A. 1996, ApJ, 463, 707

Gnedin, O. Y., Zhao, H., Pringle, J. E., Fall, S. M., Livio, M., & Meylan, G. 2002, ApJ, 568, L23

Grindlay, J. E., Camilo, F., Heinke, C. O., Edmonds, P. D., Cohn, H., & Lugger, P. 2002, ApJ, 581, 470

Hall, D. S. 1989, Space Sci. Rev., 50, 219

Hathaway, D. H. 2010, Living Reviews in Solar Physics, 7, 1

Heggie, D. C. 1975, MNRAS, 173, 729

Heggie, D. C. & Hut, P. 2003, The Gravitational Million-Body Problem: A Multidisciplinary Approach to Star Cluster Dynamics (Cambridge; New York: Campridge University Press)

Heinke, C. O., Grindlay, J. E., Edmonds, P. D., Cohn, H. N., Lugger, P. M., Camilo, F., Bogdanov, S., & Freire, P. C. 2005, ApJ, 625, 796

Heinke, C. O., Grindlay, J. E., Lugger, P. M., Cohn, H. N., Edmonds, P. D., Lloyd, D. A., & Cool, A. M. 2003, ApJ, 598, 501

Heinke, C. O., Wijnands, R., Cohn, H. N., Lugger, P. M., Grindlay, J. E., Pooley, D., & Lewin, W. H. G. 2006, ApJ, 651, 1098

Hessels, J., Possenti, A., Bailes, M., Bassa, C., Freire, P. C. C., Lorimer, D. R., Lynch, R., Ransom, S. M., & Stairs, I. H. 2015, Advancing Astrophysics with the Square Kilometre Array (AASKA14), 47

Hessels, J. W. T., Ransom, S. M., Stairs, I. H., Freire, P. C. C., Kaspi, V. M., & Camilo, F. 2006, Science, 311, 1901

Hobbs, G. 2013, Classical and Quantum Gravity, 30, 224007

Hotan, A. W., van Straten, W., & Manchester, R. N. 2004, , 21, 302

Ivanova, N., Heinke, C. O., Rasio, F. A., Belczynski, K., & Fregeau, J. M. 2008, MNRAS, 386, 553

Jacoby, B. A., Cameron, P. B., Jenet, F. A., Anderson, S. B., Murty, R. N., & Kulkarni, S. R. 2006, ApJ, 644, L113

Johnston, K. V., Sigurdsson, S., & Hernquist, L. 1999, MNRAS, 302, 771

Kaplan, D. L., Escoffier, R. P., Lacasse, R. J., O'Neil, K., Ford, J. M., Ransom, S. M., Anderson, S. B., Cordes, J. M., Lazio, T. J. W., & Kulkarni, S. R. 2005, PASP, 117, 643

Keith, M. J., Coles, W., Shannon, R. M., Hobbs, G. B., Manchester, R. N., Bailes, M., Bhat, N. D. R., Burke-Spolaor, S., Champion, D. J., Chaudhary, A., Hotan, A. W., Khoo, J., Kocz, J., Osłowski, S., Ravi, V., Reynolds, J. E., Sarkissian, J., van Straten, W., & Yardley, D. R. B. 2013, MNRAS, 429, 2161

King, I. 1962, AJ, 67, 471

Kiziltan, B., Kottas, A., De Yoreo, M., & Thorsett, S. E. 2013, ApJ, 778, 66

Kroupa, P. 2001, MNRAS, 322, 231

Küpper, A. H. W., Maschberger, T., Kroupa, P., & Baumgardt, H. 2011, MNRAS, 417, 2300

Lanza, A. F. & Rodonò, M. 1999, A&A, 349, 887

Lanzoni, B., Ferraro, F. R., Dalessandro, E., Mucciarelli, A., Beccari, G., Miocchi, P., Bellazzini, M., Rich, R. M., Origlia, L., Valenti, E., Rood, R. T., & Ransom, S. M. 2010, ApJ, 717, 653

Lattimer, J. M. & Prakash, M. 2004, Science, 304, 536

Lazaridis, K., Verbiest, J. P. W., Tauris, T. M., Stappers, B. W., Kramer, M., Wex, N., Jessner, A., Cognard, I., Desvignes, G., Janssen, G. H., Purver, M. B., Theureau, G., Bassa, C. G., & Smits, R. 2011, MNRAS, 414, 3134

Lewin, W. H. G., van Paradijs, J., & Taam, R. E. 1993, Space Sci. Rev., 62, 223

Linares, M., Bahramian, A., Heinke, C., Wijnands, R., Patruno, A., Altamirano, D., Homan, J., Bogdanov, S., & Pooley, D. 2014, MNRAS, 438, 251

Lorimer, D. R., Faulkner, A. J., Lyne, A. G., Manchester, R. N., Kramer, M., McLaughlin, M. A., Hobbs, G., Possenti, A., Stairs, I. H., Camilo, F., Burgay, M., D'Amico, N., Corongiu, A., & Crawford, F. 2006, MNRAS, 372, 777

Lorimer, D. R. & Kramer, M. 2012, Handbook of Pulsar Astronomy

Lugger, P. M., Cohn, H. N., & Grindlay, J. E. 1995, ApJ, 439, 191

Lynch, R. S., Freire, P. C. C., Ransom, S. M., & Jacoby, B. A. 2012, ApJ, 745, 109

Lyne, A. G., Johnston, S., Manchester, R. N., Staveley-Smith, L., & D'Amico, N. 1990, Nature, 347, 650

Lyne, A. G., Mankelow, S. H., Bell, J. F., & Manchester, R. N. 2000, MNRAS, 316, 491

Manchester, R. N., Hobbs, G. B., Teoh, A., & Hobbs, M. 2005, VizieR Online Data Catalog, 7245, 0

Marinari, E. & Parisi, G. 1992, EPL (Europhysics Letters), 19, 451

Massari, D., Ferraro, F. R., Mucciarelli, A., Origlia, L., Dalessandro, E., & Lanzoni, B. 2014, Mem. Soc. Astron. Italiana, 85, 249

Massari, D., Mucciarelli, A., Dalessandro, E., Ferraro, F. R., Origlia, L., Lanzoni, B., Beccari, G., Rich, R. M., Valenti, E., & Ransom, S. M. 2012, ApJ, 755, L32

Miocchi, P., Lanzoni, B., Ferraro, F. R., Dalessandro, E., Vesperini, E., Pasquato, M., Beccari, G., Pallanca, C., & Sanna, N. 2013, ApJ, 774, 151

Nice, D. J., Arzoumanian, Z., & Thorsett, S. E. 2000, in Astronomical Society of the Pacific Conference Series, Vol. 202, IAU Colloq. 177: Pulsar Astronomy - 2000 and Beyond, ed. M. Kramer, N. Wex, & R. Wielebinski, 67

Nice, D. J. & Taylor, J. H. 1995, ApJ, 441, 429

Nice, D. J. & Thorsett, S. E. 1992, ApJ, 397, 249

Nice, D. J. & Thorsett, S. E. 1996, in Astronomical Society of the Pacific Conference Series, Vol. 105, IAU Colloq. 160: Pulsars: Problems and Progress, ed. S. Johnston, M. A. Walker, & M. Bailes, 523

Origlia, L., Massari, D., Rich, R. M., Mucciarelli, A., Ferraro, F. R., Dalessandro, E., & Lanzoni, B. 2013, ApJ, 779, L5

Ozel, F. & Freire, P. 2016, ArXiv e-prints

Pallanca, C., Dalessandro, E., Ferraro, F. R., Lanzoni, B., Rood, R. T., Possenti, A., D'Amico, N., Freire, P. C., Stairs, I., Ransom, S. M., & Bégin, S. 2010, ApJ, 725, 1165

Pan, Z., Hobbs, G., Li, D., Ridolfi, A., Wang, P., & Freire, P. 2016, MNRAS, 459, L26

Papitto, A., Ferrigno, C., Bozzo, E., Rea, N., Pavan, L., Burderi, L., Burgay, M., Campana, S., di Salvo, T., Falanga, M., Filipović, M. D., Freire, P. C. C., Hessels, J. W. T., Possenti, A., Ransom, S. M., Riggio, A., Romano, P., Sarkissian, J. M., Stairs, I. H., Stella, L., Torres, D. F., Wieringa, M. H., & Wong, G. F. 2013, Nature, 501, 517

Parsons, S. G., Marsh, T. R., Copperwheat, C. M., Dhillon, V. S., Littlefair, S. P., Hickman, R. D. G., Maxted, P. F. L., Gänsicke, B. T., Unda-Sanzana, E., Colque, J. P., Barraza, N., Sánchez, N., & Monard, L. A. G. 2010, MNRAS, 407, 2362

Patterson, J. 1984, ApJS, 54, 443

Phinney, E. S. 1993, in Astronomical Society of the Pacific Conference Series, Vol. 50, Structure and Dynamics of Globular Clusters, ed. S. G. Djorgovski & G. Meylan, 141

Phinney, E. S., Evans, C. R., Blandford, R. D., & Kulkarni, S. R. 1988, Nature, 333, 832

Pletsch, H. J. & Clark, C. J. 2015, ArXiv e-prints

Podsiadlowski, P. 1991, Nature, 350, 136

Pooley, D., Lewin, W. H. G., Anderson, S. F., Baumgardt, H., Filippenko, A. V., Gaensler, B. M., Homer, L., Hut, P., Kaspi, V. M., Makino, J., Margon, B., McMillan, S., Portegies Zwart, S., van der Klis, M., & Verbunt, F. 2003, ApJ, 591, L131

Prager, B., Ransom, S., Freire, P., Hessels, J., Stairs, I., Arras, P., & Cadelano, M. 2016, ArXiv e-prints

Pryor, C. & Meylan, G. 1993, in Astronomical Society of the Pacific Conference Series, Vol. 50, Structure and Dynamics of Globular Clusters, ed. S. G. Djorgovski & G. Meylan, 357

Ransom, S. 2011, PRESTO: PulsaR Exploration and Search TOolkit, Astrophysics Source Code Library

Ransom, S. M., Hessels, J. W. T., & Stairs, I. H. in prep 2017, ApJ

Ransom, S. M., Hessels, J. W. T., Stairs, I. H., Freire, P. C. C., Camilo, F., Kaspi, V. M., & Kaplan, D. L. 2005, Science, 307, 892

Ransom, S. M., Stairs, I. H., Backer, D. C., Greenhill, L. J., Bassa, C. G., Hessels, J. W. T., & Kaspi, V. M. 2004, ApJ, 604, 328

Reiners, A., Basri, G., & Browning, M. 2009, ApJ, 692, 538

Reynolds, M. T., Callanan, P. J., Fruchter, A. S., Torres, M. A. P., Beer, M. E., & Gibbons, R. A. 2007, MNRAS, 379, 1117

Roberts, M. S. E. 2013, in IAU Symposium, Vol. 291, Neutron Stars and Pulsars: Challenges and Opportunities after 80 years, ed. J. van Leeuwen, 127–132

Romani, R. W., Filippenko, A. V., & Cenko, S. B. 2015, ApJ, 804, 115

Romani, R. W. & Sanchez, N. 2016, ApJ, 828, 7

Roy, J., Ray, P. S., Bhattacharyya, B., Stappers, B., Chengalur, J. N., Deneva, J., Camilo, F., Johnson, T. J., Wolff, M., Hessels, J. W. T., Bassa, C. G., Keane, E. F., Ferrara, E. C., Harding, A. K., & Wood, K. S. 2015, ApJ, 800, L12

Ruderman, M., Shaham, J., & Tavani, M. 1989, ApJ, 336, 507

Scargle, J. D. 1982, ApJ, 263, 835

Schroeder, J. & Halpern, J. 2014, ApJ, 793, 78

Schwarz, R., Schwope, A. D., Vogel, J., Dhillon, V. S., Marsh, T. R., Copperwheat, C., Littlefair, S. P., & Kanbach, G. 2009, A&A, 496, 833

Shaifullah, G., Verbiest, J. P. W., Freire, P. C. C., Tauris, T. M., Wex, N., Osłowski, S., Stappers, B. W., Bassa, C. G., Caballero, R. N., Champion, D. J., Cognard, I., Desvignes, G., Graikou, E., Guillemot, L., Janssen, G. H., Jessner, A., Jordan, C., Karuppusamy, R., Kramer, M., Lazaridis, K., Lazarus, P., Lyne, A. G., McKee, J. W., Perrodin, D., Possenti, A., & Tiburzi, C. 2016, MNRAS, 462, 1029

Sharma, S., Bland-Hawthorn, J., Binney, J., Freeman, K. C., Steinmetz, M., Boeche, C., Bienaymé, O., Gibson, B. K., Gilmore, G. F., Grebel, E. K., Helmi, A., Kordopatis, G., Munari, U., Navarro, J. F., Parker, Q. A., Reid, W. A., Seabroke, G. M., Siebert, A., Watson, F., Williams, M. E. K., Wyse, R. F. G., & Zwitter, T. 2014, ApJ, 793, 51

Shklovskii, I. S. 1970, Soviet Ast., 13, 562

Simon, J. D. & Geha, M. 2007, ApJ, 670, 313

Skrutskie, M. F., Cutri, R. M., Stiening, R., Weinberg, M. D., Schneider, S., Carpenter, J. M., Beichman, C., Capps, R., Chester, T., Elias, J., Huchra, J., Liebert, J., Lonsdale, C., Monet, D. G., Price, S., Seitzer, P., Jarrett, T., Kirkpatrick, J. D., Gizis, J. E., Howard, E., Evans, T., Fowler, J., Fullmer, L., Hurt, R., Light, R., Kopan, E. L., Marsh, K. A., McCallon, H. L., Tam, R., Van Dyk, S., & Wheelock, S. 2006, AJ, 131, 1163

Stairs, I. H. 2002, in Astronomical Society of the Pacific Conference Series, Vol. 278, Single-Dish Radio Astronomy: Techniques and Applications, ed. S. Stanimirovic, D. Altschuler, P. Goldsmith, & C. Salter, 251–269

Stairs, I. H., Begin, S., Ransom, S., Freire, P., Hessels, J., Katz, J., Kaspi, V., & Camilo, F. 2006, in Bulletin of the American Astronomical Society, Vol. 38, American Astronomical Society Meeting Abstracts, 1118

Stappers, B. W., Bailes, M., Lyne, A. G., Camilo, F., Manchester, R. N., Sandhu, J. S., Toscano, M., & Bell, J. F. 2001, MNRAS, 321, 576

Stierwalt, S., Besla, G., Patton, D., Johnson, K., Kallivayalil, N., Putman, M., Privon, G., & Ross, G. 2015, ApJ, 805, 2

Stovall, K., Lynch, R. S., Ransom, S. M., Archibald, A. M., Banaszak, S., Biwer, C. M., Boyles, J., Dartez, L. P., Day, D., Ford, A. J., Flanigan, J., Garcia, A., Hessels, J. W. T., Hinojosa, J., Jenet, F. A., Kaplan, D. L., Karako-Argaman, C., Kaspi, V. M., Kondratiev, V. I., Leake, S., Lorimer, D. R., Lunsford, G., Martinez, J. G., Mata, A., McLaughlin, M. A., Roberts, M. S. E., Rohr, M. D., Siemens, X., Stairs, I. H., van Leeuwen, J., Walker, A. N., & Wells, B. L. 2014, ApJ, 791, 67

Strader, J., Smith, G. H., Larsen, S., Brodie, J. P., & Huchra, J. P. 2009, AJ, 138, 547

Swiggum, J. K., Lorimer, D. R., McLaughlin, M. A., Bates, S. D., Champion, D. J., Ransom, S. M., Lazarus, P., Brazier, A., Hessels, J. W. T., Nice, D. J., Ellis, J., Senty, T. R., Allen, B., Bhat, N. D. R., Bogdanov, S., Camilo, F., Chatterjee, S., Cordes, J. M., Crawford, F., Deneva, J. S., Freire, P. C. C., Jenet, F. A., Karako-Argaman, C., Kaspi, V. M., Knispel, B., Lee, K. J., van Leeuwen, J., Lynch, R., Lyne, A. G., Scholz, P., Siemens, X., Stairs, I. H., Stappers, B. W., Stovall, K., Venkataraman, A., & Zhu, W. W. 2014, ApJ, 787, 137

Tauris, T. M. & van den Heuvel, E. P. J. Formation and evolution of compact stellar X-ray sources, ed. W. H. G. Lewin & M. van der Klis, 623–665

Thompson, C., Blandford, R. D., Evans, C. R., & Phinney, E. S. 1994, ApJ, 422, 304

Turk, P. J. & Lorimer, D. R. 2013, MNRAS, 436, 3720

Valenti, E., Ferraro, F. R., & Origlia, L. 2007, AJ, 133, 1287

van der Marel, R. P. & Anderson, J. 2010, ApJ, 710, 1063

Verbiest, J. P. W., Bailes, M., Coles, W. A., Hobbs, G. B., van Straten, W., Champion, D. J., Jenet, F. A., Manchester, R. N., Bhat, N. D. R., Sarkissian, J. M., Yardley, D., Burke-Spolaor, S., Hotan, A. W., & You, X. P. 2009, MNRAS, 400, 951

Verbunt, F. & Freire, P. C. C. 2014, A&A, 561, A11

Wolszczan, A. & Frail, D. A. 1992, Nature, 355, 145

Yoshino, A. & Ichikawa, T. 2008, PASJ, 60, 493